LLC RESONANT INVERTER FOR INDUCTION HEATING APPLICATIONS

MR. SAICHOL CHUDJUARJEEN

A THESIS SUBMITTED IN PARTIAL FULFILLMENT
OF THE REQUIREMENTS FOR
THE DEGREE OF DOCTOR OF PHILOSOPHY OF ENGINEERING
(ELECTRICAL AND COMPUTER ENGINEERING)
FACULTY OF ENGINEERING
KING MONGKUT'S UNIVERSITY OF TECHNOLOGY THONBURI
2011

LLC Resonant Inverter for Induction Heating Applications

Mr. Saichol Chudjuarjeen M.Eng. (Electrical Engineering)

A Thesis Submitted in Partial Fulfillment
of the Requirement for
the Degree of Doctor of Philosophy of Engineering (Electrical and Computer Engineering)
Faculty of Engineering
King Mongkut's University of Technology Thonburi
2011

Thesis Committee

…… Chairman of Thesis Committee
(Assoc. Prof. Tanes Tanitteerapan, Ph.D.)

……. Member and Thesis Advisor
(Asst. Prof. Anawach Sangswang, Ph.D.)

……. Member
(Asst. Prof. Sumate Naetiladdanon, Ph.D.)

……. Member
(Asst. Prof. Wanchak Lenwari, Ph.D.)

……. Member
(Lect. Prasopchok Hothongkham, D.Eng.)

Thesis Title	LLC Resonant Inverter for Induction Heating Applications
Thesis Credits	36
Candidate	Mr. Saichol Chudjuarjeen
Thesis Advisor	Asst. Prof. Dr. Anawach Sangswang
Program	Doctor of Philosophy
Field of Study	Electrical and Computer Engineering
Department	Computer Engineering
Faculty	Engineering
B.E.	2554

Abstract

This thesis proposes a modified LLC resonant load configuration of a full-bridge inverter for induction heating applications. The LLC load configuration is a combination of a series inductor, a matching transformer, and an inductor and a capacitor connected in parallel. The proposed control is a modification of the classical LLC load by moving the series inductor to the primary winding of the matching transformer. The proposed configuration has the benefit of smaller inductance and inherent short-circuit protection capability in case that the short circuit occurs at the induction coil or from transformer saturation. The output power is controlled by using the asymmetrical voltage cancellation technique. With the use of a phase-locked loop control, the operating frequency is automatically adjusted to maintain the desired constant lagging phase angle under load parameter variation during the heating process. The proposed technique has the benefit of turn on switching loss being zero through zero voltage switching. A design procedure is presented that covers the LLC load configurations in the case of low quality factor ($Q < 10$). The validity of the proposed method is verified through computer simulation and hardware experiment at the operating frequency of 108.7 to 110.6 kHz. A correlation between theory, computer simulation and the experiment has been observed.

Keywords : Asymmetrical control / Induction heating / LLC resonant load / Parallel resonant inverter (PRI)/ Series resonant inverter (SRI) / Zero-voltage switching

หัวข้อวิทยานิพนธ์	อินเวอร์เตอร์เรโซแนนซ์แบบแอลแอลซีสำหรับงานให้ความร้อนแบบเหนี่ยวนำ
หน่วยกิต	36
ผู้เขียน	นายสายชล ชุดเจือจีน
อาจารย์ที่ปรึกษา	ผศ. ดร.อนวัช แสงสว่าง
หลักสูตร	ปรัชญาดุษฎีบัณฑิต
สาขาวิชา	วิศวกรรมไฟฟ้าและคอมพิวเตอร์
ภาควิชา	วิศวกรรมคอมพิวเตอร์
คณะ	วิศวกรรมศาสตร์
พ.ศ.	2554

บทคัดย่อ

วิทยานิพนธ์นี้นำเสนอการปรับปรุงวงจรเรโซแนนซ์แบบแอลแอลซีที่ใช้กับวงจรอินเวอร์เตอร์ชนิดเต็มบริดจ์สำหรับงานให้ความร้อนแบบเหนี่ยวนำ โหลดเรโซแนนซ์แบบแอลแอลซีประกอบด้วย ตัวเหนี่ยวนำความถี่สูง หม้อแปลงความถี่สูง และ ขดลวดเหนี่ยวนำที่ต่อขนานกับคาปาร์ซิเตอร์ โดยออกแบบให้ตัวเหนี่ยวนำความถี่สูงอยู่ด้านปฐมภูมิของหม้อแปลงความถี่สูง ซึ่งมีข้อดีคือ ตัวเหนี่ยวนำความถี่สูงรับภาระกระแสลดลงและสามารถป้องกันการลัดวงจรที่ขดลวดให้ความร้อนและลัดวงจรที่หม้อแปลงความถี่สูงเนื่องมาจากการอิ่มตัวของแกนเหล็กได้ การปรับกำลังด้านออกทำได้โดยใช้วิธีการควบคุมแบบอสมมาตร ที่มีการควบคุมให้ทำงานที่มุมเฟสล้าหลังคงที่ตลอดย่านการทำงาน เพื่อให้ได้การทำงานของสวิตซ์ในสภาวะนำกระแสเป็นศูนย์ซึ่งจะช่วยลดการสูญเสียของสวิตซ์ได้ ขั้นตอนการออกแบบโหลดเรโซแนนซ์แบบแอลแอลซีที่ใช้สำหรับขดลวดตัวประกอบคุณภาพ (Quality factor) ค่าน้อย ($Q < 10$) ได้ถูกนำเสนอ งานวิจัยที่นำเสนอถูกทดสอบโดยผลการจำลองด้วยคอมพิวเตอร์และผลการทดลองจริงที่ความถี่ทำงาน 108.7 ถึง 110.6 กิโลเฮิร์ต ซึ่งผลมีความสอดคล้องกันทฤษฎีและผลการจำลองด้วยระบบคอมพิวเตอร์

คำสำคัญ : การควบคุมแบบอสมมาตร / การสวิตซ์ที่แรงดันเป็นศูนย์ / การให้ความร้อนแบบเหนี่ยวนำ / วงจร โหลดเรโซแนนซ์แบบอนุกรมและขนาน / อินเวอร์เตอร์เรโซแนนซ์แบบขนาน / อินเวอร์เตอร์เรโซแนนซ์แบบอนุกรม

ACKNOWLEDGEMENTS

I am greatly indebted to many persons for helping me to complete this dissertation. First, I am most grateful to my advisors, Assoc. Prof. Dr. Anawach Sangswang for teaching me research methodology, paper writing and kindly suggestions on this research. I would like to thank Asst. Prof. Chayant koompai for his guidance, the opportunities and learning experiences he has given me are deeply appreciated. I would also like to thank the other members of my thesis committee: Dr. Tanes Tanitteerapan, Dr. Sumate Naetiladdanon, Dr. Wanchak Lenwari, and Dr. Prasopchok Hothongkham. I am very grateful for their help, taking their time and efforts in reviewing my dissertation.

I also would like to thank all seniors in Induction Heating Labs at Electrical Engineering Department, King Mongkut's University of Technology Thonburi for their friendship and moral support.

Special thanks to the Thailand Graduate Institute of Science and Technology, for the financial support.

I would like to extend my gratitude to Dr. Chika O. Nwankpa for his guidance and support, and specially for the excellent course offered by him. I would also like to thank the rest of the CEPE graduate students for their friendship and moral support when I researched at Drexel University.

Finally, this thesis could never have become a reality without the love and support of all my family and most especially that of my parents Sawat and Pethpranee, my wife Patcharamon and son Nipitphon.

CONTENTS

PAGE

ENGLISH ABSTRACT ii
THAI ABSTRACT iii
ACKNOWLEDGEMENTS vi
CONTENTS v
LIST OF TABLES vii
LIST OF FIGURES viii
LIST OF SYMBOLS xii

CHAPTER
1. INTRODUCTION 1
1.1 Literature Reviews 2
1.2 Motivation 17
1.3 Objective and approach 18
1.4 Organization of Thesis 19

2. PRINCIPLES OF INDUCTION HEATING 18
2.1 Induction Heating Effects 18
2.2 Load Characteristics 21
2.3 Induction Heating Applications 23
2.4 High Frequency Induction Heating Inverters 25
2.5 Control of Series Resonant Inverter 30
2.6 *L-LC* Resonant with Voltage Source Inverter 37

3. LLC RESONANT INVERTER 41
3.1 Circuit Description 41
3.2 Modes of Operation 42
3.3 Circuit Analysis 46
3.4 Current Gain 50
3.5 Switching and Conduction Losses 52
3.6 Proposed Control Strategy 57
3.7 Design Procedure 58

4. SIMULATION AND EXPERIMENTAL RESULTS 60
4.1 Resonant Inverter without the Matching Transformer 60
4.2 Resonant Inverter with the Matching Transformer 65

5. CONCLUSIONS 78
5.1 Summary of Contributions 78
5.2 Future Work 78

REFERENCES 80

APPENDIX 87

A Solving of LLC Resonant Load 88
B Fourier of Asymmetrical waveform 90
C Publications 94

CURRICULUM VITAE **115**

LIST OF TABLES

TABLES **PAGE**

1.1 Power losses and efficiency 12
4.1 Design specification and circuit parameters 41
4.2 Loss on components under asymmetrical control 41
4.3 Experimental results 72

LIST OF FIGURES

FIGURE **PAGE**

1.1 Characteristics of inverter for induction heating applications 1
1.2 (a) A full-bridge voltage source inverter and (b) voltage and current output waveforms of inverter 3
1.3 Half-bridge series resonant inverter 4
1.4 Switching frequency and input power 4
1.5 Power losses (P_s) and input power (P_i) 4
1.6 Full bridge voltage source inverter operating above resonance (ZVS) 5
1.7 Pulse density of square wave in PDM 5
1.8 Input voltage and current waveforms of inverter 5
1.9 Output voltage and current waveforms of inverter 6
1.10 The full-bridge voltage source inverter 6
1.11 Half – bridge inverter 7
1.12 Full – bridge inverter 7
1.13 1SW-ZVS inverter 7
1.14 1SW-ZCS inverter 8
1.15 Half-bridge series resonant inverter 9
1.16 Output voltage and current Waveforms of inverter operated at resonant frequency (a) typical wave forms (b) Experimental waveform 9
1.17 Input power versus inverter switching frequency 9
1.18 Output power versus inverter switching frequency 10
1.19 The full-bridge current source inverter 10
1.20 Topology and control (a) full bridge voltage source inverter (b) typical waveforms for the control strategies AVC control 11
1.21 Experimental waveforms of the output voltage and the output current with AVC control 11
1.22 The efficiency comparison between the proposed control technique and the conventional PS control and ADC control 12
1.23 Waveforms of the synthesis signal 12
1.24 The block diagram of the class-D inverter 13
1.25 The efficiency comparison between the proposed power control and the conventional PFM control scheme 13
1.26 Half-bridge series resonant inverter 14
1.27 Schematic and control of inverter 14
1.28 The experimental waveforms of DM control at output power of 150W 14
1.29 Efficiency comparisons of three controls 15
1.30 *L-LC* resonant inverter in full-bridge configuration 15
1.31 Schematic and control parameter of PDM 16
1.32 The full-bridge current source inverter 16
1.33 The experimental waveforms of power efficiency with FL algorithm 16
1.34 The experimental waveforms of power efficiency with PL algorithm 17
1.35 Previous *L-LC* configuration 18
1.36 Proposed LLC configuration 18
2.1 Induction heating load 20
2.2 Equivalent circuit of induction coil 20
2.3 Induction-heating load representation 22
2.4 Example of the load characteristics as a function of temperature 23

2.5 Induction-heating systems and processes 24
2.6 Power semiconductors used for induction heating 24
2.7 Power-frequency diagram for typical induction heat treating applications 25
2.8 Induction heating basic block diagram. 25
2.9 Induction heating treating inverter 26
2.10 Full bridge current source inverter with parallel resonant load 27
2.11 Output voltage and current wave forms of full bridge current source inverter operating above resonant frequency (ZCS) 27
2.12 Full bridge voltage source inverter with series resonant load 28
2.13 Output voltage and current waveforms of full bridge voltage source inverter operating above resonant frequency (ZVS) 28
2.14 Parallel and series resonant circuits 28
2.15 Parallel and series resonant circuits with sinusoidal voltage source 29
2.16 Wave forms of full bridge voltage source inverter operating with PFM 30
2.17 Normalized output power versus ratio of f_s/f_0 with PFM 31
2.18 Wave forms of full bridge voltage source inverter operating with PDM (a) Duty cycle =1, (b) Duty cycle =0.5, and (c) Duty cycle =0.25 33
2.19 Normalized output power versus ratio of duty cycle with PDM 33
2.20 Wave forms of full bridge voltage source inverter operating with ADC 34
2.21 Normalized output power versus ratio of duty cycle with ADC 35
2.22 Wave forms of full bridge voltage source inverter operating with PS 36
2.23 Normalized output power versus alpha angle with PS 37
2.24 *L-LC* resonant with full bridge voltage source inverter topology 38
2.25 Output voltage and current wave form of *L-LC* resonant full bridge voltage source inverter operating above resonant frequency (ZVS) 38
2.26 Equivalent circuit of *L-LC* resonant load 38
2.27 Steady-state behavior of the *L-LC* oscillator 39
2.28 Switching angle ϕ for different applications (Q-factors) and designs of current gain (β) 40
3.1 Full-bridge LLC resonant inverter. 41
3.2 Equivalent circuit 41
3.3 Modes of operation of inverter operations without stray capacitance 42
3.4 Typical waveforms of inverter operations with stray capacitance 43
3.5 Modes of operation of inverter operations with stray capacitance 44
3.6 Typical waveforms of inverter operations with stray capacitance 45
3.7 Output power (P_o) versus α 47
3.8 The output power as a function of α and inductance variation 49
3.9 Frequency response: output power (P_o) at various Q factors 50
3.10 Frequency response: output current (i_o) at various Q factors 50
3.11 Current gain and power angle at various Q factors (Q<10) 52
3.12 Theoretical waveforms of the turn off loss of switches 53
3.13 Theoretical waveforms of the conduction loss of the switch S_3 and the switch S_4 55
3.14 Proposed control block diagram of the LLC resonant inverter 57
3.15 Waveforms of the asymmetrical gate drive signal 58
4.1 Full-bridge series and parallel resonant inverter 60
4.2 Voltage and current waveforms at 100 % duty cycle 61
4.3 Simulation results with α = 70° 61
4.4 v_o and i_s waveforms at 93.45 kHz (i_s: 50 A/div, v_o: 50 V/div and Time: 5 div.) 62

4.5 v_C and i_o waveforms at 93.45 kHz (i_o: 20 A/div, v_C: 50 V/div and Time: 2 div.) 62
4.6 v_o and i_s waveforms at 95.7 kHz with (i_s: 20 A/div, v_o: 100 V/div and Time: 2 div.) 63
4.7 v_C and i_o waveforms at 95.7 kHz with (i_o: 20 A/div, v_C: 50 V/div and Time: 2 div.) 63
4.8 Simulated output voltage and current waveforms of the LLC full-bridge inverter with no phase shift at the full load (i_s: 4A/div, v_o: 50 V/div and Time: 2 div.) 65
4.9 Simulated load voltage and induction coil current waveforms of the LLC full-bridge inverter with no phase shift at the full load (i_o: 100 A/div, v_C: 50 V/div and Time: 2 div.) 65
4.10 Simulated voltage and current waveforms of the LLC full-bridge inverter at the S_4 with no phase shift at the full load (i_{s4}: 4 A/div, v_{s4}: 100 V/div and Time: 2 div.) 66
4.11 Simulated output voltage and current waveforms of the LLC full-bridge inverter at 62.5% load (i_s: 1.33A/div, v_o: 100 V/div and Time: 2 div.) 66
4.12 Simulated load voltage and induction coil current waveforms of the LLC full-bridge inverter at 62.5% load (i_o: 100 A/div, v_C: 50 V/div and Time: 2 div) 67
4.13 Simulated voltage and current waveforms of the LLC full-bridge inverter at the S_4 at 62.5% load (i_{s4}: 4 A/div, v_{s4}: 100 V/div and Time: 2 div.) 67
4.14 Simulated output voltage and current waveforms of the LLC full-bridge inverter at 32% load. (i_{s4}: 1.33A /div, v_o: 100V/div and Time: 2 div.) 68
4.15 Simulated load voltage and induction coil current waveforms of the LLC full-bridge inverter at 32% load (i_o: 100 A/div, v_C: 50 V/div and Time: 2 div.) 68
4.16 Simulated voltage and current waveforms of the LLC full-bridge inverter at the S_4 at 32% load (i_{s4}: 4 A/div, v_{s4}: 100 V/div and Time: 2 div.) 69
4.17 Experimental output voltage and current waveforms of the LLC full-bridge inverter with no phase shift at the full load (i_s: 2A/div, v_o: 100 V/div and Time: 2 div.) 70
4.18 Experimental load voltage and induction coil current waveforms of the LLC full-bridge inverter with no phase shift at the full load (i_o: 100 A/div, v_C: 50 V/div and Time: 2 div.) 70
4.19 Experimental voltage and current waveforms of the LLC full-bridge inverter at the S_4 with no phase shift at the full load (i_{s4}: 2.7 A/div, v_{s4}: 100 V/div and Time: 2 div.) 71
4.20 Experimental output voltage and current waveforms of the LLC full-bridge inverter at 62.5% load (i_s: 2A/div, v_o: 100 V/div and Time: 2 div.) 71
4.21 Experimental load voltage and induction coil current waveforms of the LLC full-bridge inverter at 62.5% load (i_o: 40 A/div, v_C: 20 V/div and Time: 2 div) 72
4.22 Experimental voltage and current waveforms of the LLC full-bridge inverter at the S_4 at 62.5% load (i_{s4}: 2.7A/div, v_{s4}: 100 V/div and Time: 2 div.) 72
4.23 Experimental output voltage and current waveforms of the LLC full-bridge inverter at 32% load (i_s: 2A/div, v_o: 100V/div and Time: 2 div.) 73
4.24 Experimental load voltage and induction coil current waveforms of the LLC full-bridge inverter at 32% load (i_o: 40A/div, v_C: 20V/div and Time:2 div.) 73
4.25 Experimental voltage and current waveforms of the LLC full-bridge inverter at the S_4 at 32% load (i_s 4: 2.7 A/div, v_{s4}: 100 V/div and Time: 2 div.) 74
4.26 Output voltage (v_o) vs and alpha angle (α) 75
4.27 Output power (P_o) vs and alpha angle (α) 75
4.28 Operating frequency (f_s) vs and alpha angle (α) 76

4.29 Efficiency comparisons between the calculation, asymmetrical control and pulse frequency modulation 77
5.1 LLC resonant inverter connected in parallel for higher applications. 79
B.1 Asymmetrical voltage waveform 90
C.1 Turn off loss at S_4 91
C.2 Diagram of turn off losses 92
C.3 Diagram of current of S_1 and S_2 93
C.4 Diagram of current of S_3 and S_4 93

LIST OF SYMBOLS

SYMBOL		UNIT
δ	Skin depth	mm.
ρ	Resistivity	Ω-m
L_S	Series inductor	H
C_b	Blocking capacitor	F
C_{oss}	Stray capacitance	F
C_p	Resonant capacitor	F
L_{coil}	Induction coil inductor	H
R_{eq}	Coil resistance	ohms
f_s	Switching frequency	Hz
f_r	Resonant frequency	Hz
α	Alpha angle	degree
D	Duty cycle	percent
ϕ	Power angle	degree
i_s	Output current of inverter	A
i_o	Coil current	A
v_o	Output voltage of inverter	V
v_C	Resonant capacitor voltage	V
V_{DC}	DC voltage	V
t_{Coss}	Charging time of stray capacitance	sec
t_r	Rise time	sec
t_f	Fall time	sec
t_{on}	Turn on time	sec
V_{DC}	DC voltage	V

CHAPTER 1 INTRODUCTION

Induction heating is a well-known technique to produce very high temperature. Every useful work piece of metal has gone through some kind of induction heat treatment. Metals are melted for alloy steels. Other applications are forging, soldering, or molding. They are quickly heated and then cooled for surface hardening, or heated to medium temperatures for annealing to increase litheness. One or several of these heat treatments is applied to every gear, chassis, drive shaft, screw, car door, or needle. Many heating methods exist in industry to perform these heating tasks. Of all methods, induction heating is the most efficient and effective because the heat is actually generated inside the work piece.

For applications like steel melting, brazing, and surface hardening, an appropriate frequency must be used depending on the work-piece geometry and skin-depth requirements [1], [2]. In the 1930's, the applied currents were taken directly from the 60 Hz or 50 Hz of ac power line when the induction heating was introduced to the industry. The induction heating applications can be classified as low frequencies (f < 3 kHz), medium frequencies (1 kHz < f < 100 kHz), and high frequency (f >100 kHz) [68]. Since the 1980's, research has been focused on the design of solid state ac switching power supplies that operates in the 10 kHz -500 kHz frequency range. Solid-state power can reach efficiencies of around 90%, but their transistors cannot handle high power levels.

Recent development of power semiconductor devices, new circuit techniques, and control schemes in high-frequency circuits using advanced power devices such as MOSFETs and insulated gate bipolar transistors (IGBTs) have progressed the induction heating applications continuously [1]–[18]. Various resonant inverters using power devices such as MOSFETs and IGBTs offer reduced switching loss by soft-switching technique and attractive possibilities in developing high-frequency operation, high efficiency, small size, and light weight.

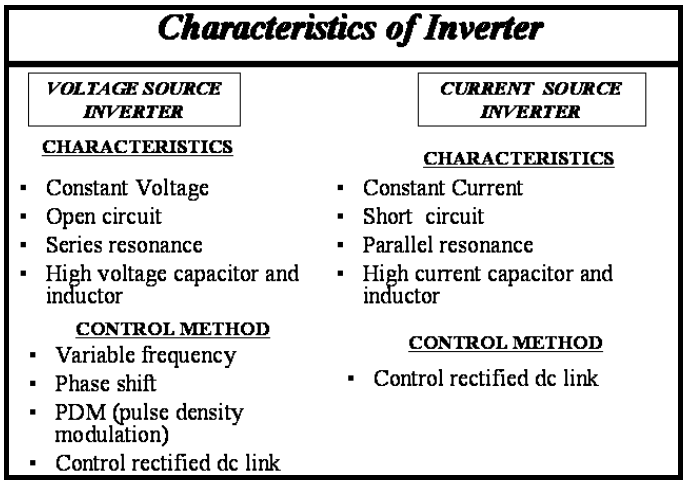

Figure 1.1 Characteristics of inverter for induction heating applications

An overview of characteristics and control methods of the voltage source and the current source topology is illustrated in Figure 1.1. Various control methods used in voltage source inverter for improving the efficiency are variable frequency or pulse

frequency modulation (PFM), phase shift (PS), pulse density modulation (PDM) and control rectified dc link. A large number of topologies have been developed in this area. Current-fed and voltage-fed inverters are among the most commonly used types [2]. A Current Source Inverter (CSI) has a limited number of control methods, but it is less affected by input voltage ripples and it has short circuited protection capability [2]–[5]. Voltage-fed or Current-fed inverter for induction heating applications have employed many switches such as MOSFET, SIT, SCR. MOSFETs are the solid-state devices suitable for high frequency induction heating applications. When MOSFETs are used for high frequency applications, switching losses increase significantly resulting in low efficiencies, and in some cases, device destruction. To reduce the switching losses, MOSFETs are operated with soft-switching, that is, with zero voltage turn-on (ZVS), or zero current turn-off (ZCS). Because of inherent characteristic of the MOSFETs, certain circuit topologies and switching strategies are more suitable and economical than others.

Voltage-source resonant inverters (VSI) are widely used in applications that require output power control capability where a zero-voltage switching (ZVS) condition must be met to ensure a high efficiency [4-7]. Recent developments in switching schemes and control methods have made the voltage-source resonant inverters widely used in applications that require output power control capability. For example, in pulse-frequency modulation (PFM), the output power can be controlled by varying the switching frequency while the inverter operates under zero- voltage switching (ZVS) scheme [3]. This variable-frequency operation has several disadvantages [1, 4] including a wide noise spectrum which makes it difficult to control electromagnetic interference (EMI), more complex filtering of the output-voltage ripple, and poor utilization of magnetic components. The pulse-density modulation (PDM) method regulates the output power by varying the period in which the inverter supplies high-frequency current to the induction coil [4, 5]. The PDM has the demerit that the power is a problem to the flicker regulations. The phase-shift (PS) control technique in [6, 8,16] varies the output power by shifting the phase of the switch conduction sequences. The asymmetrical duty-cycle (ADC) control technique employs an unequal duty-cycle operation of the switches in the converter [9-12]. The asymmetrical voltage-cancellation (AVC) is then proposed in [13] where the authors describe voltage-cancellation for conventional fixed-frequency control strategies. In [13], the AVC is implemented in a full-bridge series resonant inverter. By using the mentioned techniques in fix frequency and the optimum duty cycle for ZVS operation, it is rather difficult to control the output power due to variation of parameters in the resonant load during the heating process.

The series-resonant inverter needs an output transformer for matching the output power to the load. Most induction heating applications require accuracy in output power control capability. For example, cooking appliances require accurate power control over a wide range of power for different cooking purposes where a ZVS condition must be met to ensure high efficiency [16-23]. The reviews of research are described in the next section.

1.1 LITERATURE REVIEWS

In 1995, L. Grajales et al. [6, 68] proposed the analysis and design of a 500 kHz series resonant inverter for induction heating with small-signal analysis of a phase-shift controller where the full bridge topology and output wave form are shown in Figure1.2.

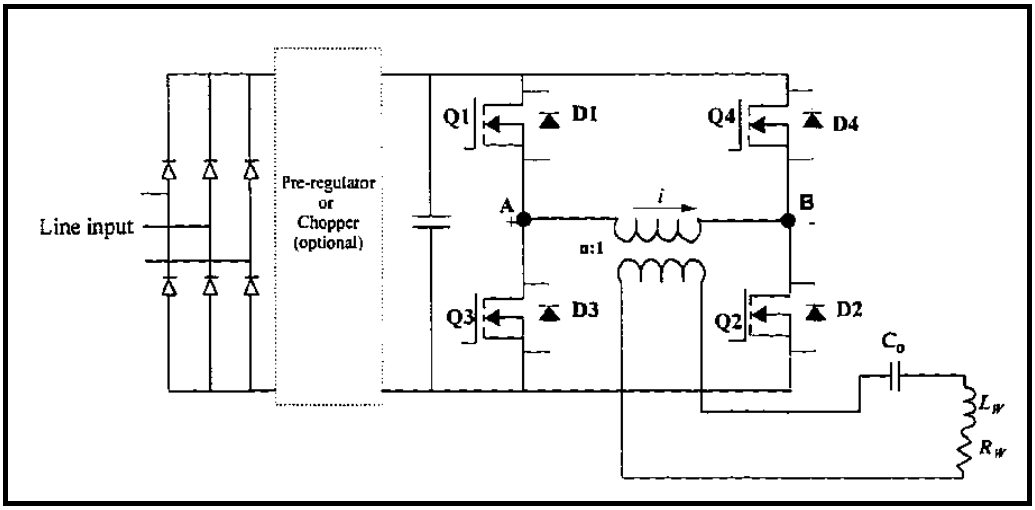

(a)

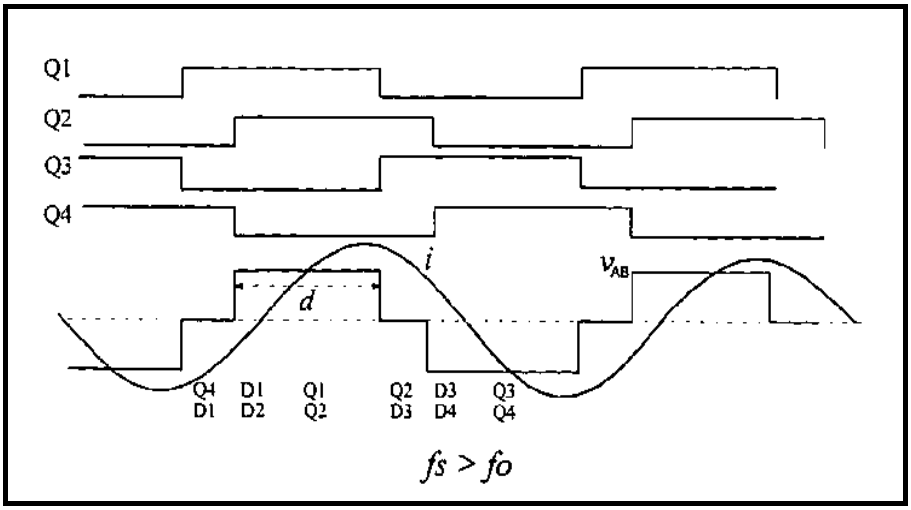

(b)

Figure 1.2 (a) A full-bridge voltage source inverter and (b) voltage and current output waveforms of inverter [6, 68]

A new phase-shift controlled series-resonant inverter operating at zero voltage switching (ZVS) is used as the power supply for an induction heating system. This system has two control loops: the phase-shift control loop regulates the output power, and the frequency control loop ensures ZVS for all load conditions. This control allows above resonant frequency control for induction heating. The output current and output power of inverter have been controlled by adjusting the pulse width of voltage across the switches. The drawback of increasing the switching frequency is overcome by the reduction in the turn-off current.

In 1995, Henry W. Koertzen et al. [64] proposed a design of the half-bridge series resonant inverter for induction cooking appliances. The switching frequency (f_s) is between 20 kHz up to 100 kHz operating above the resonant frequency (f_r) to control the output power (50W to 2,250W), as shown in Figures 1.3 and 1.4.

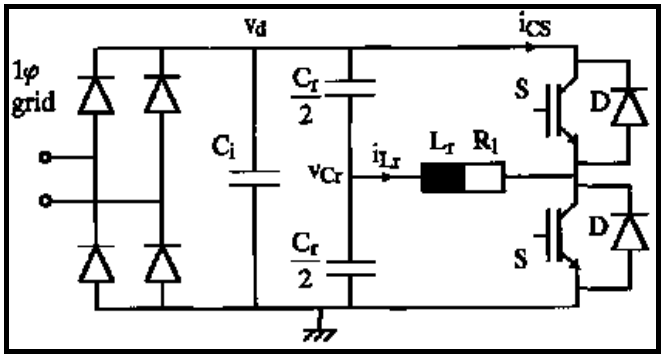

Figure 1.3 Half-bridge series resonant inverter [64]

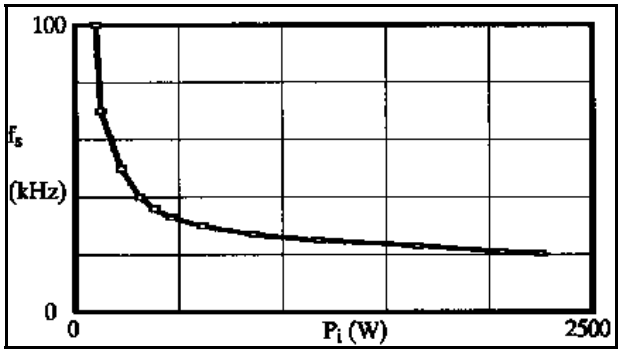

Figure 1.4 Switching frequency and input power.

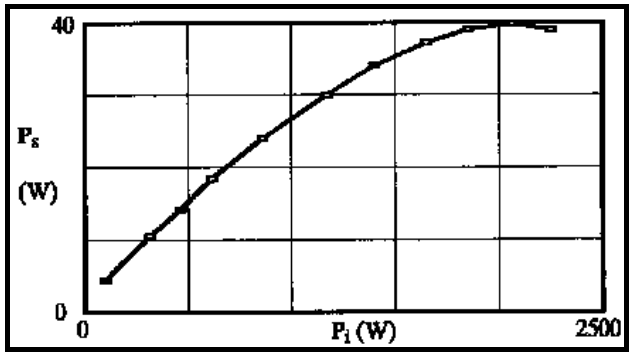

Figure 1.5 Power losses (P_s) and input power (P_i) [64]

The relationship between the input power (P_i) and power loss (P_s) is experimentally obtained as depicted in Figure 1.5. The efficiency is higher than 95%. As a result, the half-bridge series resonant inverter is considered the most proper for induction cooking appliances because of its high efficiency, system and control simplicity, compactness, low cost, and high power factor. In addition, only a small capacitor (C_i) is required in the input source.

In 1996, Hideaki Fujita and Hirofumi Akagi et al. [39] proposed a power control scheme of the full-bridge series resonant inverter for induction melting applications (4kW), based on the pulse density modulation (PDM), ZCS and ZVS condition for reduce switching losses of semiconductor devices. The switching devices under consideration are 4 MOSFETs. Lossless snubbing circuits which consist of four capacitors (C_1, C_2, C_3 and C_4) are used to achieve ZVS condition, as shown in Figure. 1.6.

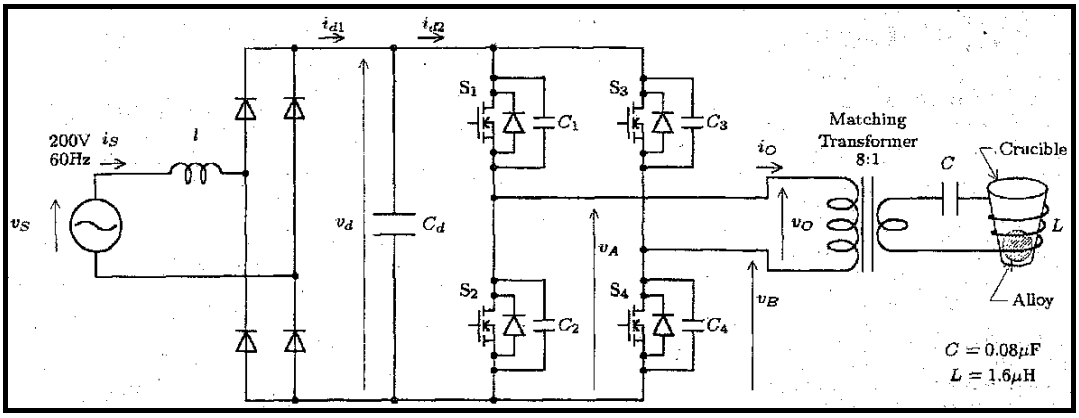

Figure 1.6 Full bridge voltage source inverter operating above resonance (ZVS) [39]

The switching frequency (f_s) is set to 450 kHz, and they control the output power of the inverter by regulating the pulse density of the square wave in PDM between 1/16 (light load) and 16/16 (full load), as shown in Figure 1.7.

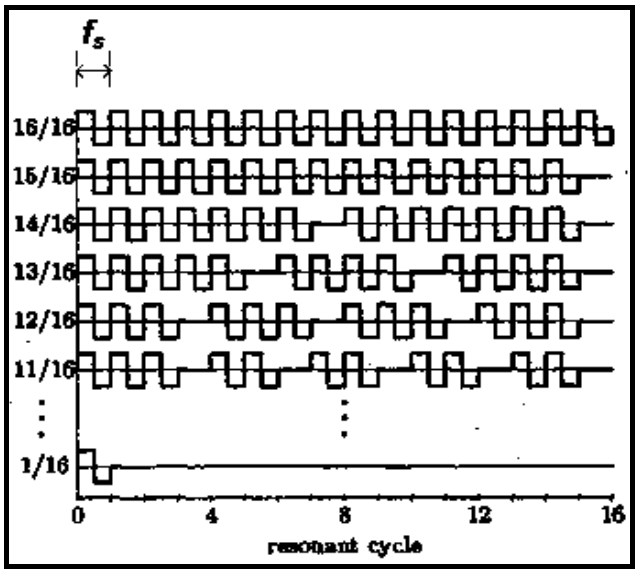

Figure 1.7 Pulse density of square wave in PDM [39]

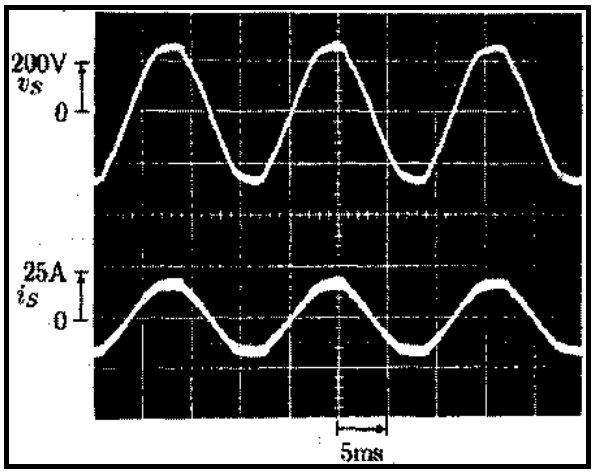

Figure 1.8 Input voltage and current waveforms of inverter [39]

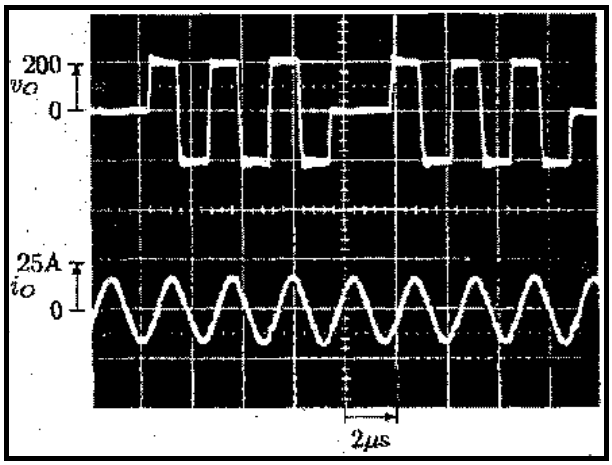

Figure 1.9 Output voltage and current waveforms of inverter [39]

Figure 1.8 shows the experimental waveforms of the input voltage and current at 2 kW. The input current waveform is nearly sinusoidal waveform which implies a high input power factor. Figure 1.9 shows the experimental waveforms of the output voltage and current at the same 2 kW. Then, the power control scheme is proper for induction melting applications due to its high power factor and low switching losses with ZCS-ZVS conditions. However, it results in power fluctuation in the power line which may cause damages to sensitive devices with high switching frequency (with PDM).

In 1998, Atsushi Okuno and et al. [54] proposed a feasible development of soft-switched using static induction transistors (SIT's) inverter with load-adaptive frequency-tracking control scheme for induction heating as shown in Figure 1.10.

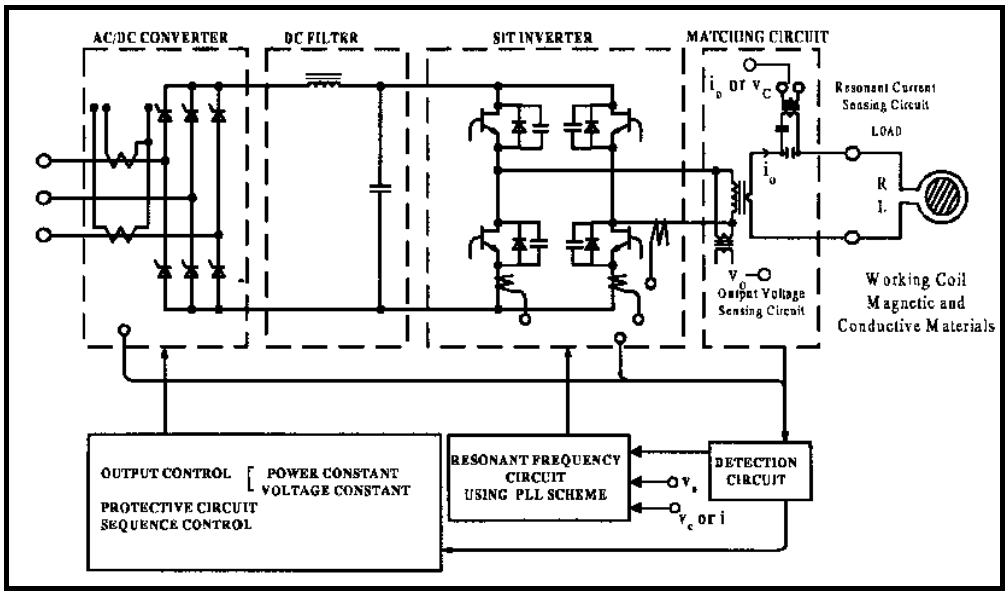

Figure 1.10 The full-bridge voltage source inverter [54].

This paper proposed a pulse amplitude modulated voltage source-type series load-resonant inverter using the latest high-power SIT's, operating at the frequency slightly higher than the resonant frequency with load-adaptive tuned operating frequency-

tracking scheme. However, the power factor is low when the firing angle of the rectifier decreases.

In 2002, S. Llorente and et al. [67] reviews a comparison of four inverters suitable for induction cookers (3 kW). The authors discuss the half-bridge inverter (HB), full-bridge inverter (FB), single-switch ZVS (1SW-ZVS) and single-switch ZCS (1SW-ZCS) as shown in Figure 1.11-1.14. The proposed controls are focused on a power device stress, efficiency, power control and electromagnetic emissions. The switching device under consideration is IGBTs, and the switching frequency (f_s) is equal to 50 kHz, above the resonant frequency (f_r), to control the output power at full load of 1000 W and 3000 W. These controls are implemented in an Altera EPM9320ALC with VHDL hardware description language.

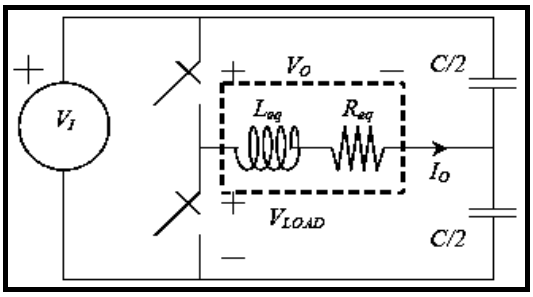

Figure 1.11 Half – bridge inverter [67]

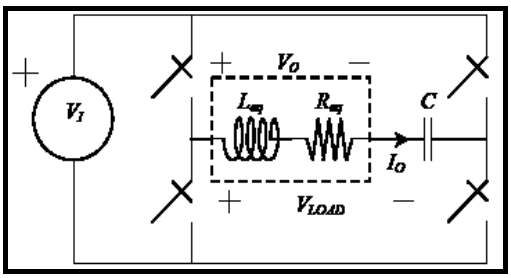

Figure 1.12 Full – bridge inverter [67]

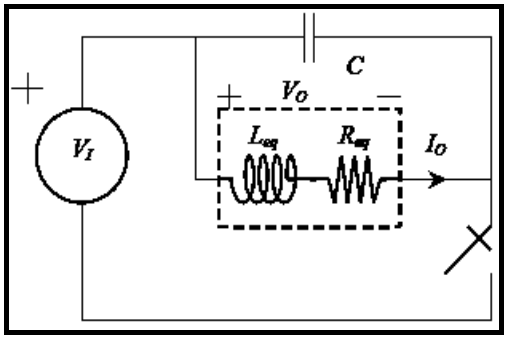

Figure 1.13 1SW-ZVS inverter [67]

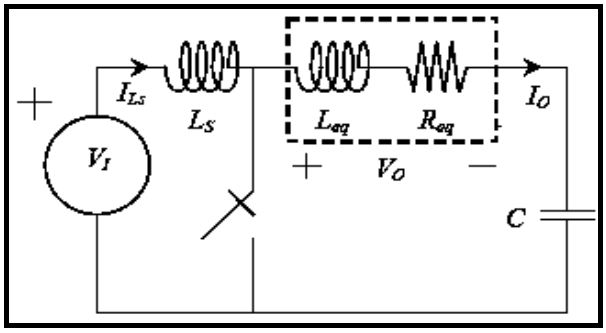

Figure 1.14 1SW-ZCS inverter [67]

Table 1.1 shows the values of components and semiconductor stresses among four inverters. The system efficiency can be calculated and considered from the power loss P_{tot} of the system that depends on the switching loss P_{SW} in each device.

The efficiency of systems, are shown in Table 1.1.

Table 1.1 Power losses and efficiency [67].

	P_{sw} (W)	P_{tot} (W)	η (%)
Full-bridge	9.540	38.162	98.74
Half-bridge	24.838	49.676	98.37
1SW-ZVS	71.081	71.081	97.68
1SW-ZCS	57.421	57.421	98.12

From Table 1.1, the efficiency of the full-bridge inverter is higher than other inverters because it has lower semiconductor stress depending on the maximum voltages across and the currents flow through the switches. For this reason, the switching losses and the overall losses of full-bridge inverter are lower than three inverters (HB, 1SW-ZCS and 1SW-ZVS) and to obtain high efficiency. However, this control is the most complex because there are many switches to control. Therefore, the half-bridge inverter is mostly chosen and suitable than the other inverters for induction cooking because it has similar advantages to those of the full-bridge inverter such as high efficiency, and control simplicity due to its low number of switches. The control is easy to implement with lower cost than the full-bridge inverter. While the single switch ZCS and ZVS controls are simple due to its lower number of switches, their efficiency is suffered from the high semiconductor stress.

In 2002, P. Viriya et al. [4] proposed a power control of the half-bridge series resonant inverter for induction cooker (2 kW) as shown in Figure 1.15 based on square wave modulation (SW) by varying the switching frequency (f_s) and using the Thevenin short-open circuit method to analyze the proposed circuit characteristics. The switching frequency (f_s) is at 30, 35 and 40 kHz, depending on the loads. Moreover, a comparison of the testing results, between the theoretical and experimental perspectives are presented. The output voltage and current waveforms are shown in Figure 1.16.

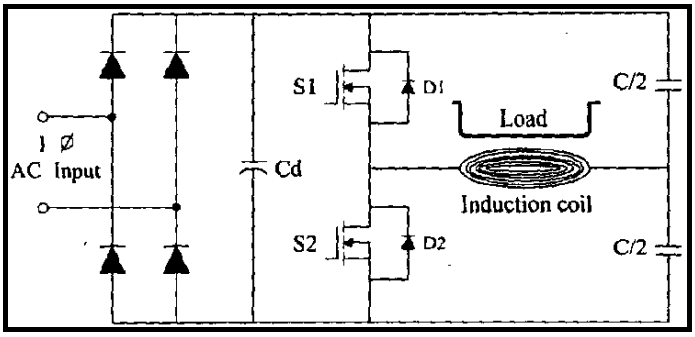

Figure 1.15 Half-bridge series resonant inverter [4]

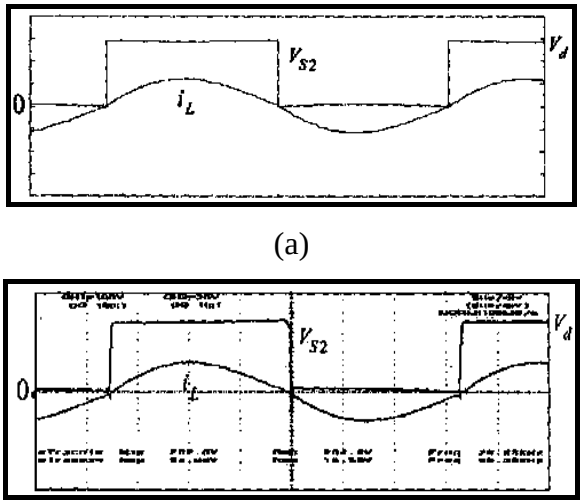

Figure 1.16 Output voltage and current waveforms of inverter operated at resonant frequency (a) typical wave forms (b) Experimental waveform [4]

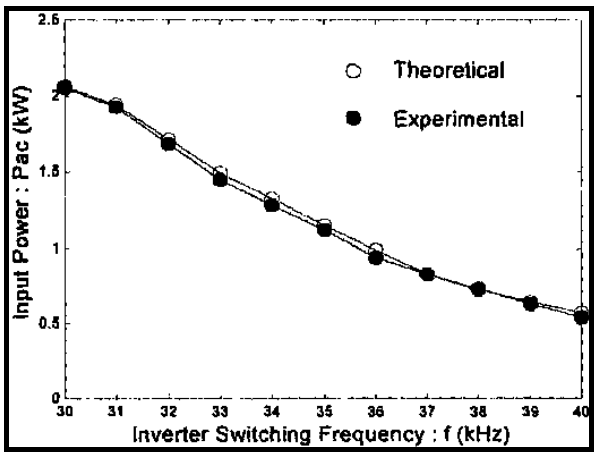

Figure 1.17 Input power versus inverter switching frequency [4]

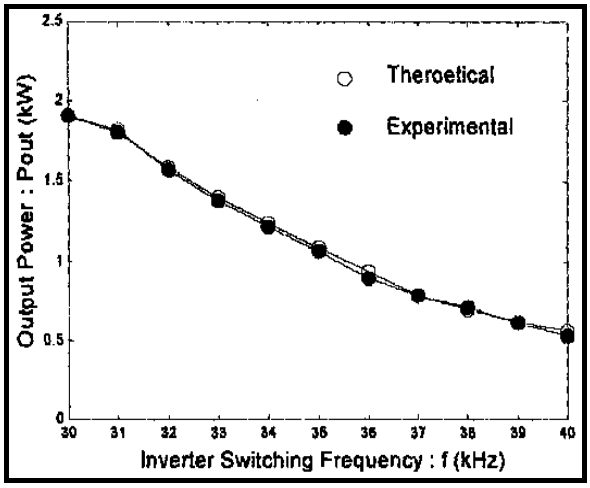

Figure 1.18 Output power versus inverter switching frequency [4]

Figures 1.17 and 1.18 show comparisons of the input and output power variation between the theoretical calculations and the experimental results at the switching frequency (f_s) from 30 kHz (2 kW) to 40 kHz (500 W), depending on the loads. This proposed power control is complex and it is rather difficult to filter the output-voltage ripple out.

In 2004, S. Chudjuarjeen, C. Koompai and V. Monyakul [2] proposed a full-bridge current-fed inverter with automatic frequency control for forging application as shown in Figure 1.19.

This research describes the IGBT full-bridge current-fed inverter for forging application. The operating frequency is automatically adjusted to maintain constant leading phase angle when parameters of the induction heating load are varied. The output power is controlled by the input current setting. The load voltage is controlled to protect the IGBTs. In controlling the output power, the input power factor also decreases when the firing angle of the phase-controlled rectifier is adjusted in the manner that increases the output power.

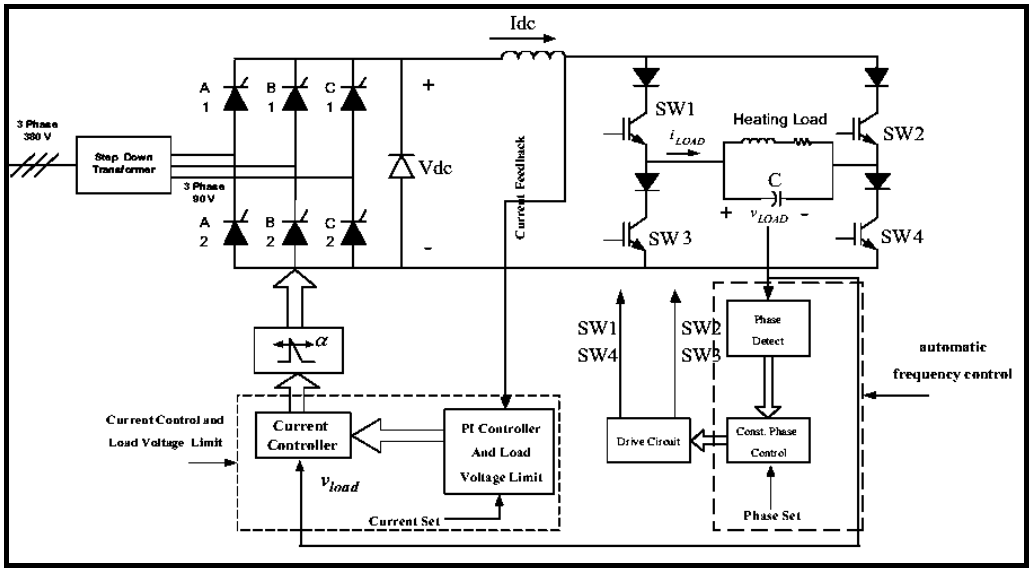

Figure 1.19 The full-bridge current source inverter [2]

In 2004, Jose M. Burdio et al. [13] proposed a control technique and analyzed the asymmetrical voltage-cancellation (AVC) control by using the full-bridge series resonant inverter for induction cooking appliances (2 kW) as shown in Figure 1.20 (a). This technique is used to control the output power by adjusting the control angle (α) while the switching period T_s is constant. The proposed control technique is focused on ZVS condition to minimize losses in the switches of the inverter as shown in Figure 1.20(b). The experimental output voltage and current waveforms is shown in Figure 1.21. This paper also presents a comparison of the testing results of the conventional phase-shift (PS) and asymmetrical duty-cycle control (ADC).

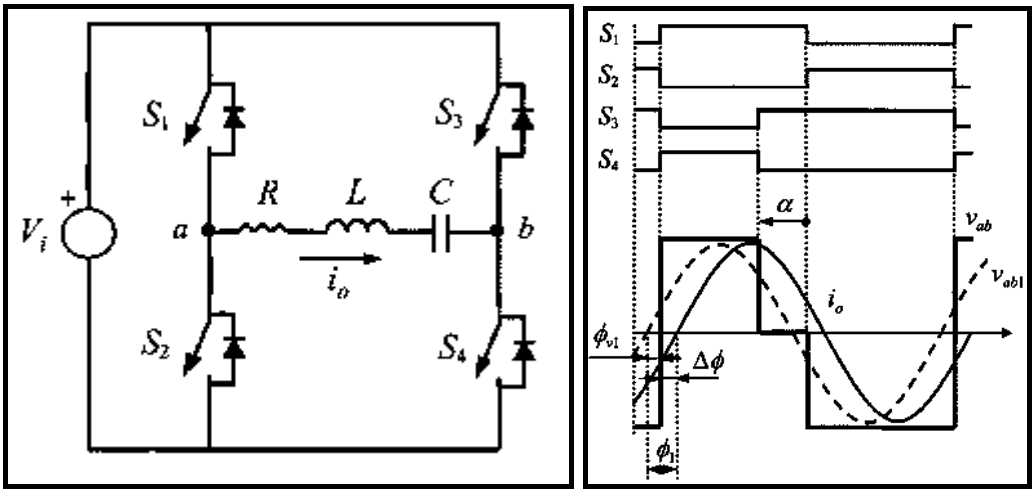

(a) (b)

Figure 1.20 Topology and control (a) full bridge voltage source inverter

(b) typical waveforms for the control strategies AVC control [13]

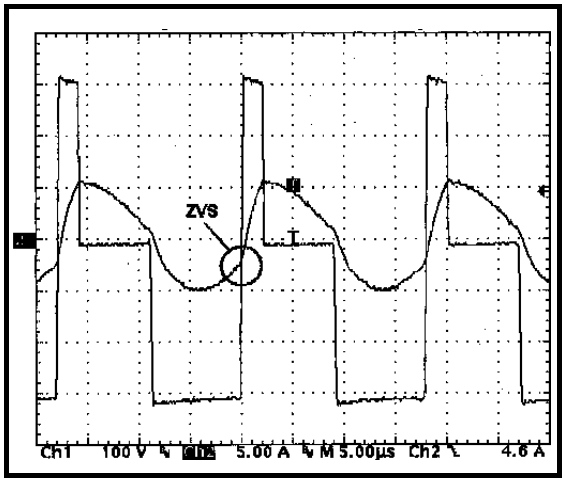

Figure 1.21 Experimental waveforms of the output voltage and the output current with AVC control [13]

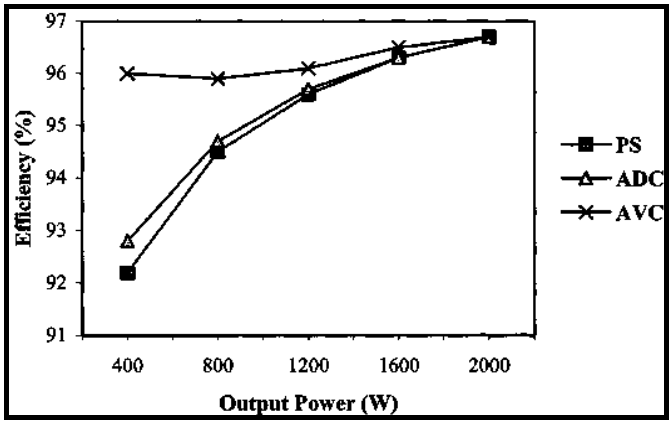

Figure 1.22 The efficiency comparison between the proposed control technique and the conventional PS control and ADC control [13]

Figure 1.22 shows a comparison of the efficiency between the proposed control technique and the conventional control (the PS control and the ADC control) at a switching frequency f_p = 55.5 kHz. The performance of the proposed control technique is proper for induction cooking applications because of its small losses with ZVS condition, and its higher efficiency than the other conventional control. The demerit of this control is not suitable for the parameters variation load applications such as melting, forging and etc.

In 2007, Nam-Ju Park et al. [4] proposed a power control of the Class-D inverter for induction heating jar application based on ZVS, and PDM using the half-bridge inverter by varying the duty ratio (D_{power}=D) of low frequency (f_p) and combine with the fixed high frequency (f_s). The switching devices under consideration are two IGBTs. The low frequency (f_p) is fixed at 5.4 Hz, while the high frequency (f_s) is kept constant at 42.8 kHz. The switching signal (D_{sw}) as shown in Figure 1.23 is sent to the gate drive circuit to generate the gate signals for the inverter, as shown in Figure 1.24.

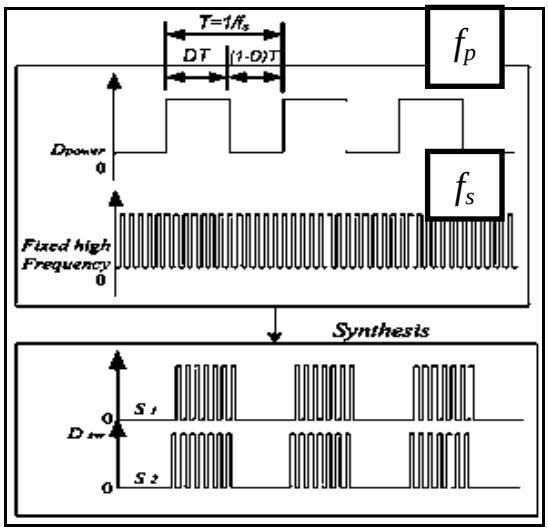

Figure 1.23 Waveforms of the synthesis signal [4]

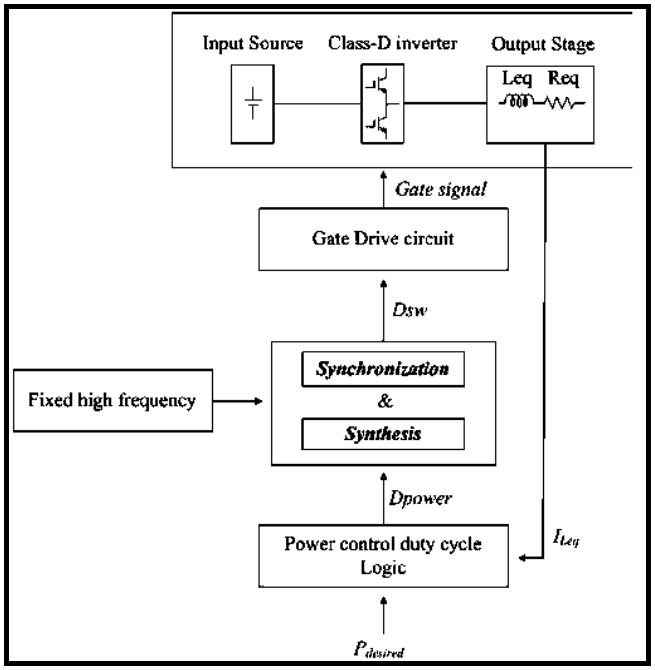

Figure 1.24 The block diagram of the class-D inverter [4]

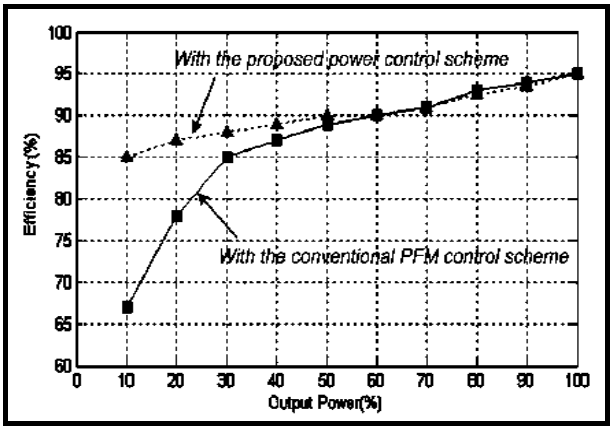

Figure 1.25 The efficiency comparison between the proposed power control and the conventional PFM control scheme [4]

Figure 1.25 shows a comparison of efficiency between the proposed power control and the conventional PFM control from 10% to full load. The proposed power control is proper for induction heating jar applications due to simplicity, low switching losses with ZVS condition, and its high efficiency than the conventional PFM control. However, the PDM method causes power fluctuation in the power line.

In 2007, I. Millan et al. [66] proposed a power control of the half-bridge series resonant inverter for induction cooking appliance as shown in Figure 1.26. This is based on ZCS condition and the discontinuous current mode (DM). The switching device under consideration uses two MOSFETs controlled by varying the switching frequency (f_s), the duty cycle (β), and α_+, α_- parameters, as shown in Figure 1.27. The α_+, α_- parameter can be defined as: $\alpha_+ = \alpha_- = 180 - \frac{180}{f_{no}/f_s} \bullet \frac{7}{2}$, where f_{no} is the natural frequency.

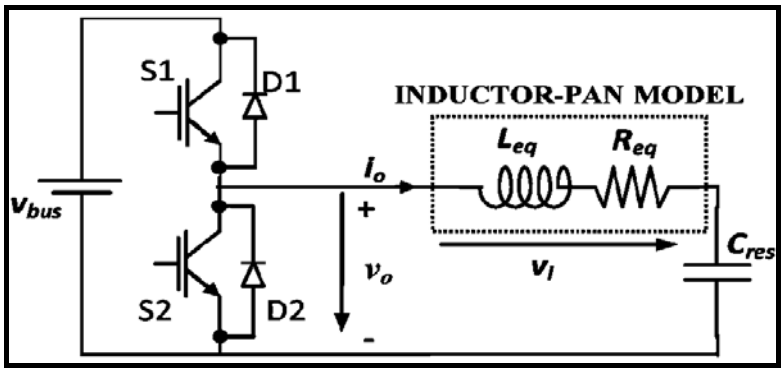

Figure 1.26 Half-bridge series resonant inverter [66]

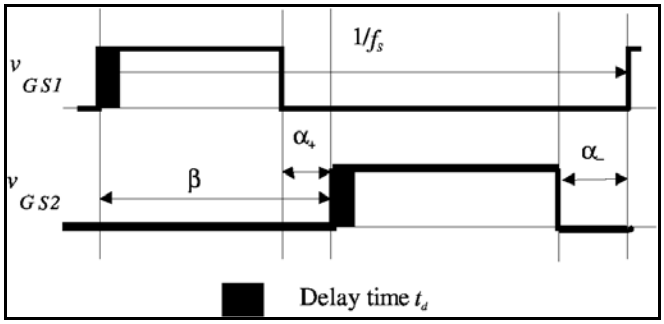

Figure 1.27 Schematic and control of inverter [66]

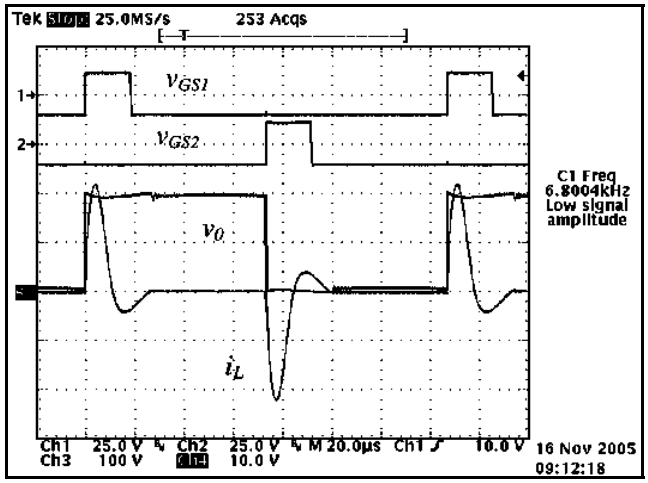

Figure 1.28 The experimental waveforms of DM control at output power of 150W [66]

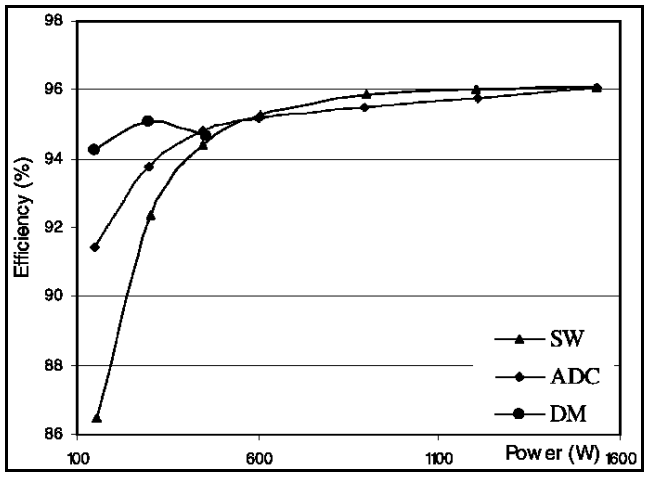

Figure 1.29 Efficiency comparisons of three controls [66]

Figure 1.28 shows the experimental waveform of DM control at output power of 150W and f_s is 6.8 kHz. Figure 1.29 shows a comparison between the proposed control (DM), square wave control (SW) and asymmetrical duty-cycle control ADC. The proposed power control has higher efficiency than SW and ADC in the low power range. Then, it is proper to control the output power for induction cooking applications in the low power range. Moreover, it has low switching losses because the switches are turned off at zero current (ZCS condition). Due to controlling in discontinues mode, the control circuit is complicated.

In 2007, Jose M. Espi and et al. [25] proposed the design of an *L-LC* resonant inverter for induction heating applications as shown in Figure 1.30.

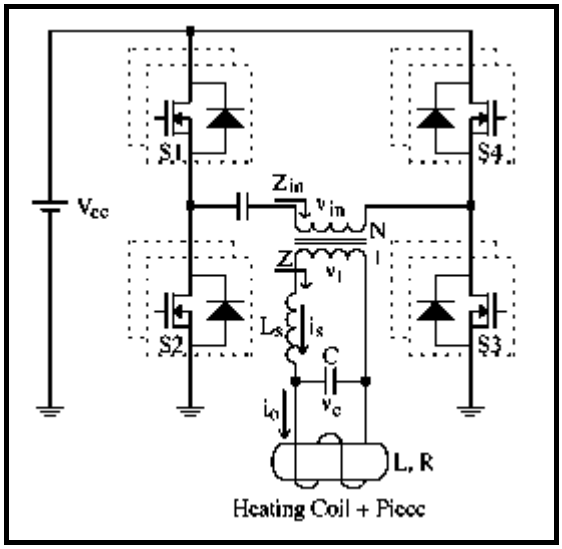

Figure 1.30 *L-LC* resonant inverter in full-bridge configuration [25]

The output power of their topology is controlled by using pulse frequency modulation (PFM) resulting in low efficiency and is difficult to filter out the output-voltage ripple. The proposed *L-LC* is suitable for high quality factor (Q) load such as tube welding, high-frequency hardening, or heating of materials with small equivalent resistance like brass, aluminum, etc.

In 2009, Oscar Lucia et al. [18] proposed a control algorithm among frequency limit control (FL) and power limit control (PL). Both of the FL and PL are based on square wave control (SW) and pulse density modulation (PDM) by using the half-bridge series resonant inverter for induction cooking appliances (3 kW). The PDM is used to control the output power in the low power range by adjusting t_{on} and T_{PDM} and $f_{s,pdm}$, as shown in Figure 1.31. While the SW modulation is used in the medium/high power range by adjusting the switching frequency (f_s), as shown in Figure 1.32.

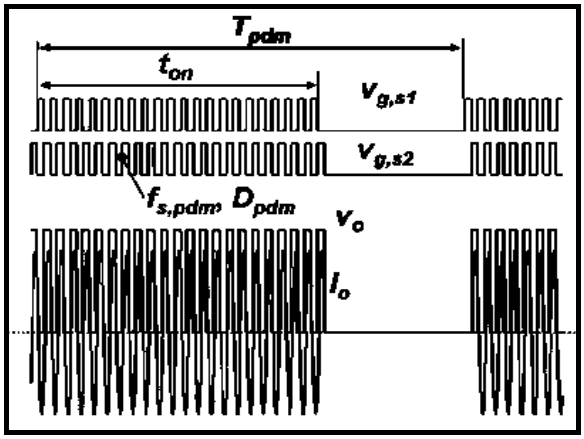

Figure 1.31 Schematic and control parameter of PDM [18]

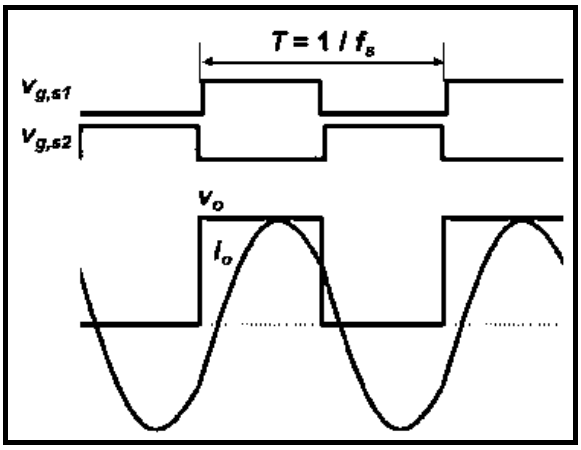

Figure 1.32 Schematic and control parameter of SW modulation [18]

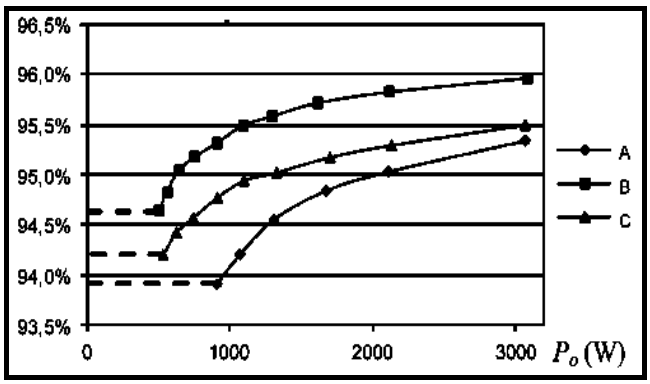

Figure 1.33 The experimental waveforms of power efficiency with FL algorithm [18]

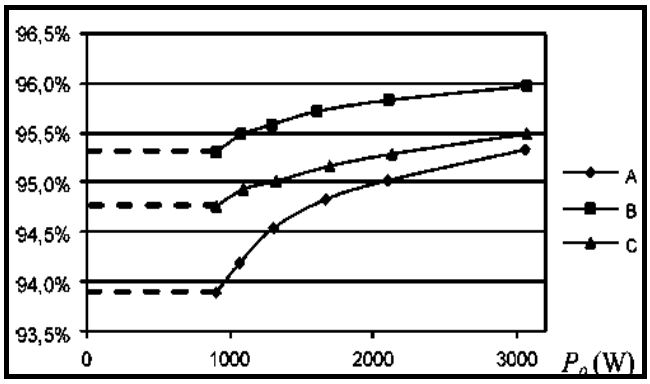

Figure 1.34 The experimental waveforms of power efficiency with PL algorithm [18]

Figure 1.33 shows the experimental results of power efficiency with FL algorithm while Figure 1.34 shows the experimental results with FL algorithm. PL has higher efficiency, but it has undesirable performance due to the discontinuity of the output power causing intermittent heating effect to the cooking materials. FL on the other hand, has better performance due to lower flicker emission, but the efficiency is low. The controls are complex and cause power fluctuation in the low power range with PDM control, when the switches are turn-on and turn-off.

1.2 Motivation

The use of high-frequency currents for heat treatment of metals such as surface hardening, brazing, and soldering has continually been increasing. Much attention has been focused upon the development of inverters capable of supplying high-power to induction heating loads at frequencies ranging from 10 to 200 kHz. A variety of different operating principles and inverter circuit configurations exist, each of which have their own particular merits as mentioned in the previous section. Considerable interest has recently been shown in the resonant inverter circuits as these configurations offer reduced power device switching losses and attractive possibilities in developing higher frequency of operation, higher efficiency, lighter weight through higher power density, and overall system simplicity in terms of inverter control, protection, and maintainability.

In high temperature applications, a high current must flow in the surface of the metal for heating effect. The series-resonant inverter may need a transformer for matching the output power and high current in the induction coil, because the induction heating technique requires high frequency current supply that is capable of inducing high frequency eddy current in the work piece that results in the heating effect [1-3].

Previous work has shown that an *L-LC* configuration can offer a better performance than the series-resonant while providing short-circuit immunity and lower current on the transformer's secondary [24, 25]. Note that the closed-loop PFM method presented in [25] may sacrifice the efficiency due to switching losses at high frequency operation. However, the LLC resonant load offers better performance with high quality factor ($Q > 30$) and only requires a small series inductance in the circuit configuration. This implies that the output transformer can be omitted. The disadvantage of the *L-LC* resonant load is that the output current may no longer be sinusoid in the case of low Q ($Q < 10$) [26]. The current in the induction coil is unavoidably small and distorted. Therefore, the

system efficiency is the price to pay. It is evident that the following issues are left unaddressed.

- Improving the *L-LC* resonant load for low Q (Q < 10)
- Improving the AVC for high temperature induction heating applications.

1.3 Objective and Approach

This thesis presents an improved LLC resonant inverter with asymmetrical control technique. The thesis includes the LLC resonant load design and the proposed control of resonant voltage source inverter. The objectives of the research are:

- Improving efficiency of LLC resonant inverter for induction heating applications.
- To improve the AVC control method that can adjust the output power to the induction coil for LLC resonant load when parameters at the coil change.
- Improving the LLC load configuration used for Low quality factor load of induction heating applications.

The *L-LC* is a combination of a series inductor (L_s), a matching transformer, and an inductor and a capacitor connected in parallel as illustrated in figure 1.35. In the case of low Q (Q < 10), an improved LLC resonant load that we proposed is modified by moving L_s to the primary of matching transformer as shown in figure 1.36. With the high Q load, L_s will be high whereas it is low with the low Q. The nonlinearity of the leakage inductance of matching transformer makes it difficult to design in the case low Q. So the bringing of the inductor L_s at primary of matching transformer make it easier to design and build the inductor L_s because the primary current is reduced by the transformation ratio of the matching transformer. The new location of L_s enables short-circuit capability inherently especially in case a short circuit occurs at the induction coil or from transformer saturation.

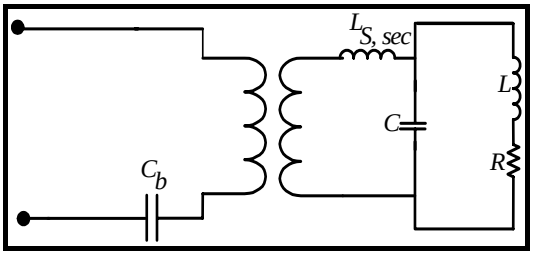

Figure 1.35 Previous *L-LC* configuration

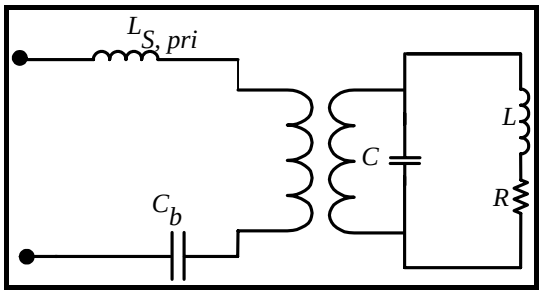

Figure 1.36 Proposed LLC configuration

The reviews of the induction cooking are on a series resonant load where the load temperature is low and parameters remain rather constant. For the high temperature applications, when work piece is heated, the phase lock loop control will be needed to

address the issue of parameter variation. The AVC technique reviewed on induction cooking application for output power control is more efficient than other methods (PFM, PS, and ADC), so the AVC technique can be combined with the use of a phase-locked loop control. The operating frequency can be automatically adjusted to maintain a small constant lagging phase angle and the output power can be controlled under load-parameter variation during the heating process.

1.4 Organization of Thesis

The structure of the research work is reflected in the divisions of the thesis:

1. In chapter 2, the overviews of Induction heating and its characteristics in power electronic applications such as induction heating load characteristics, high frequency induction heating inverters, the control of series inverter, and *L-LC* resonant voltage source inverter are reviewed and described.

2. In chapter 3, analysis and design of LLC Full-bridge resonant inverter are given along with the proposed control strategy and the design procedure of the major components. The design procedure includes the series inductor (L_s) and matching transformer value derivation. Moreover, this chapter shows the calculation of switching and conduction losses of all switches.

3. In chapters 4, this chapter includes simulation and experimental results of LLC full-bridge resonant inverter. The experimental results are compared with both the calculation and simulation. In addition, this chapter shows the efficiency from the calculation together with experimental results of the proposed control and the pulse frequency modulation.

4. Chapter 5 concludes this research by reiterating the summary of contributions and future work is discussed.

CHAPTER 2 PRINCIPLES OF INDUCTION HEATING

In many heating processes, high purity of the work-pieces is an important requirement. The induction heating method is the suitable method for such applications due to the non-contact between the induction coil and the work-pieces. This chapter describes the principle of induction heating and related circuit operations.

2.1 Induction Heating Effects

Basically, an induction heating coil consists of an induction coil and work piece. The induction coil is always constructed of copper, and is generally water-cooled and has a refractory lining. It is closely coupled to the work piece and it is supplied by alternating current. The magnetic field, induced in the induction coil when energized, causes eddy currents in the work-piece and increases the heating effect as shown in Figure 2.1 and its equivalent circuit is shown in Figure 2.2.

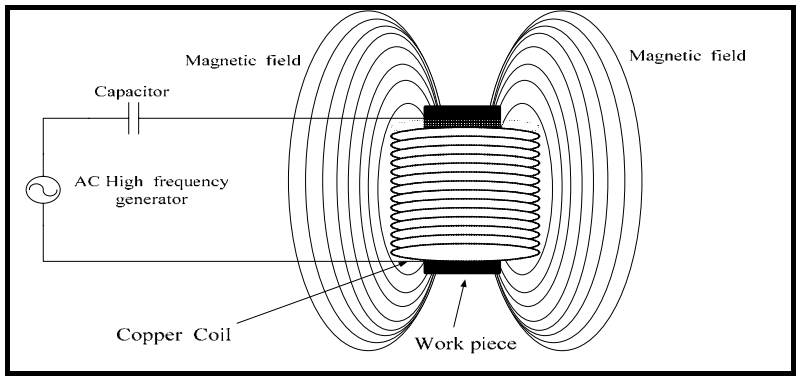

Figure 2.1 Induction heating load [58]

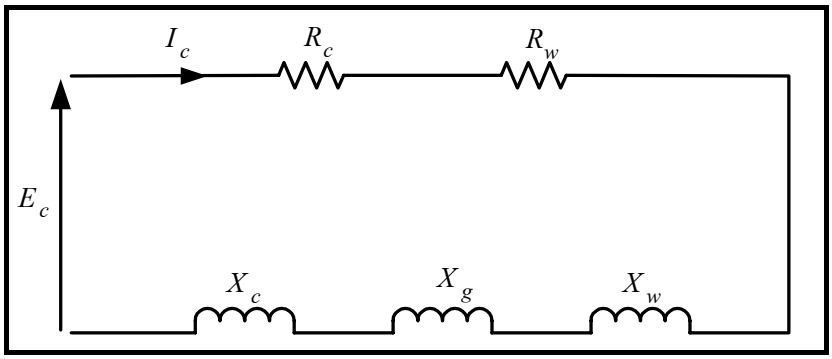

Figure 2.2 Equivalent circuit of induction coil [58]

When $$Z = (R_w + R_c) + j(X_g + X_w + X_c) \quad (2.1)$$

Work reactance, $$R_w = K(\mu_r p A_w) \quad \text{ohms} \quad (2.2)$$

Coil resistance, $$R_c = K\left(\frac{k_r \pi d_c \delta_c}{2}\right) \quad \text{ohms} \quad (2.3)$$

Gap reactance, $X_g = K(A_g)$ ohms (2.4)

Work reactance, $X_w = K(\mu_r q A_w)$ ohms (2.5)

Coil reactance, $X_c = K\left(\frac{k_r \pi d_c \delta_c}{2}\right)$ ohms (2.6)

where $K = 2\pi f \mu_0 [\frac{N_c^2}{l_c}]$; μ_r is the relative permeability; A_w is the cross section area of work-piece; A_g is the area of gap; k_r is the coil correction factor that ranging from 1-1.5; N_c is the number turn of induction coil; l_c is the length of gap and d_c is the diameters of induction coil. (p and q are function for a solid cylinder)

Induction heating occurs when a piece of conductive material is placed inside a coil delivering a varying magnetic field. The magnetic field that induces eddy currents is the conductive work piece, and heat increases in the piece due to losses, where R is the resistance of the current path in the piece. In practice, the conductive material can be either ferromagnetic [57] (such as iron or steel) or nonferromagnetic (such as silver or aluminum). In ferromagnetic materials, additional heating occurs from hysteresis losses, but its contribution is not important compared to the heating caused by eddy currents [68]. When a conductive work piece is placed inside the coil, the magnetic field is distributed such that it is strong at the air gap between the coil and the work piece and is intensity decreases as it penetrates the conductive material. The eddy currents, induced by the magnetic field of the surface and inside the work piece, move in the opposite direction to the coil current. For induction heating, the eddy currents at the surface are always stronger than those closer to the center of the work piece; this phenomenon called skin effect.

A qualitative measurement of the skin effect is the skin depth. The skin depth, or depth of penetration, δ is the distance at which the magnitude of the magnetic field has decayed by e^{-1} which corresponds to

$$\delta = \sqrt{\frac{2\rho}{\mu \omega_s}} \tag{2.7}$$

Where ω_s is the switching frequency (rad/sec), ρ is the resistivity (Ω-m), and μ is the permeability of the material, $\mu = \mu_0 \mu_r$

Hence, as the skin depth decreases, the skin effect is more apparent. For induction heating applications, it is important to specify the desired skin depth because it determines the operating frequency of the power supply. For example, deep depth induction heating applications require low operating frequencies. In addition, most induction heating applications require heating a work piece at a given temperature for a specific amount of time. Thus, the power supply must also provide the necessary output power to meet these specifications.

2.2 Load Characteristics

As stated earlier, the operating frequency and the output power are the two main specifications for an induction heating power supply. To meet the output power specification, the resistance of the load must be estimated. Also, for most cases, to meet the operating frequency specification the inductance of the load must also be known.

During a heating process, the load resistance and inductance vary, especially when temperature of work piece reaches Curie temperature. Figure 2.3 shows a common induction heating load representation, where the coil and work-piece resistance and inductance are represented as variable resistance (R_w), and inductance (L_w), connected in series [68].

An example of the variations of the load resistance and inductance for a ferrous work piece as a function of temperature is presented in Figure 2.4. The exact values of L_w and R_w, and the temperature range are not the important characteristics of Figure 2.4 because they vary with the application. The shape of the curves is significant since, as the temperature of the work-piece increases, L_w and R_w increase. However, as the temperature approaches the curie point, L_w and R_w decrease to values lower than when the piece was cold. It should be pointed out that in most induction heating applications the resistance variations are greater than the inductance variations.

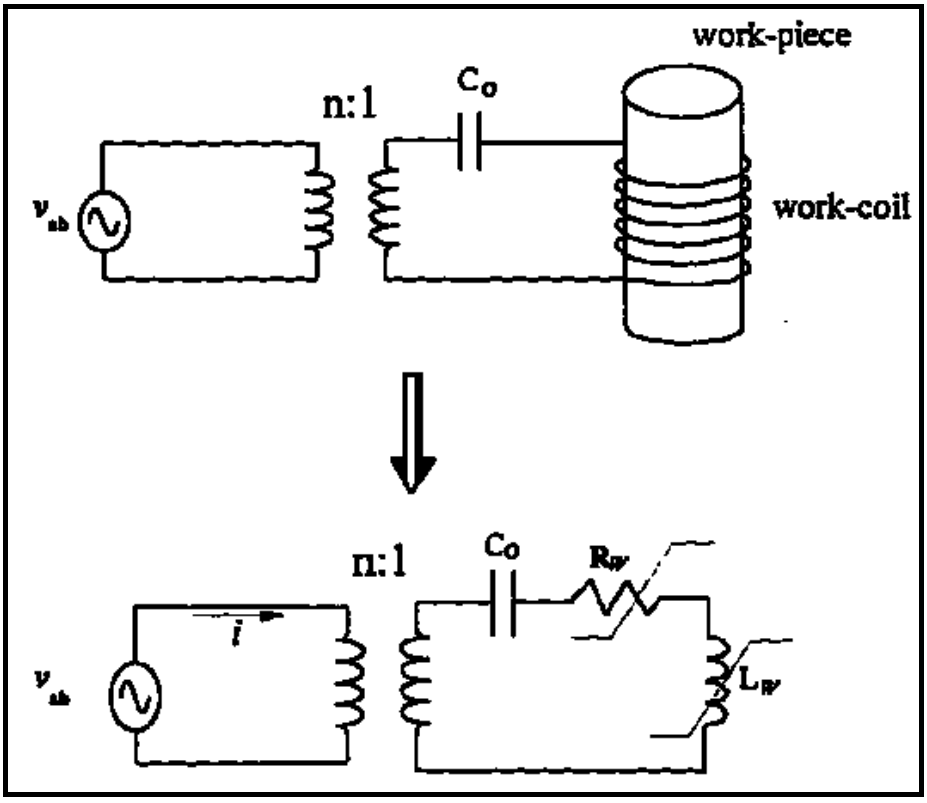

Figure 2.3 Induction-heating load representation [68]

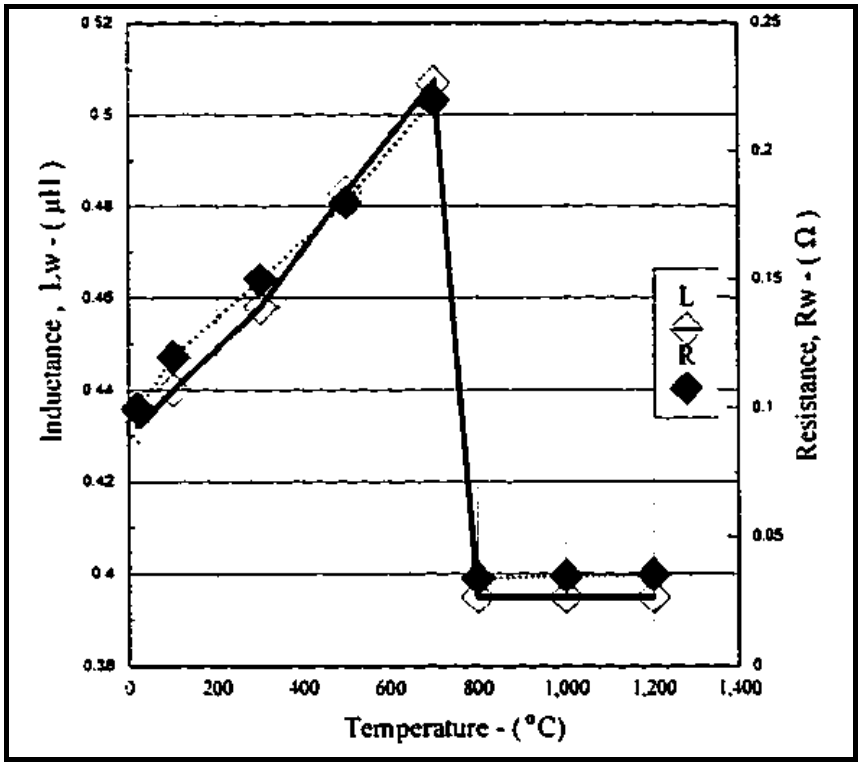

Figure 2.4 Example of the load characteristics as a function of temperature (experimenatal data) [69]

2.3 Induction Heating Applications

The operating frequency and the power level specifications given for the design of an induction heating power supply determine the type of switching device to be used in power state. Many different power supply types and models are available to meet the heating requirements of a nearly endless variety of induction heating applications. The specific application will dictate the frequency, power level, and other inductor parameters such as coil voltage, current, and power factor. Figure 2.5 illustrates this power versus frequency relationship for common induction heat treating applications. Figure 2.6 illustrates power semiconductors used for induction heating such as thyristor, IGBT, MOSFET, and vacuum tube. Frequency is a very important parameter in induction heat treatment because it is the primary control over the depth of current penetration. Determination of operating frequency is an important step in the design of induction heating power supplies because the power components must be rated for operation at the specified frequency. The power circuit must ensure that these components are operated with an adequate margin to yield high reliability at this frequency and Figure 2.7 shows the main power systems, their power ranges, and major applications.

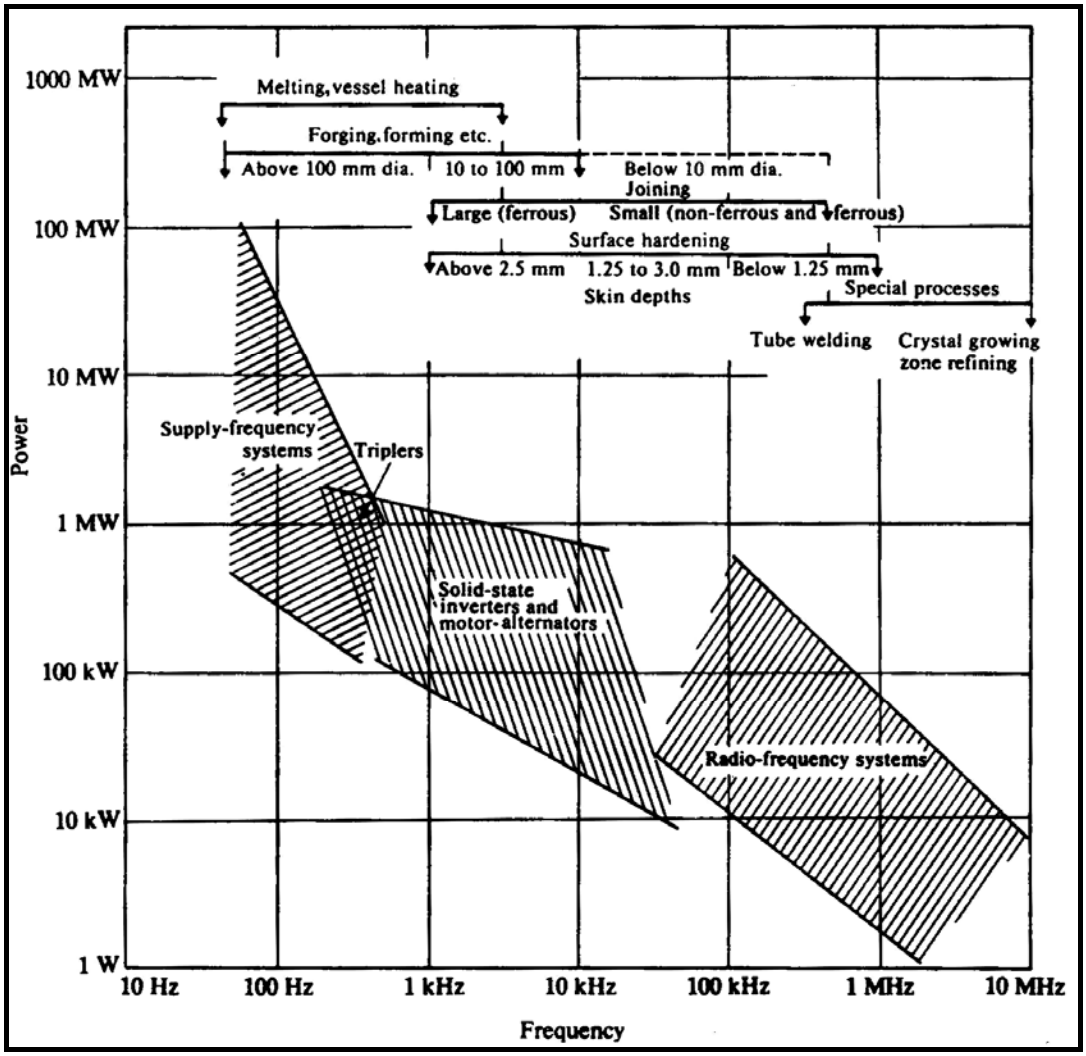

Figure 2.5 Induction-heating systems and processes [58]

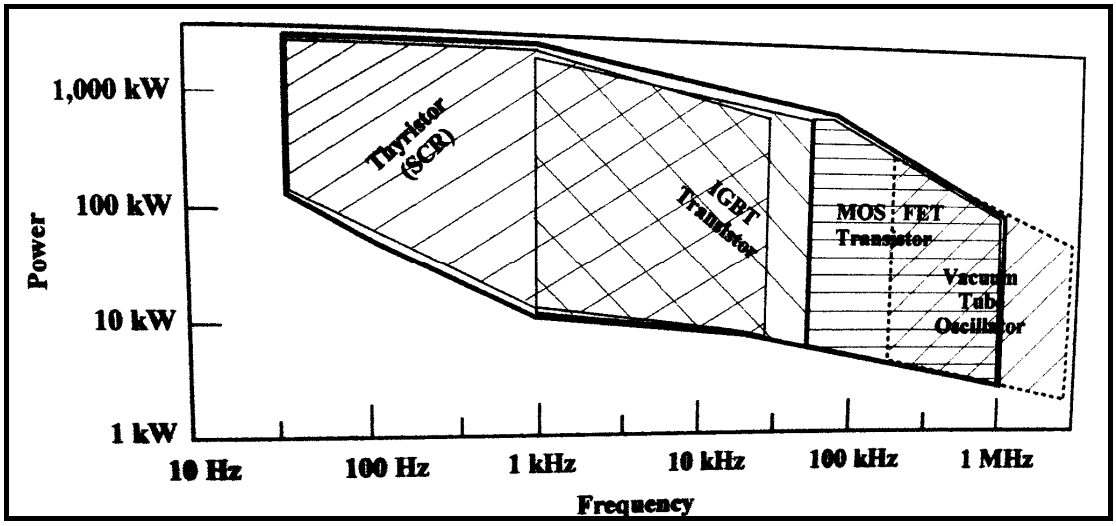

Figure 2.6 Power semiconductors used for induction heating [59]

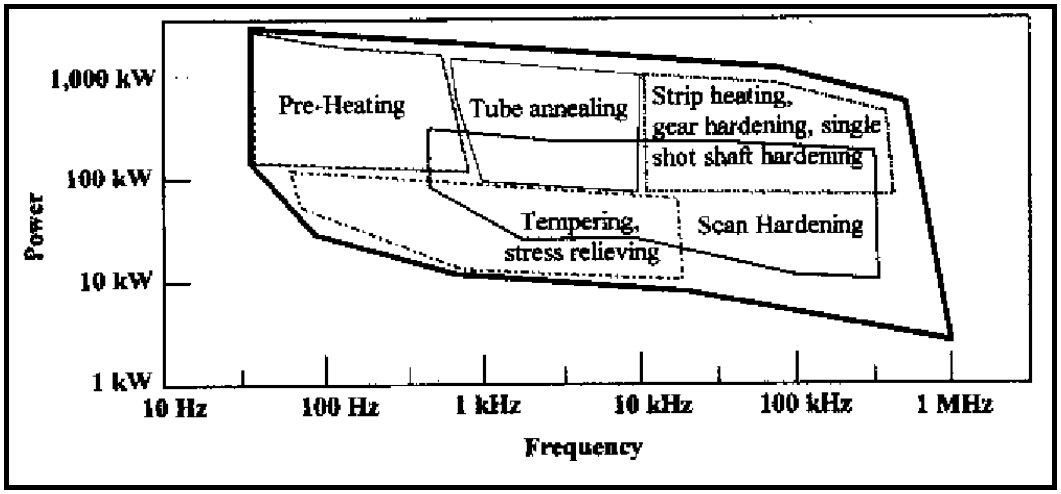

Figure 2.7 Power-frequency diagram for typical induction heat treating applications [58]

The dimension of the work piece, frequency, power level and applications of induction heating are correlated and must be considered altogether in selection of the type of inverter which is suitable. The high frequency induction heating inverters will be presented in the next section.

2.4 High Frequency Induction Heating Inverters

As mentioned earlier, the heating effects and the resonant circuit require high-frequency operation. Induction heating inverters are typically used to change the available utility line frequency power to single-phase power at a frequency suitable for the induction heating process. A large number of topologies have been developed in this area. Current-source and voltage-source inverters are among the most commonly used types.

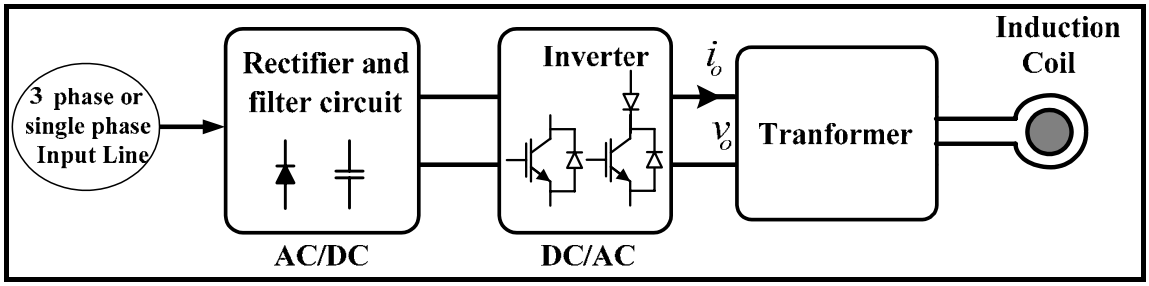

Figure 2.8 Induction heating basic block diagram.

The basic block diagram of an induction heating system applied to nearly all induction heating system is shown in Figure 2.8. The input signal is generally three or single phase. The first block represents the AC to DC converter or rectifier. This section may provide a fixed DC voltage, a variable DC voltage, or a variable direct current. The second block represents the inverter that can be either a current- or voltage source inverter. The third block represents the load-matching components, converting the output of the inverter to the level required by the induction coil.

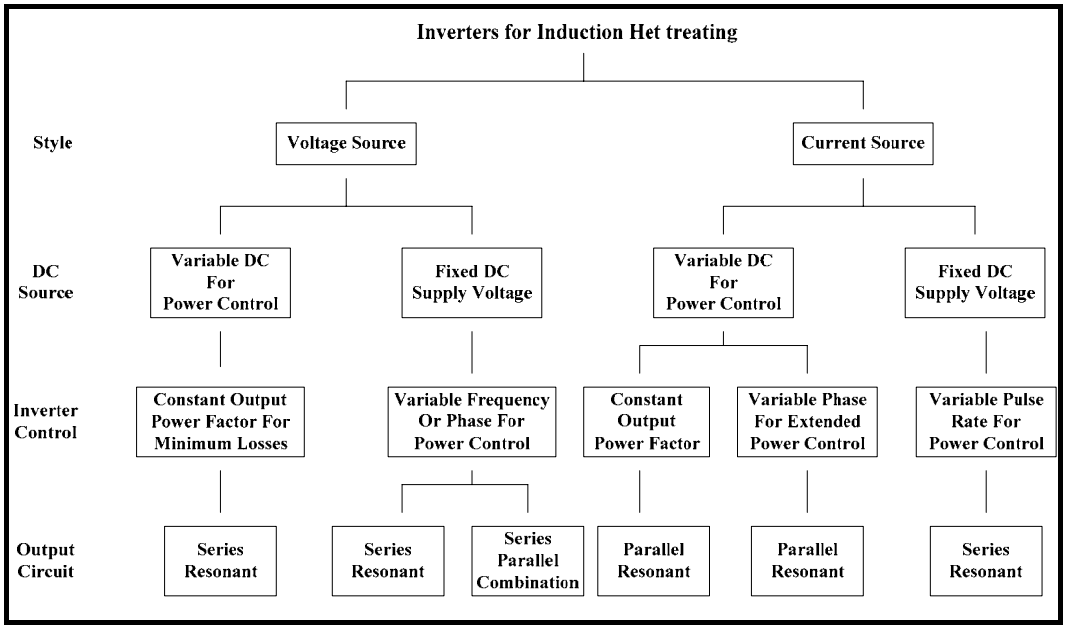

Figure 2.9 Induction heating treating inverter [59]

The classification of the inverters commonly used in induction heating power supplies is depicted in Figure 2.9. Two major types are voltage and current sources. The chart further divides the DC source into fixed and variable. The control of the inverter is done by varying either the phase angle or the operating frequency. The load circuit connection is categorized into series resonant, parallel resonant and series parallel combination resonant loads. The characteristics of current and voltage source inverters will be presented in the next section.

2.4.1 Current Source Inverter

The current source inverter is suitable for high power induction heating applications because of the short-circuit protection capability and superior no-load performance due to the current-limiting dc link characteristic. Figure 2.10 and 2.11 show full bridge current source inverter and output voltage and current wave forms operating above resonant frequency.

The current source inverter needs a switch that can block a bipolar voltage. Appropriate switching operations are achieved by connecting a switch and diode in series. The output voltage of the inverter is sinusoidal, in the case of low damping factor, and the operating frequency is near the resonant frequency. The inverter is designed to operate at a little higher inverter frequency than a resonant frequency, to achieve zero-current soft-switching [5] which reduces loss at IGBTs switches and avoids spike voltage. The voltage across the switch has both positive and negative values. The positive voltage is blocked by the IGBT and the negative voltage is blocked by the diode. The current source inverter (CSI) in Figure 2.10, is controlled by adjusting the DC bus for power control as mentioned earlier [2].

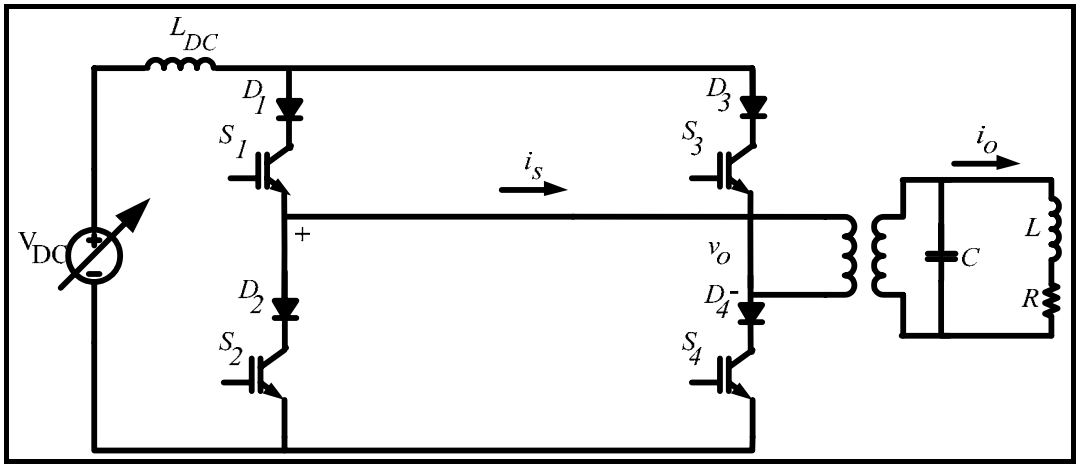

Figure 2.10 Full bridge current source inverter with parallel resonant load

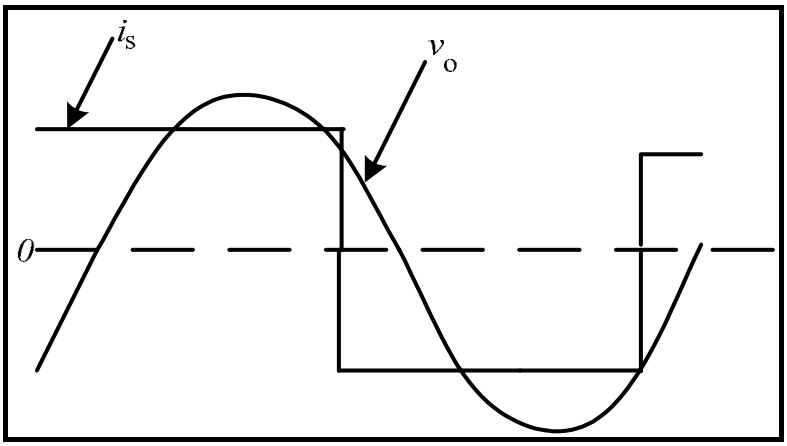

Figure 2.11 Output voltage and current wave forms of full bridge current source inverter operating above resonant frequency (ZCS)

2.4.2 Voltage Source Inverter

When used for induction heating, the voltage source inverter (VSI), has the simplest circuit of all existing topologies. It uses the transformer leakage inductance and the load inductance as the resonant inductor. The VSI operating at ZVS has the least number of power components and consequently it is cheaper than CSI. The most common inverter configuration is the full bridge as shown in Figure 2.12. It consists of four switches with antiparallel diode connected in each of the switch. The output is located in the center of full bridge so that when switches S_1 and S_4 are closed, current flows from the DC supply through the output circuit from left to right. When switches S_1 and S_4 are opened and switches S_3 and S_2 are closed, the current flows in the opposite direction, from right to left. As this process is repeated, an alternating current is generated at a frequency determined by the rate at which the switches are opened and closed. The output voltage and current wave forms operating above resonant frequency is shown in Figure 2.13. It should be noted that when using the VSI full bridge inverter with series resonant load for induction heating applications, there is a possibility for the load inductor to become shorted, and then the inverter must be protected against short circuits with fast over current sensors.

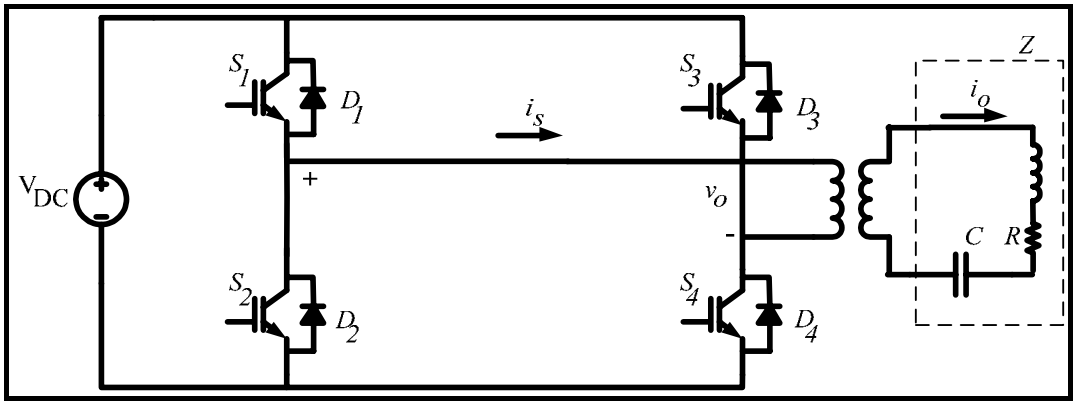

Figure 2.12 Full bridge voltage source inverter with series resonant load

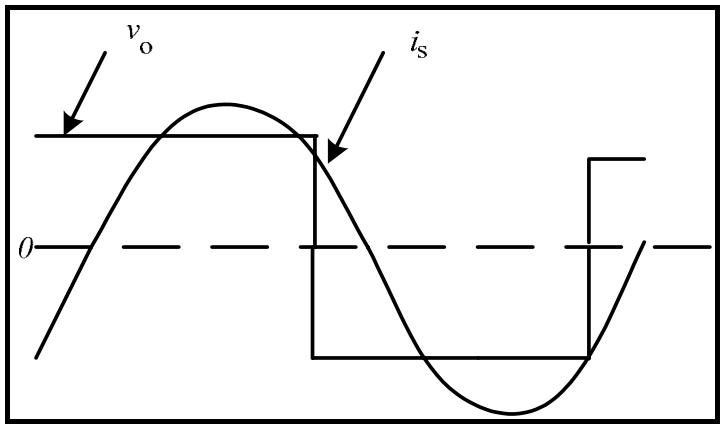

Figure 2.13 Output voltage and current waveforms of full bridge voltage source inverter operating above resonant frequency (ZVS)

2.4.3 Resonant Circuit Load of Induction Heating Inverter

In general, the resonant inverters need to use the load resonant circuit such as series or parallel resonant circuit because they can operate in soft switching.

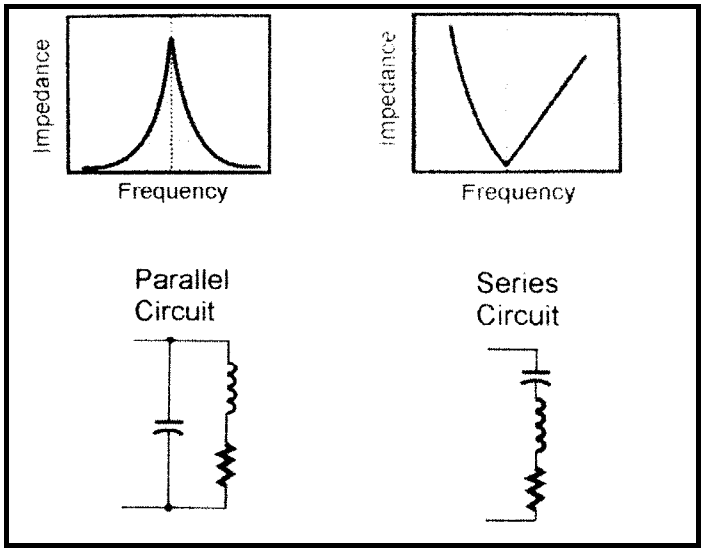

Figure 2.14 Parallel and series resonant circuits [58]

Figure 2.14 shows the characteristics of series resonant and parallel resonant circuits. Looking at the parallel circuit, it is easy to see that if the capacitor is not in the circuit, then the given voltage applied to the circuit at a constant frequency will result in a specific amount of power depending on the impedance of circuit. When sufficient capacitance is added to the circuit to adjust the load circuit near resonant frequency, the circuit impedance increases and the amount of current drawn from the power supply drastically declines. The circuit voltage required to achieve a specific power level is the same as with the initial case of zero capacitance, but now the higher current required by the load is being supplied by the capacitor rather than the power supply.

In a parallel resonant circuit we have a quality factor (Q) increase in current in the resonant tank circuit which is compared with the input current from the power supply (Figure 2.15). This resemblance can be repeated for the case of the series resonant circuit to realize that with the calculated change in circuit impedance the circuit current will be much higher for a given input voltage when the circuit is operated near the resonant frequency because the impedance is approaching zero. The load coil current required for a given power is the same for the given load circuit regardless of whether the connection is series or parallel, but because the overall impedance has fallen and the required current is fixed, the required driving voltage is approximately a factor of Q lower than the coil voltage. So, we have a Q increase in current in the parallel circuit and a Q rise in voltage with the series-connected circuit (Figures 2.14 and 2.15). It is therefore imperative to have an understanding of what type of circuit connection exists in order to understand the effect that changes in value of the tuning components will have on the power supply and workstation components [58].

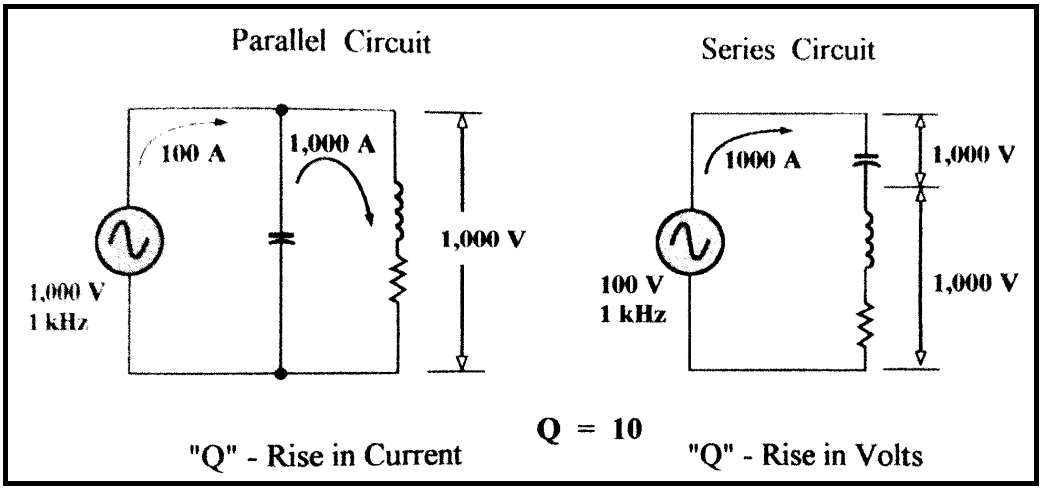

Figure 2.15 Parallel and series resonant circuits with sinusoidal voltage source [58]

As shown in Figure 2.15, the parallel resonant circuit is suitable for current source inverter because it can block the reverse current. And series resonant circuit is suitable for voltage source inverter because it can conduct the bidirectional current from the load. The current source inverter can not open circuit but the voltage source inverter can open circuit. This characteristic makes the voltage source inverter having various output power control such as pulse frequency modulation, pulse density modulation, asymmetrical duty cycle control and phase shift control which are shown in the next section.

2.5 Control of Series Resonant Inverter

The voltage-source inverters (VSI) with series resonant load are widely used in applications that require output power control capability where a zero-voltage switching (ZVS) condition must be met to ensure a high efficiency. The many control methods are researched to improve the efficiency. In this section, the popular control methods the VSI based on full bridge voltage source topology are presented.

2.5.1 Power Frequency Modulation (PFM)

One of the popular methods of switching is pulse frequency modulation (PFM). The output power is controlled by varying the switching frequency while the inverter operates under zero-voltage switching (ZVS) scheme. The output voltage and current waveforms of the PFM control are shown in Figure 2.16.

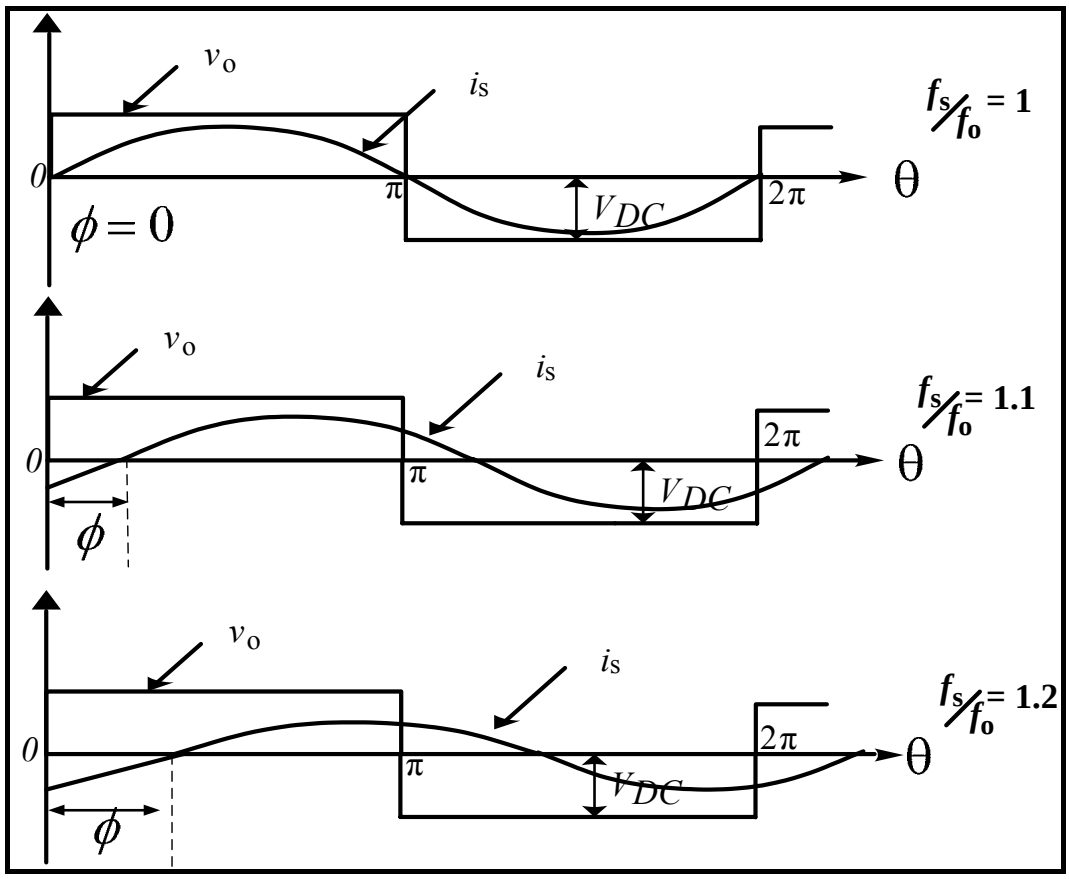

Figure 2.16 Wave forms of full bridge voltage source inverter operating with PFM

The output voltage may be expanded using a Fourier series expansion as,

$$V_o = \frac{V_{DC}}{\pi} \sum_{n=1}^{\infty} \frac{1}{n} (2 - 2\cos n\pi) \sin n\omega_s t \tag{2.8}$$

As illustrated in Figure 2.15, the output current assumes the sinusoidal behavior at the frequency around the resonant frequency. The output current is given as,

$$i_S = I_{s,m} \sin(\omega_s t - \phi) \tag{2.9}$$

where $I_{s,m} = \frac{4}{\pi}\frac{V_{DC}}{Z}$ and ϕ is the angle between the voltage v_o and current i_s. From (2.8) and (2.9), the output power is calculated as,

$$P_o = \frac{1}{2}\left(\frac{4V_{DC}}{\pi Z_0\left(\frac{1}{Q^2}+\left(\frac{\omega_s}{\omega_0}-\frac{\omega_0}{\omega_s}\right)\right)}\right)^2 R$$

$$= \frac{V_{DC}{}^2 R}{Z_0^2}\frac{(4)^2}{2\pi^2\left[\frac{1}{Q^2}+\left(\frac{\omega_s}{\omega_0}-\frac{\omega_0}{\omega_s}\right)\right]} \qquad (2.10)$$

where, the characteristic impedance Z_0 is given as, $Z_0 = \sqrt{\frac{L}{C}}$. From equation 2.10, the normalized output power is found as,

$$\frac{P_o}{V_{DC}{}^2 R/Z_0^2} = \frac{(4)^2}{2\pi^2\left[\frac{1}{Q^2}+\left(\frac{\omega_s}{\omega_0}-\frac{\omega_0}{\omega_s}\right)^2\right]} \qquad (2.11)$$

Normalized output power

$\frac{P_o}{Vd^2 R/Z_0^2}$

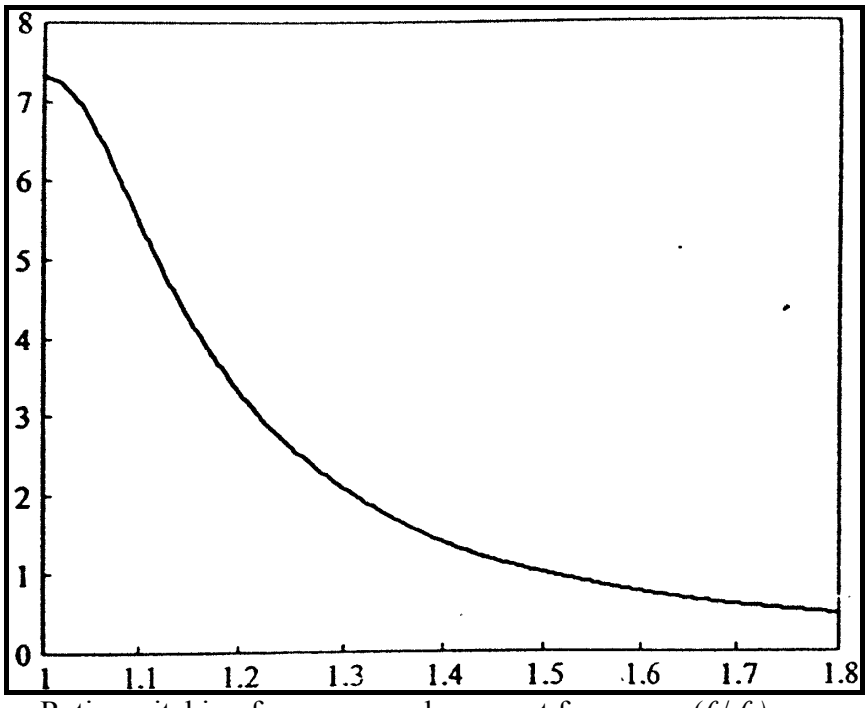

Ratio switching frequency and resonant frequency (f_s/f_0)

Figure 2.17 Normalized output power versus ratio of f_s/f_0 with PFM

2.5.2 Pulse Density Modulation (PDM)

In addition to the PFM control, another widely adopted control method is PDM which consists of the high frequency and low frequency. The described PDM control strategy is shown in Figure 2.18 (a), (b) and (c). The output power of the full bridge series resonant inverter is controlled by adjusting the pulse density of the square-wave voltage. By adjusting the duty cycle of the fixed low frequency signal, the output power is easily controlled in a wide load and line range.

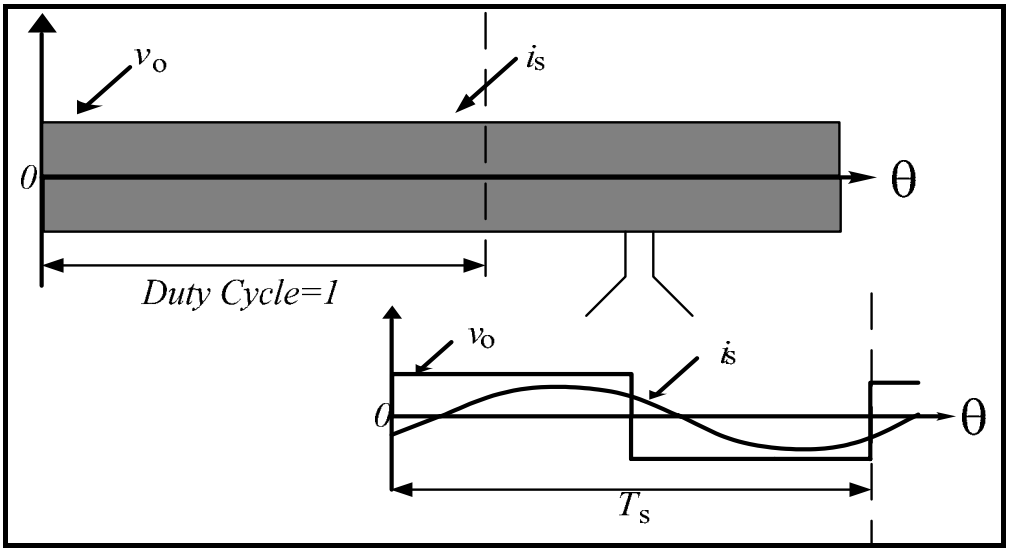

(a)

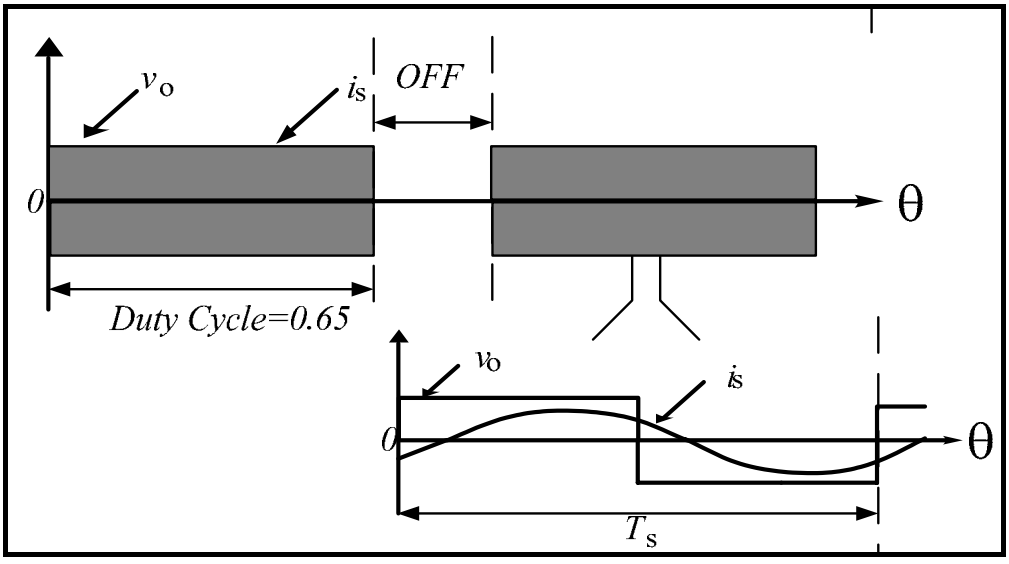

(b)

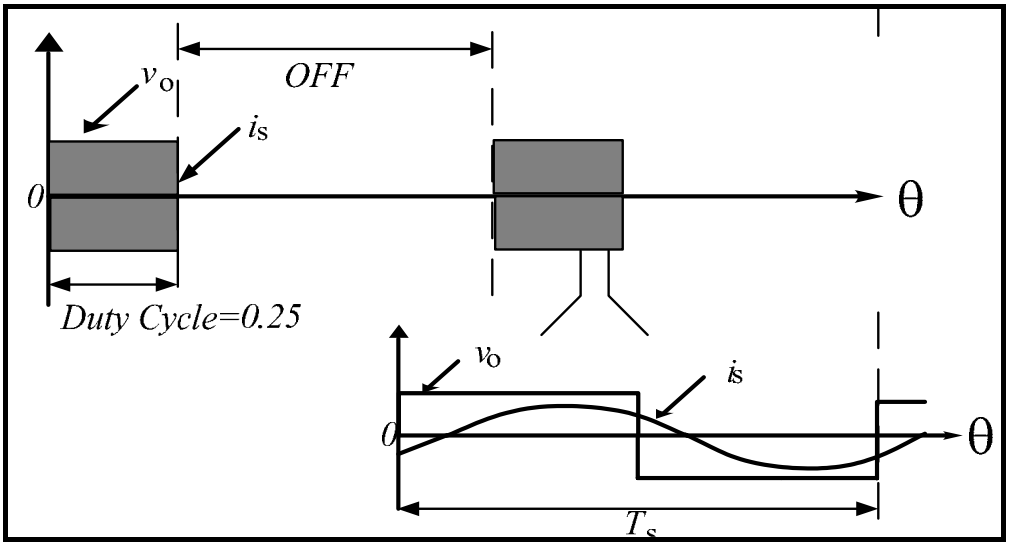

(c)

Figure 2.18 Wave forms of full bridge voltage source inverter operating with PDM (a) Duty cycle =1, (b) Duty cycle =0.5, and (c) Duty cycle =0.25

Normalized output power

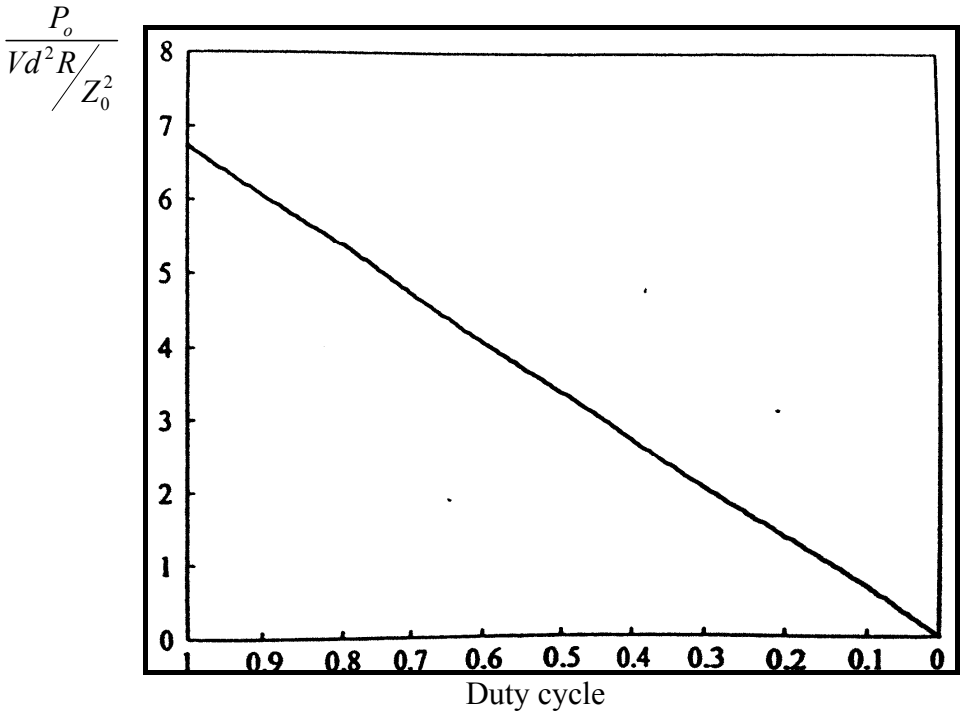

Figure 2.19 Normalized output power versus ratio of duty cycle with PDM

Note that the amplitude of output current and voltage are not affected under duty cycle variation but, the average output power decreases. Figure 2.19 shows normalized output power versus ratio of duty cycle with PDM, which is provided by multiplying between equation (2.11) and duty cycle of low frequency where the f_s/f_0 and the power angle ϕ is constant.

2.5.3 Asymmetrical Duty Cycle (ADC)

Recent trends suggest asymmetrical duty-cycle (ADC) control to supply low/medium power with improved efficiency. The ADC control technique can be used in half-bridge or full-bridge topologies. It is based on an unequal duty-cycle operation of the switches in the converter.

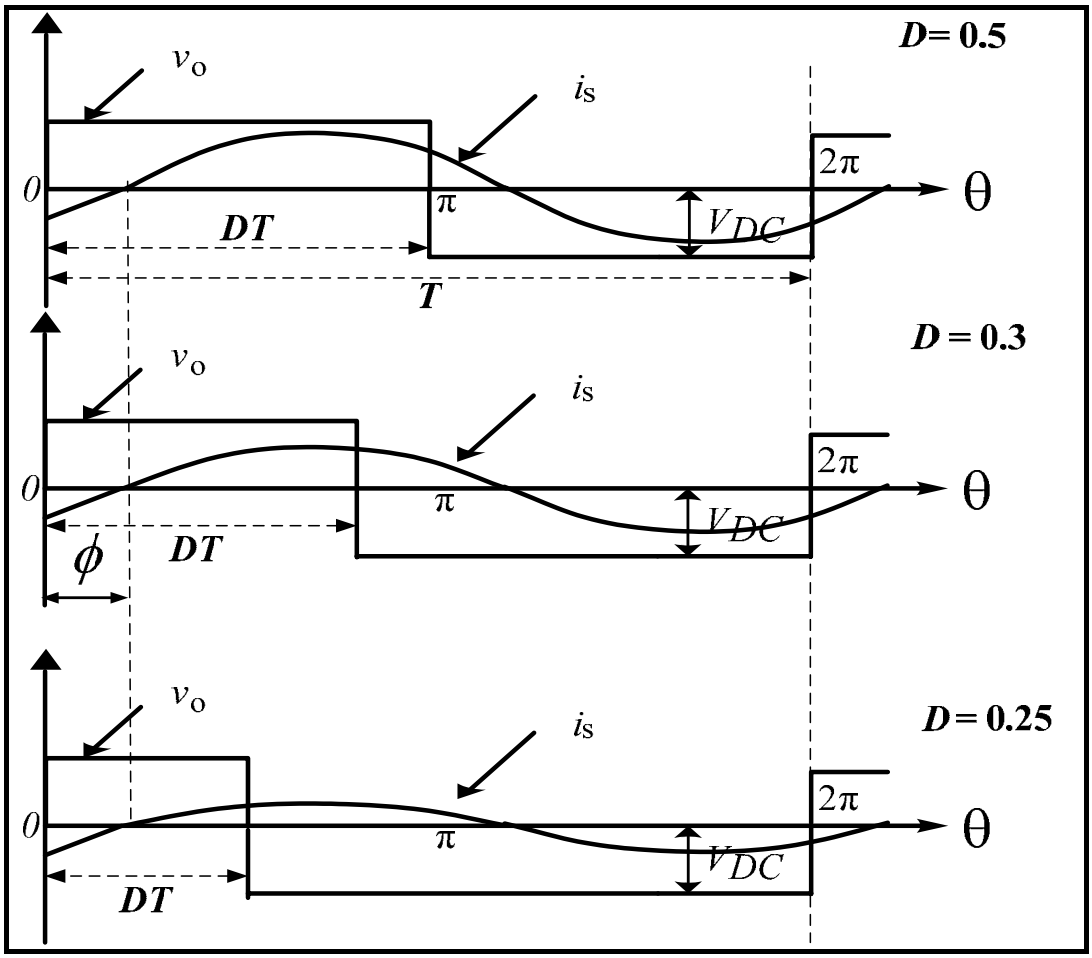

Figure 2.20 Wave forms of full bridge voltage source inverter operating with ADC

The output voltage V_o and the current i_s are defined as

$$V_o = (2D-1)V_{DC} + \frac{V_{DC}}{\pi}\sum_{n=1}^{\infty}\frac{1}{n}[(2\sin 2n\pi D)\cos n\omega_s t + (2-2\cos 2n\pi D)\sin n\omega_s t] \quad (2.12)$$

$$i_s = \frac{V_{DC}}{\pi}\frac{1}{Z}[(2\sin 2\pi D)\cos(\omega_s t-\phi) + (2-2\cos 2\pi D)\sin(\omega_s t-\phi)] \quad (2.13)$$

From (2.12) and (2.13), the output power is found as,

$$P_o = \frac{V_{DC}^2 R(2\sin 2\pi D)^2 + (2-2\cos 2\pi D)^2}{2\pi^2 Z_0^2\left(\frac{1}{Q^2} + \left(\frac{\omega_s}{\omega_0} - \frac{\omega_0}{\omega_s}\right)\right)^2}$$

$$= \frac{V_{DC}^2 R}{Z_o^2} \frac{(2\sin 2\pi D)^2 + (2 - 2\cos 2\pi D)^2}{2\pi^2 \left[\frac{1}{Q^2} + \left(\frac{\omega_s}{\omega_0} - \frac{\omega_0}{\omega_s} \right)^2 \right]} \tag{2.14}$$

Therefore, the normalized output power is

$$\frac{P_o}{V_{DC}{}^2 R / Z_o^2} = \frac{(2\sin 2\pi D)^2 + (2 - 2\cos 2\pi D)^2}{2\pi^2 \left[\frac{1}{Q^2} + \left(\frac{\omega_s}{\omega_0} - \frac{\omega_0}{\omega_s} \right)^2 \right]} \tag{2.15}$$

Normalized output power

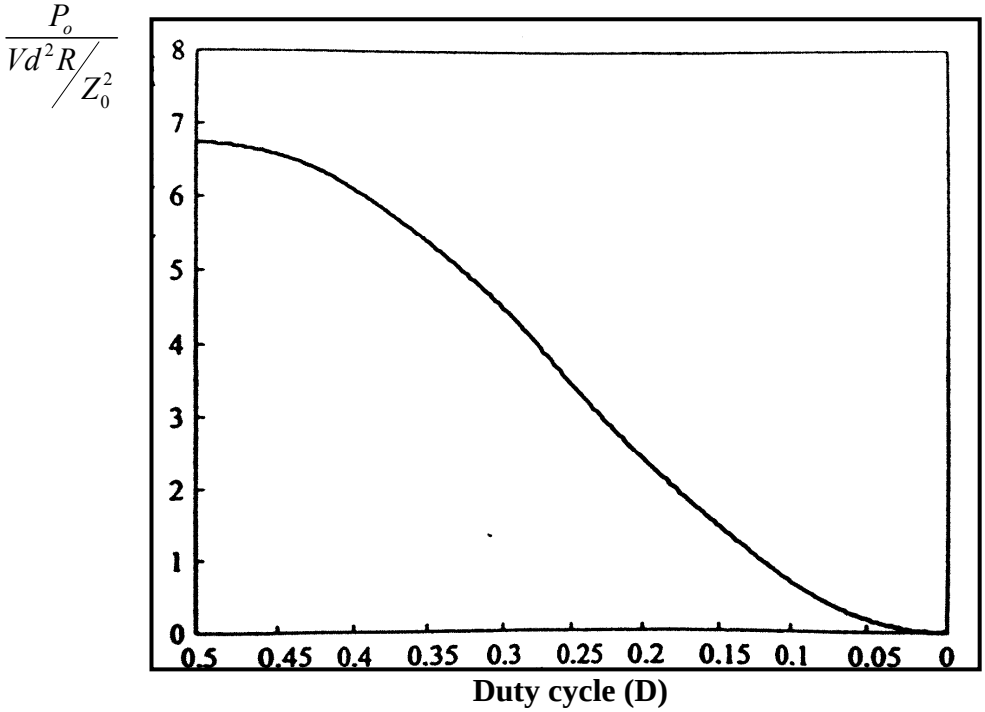

Figure 2.21 Normalized output power versus ratio of duty cycle with ADC

At constant power angle (ϕ), the output voltage and current in this control method will be decreased providing that the duty cycle is decreased. From equation 2.15, we can plot the normalized output power as a function of duty cycle which is shown in Figure 2.20. The output power will be decreased when the percent of duty cycle increase.

2.5.4 Phase Shift (PS)

The phase-shift (PS) is incorporated for a full bridge inverter in which one bridge leg is leading the other by shifting gate signal. The PS control technique allows output voltage or power variations by phase shifting the sequences of conduction for the switches, achieving a symmetrical voltage cancellation.

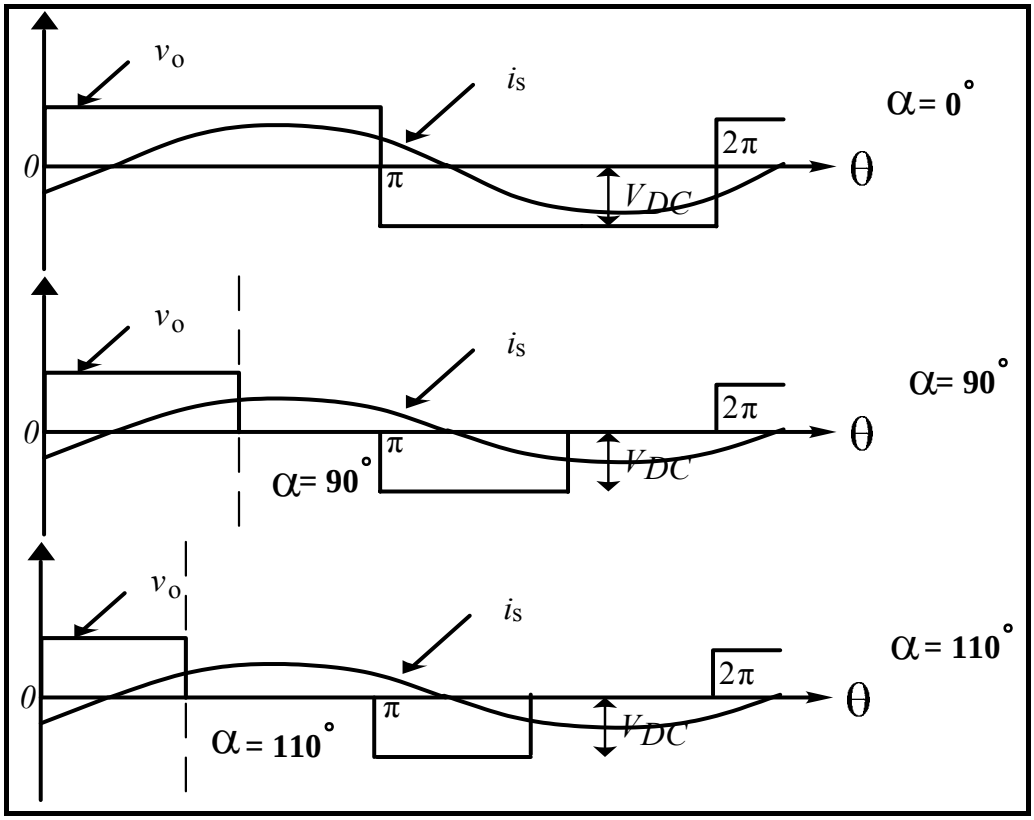

Figure 2.22 Wave forms of full bridge voltage source inverter operating with PS

The output voltage and current are defined in (2.16) and (2.17)

$$V_o = \frac{2V_{DC}}{\pi}\sum_{n=1}^{\infty}\frac{1}{n}[(1-\cos n\pi)\cos\frac{n\alpha}{2}]\sin n\omega_s t \tag{2.16}$$

$$i_S = \frac{2V_{DC}}{\pi}\frac{1}{Z}[(1-\cos\pi)\cos\frac{\alpha}{2}]\sin(\omega_s t-\phi) \tag{2.17}$$

From equation 2.16-2.17, the output power can find in (2.18)

$$\begin{aligned} P_o &= \frac{2{V_{DC}}^2 R\left([(1-\cos\pi)\cos\frac{\alpha}{2}]\right)^2 R}{\pi^2 Z_0^2\left(\frac{1}{Q^2}+\left(\frac{\omega_s}{\omega_0}-\frac{\omega_0}{\omega_s}\right)\right)^2} \\ &= \frac{{V_{DC}}^2 R}{Z_o^2}\frac{2\left([(1-\cos\pi)\cos\frac{\alpha}{2}]\right)^2}{\pi^2\left[\frac{1}{Q^2}+\left(\frac{\omega_s}{\omega_0}-\frac{\omega_0}{\omega_s}\right)^2\right]} \end{aligned} \tag{2.18}$$

From equation 2.18, the normalized output power can find in (2.19)

$$\frac{P_o}{V_{DC}{}^2 R / Z_o^2} = \frac{2\left([(1-\cos\pi)\cos\frac{\alpha}{2}]\right)^2}{\pi^2\left[\frac{1}{Q^2}+\left(\frac{\omega_s}{\omega_0}-\frac{\omega_0}{\omega_s}\right)^2\right]} \tag{2.19}$$

Normalized output power

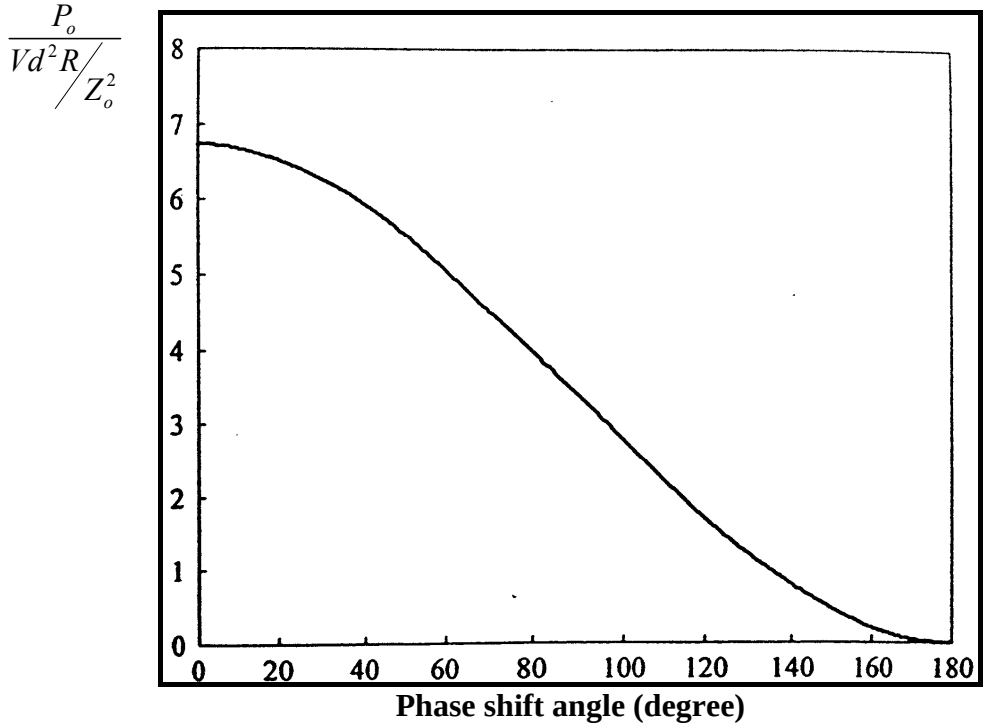

Figure 2.23 Normalized output power versus alpha angle with PS

At constant power angle (ϕ), the output voltage and current of this control is decreased when increasing the alpha angle (α). From equation 2.19, we can plot the normalized output power as a function of phase shift angle which is shown in Figure 2.23. The output power will be decreased when the phase shift angle increase.

2.6 *L-LC* Resonant with Voltage Source Inverter

The three element *L-LC* resonant load [24]–[26] can offer a better performance than the traditional series resonant load, particularly due to its short-circuit immunity and lower transformer secondary current. Figures 2.24 and 2.25 show the *L-LC* resonant inverter topology and the corresponding output voltage and current waveforms operating above the resonant frequency (ZVS), respectively. The difference between this circuit power stage configuration and that of the current source inverter with parallel resonant load presented in Figure 2.10 is that in this case the inductance L_S is several times larger than the parasitic inductance, L.

In addition, the inverter's resonant frequency is a function of the parallel capacitor C, the load inductor, L, and of L_S. The inverter is operated with variable frequency to simultaneously regulate the output power and maintain ZVS operation. An important advantage of this inverter is that, unlike the series resonant voltage source inverter, it is

immuned against load shorts because L_S is considerably larger than L. However, the turn-off losses remain as in the series resonant voltage source inverter [24].

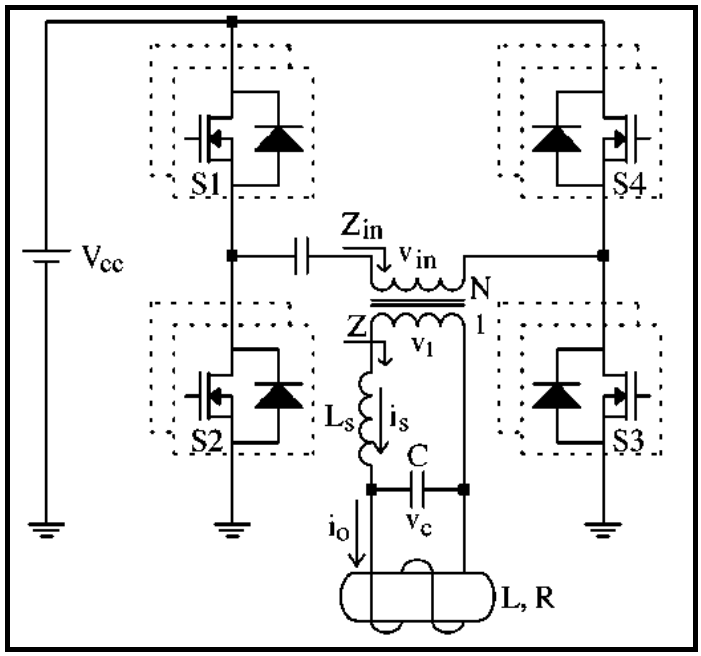

Figure 2.24 *L-LC* resonant with full bridge voltage source inverter topology [24]

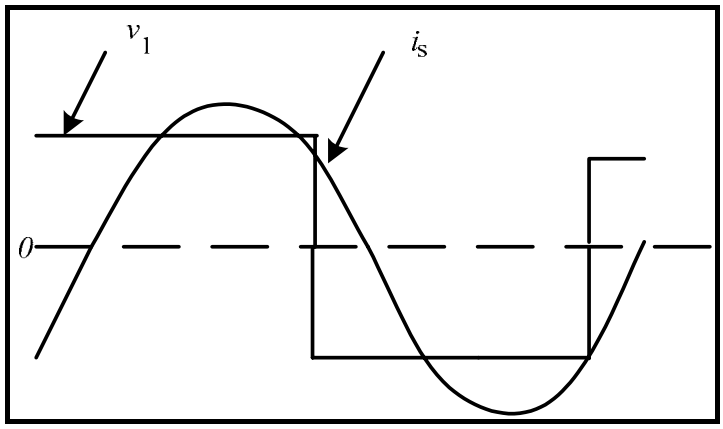

Figure 2.25 Output voltage and current wave form of *L-LC* resonant full bridge voltage source inverter operating above resonant frequency (ZVS)

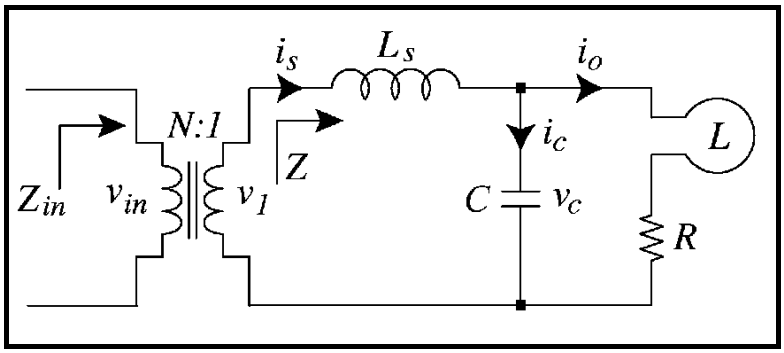

Figure 2.26 Equivalent circuit of *L-LC* resonant load [24]

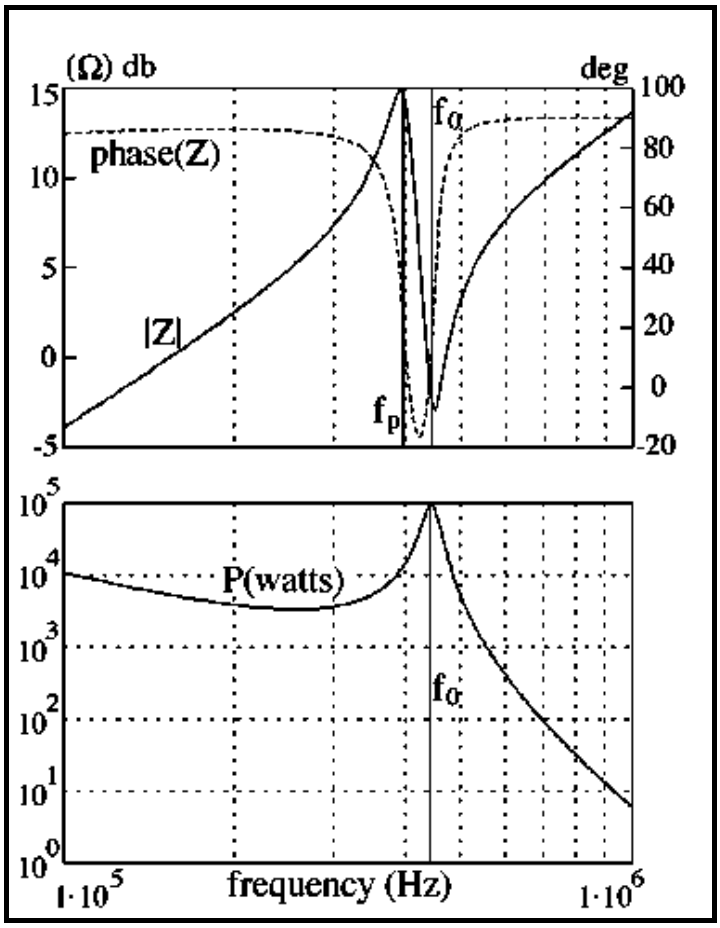

Figure 2.27 Steady-state behavior of the *L-LC* oscillator [24]

Substituting the heating coil and the piece by its equivalent *L–R* series network results in the *L-LC* resonant load, as depicted in Figure

As revealed in Figure 2.24, this three-element oscillator exihibits a parallel resonant behavior (maximum impedance) at the resonant frequency of the parallel ending of the *L-LC* resonant load (ω_p), and a series resonant behavior (minimum impedance) at the resonant frequency of the *L-LC* resonant load (ω_0). Below ω_p and above ω_0, the oscillator is inductive (current lagging mode), and between ω_p and ω_0, it can either be capacitive (current leading mode) or inductive, depending on the choice of parameters.

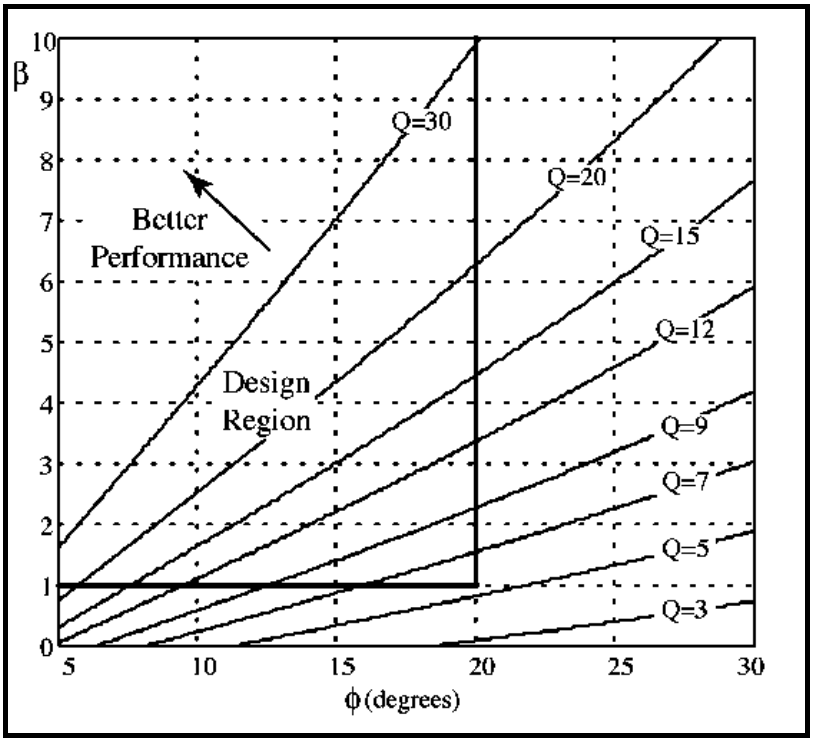

Figure 2.28 Switching angle ϕ for different applications (Q-factors) and designs of current gain (β) [24]

Figure 2.28 plots the values of β for different switching angles and Q-factors which is proposed in [24]. The design region corresponds with acceptable switching angles ($\phi <$ 20◦) and current gains ($\beta > 1$). As we can see, there is only design solution for $Q > 6$. Moreover, high current accretion (values of β) are suitable for high Q-factors. In other words, the *L-LC* performs better in high Q applications ($Q > 30$.), typically high frequency applications such as gold melting, copper tube welding, high-frequency hardening, and heating of materials with small equivalent resistance R like copper, brass, aluminum, etc.

CHAPTER 3 LLC RESONANT INVERTER

In this chapter, the proposed LLC resonant inverter configuration is described. Details of the control strategy, the design procedure of the series inductor (L_s) and matching transformer are presented. This chapter also provides a calculation of switching and conduction losses of all switches.

3.1 Circuit Description

An LLC resonant inverter configuration for induction heating applications that we propose is shown in Figure 3.1. The inverter consists of four switches with antiparallel diodes, a resonant capacitor (C_p), a series inductor (L_s) in which the leakage reactance of the transformer is included and an induction coil that comprises a series combination of a resistor (R_{eq}) and an induction coil inductor (L_{coil}) [27, 28]. A DC blocking capacitor (C_b) is inserted in series with the transformer primary winding. The stray capacitance of MOSFET switching device S_1, S_2, S_3 and S_4 are noted as C_{oss1} , C_{oss2} , C_{oss3} and C_{oss4} respectively.

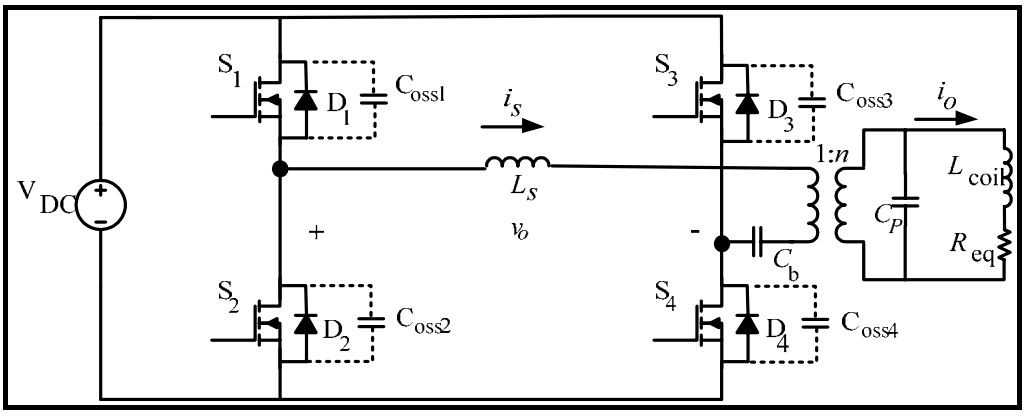

Figure 3.1 Full-bridge LLC resonant inverter.

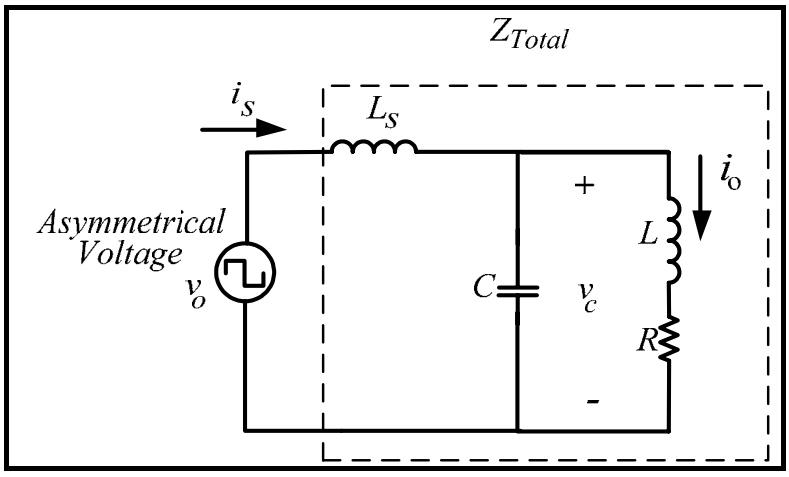

Figure 3.2 Equivalent circuit

An equivalent circuit of the full-bridge LLC inverter system in Figure 3.1 is shown in Figure 3.2 where the input voltage can be viewed as an asymmetrical ac voltage

supplied to the system. With a negligible value of C_b, it is noted that the capacitor C, the inudctor L, and the resistor R represent the equivalent capacitor C_p, inductor L_{coil}, and the resistor R_{eq} referred to the primary side of the transformer, respectively. The total impedance to the asymmetrical voltage source (v_o) is denoted by Z_{total}. The current i_s and i_o are the input and output currents, respectively.

3.2 Modes of Operation

In this section, the mode operations of inverter with and without stray capacitance (C_{oss}) are presented. For simplicity and without loss of generality, the case where the switches with no C_{oss} is discussed first.

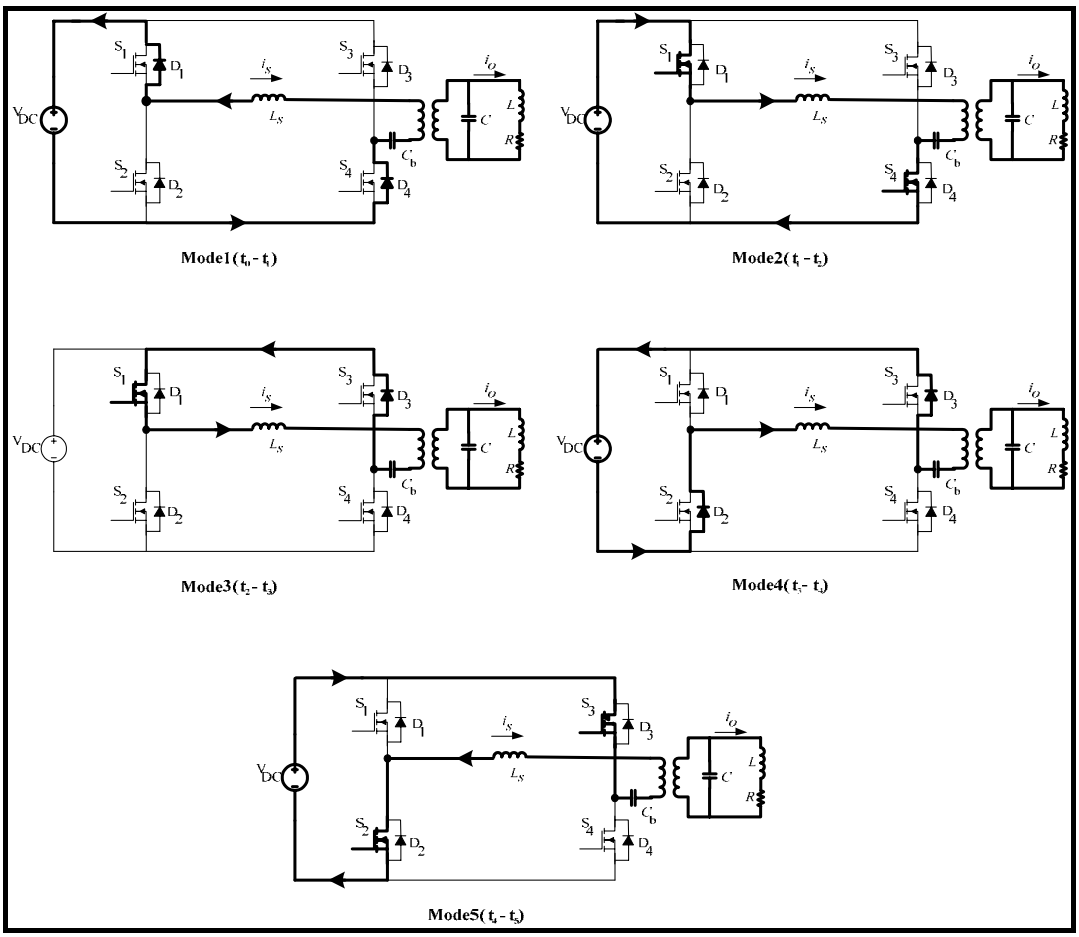

Figure 3.3 Modes of operation of inverter operations without stray capacitance

3.2.1 Modes of Operation without Stray Capacitance

The asymmetrical voltage signal in Figure 3.2 is realized from shifting the gate drive signals of the switches S_3 and S_4 to the desired shifting angle as shown in Figure 3.3. The current and voltage waveforms are also shown in this figure. The operation of the inverter without stray capacitance is shown in Figure 3.3. Five modes of operation exist within one switching cycle. The corresponding circuit topology for each mode of operation is illustrated in Figure 3.4. The analysis is as follow

1) Mode 1 (t_0−t_1): While switches S_2 and S_3 are off, at $t = t_0$, switches S_1 and S_4 receive positive gating signals. The negative input current *(*i_s) flows through diodes D_1 and D_4.

2) Mode 2 (t_1−t_2): At $t = t_1$, as soon as the antiparallel diodes D_1 and D_4 are off, switches S_1 and S_4 conduct and the ZVS operation is achieved. During this mode, the positive input current (i_s) flows.

3) Mode 3 (t_2−t_3): At $t = t_2$, while the switch S_1 still conducts, the switch S_4 is turned off and the antiparallel diode D_3 conducts. At the same instance, the switch S_3 receives positive gating signals. The interval t_2−t_3 defines the shifted angle α that is used for output power control.

4) Mode 4 (t_3−t_4): At $t = t_3$, the switch S_1 is turned off. Similar to that in Mode 1, the diode D_2 starts conducting positive input current i_s together with the diode D_3.

5) Mode 5 (t_4−t_5): At $t = t_4$, when the antiparallel diodes D_2 and D_3 are off, the switches S_2 and S_3 which already received positive gating signals, conduct and the ZVS opeation is achieved. During this mode, the input current i_s becomes negative. At this point, a full cycle of operation is accomplished. The next operating cycle continues to repeat from modes 1 to 5.

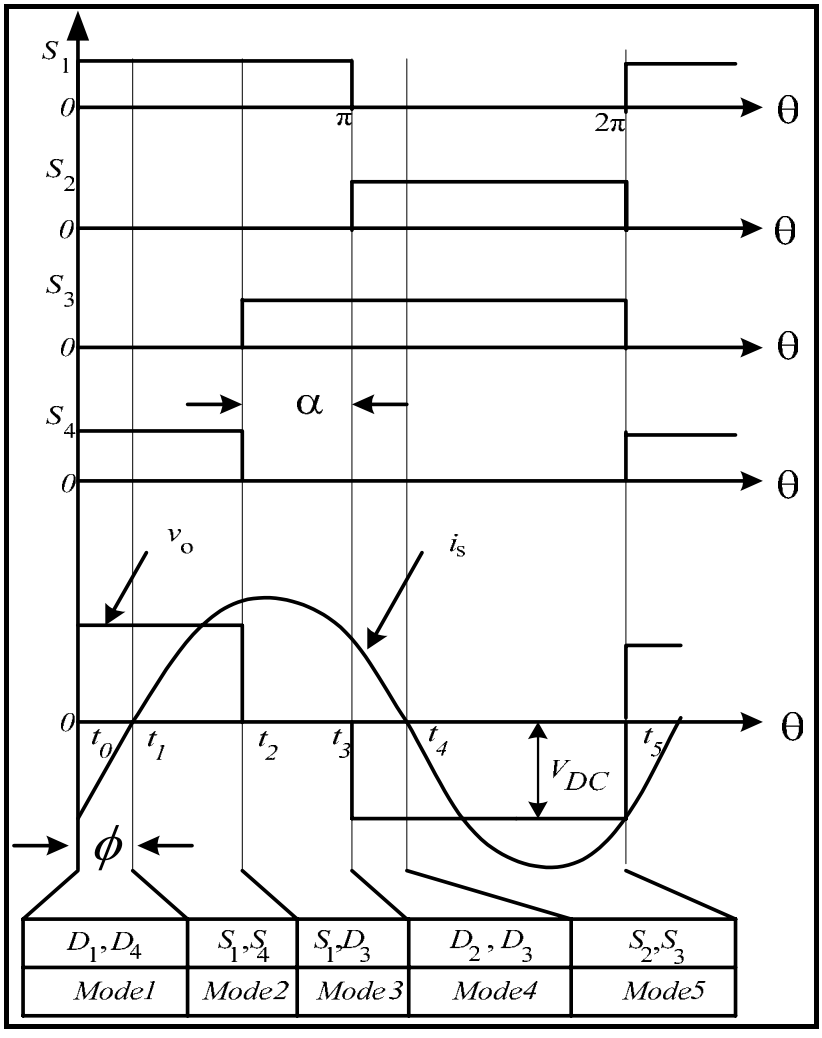

Figure 3.4 Typical waveforms of inverter operations with stray capacitance

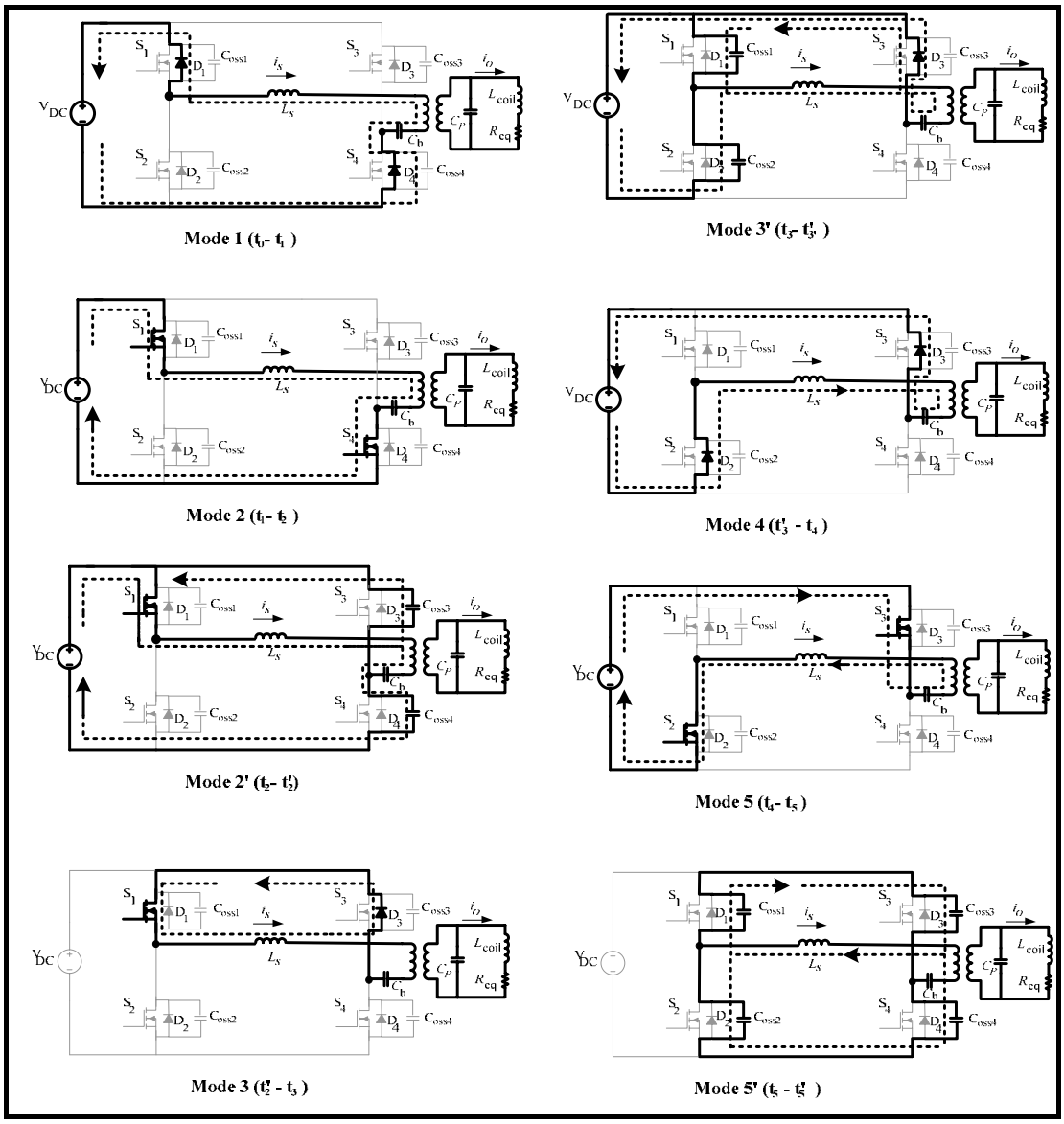

Figure 3.5 Modes of operation of inverter operations with stray capacitance

3.2.2 Modes of Operation with Stray Capacitance

Next, the stray capacitance in the switching device is taken into consideration. With the mentioned shifted gate drive signals, eight modes of operation exist within one switching cycle when the stray capacitances are taken into account.

The corresponding waveforms and circuit topology for each mode of operation are illustrated in Figure 3.5 and 3.6, respectively. The analysis is as follows.

1) Mode 1 (t_0−t_1): While switches S_2 and S_3 are off, at $t = t_0$, switches S_1 and S_4 receive positive gating signals. The negative input current (i_s) flows through diodes D_1 and D_4.

2) Mode 2 (t_1−t_2): At $t = t_1$, as soon as the antiparallel diodes D_1 and D_4 are off, switches S_1 and S_4 conduct and the ZVS operation is achieved. During this mode, the positive input current (i_s) flows.

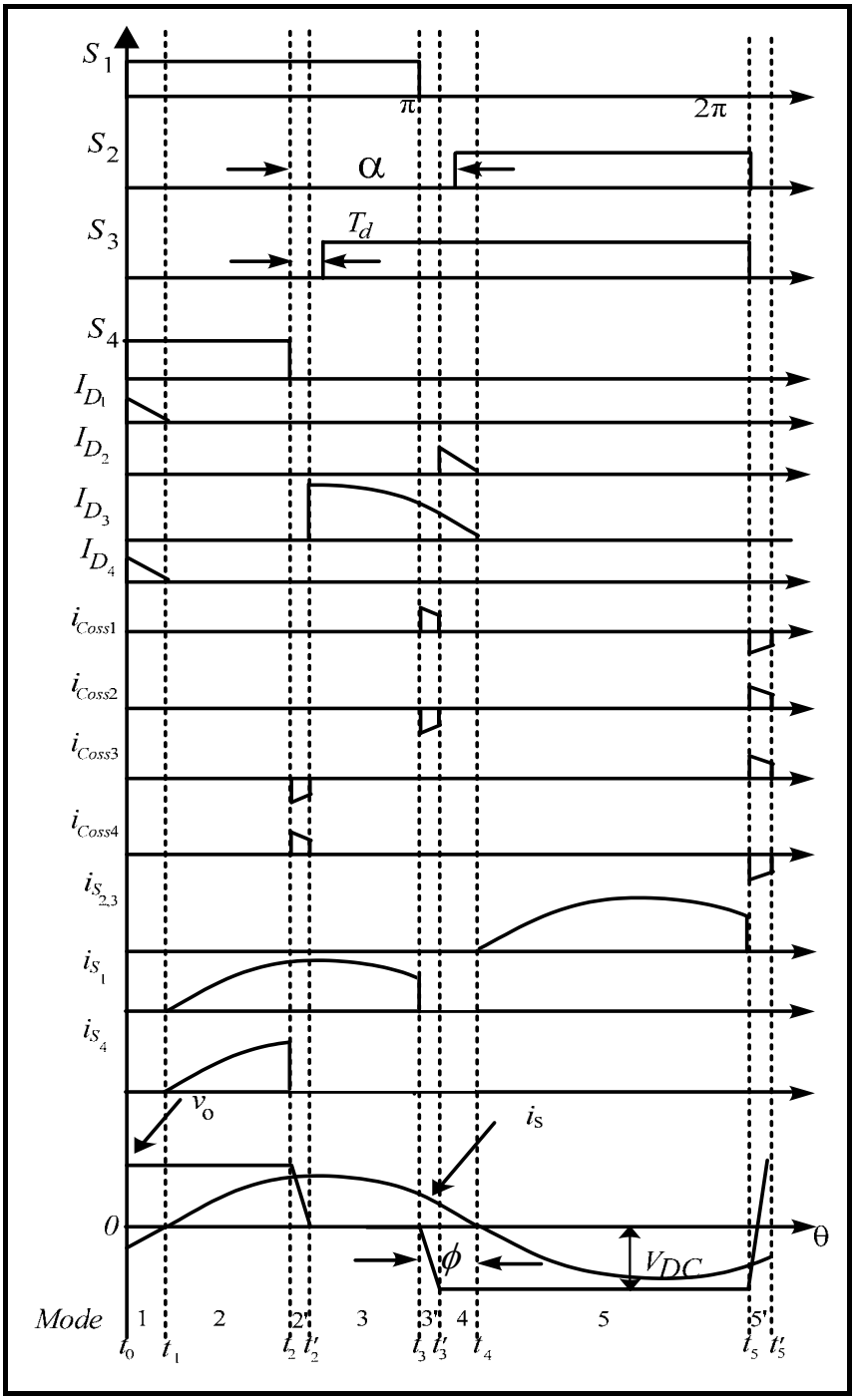

Figure 3.6 Typical waveforms of inverter operations with stray capacitance

3) Mode 2' (t_2−t'_2): At $t = t_2$, after the switch S_4 is off, the current flows in the same direction. The charge in C_{oss3} is gradually decreasing whereas the charge in C_{oss4} is slowly increasing. At this stage the output voltage changes from + V_{DC} to 0.

4) Mode 3 (t'_2−t_3): At $t = t'_2$, while the switch S_1 still conducts, the switch S_4 is turned off and the antiparallel diode D_3 conducts. After the switch dead time, the switch S_3 receives a positive gating signal.

5) Mode 3' (t_3−t'_3): During this period, all switches are off simultaneously. A part of positive current i_s flows through the antiparallel diode D_3 and C_{oss2}. At the same time, the charge in the capacitor C_{oss2} decreases whereas the charge in the capacitor C_{oss1} increases. In this operation, the output voltage v_o changes from zero to $-V_{DC}$.

6) Mode 4 (t'_3–t_4): At $t = t'_3$, the switch S_1 is already turned off. Similar to that in Mode 1, the diode D_2 starts conducting positive input current i_s together with the diode D_3. After the switch dead time, the switch S_2 receives a positive gating signal. The shifted angle α is from t_2 to the moment the switch S_2 is on.

7) Mode 5 (t_4–t_5): At $t = t_4$, when the antiparallel diodes D_2 and D_3 are off, the switches S_2 and S_3 which already received positive gating signals, conduct and the ZVS opeation is achieved. During this mode, the current i_s becomes negative.

8) Mode 5' (t_5–t'_5): At $t = t_5$, after the switches S_2 and S_3 are turned off, the negative current i_s flows through stray capacitors, C_{oss1}, C_{oss2}, C_{oss3} and C_{oss4}. The charges in C_{oss1} and C_{oss4} decrease while the charges in C_{oss2} and C_{oss3} increase. At this point, a full cycle of operation is accomplished. In this operation, v_o changes from $-V_{DC}$ to $+V_{DC}$. The next operating cycle continues to repeat from modes 1 to 5'.

In many cases, the stray capacitance may be neglected and the modes of operation for one switching period are reduced to 5 modes (i.e. modes $1 \rightarrow 2 \rightarrow 3 \rightarrow 4 \rightarrow 5$). Note that in this work, it is assumed that the charging time of the stray capacitor (t_{coss}) is smaller than the switch's dead time.

3.2 Circuit Analysis

In order to understand the preliminary characteristics of voltages and currents of the main and load circuits, a mathematical approach is required. With the circuit operation in the previous section, the steady-state characteristics are analyzed in this section. The steady-state analysis of the full-bridge LLC inverter is based on the following assumptions.

1) All circuit components are ideal. This is because switching devices, inductors, capacitor and a transformer in the circuit consists of small parasitic and may be negligible compared with the circuit operating characteristics. This simplification helps facilitate the circuit analysis.

2) The dc input voltage, V_{DC}, is constant because the capacitor on the dc bus is assumed to be sufficiently large. This allows the ripple voltage on the dc bus to be neglected which greatly simplifies the analysis of the output voltage of the inverter.

3) The effects of stray capacitance are neglected because their capacitance (in the order of nanofarad) is much less than the resonant capacitor, C_p (in order of microfarad). Therefore, the effects of the stray capacitance on the operating characteristics particularly load current and voltage are essentially negligible.

From Figures 3.2 and 3.3, the relationship between the load voltage (i.e. the capacitor voltage: v_c) and the inverter output voltage (v_o) is given as,

$$\frac{V_c}{V_o} = \frac{R + j\omega L}{(j\omega L_s \times j\omega C)(R + j\omega L) + j\omega L_s + R + j\omega L)} \tag{3.1}$$

where $L = n^2 L_{coil}$, $R = n^2 R_{eq}$ and $C = \frac{C_p}{n^2}$ given that n is the transformation ratio of the transformer. The resonant frequency of the system in Figure 3.2 is given as,

$$\omega_o = \sqrt{\frac{L + L_s}{L \cdot L_s \cdot C}} \tag{3.2}$$

Note that the inverter is designed to operate such that the switching frequency (ω) is slightly higher than the resonant frequency (ω_0) for ZVS operation. This enables us to take only the fundamental component (V_1) of the inverter output voltage (v_o) in Figure 3.2 into account. The load voltage is given as,

$$V_C = \left(-\frac{L}{L_s} - j \frac{L^2}{R L_s} \sqrt{\frac{L + L_s}{L \cdot L_s \cdot C}} \right) \cdot V_1 \tag{3.3}$$

The fundamental component V_1, of the capacitor voltage v_C in (3.3) can be obtained from the following coefficients of Fourier series of the inverter output voltage v_o [13],

$$\left.\begin{aligned} \hat{V}_n &= \frac{V_m}{\pi} \sqrt{a_n^2 + b_n^2} \\ \phi_{vn} &= \tan^{-1} \frac{a_n}{b_n} \\ b_n &= \frac{V_m}{n\pi} \left[2 - (-1)^n - \cos n(180 - \alpha) \right] \\ a_n &= \frac{V_m}{n\pi} \left[-\sin n(180 - \alpha) \right] \end{aligned}\right\} \tag{3.4}$$

where V_m is the dc input voltage assuming the same value as V_{DC}, ϕ_{vn} is the phase of the nth hamornic of v_o and α is the shifted angle of the switch S_4, as shown in Figure 3.6. Using (3.4), the amplitude of the fundamental voltage v_1 can be calculated as,

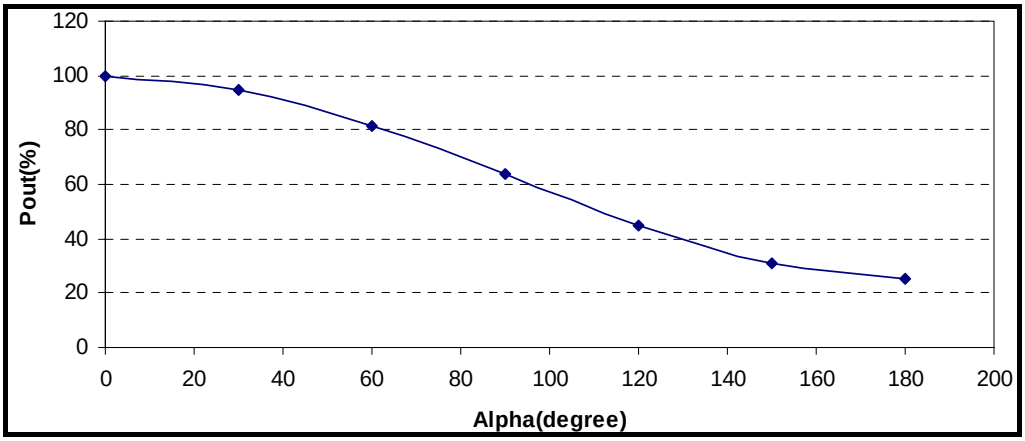

Figure 3.7 Output power versus α

$$\hat{V}_1 = \frac{V_m}{\pi} \times \sqrt{\sin^2(180-\alpha) + (3-\cos(180-\alpha))^2} \tag{3.5}$$

and the average output power (P) at the load can be obtained as [24],

$$P_o = V_1^2 \,\mathrm{Re}\left\{ Z_{total}(j\omega_0)^{-1} \right\} \tag{3.6}$$

which is expanded to

$$P_o = \frac{V_m^2}{2R\pi^2}(\sin^2(180-\alpha) + (3-\cos(180-\alpha))^2)\left(\frac{L}{L_s}\right)^2 . \tag{3.7}$$

For the zero power angle ϕ, the output power P_o in (3.7) depends on the shifted angle α. Figure. 3.7 shows the relationship of the output power and α, obtained using (3.7). It is seen that an increase of α results in reduction of the output power. Meaning that the output power can be controlled through an adjustment of α.The greater the angle α, the less power delivered to the load. By substituting α with 0° and 180° in (3.7), the output power P_o results in 100% and 24.97%, respectively. Notice that the output power P_o does not reach zero through the setting of α because the voltage reduction in the asymmetrical control is through the positive cycle. The negative cycle of the output voltage remain unaffected. The equivalent circuit in Figure 3.2 receives only negative cycle of the asymmetrical input voltage. Based on the superposition principle, there always exists a small amount of output current flowing through the load. Another interesting aspect of (3.7) is that it can be used to predict the parameter variation, especially the inductor L. As mentioned in the previous chapter, the induction coil inductance varies as the work-piece is heated. Therefore, the relationship of the output power, the shifted angle α and the inductance L is depicted in Figure 3.8.

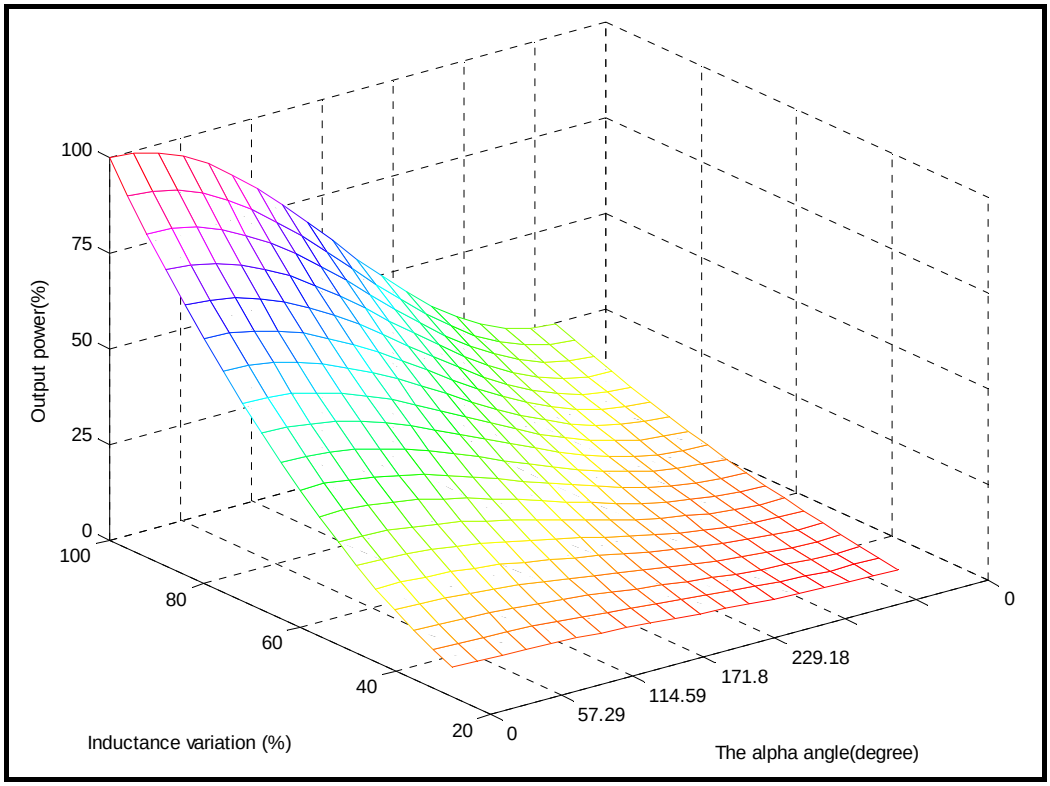

Figure 3.8 The output power as a function of α and inductance variation

For LLC resonant load, the inductance variation causes the output power to change. The inductance variation in percentage lower than 100% indicates the reduction of the inductance L from its nominal value. Notice that the inductance reduction and the increase of the alpha angle result in the decrease of the output power. This relationship is governed by (3.7). Evidently, the output power control can be effectively done through changing the alpha angle and becomes less effective when the inductance is chaged under heating condition.

From (3.7) we can define the output power as a function of Q that is shown in (3.8). The output power P_o is essentially directly proportional to the quality factors (Q), providing that the angle is kept constant.

$$P_o = \frac{V_1^2 \sqrt{CL_s}\, Q \tan\phi}{\tan\phi \sqrt{Q \tan\phi - 1}} \tag{3.8}$$

The frequency response of the output power (P_o) under different quality factors (Q) is shown in Figure 3.9 with the angle α set to zero. At higher Q factor, the inverter operates close to the resonant frequency, ω_0, (i.e. the normalized frequency f_s/f_b is close to 1). Unlike the induction coil current (i_o) shown in Figure 3.10, the Q factor has negligible effect on the resonant frequency. That is the peak value of i_o occurs at the same frequency regardless of the Q factors. The peak value of i_o is related to the RLC parallel end in Figure 3.2 where L_s does not play a roll in the frequency response of i_o. The necessity and the design of L_s is discussed in the next section.

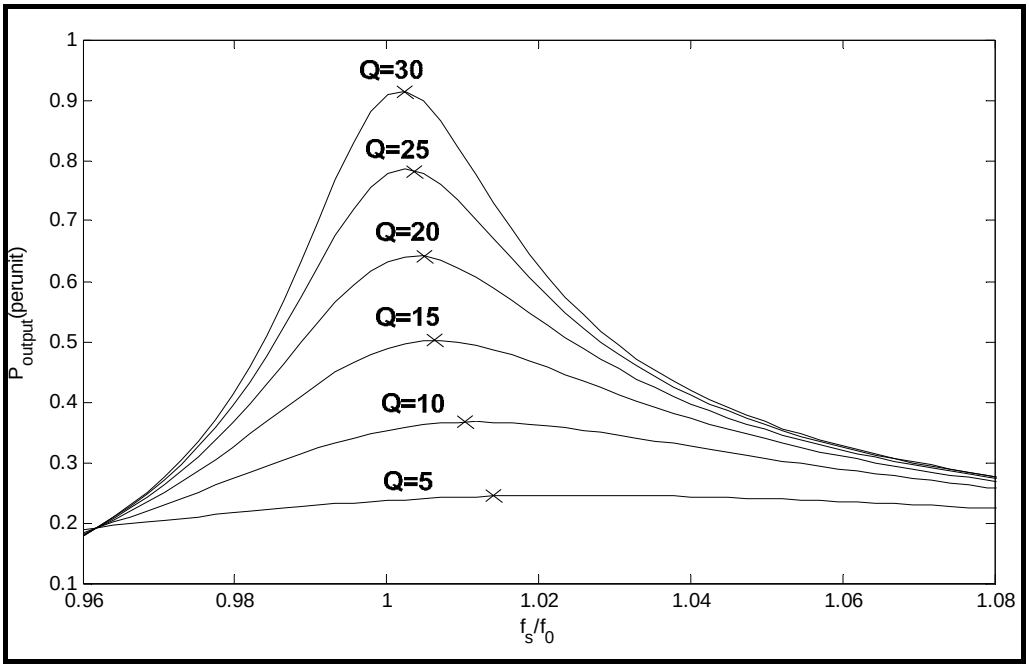

Figure 3.9 Frequency response: output power (P_o) at various Q factors

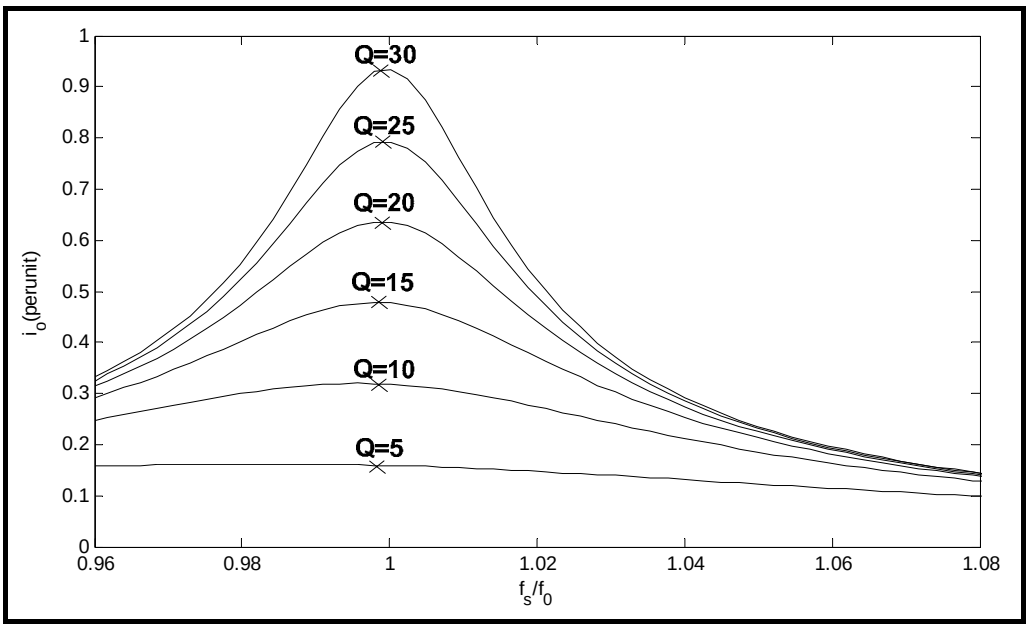

Figure 3.10 Frequency response: output current (i_o) at various Q factors

3.4 Load Current Gain

Referring to Figure 3.2, the total impedance (Z_{total}) can be expressed as,

$$Z_{Total}(\omega) = \frac{R - \omega^2 CL_s R + j\omega L_s + j\omega L - j\omega^3 L_s L}{-\omega^2 CL + j\omega CR} \tag{3.9}$$

At resonant frequency (ω_0),

$$Z_{Total}(\omega_0) = \frac{\omega_0 L_s^2 R(L^2\omega_0 + jR(L_s + L))}{-L\omega_0 - R^2(L_s^2 + L_s L + L^2)} \tag{3.10}$$

The switching angle ϕ is given as

$$\phi = arg\left\{ Z_{Total}(j\omega_0) \right\} = arctan\left(\frac{R(L_s + L)}{L^2\omega_0} \right) \rangle\ 0 \tag{3.11}$$

This results in,

$$\frac{L_s}{L} = \frac{L\omega_0}{R} tan\phi \text{ - } 1 \tag{3.12}$$

The current gain is found as,

$$\frac{I_o}{I_s} = \frac{1}{j\omega C Z_P(j\omega)} \tag{3.13}$$

where $Z_P(j\omega) = \frac{1}{j\omega C} /\!/ (j\omega L + R)$. The current gain at resonant frequency (ω_0) is given as,

$$\left| \frac{I_o}{I_s}(\omega_0) \right| = \frac{L_s}{L} \frac{1}{\sqrt{\frac{CL_s R^2(L + L_s)}{L^3} + 1}} \tag{3.14}$$

Therefore, the coil current at resonance can be expressed as,

$$I_o = \frac{L_s}{L} I_s \cos\phi \tag{3.15}$$

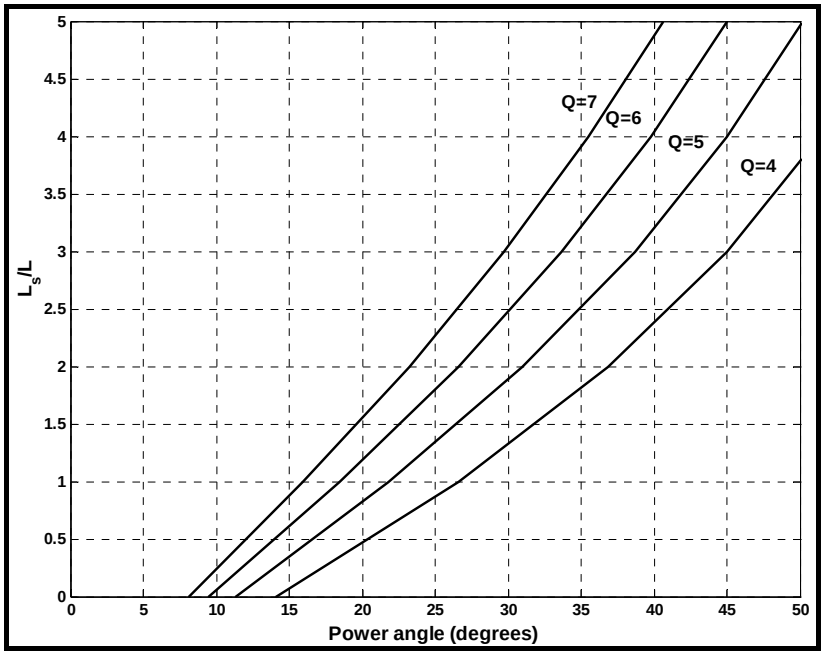

Figure 3.11 Current gain and power angle at various Q factors (Q<10)

From (3.15), we can plot the current gain (L_s/L) and power angle at various Q factors, from 4 to 7, in Figure 3.11. At the frequency above resonance, there is always a positive power angle ϕ (i.e. lagging current operation). A high efficiency inverter with LLC topology can be achieved by introducing a small positive switching angle and high current gain in the design. From (3.11) and (3.14), it is deduced that a suitable load would be applications with high quality factor (Q) such as, brazing, surface hardening and tube welding. For applications with low Q (less than 10), it is very difficult to obtain both high current gain and resonant operations at the same time. One of the possible solutions would be to increase the power angle ϕ. This means that the operating frequency must be adjusted further away from the resonant frequency which results in the operation of the inverter under low efficiency. This is where the high frequency transformer is introduced to match the output current and power. In addition to improving the system efficiency, the important advantage of the inclusion of the transformer is the inherent current limiting capability in case of transformer saturation. The inductor L_s carries low current because it is located on the primary side. Therefore, it is easier and cheaper to construct such an inductor.

3.5 Switching and Conduction Losses

A majority of power loss in the typical power electronic converters is the switching loss. For the case of resonant inverters, the conduction loss is of similar importance. The LLC resonant inverter in this work consists of 4 MOSFETs (S_1-S_4). The loss of switches can be divided into two parts: the switching loss and conduction loss which are derived in this section.

3.5.1 Switching Loss

To maintain the operation under ZVS conditions, the power angle ϕ must be kept greater than both the dead time and charging time of the stray capacitors [31, 32]. This allows sufficient time for the diodes to conduct while keeping the voltage across the switch at zero. For the operation at the frequency above resonance, the turn-on

switching loss of all switches is zero, but there still is a turn-off switching loss for every switch. It is seen in Figure 3.6 during t_3-t_4 interval that, the switch S_4 turns off at a larger current as α becomes larger. This results in a higher switching loss. To consider the switching loss in details, the current and voltage transition at turn off are illustrated in Figure 3.12.

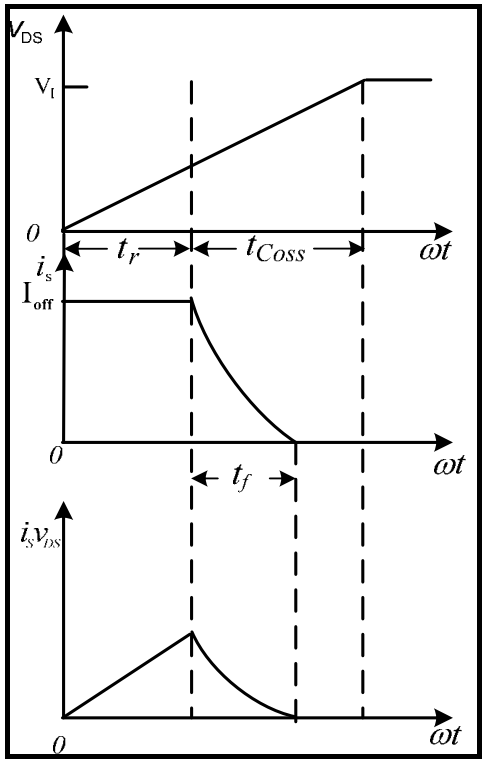

Figure 3.12 Theoretical waveforms of the turn off loss of switches

The drain to source voltage v_{DS} during rise time (t_r) is given as

$$v_{DS} = V_I \left(\frac{\omega t}{\omega t_r} \right) \tag{3.16}$$

where V_I is the voltage across the switch while the switch is turned off which is the same as the dc input voltage (V_{DC}). While the switch current is a small portion of a sinusoid and can be approximated by a constant

$$i_S = I_{OFF} \tag{3.17}$$

where I_{OFF} is the current through the switch before turning off.

The power loss associated with the voltage during rise time (P_{tr}) is given as,

$$P_{tr} = \frac{1}{2\pi} \int_0^{\omega t_r} i_S v_{DS} d(\omega t) = \frac{t_r V_I I_{OFF}}{2T} \tag{3.18}$$

During fall time (t_f), the switch current can be approximated by a parabola function as

$$i_S = I_{OFF}\left[1 - \frac{\omega t}{\omega t_f}\right]^2 \tag{3.19}$$

while the drain to source voltage is (3.16) The power loss associated with t_f (P_{tf}) is provided as,

$$P_{tf} = \frac{1}{2\pi}\int_{\omega t_r}^{\omega t_f} i_S v_{DS} d(\omega t) = \frac{I_{OFF} V_I (t_f - t_r)(t_f + t_r)(t_f^2 + 4t_r t_f + t_r^2)}{12T} \tag{3.20}$$

Hence, the turn-off switching loss is combined as

$$P_{off} = P_{tr} + P_{tf} = fV_I I_{OFF}\left(\frac{t_r}{3} + \frac{(t_f - t_r)(t_f + t_r)(t_f^2 + 4t_r t_f + t_r^2)}{12}\right) \tag{3.21}$$

So the turn off loss of the full-bridge LLC resonant inverter with asymmetrical control becomes

$$P_{total,off} = fV_I\left(\frac{t_r}{3} + \frac{(t_f - t_r)(t_f + t_r)(t_f^2 + 4t_r t_f + t_r^2)}{12}\right)(3I_{OFF,S_1,S_2,S_3} + I_{OFF,S_4}) \tag{3.22}$$

where $I_{OFF,S1,S2,S3}$ and I_{OFF,S_4} assume the following forms,

$$I_{OFF,S1,S2,S3} = I_m \sin(\phi) \tag{3.23}$$

and

$$I_{OFF,S_4} = I_m \sin(\alpha + \phi) \tag{3.24}$$

If a snubber capacitor is added to the circuit, the charging time (t_{Coss}) will increase and the peak of the product of i_s and v_{ds} in Figure 3.12 will decrease. Thus, the turnoff loss is decreased. The dead time must be increased to maintain approximately zero turn off loss. Clearly, the snubber capacitor can always be included. However, there is a tradeoff for adding a snubber capacitor because the power angle ϕ must cover the switch dead time and the capacitor charging time. Therefore, the increased power angle ϕ results in a reduced range of the angle α ($\alpha_{max} = \phi$-180) and therefore, the range of power adjustment will be reduced.

3.5.2 Conduction Loss

Since the intervals t_2-t'_2 and t_5-t'_5 in Figure 3.6 representing the charging and discharging periods of the stray capacitors, are small compared with the overall conduction times, therefore both intervals are neglected in the following calculation.

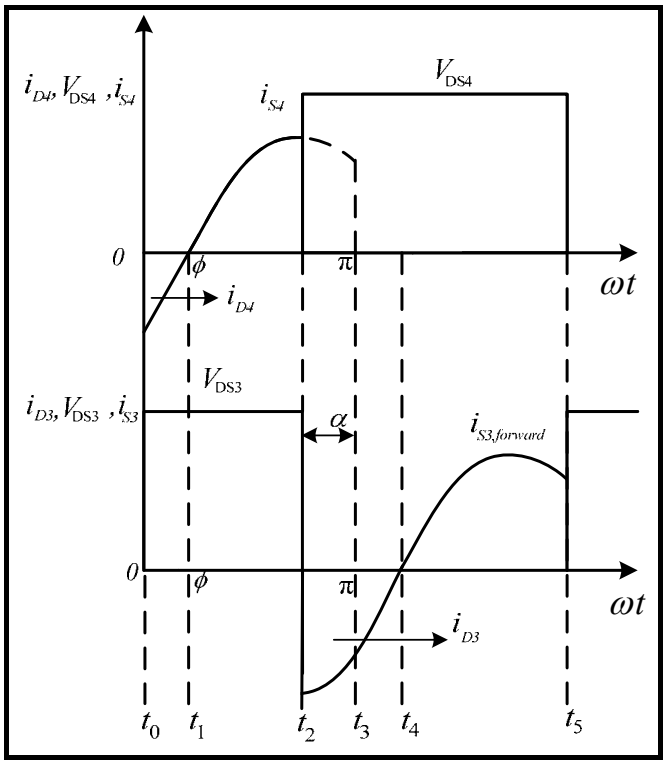

Figure 3.13 Theoretical waveforms of the conduction loss of the switch S_3 and the switch S_4

To take the switch conduction loss into account, the current and voltage at the switches S_3 and S_4, from t_0 to t_5 are illustrated in Figure 3.13. The switches S_1, S_2 and S_3 carry the same current and conduction loss through the intervals t_1-t_2 and t_4-t_5, respectively. Since the inverter current i_s is given as,

$$i_s(t) = I_{S,peak} sin(\omega t - \phi) \tag{3.25}$$

The current contribution to conduction losses of the switches S_1, S_2 and S_3 are found as

$$I_{S_{1,2,3},rms} = \sqrt{\frac{1}{2\pi}\int_{\theta}^{\pi} i_S^2(t)\, d\omega t} \tag{3.26}$$

$$I_{S_{1,2,3},rms} = \frac{I_s}{2}\sqrt{1-\frac{\phi}{\pi}+\frac{\sin\phi\cos\phi}{\pi}} \tag{3.27}$$

For the asymmetrical switch S_4, the conduction loss results from the current

$$I_{S4,rms} = \sqrt{\frac{1}{2\pi}\int_{\theta}^{\pi-\alpha} i_S^2(t)\, d\omega t} \tag{3.28}$$

which can be expanded as,

$$I_{S_4,\text{rms}} = \frac{I_s}{4\pi}\sqrt{-2(\alpha-\pi+\phi)+\sin(2(\alpha+\phi))} \tag{3.29}$$

The conduction loss of the switch is given as,

$$P_{s,loss} = \left(I_{S,\text{rms}}\right)^2 R_{DS,\text{on}} \tag{3.30}$$

The above conduction losses can be calculated by substitution of the currents in (3.27) to (3.29) into (3.30). Next, the diode conduction loss is considered. Clearly, the diodes D_1-D_4 and D_2-D_3 conduct during t_0-t_1 and t_2-t_4 intervals, respectively. In addition, the conduction loss of the diode D_3 includes the forward conduction during t_2-t_3 interval similar to the current in (3.26).

Therefore, the current contribution to the conduction loss of the diode D_3 is given as,

$$I_{D_{3,\text{rms}}} = \sqrt{\frac{1}{2\pi}\int_{\pi-\alpha}^{\pi} i_S^2(t)\sin^2\omega t d\omega t + \frac{1}{2\pi}\int_0^{\theta} i_S^2(t)\,d\omega t} \tag{3.31}$$

and is expanded as,

$$I_{D_{3,\text{rms}}} = \frac{I_s}{4\pi}\left(\sqrt{2\alpha+\sin(2\phi)-\sin(2(\alpha+\phi))}\right)+\frac{I_s}{2}\sqrt{\frac{\phi}{\pi}-\frac{\sin\phi\cos\phi}{2\pi}} \tag{3.32}$$

For the other diodes, the current contribution to the conduction loss is found as,

$$I_{\text{Diode,rms}} = \sqrt{\frac{1}{2\pi}\int_0^{\theta} i_S^2(t)\,d\omega t} \tag{3.33}$$

and

$$I_{D_{1,2,4,rms}} = \frac{I_s}{2}\sqrt{\frac{\phi}{\pi}-\frac{\sin\phi\cos\phi}{2\pi}} \tag{3.34}$$

The diode conduction loss is

$$P_{D,loss} = I_{\text{Diode,rms}} \times V_{\text{FWD,diode}} \tag{3.35}$$

Similarly, the conduction loss of each diode is computed by substituting (3.32) and (3.34) into (3.35).

3.6 Proposed Control Strategy

The work-piece geometry, conductivity and permeability of different metals have various effects on the inductance of the heating coil. In addition, the coil inductance is

also changed when heated. This is due to the fact that beyond the curie temperature, the relative permeability (μ_r) of the work piece decreases when the temperature increases. This results in the reduction of the equivalent inductance of the work piece which in turn reduces the coil inductance. On the contrary when the work piece temperature is lower than the curie temperature, the relative permeability of the work piece decreases with the temperature. Therefore, the coil inductance exhibits a change in the opposite direction [29].

Considering the fact that the resonant capacitance is fixed therefore, the resonant frequency is varied throughout the heating process. The phase-locked loop integrated circuit device for load-adaptive resonant frequency tracking is introduced to the resonant inverter to drive the operating frequency to the new resonant frequency. The proposed control scheme of the full bridge LLC resonant inverter consists of two parts:

- Power control through alpha angle (α) of the switch S_4
- Frequency control for zero voltage switching (ZVS) operation

The controller comprises a current sensor, zero-crossing detector, phase detector and voltage-controlled oscillator (VCO) as shown in Figure 3.14. The 4046 phase-locked loop integrated circuit is used for frequency control at slightly higher than the resonant frequency [70]. In typical voltage-fed inverter, the gate drive signal is in phase with the asymmetrical inverter output voltage v_o. Therefore, we can use the gate drive signal instead of the load voltage pulse for phase detection. The current signal, i_o, is compared with the voltage signal in order to detect the phase difference. The output signal of the digital phase detector is filtered by an RC low pass filter to obtain the average value that is proportional to the phase difference at the load. The block diagram of the generation of asymmetrical gate drive signals for power control is shown in Figure 3.15. The P_{ref} signal is compared with the ramp signal from the 4046 IC to generate the gate signal G_4.

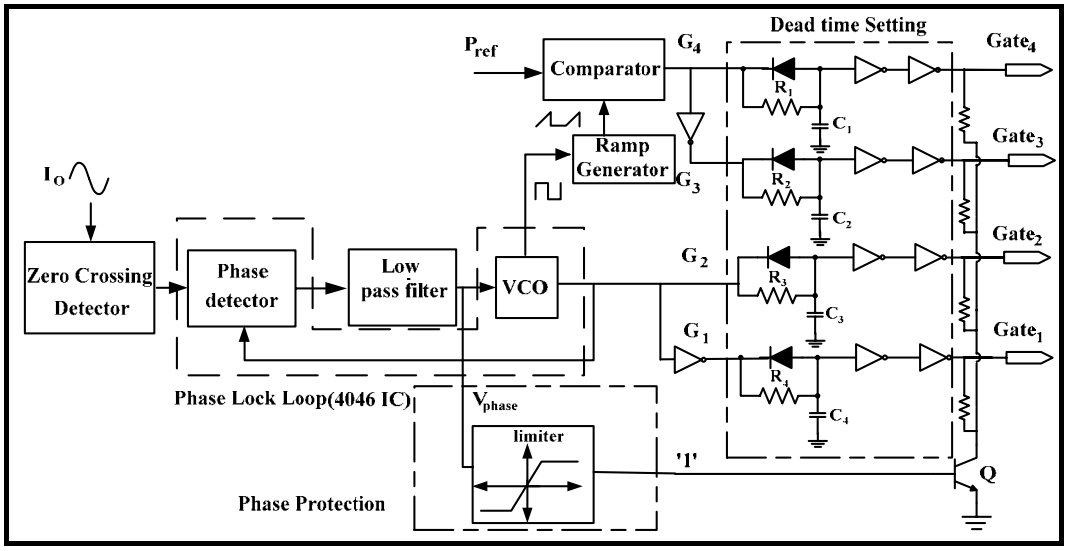

Figure 3.14 Proposed control block diagram of the LLC resonant inverter

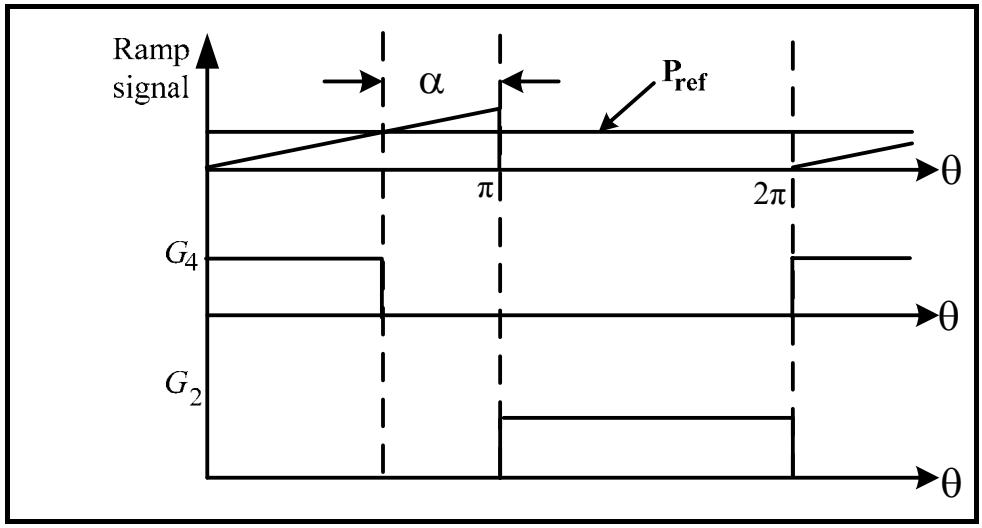

Figure 3.15 Waveforms of the asymmetrical gate drive signal

If the P_{ref} signal is greater than the ramp signal, the gate signal G_4 is set to high. Otherwise, it is set to low. This way, α is dependent on the P_{ref} signal. The gate signal G_2 is always on from π to 2π. The G_1 and G_3 signals are inversed of the G_2 and G_4 signals, respectively. Note that the ramp signal is generated from the phase detector. Therefore, its frequency is automatically adjusted to track the resonant frequency and ZVS operation at turn on is obtained. The gating signals G_1,G_2,G_3 and G_4 are sent into the dead time circuit where the dead time setting is adjusted through the pairs R_1-C_1, R_2-C_2, R_3-C_3 and R_4-C_4. A phase protection circuit with a limiter is used where the V_{phase} signal, a dc signal proportional to the phase, is put through a limiter [30]. This allows an operation in the desired frequency range for the ZVS mode. If the phase lies in the region that is out of the predetermined limits, an active signal is sent out to turn the transistor Q on and ground all gate signals S_1 to S_4. The inverter is then turned off.

3.7 Design Procedure

In this section, a design example of major components of the system in Figure 3.1 is discussed. The targeted application is a 450W induction melting system for a 30-gram aluminum work piece. The desired frequency is at 110 kHz. The readily available induction coil inductance (L_{coil}) and equivalent resistance (R_{eq}) are 1.11 μH and 100 mΩ, respectively. The power angle ϕ is set to 36 degrees. Using (3.11), the maximum series inductance ($L_{s,max}$) is obtained from (3.11) as

$$L_{s,max} = \frac{L^2 \omega_0}{R} tan\phi \text{ - } L = 5.1\mu\text{H}. \tag{3.36}$$

Next, the resonant capacitor is obtained from (3.2) as

$$C = \frac{L + L_{s,max}}{L \cdot L_s \cdot \omega_o^2} = 2.29\ \mu\text{F}. \tag{3.37}$$

Five of 30 kVAR, 400V, 100A_{rms}, 0.47 μF capacitors with the total capacitance of 2.35 μF are used as C_P. Since the available capacitance is slightly changed from the desired value, the resonant frequency is recalculated to be

$$f_o = \frac{1}{2\pi}\sqrt{\frac{L+L_{s,max}}{L \cdot L_s \cdot C}} = 108.2\ \text{kHz}. \tag{3.38}$$

From (3.14), the current gain is found as

$$\frac{L_{s,max}}{L}\cos(\phi) = 4.1. \tag{3.39}$$

3.7.1 Matching Transformer

Since the current gain of the LLC load is found to be 4.1 which is not sufficient to heat the work piece to the desired temperature therefore, a matching transformer is introduced to address the issue. To take into account only the fundamental component of the voltage, the primary current of the transformer is calculated using, which gives $I_{s,rms} = 2.72\text{A}$.

$$I_{s,rms} = \frac{\pi P_o}{2\sqrt{2}V_m \cos\phi} \tag{3.40}$$

From the calculated current gain, the maximum output current ($I_{o,max}$) is 11.15 A. To utilize only 60% of the capacitor rated current, 60A, the required current ratio for the transformer is found using that is $\text{n} = 5.38 \approx 5$.

$$I_{C_P,max} = \text{n}I_{o,max} \tag{3.41}$$

The transformer in used has the leakage reactance of 3.16 μH and must be taken into consideration. Therefore, the series inductance (L_s) of 1.94 μH is needed to combine with the transformer's leakage inductance to meet the required inductance of 5.1 μH. Note that placing L_s on the primary side of the transformer can achieve the benefit of inherent current limitation protection of the transformer saturation. This means that the required series inductance on the transformer's primary is given as,

$$L_s = 1.94\text{n}^2 = 48.5\ \mu\text{H}. \tag{3.42}$$

The above inductance in (3.42) is the desired value and an inductor is constructed for the hardware prototype.

CHAPTER 4 SIMULATION AND EXPERIMENTAL RESULTS

To validate the proposed control method and circuit configuration, a computer simulation study is performed. The proposed circuit with AVC control method is developed in a computer program. A hardware platform is then created. Computer simulation and experimental results are discussed in this chapter. The case where the LLC resonant inverter is operating without the matching transformer is considered first. Then the case with the matching transformer is included.

4.1 Resonant Inverter without the Matching Transformer

In this section, the results of LLC resonant inverter without the matching transformer are considered. A full-bridge LLC resonant inverter circuit with asymmetrical voltage-cancellation control technique as shown in Fig. 4.1 is simulated. The following parameters are used $V_{DC} = 140V, L = 4.2\,\mu H$, $R = 0.074\Omega$, C =0.98 μF and $L_S = 25.5\mu H$. The resonant frequency is at 84.66 kHz.

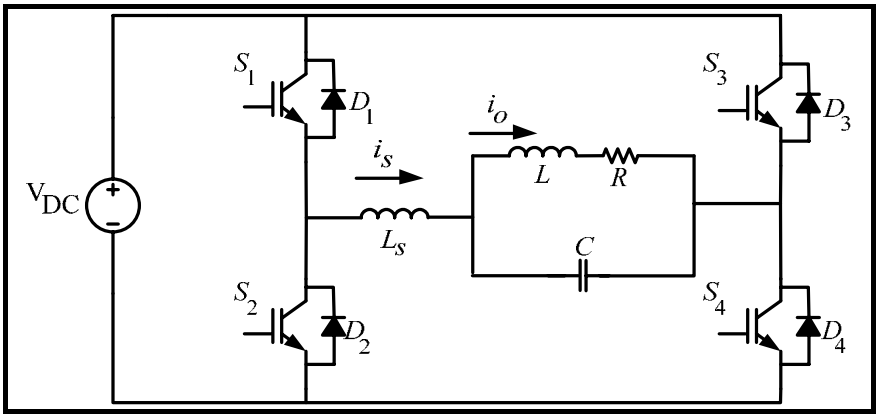

Figure 4.1 Full-bridge series and parallel resonant inverter

The inverter operates at 91 kHz. It is noted that the inductor L_S is wound on an air core to avoid saturation. The current and voltage waveforms of the system with the shifted angle (α) set to zero are shown in Figure 4.2. Next, α is adjusted to 70° to control the output power to the load and the voltage and current waveforms are shown in Figure 4.3. It is seen that the peak value of i_o is reduced from 50A to 39A. Since the voltage cancellation occurs during the negative cycle, an unsymmetrical input current where under $\alpha = 70^\circ$, the amplitude is noticeably smaller during the negative cycle is observed. Note that the effects of the load parameter variation during the heating process are not accounted for in the computer simulation. However, the effects are captured in the hardware experiment.

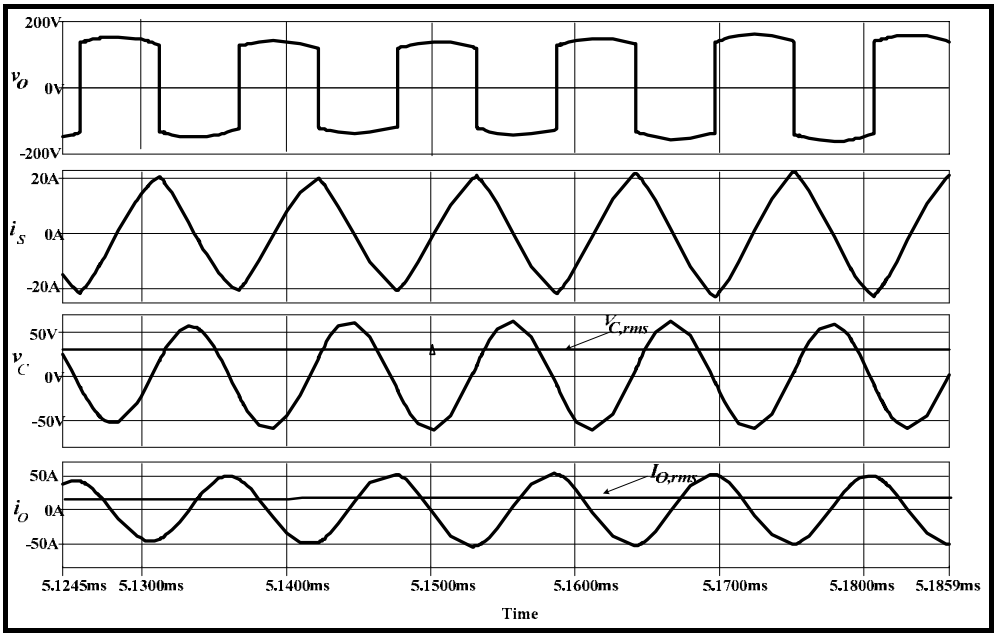

Figure 4.2 Voltage and current waveforms at 100 % duty cycle

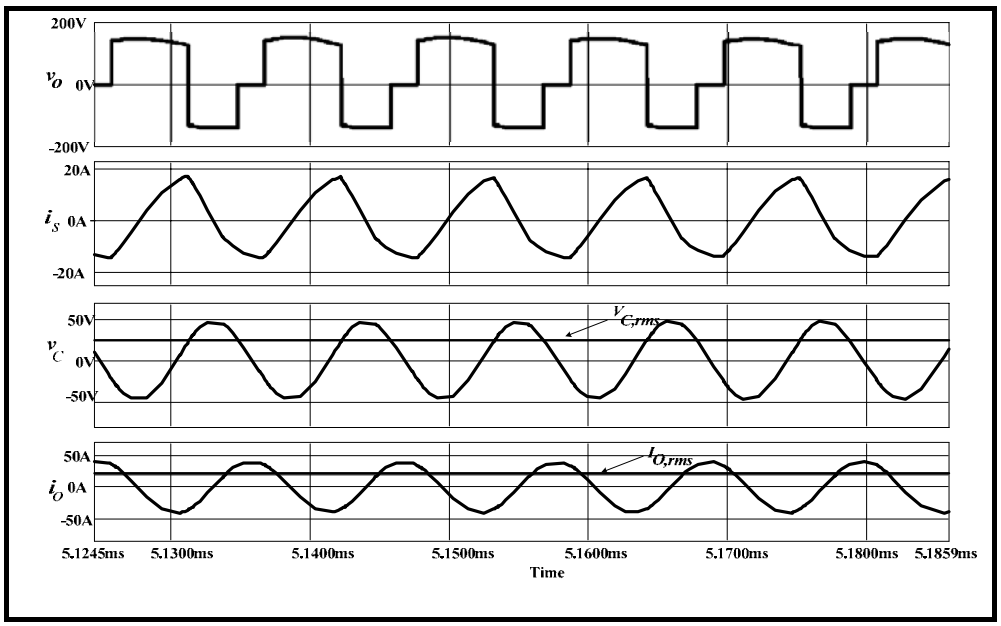

Figure 4.3 Simulation results with $\alpha = 70^{\circ}$

To verify the simulation results, a hardware setup is prepared with the same set of parameters as provided earlier. The load is a 30-grams aluminum work-piece in a graphite crucible. The IRFP460 MOSFETs are used as switching devices. The switching frequency varies from 93 kHz to 96 kHz under load parameter variation.

Note that the operating frequency of 93 kHz in the experiment is approximately 2 kHz higher than the simulation study of 91 kHz. This is due to the lower limit of the phase-lock loop control that is not able to achieve the power angle (ϕ) less than 66.76 degree. Figure 4.4 shows the measured v_o and i_S waveforms when the inverter operates at 93.45

kHz with no phase shift. This operating condition is considered the full-load condition where the input power to the inverter is at 340W. The induction coil voltage and current waveforms are shown in Figure 4.5. The load power is at 326 W providing the efficiency of 94.5%. Once the work piece temperature increases, the induction coil impedance changes in a way that the resonant frequency increases. The phase-locked loop control then increases the switching frequency to track the resonant frequency.

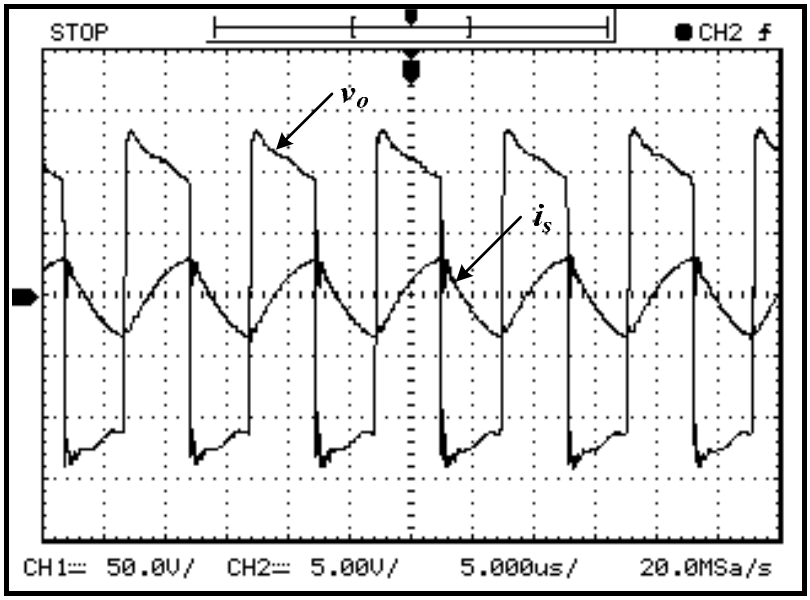

Figure 4.4 v_o and i_s waveforms at 93.45 kHz (i_s: 50 A/div, v_o: 50 V/div and Time: 5 μs / div.)

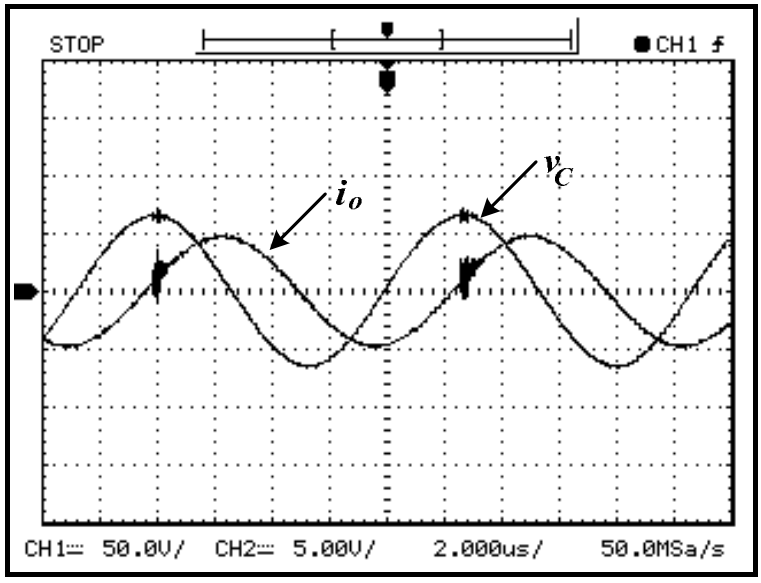

Figure 4.5 v_C and i_o waveforms at 93.45 kHz (i_o: 20 A/div, v_C: 50 V/div and Time: 2 μs / div.)

Note that the operating frequency is maintained at the frequency slightly higher than the resonant frequency. This is to ensure the zero voltage switching (ZVS) operation. The stray inductance in the dc bus wiring may have caused oscillation (ringing) in the output voltage. In addition, the shifted angle is adjusted to 70° in order to control the output

power to the load. The v_o and i_S waveforms are shown in Figure 4.6 where the input power to the inverter is at 280W and the switching frequency is automatically increased to 95.7 kHz. Figure 4.7 shows the induction coil voltage and current waveforms. The output power is reduced to 263W with the efficiency of 93.46%. The output voltage wave form is not constant due to the ripple from dc bus.

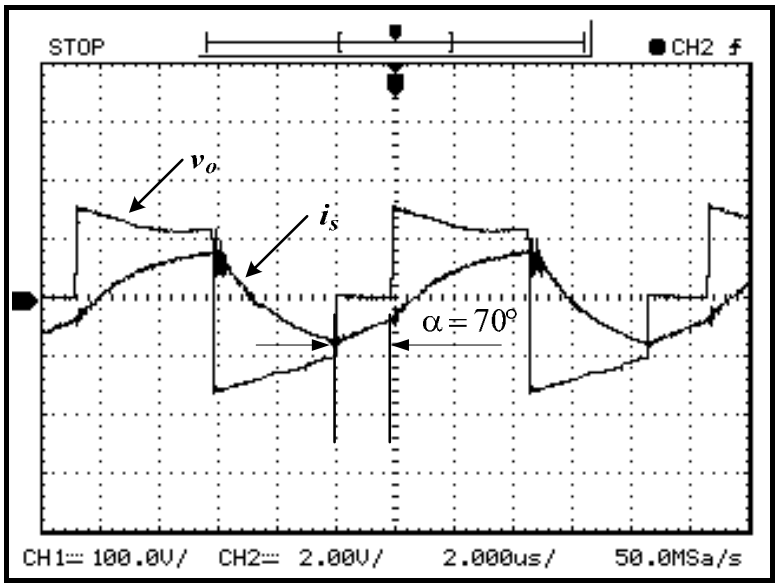

Figure 4.6 v_o and i_s waveforms at 95.7 kHz with $\alpha = 70^\circ$ (i_s: 20 A/div, v_o: 100 V/div and Time: 2 μs / div.)

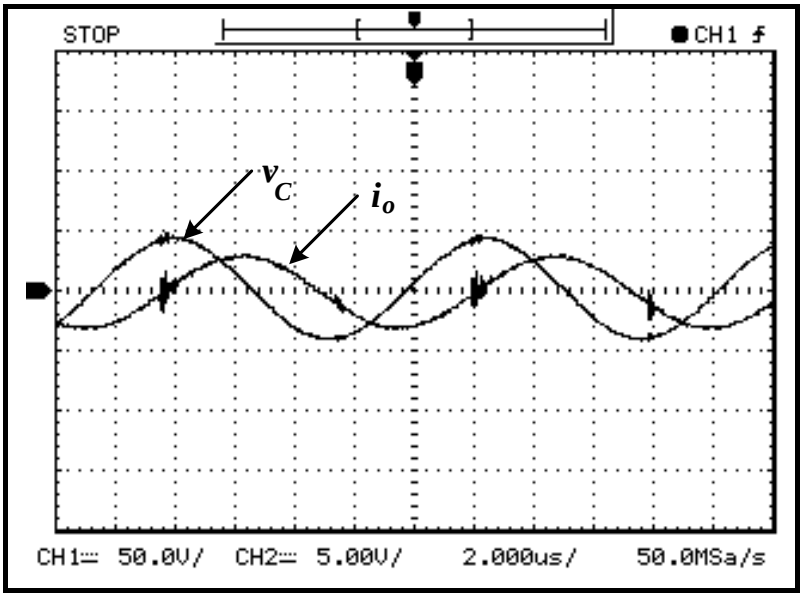

Figure 4.7 v_C and i_o waveforms at 95.7 kHz with $\alpha = 70^\circ$ (i_o: 20 A/div, v_C: 50 V/div and Time: 2 μs / div.)

From the experimental results, we can conclude that the resonant frequency tracking and the adjustment of pulse voltage together ensure the maximum power transferred to the load at the designated phase angle throughout the heating cycle with minimal loss. Due to high current at the switches and low quality factor load, Q, we need to add the matching transformer in this topology.

4.2 LLC Resonant Inverter with Matching Transformer

As stated earlier, applications with low Q load requires high load current whereas the current gain to the induction coil is low. The switch current rating must be sacrificed and the component cost is the price to pay. To address this issue, a matching is included in our topology. To improve the LLC resonant load with low Q, the series inductor L_s may be physically transferred from the transformer's secondary to the transformer's primary. To confirm the validity of the proposed topology and control scheme, a computer simulation and a hardware experiment are performed using parameters in Table 4.1. The resonant frequency calculated using (3.2) is 107.866 kHz. The load is a 30-gram aluminum work-piece in a graphite crucible. Due to load parameter variation when the work-piece temperature increases from 30ºC to 625ºC, the switching frequency is varied from 108.7 to 110.6 kHz. The angle α is varied from 0º to 144º for the purpose of output power control.

Table 4.1 Design specification and circuit parameters.

Parameter		Value
v_{AC}	input voltage	150 V_{rms}
f_o	resonant frequency	108.2 kHz
f_s	switching frequency	108.7 -110.6 kHz
C_P	parallel resonant capacitor	2.35 μF
$L_{s,total}$	series inductor+ primary leakage inductance of transformer	56 μH+79 μH (L_s+ L_{lkp})
L_{Coil}	induction coil inductor (From room temperature to 625ºC)	1.11-0.95μH
R_{eq}	equivalent resistor (with workpiece) (from room temperature to 625ºC)	$100-110\,m\Omega$
$n=n_1/n_2$	transformation ratio	5
S_1, S_2, S_3,S_4	switches	IRFP460
C_b	DC blocking capacitor	3.3 μF

Table 4.2 Component losses under asymmetrical control

Output power (%)	Loss of switches(w)				Loss of diodes (w)			
	S_1	S_2	S_3	S_4	D_1	D_2	D_3	D_4
100	3.45	3.45	3.45	3.45	2.13	2.13	2.13	2.13
50	3.05	3.05	3.05	1.98	2.13	2.13	2.97	2.13
32	2.65	2.65	2.65	0.29	2.13	2.13	3.00	2.13

Table 4.2 shows losses of switches and diodes under different load levels from 32%-100%. At 100% of rated condition, the switch S_4 carries the same loss at 3.45W as other switches. However, when the output power is reduced, the switch S_4 conduction interval becomes less as well as the loss.

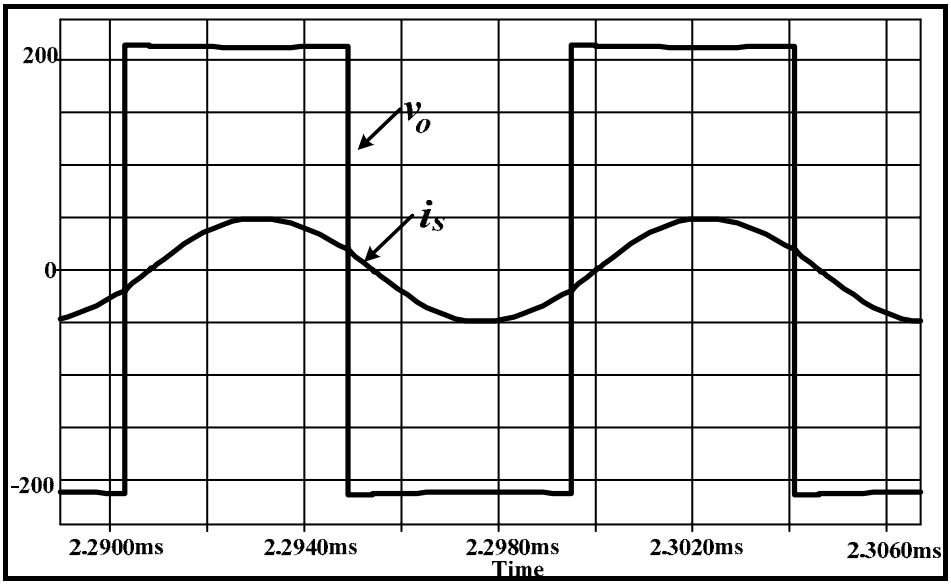

Figure 4.8 Simulated output voltage and current waveforms of the LLC full-bridge inverter with no phase shift at the full load (i_s: 4A/div, v_o: 50 V/div and Time: 2 μs / div.)

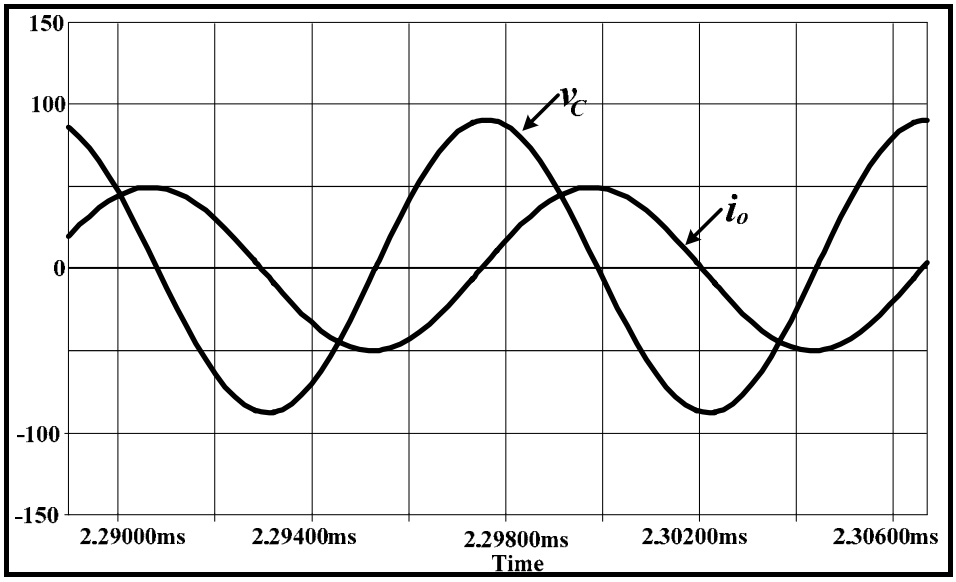

Figure 4.9 Simulated load voltage and induction coil current waveforms of the LLC full-bridge inverter with no phase shift at the full load (i_o: 100 A/div, v_C: 50 V/div and Time: 2 μs / div.)

With the circuit parameters in Table 4.1, the simulation results under the angle α at 0º, 90º and 144º are shown in Figure 4.8-4.16. As α increases, the inverter output current i_s, the output voltage v_o, induction coil current i_o and induction coil voltage v_C decrease.

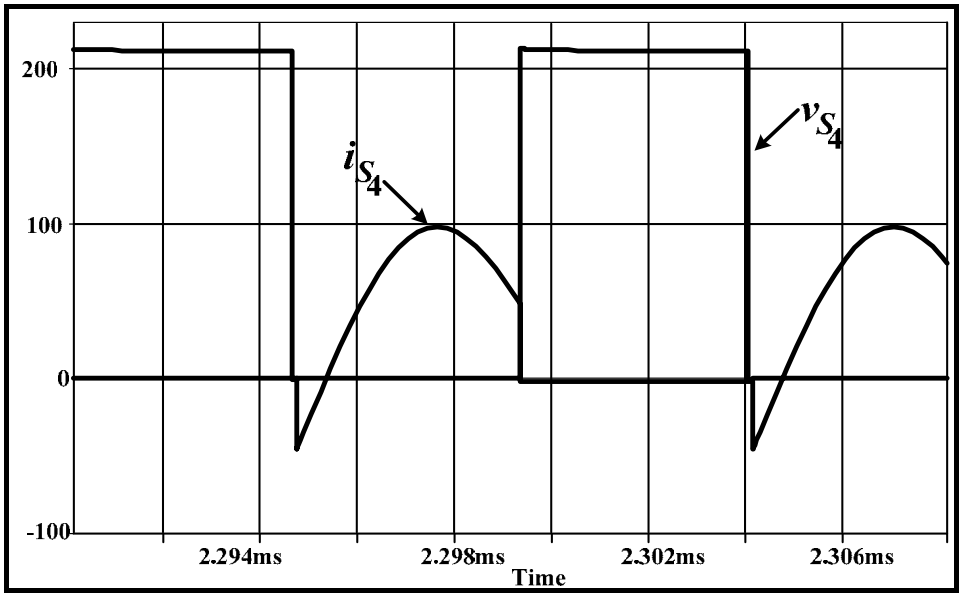

Figure 4.10 Simulated voltage and current waveforms of the LLC full-bridge inverter at the S_4 with no phase shift at the full load (i_{s4}: 4 A/div, v_{s4}: 100 V/div and Time: 2 μs / div.)

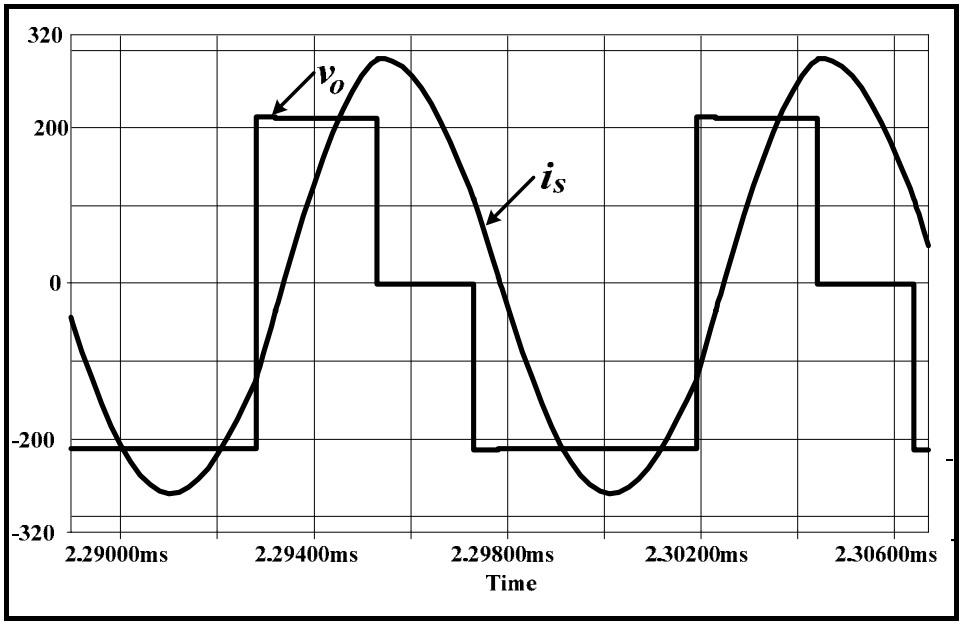

Figure 4.11 Simulated output voltage and current waveforms of the LLC full-bridge inverter at 62.5% load (i_s: 1.33A/div, v_o: 100 V/div and Time: 2 μs / div.)

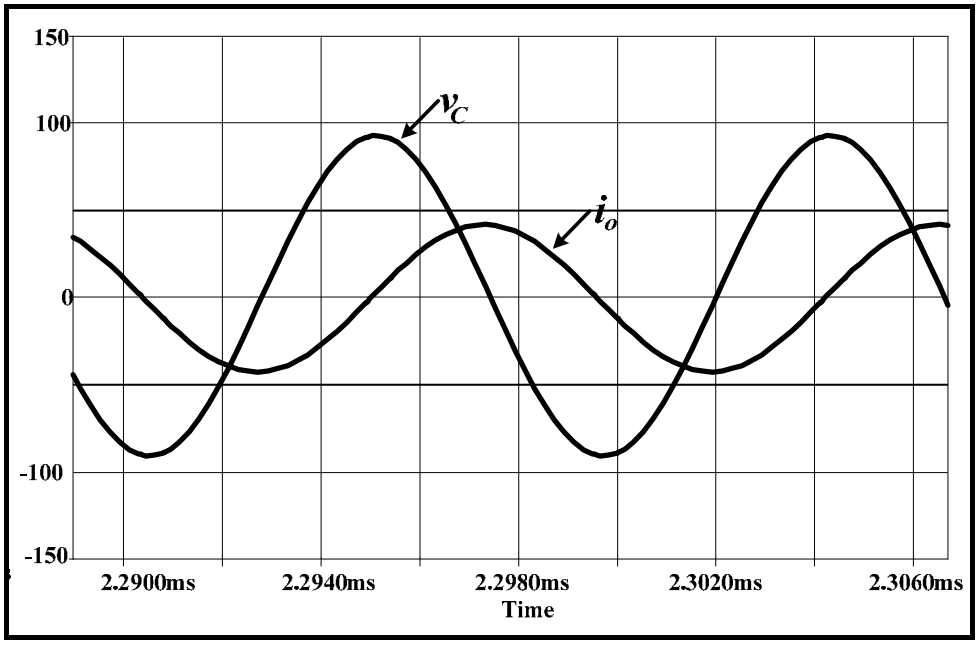

Figure 4.12 Simulated load voltage and induction coil current waveforms of the LLC full-bridge inverter at 62.5% load (i_o: 100 A/div, v_C: 50 V/div and Time: 2 μs / div)

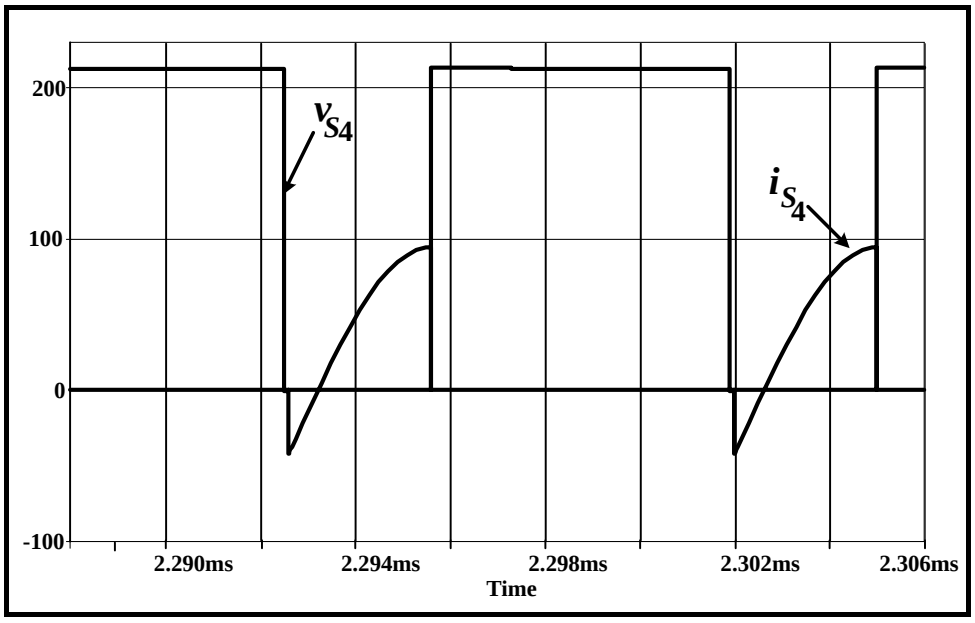

Figure 4.13 Simulated voltage and current waveforms of the LLC full-bridge inverter at the S_4 at 62.5% load (i_{s4}: 4 A/div, v_{s4}: 100 V/div and Time: 2 μs / div.)

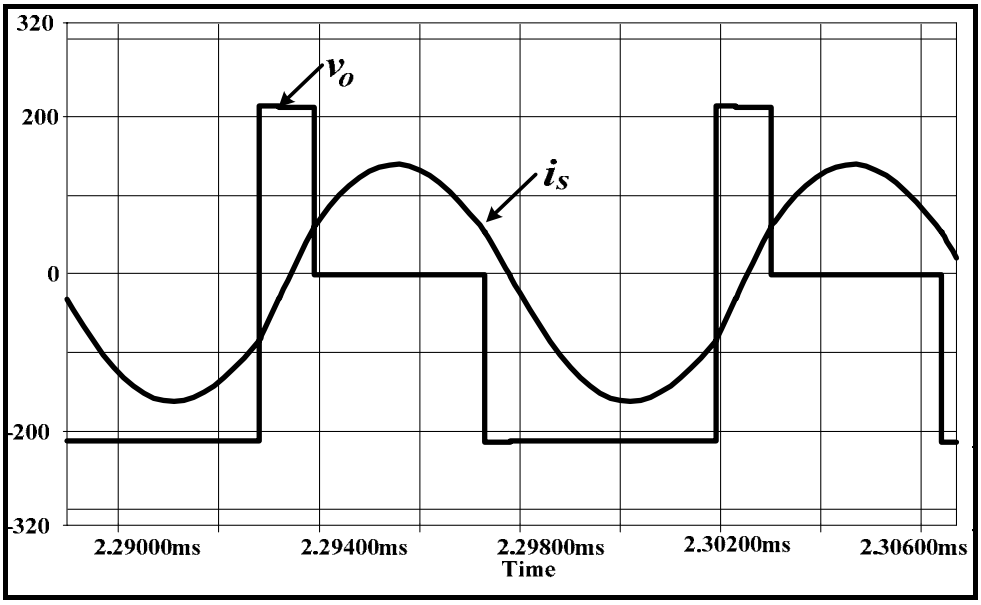

Figure 4.14 Simulated output voltage and current waveforms of the LLC full-bridge inverter at 32% load. (i_s: 1.33A /div, v_o: 100V/div and Time: 2 μs / div.)

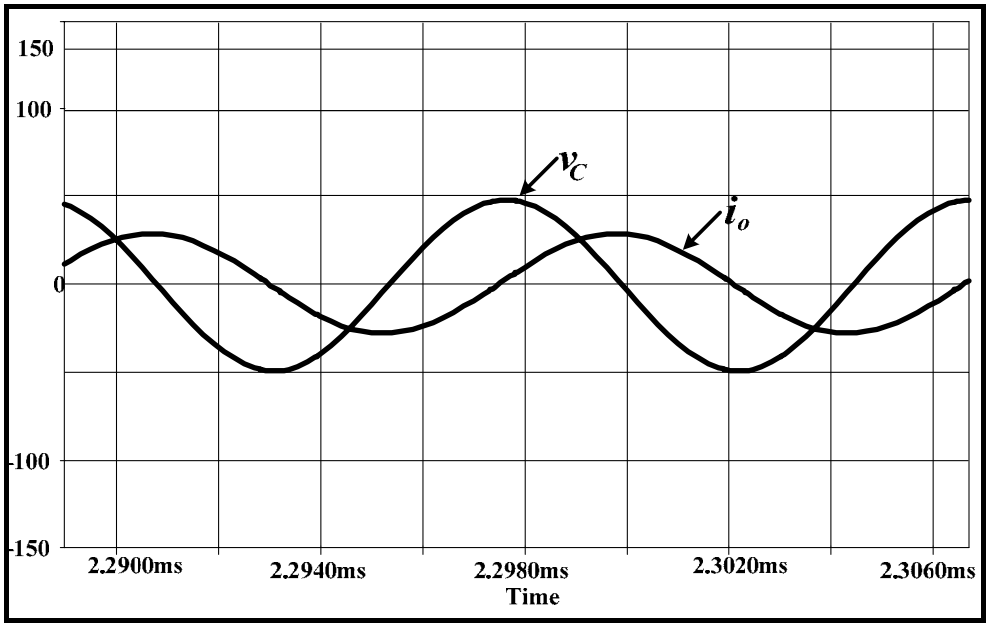

Figure 4.15 Simulated load voltage and induction coil current waveforms of the LLC full-bridge inverter at 32% load (i_o: 100 A/div, v_C: 50 V/div and Time:2 μs / div.)

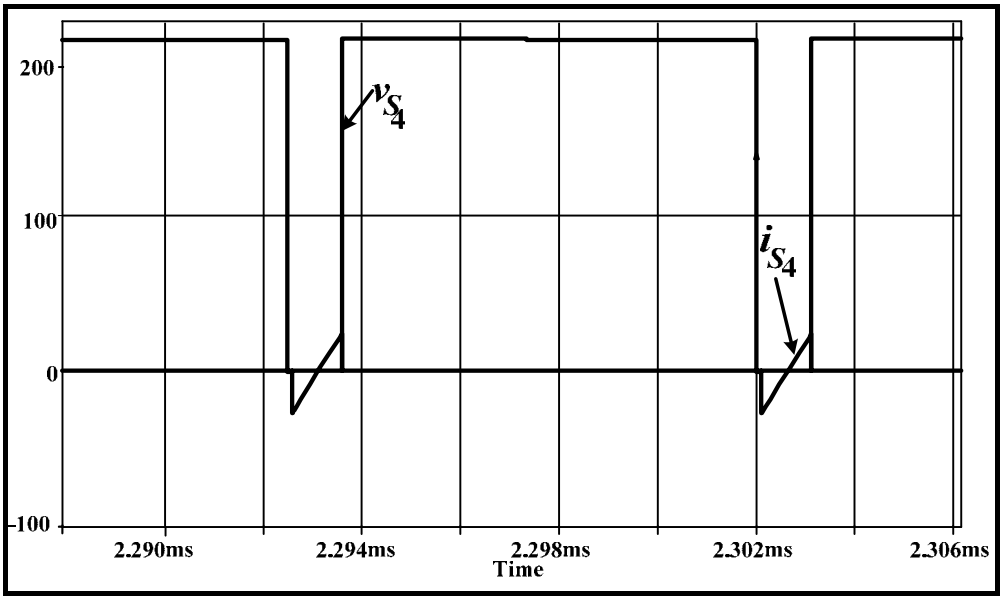

Figure 4.16 Simulated voltage and current waveforms of the LLC full-bridge inverter at the S_4 at 32% load (i_{s4}: 4 A/div, v_{s4}: 100 V/div and Time: 2 μs / div.)

The experimental results in Figures 4.17-4.25 are obtained using the same set of parameters in Table 4.1. The waveforms at full load condition (α = 0º) are shown in Figures 4.17-4.19 where the inverter operates at 108.7 kHz. Once the work piece temperature increases, the induction coil impedance changes in a way that the resonant frequency increases. The phase-locked loop control then increases the switching frequency of the inverter to track for the resonant frequency. This is to ensure the ZVS operation. The shifted angle is then adjusted to 90° to reduce the output power to 62.5%. The corresponding current and voltage waveforms are shown in Figures 4.20-4.22 along with the switching S_4 voltage and current waveforms. The switching frequency is increased to 109.17 kHz. In Figures 4.23-4.26, the i_s, v_o, i_o and v_C waveforms are obtained while the angle α is adjusted to the limit of 144°. At this point, the output power is reduced to 32.16%. The switching frequency is automatically increased to 110.6 kHz. It is seen that an increase of α results in an increase of the switching frequency. This provides an easy adjustment of the output power with fast response

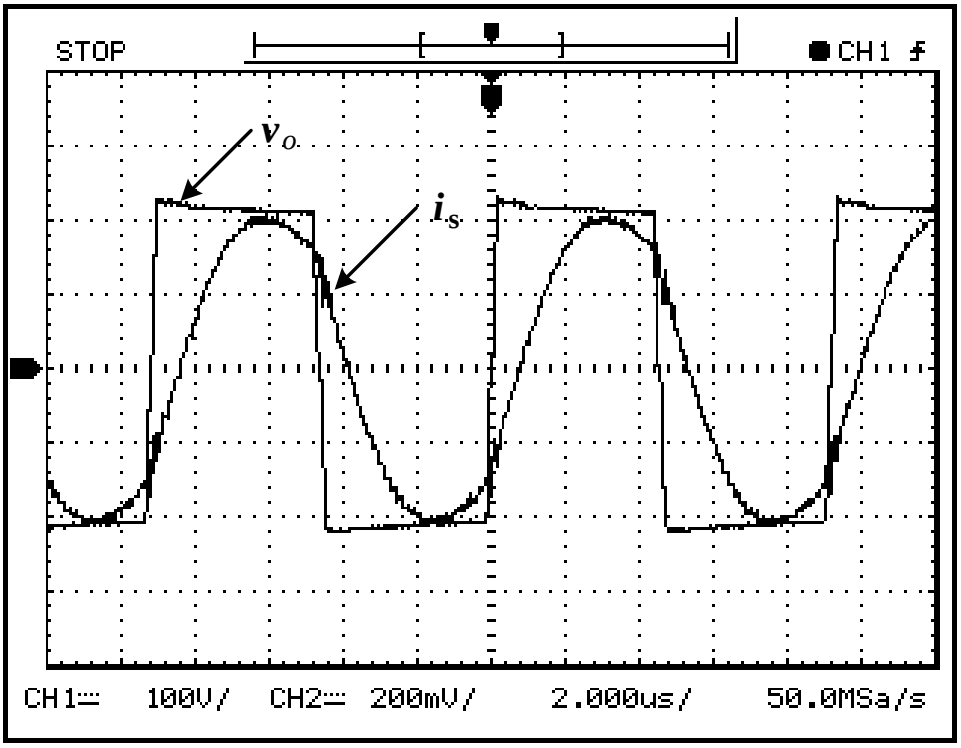

Figure 4.17 Experimental output voltage and current waveforms of the LLC full-bridge inverter with no phase shift at the full load (i_s: 2A/div, v_o: 100 V/div and Time: 2 μs / div.)

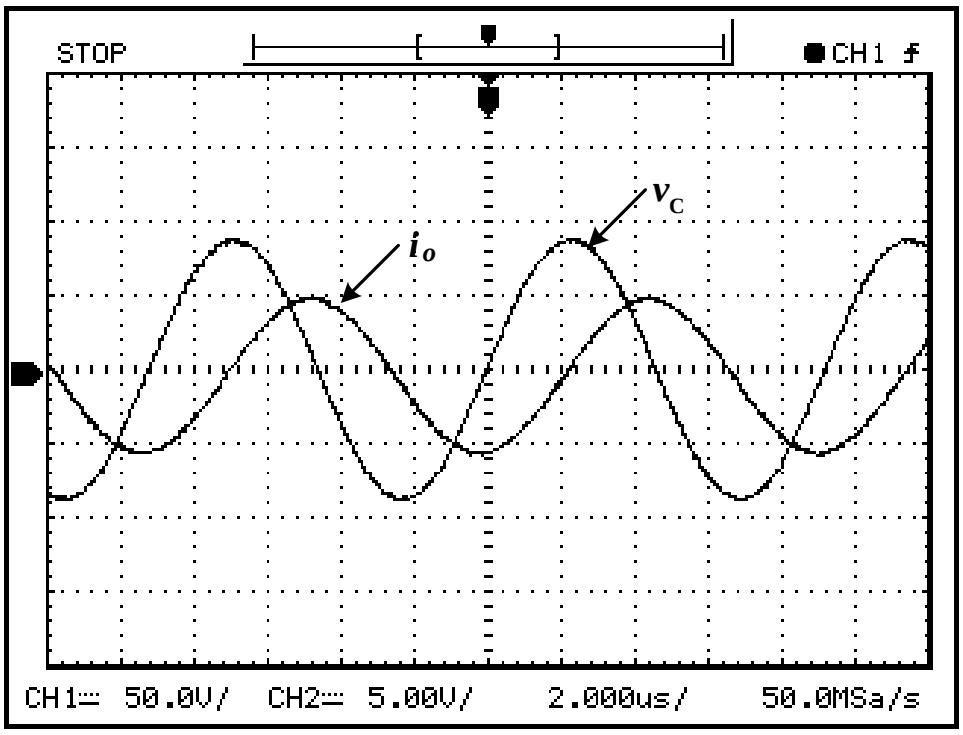

Figure 4.18 Experimental load voltage and induction coil current waveforms of the LLC full-bridge inverter with no phase shift at the full load (i_o: 100 A/div, v_C: 50 V/div and Time: 2 μs / div.)

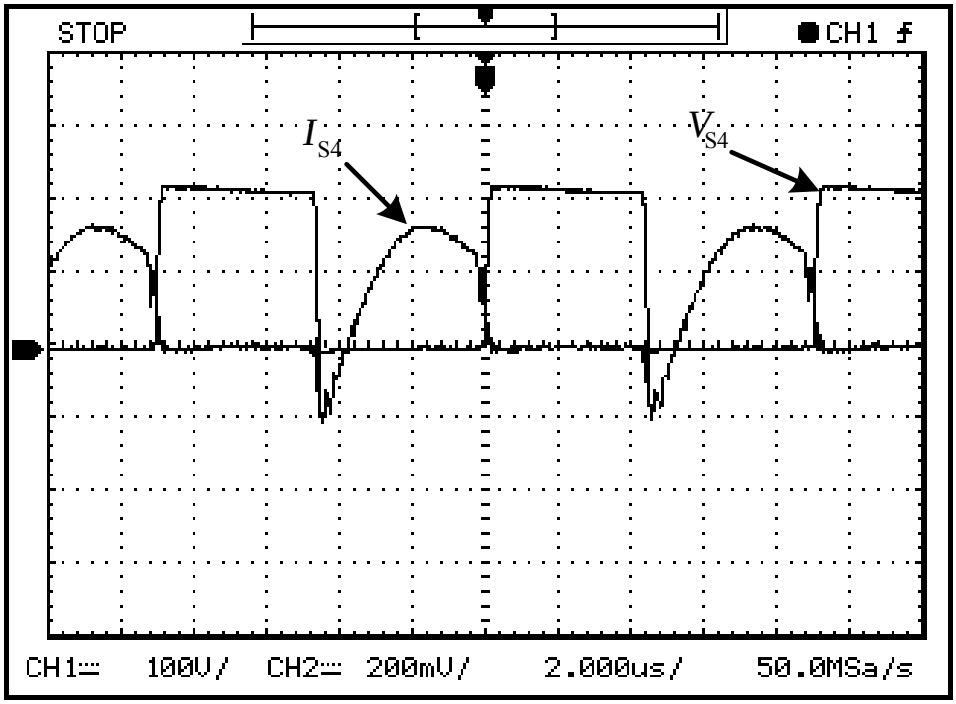

Figure 4.19 Experimental voltage and current waveforms of the LLC full-bridge inverter at the S_4 with no phase shift at the full load (i_{s4}: 2.7 A/div, v_{s4}: 100 V/div and Time: 2 μs / div.)

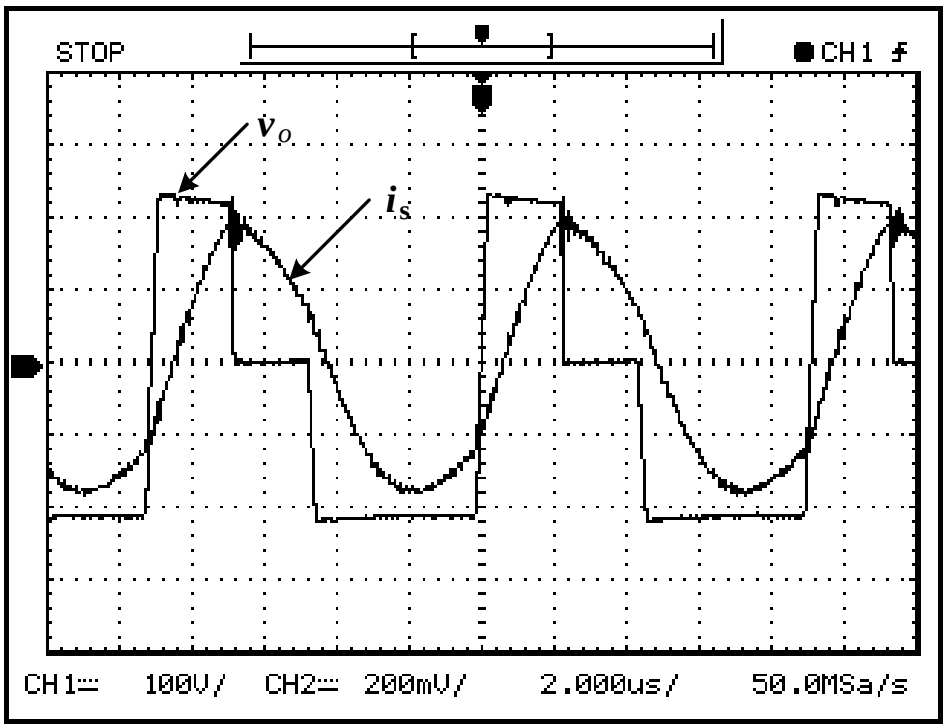

Figure 4.20 Experimental output voltage and current waveforms of the LLC full-bridge inverter at 62.5% load (i_s: 2A/div, v_o: 100 V/div and Time: 2 μs / div.)

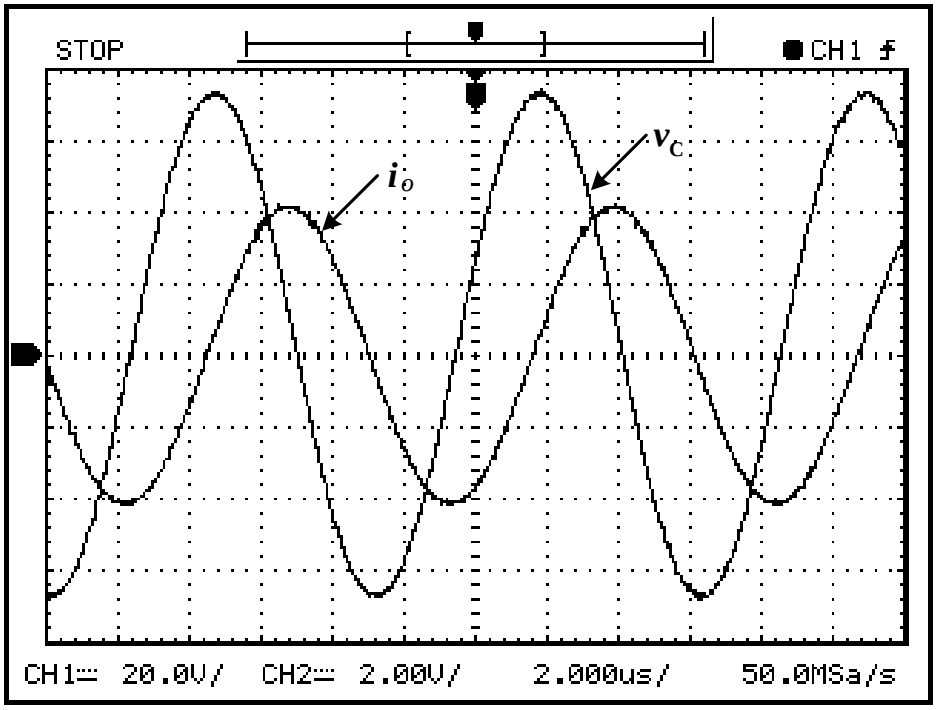

Figure 4.21 Experimental load voltage and induction coil current waveforms of the LLC full-bridge inverter at 62.5% load (i_o: 40 A/div, v_C: 20 V/div and Time: 2 μs / div)

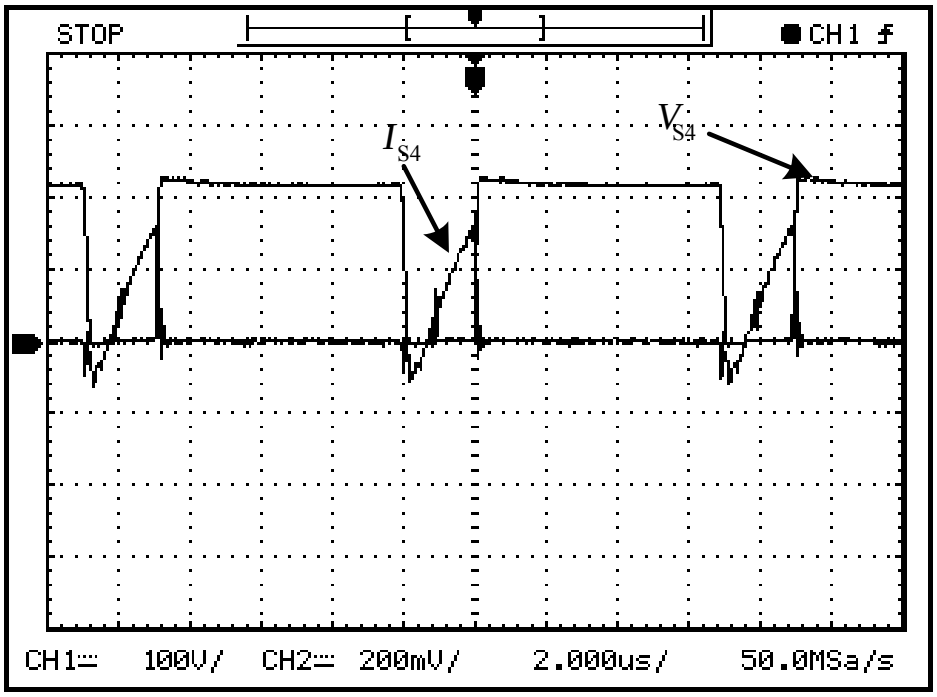

Figure 4.22 Experimental voltage and current waveforms of the LLC full-bridge inverter at the S_4 at 62.5% load (i_{s4}: 2.7A/div, v_{s4}: 100 V/div and Time: 2 μs / div.)

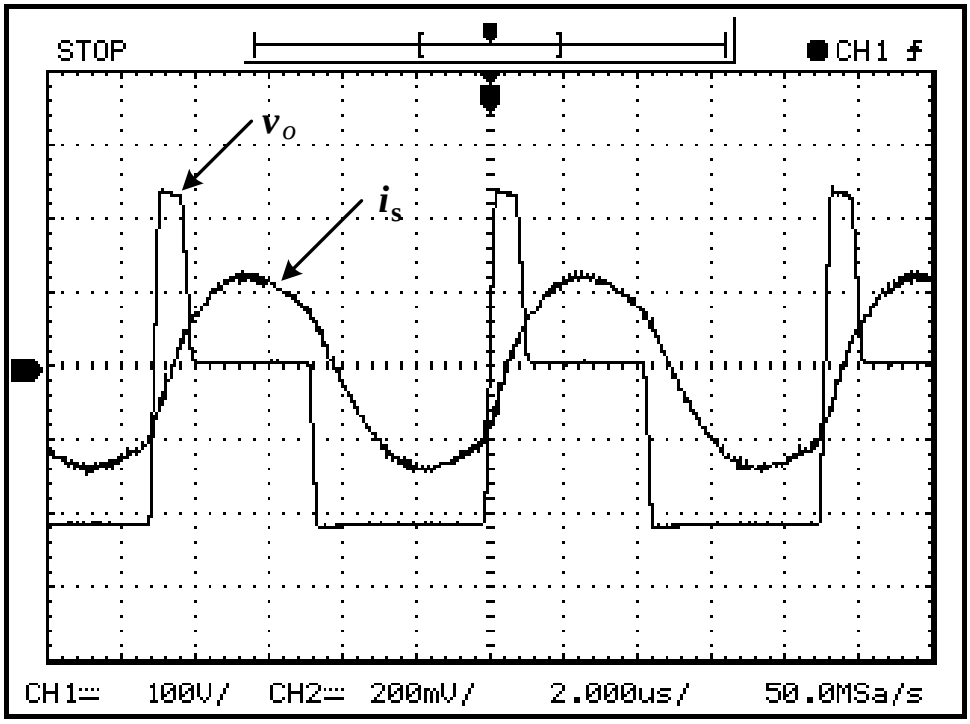

Figure 4.23 Experimental output voltage and current waveforms of the LLC full-bridge inverter at 32% load (i_s: 2A/div, v_o: 100V/div and Time: 2 μs / div.)

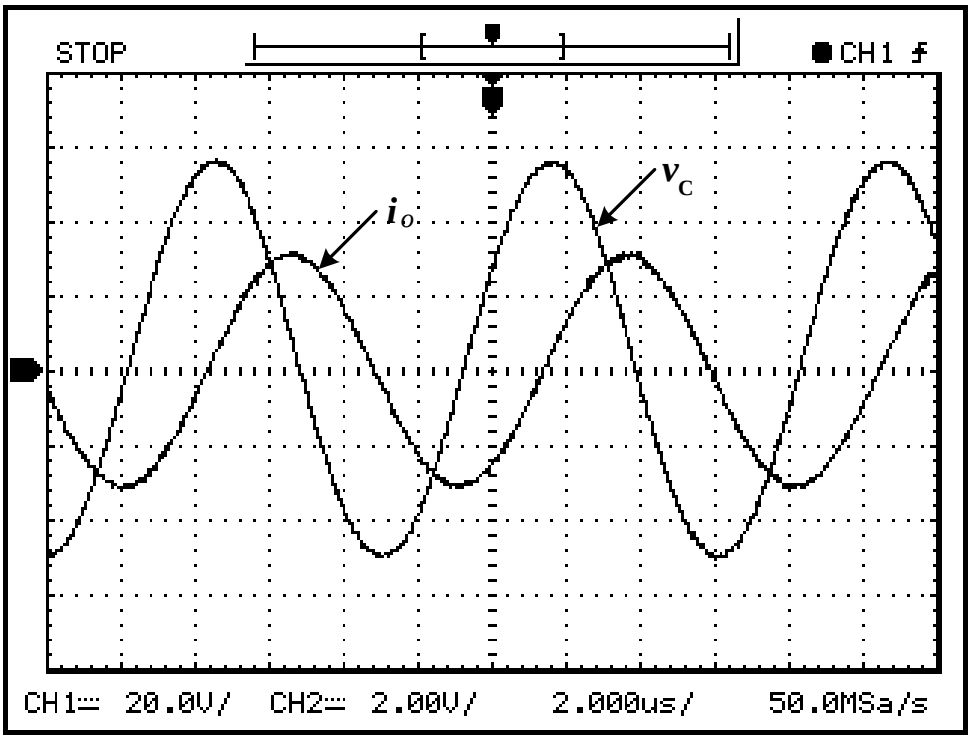

Figure 4.24 Experimental load voltage and induction coil current waveforms of the LLC full-bridge inverter at 32% load (i_o: 40A/div, v_C: 20V/div and Time:2 μs / div.)

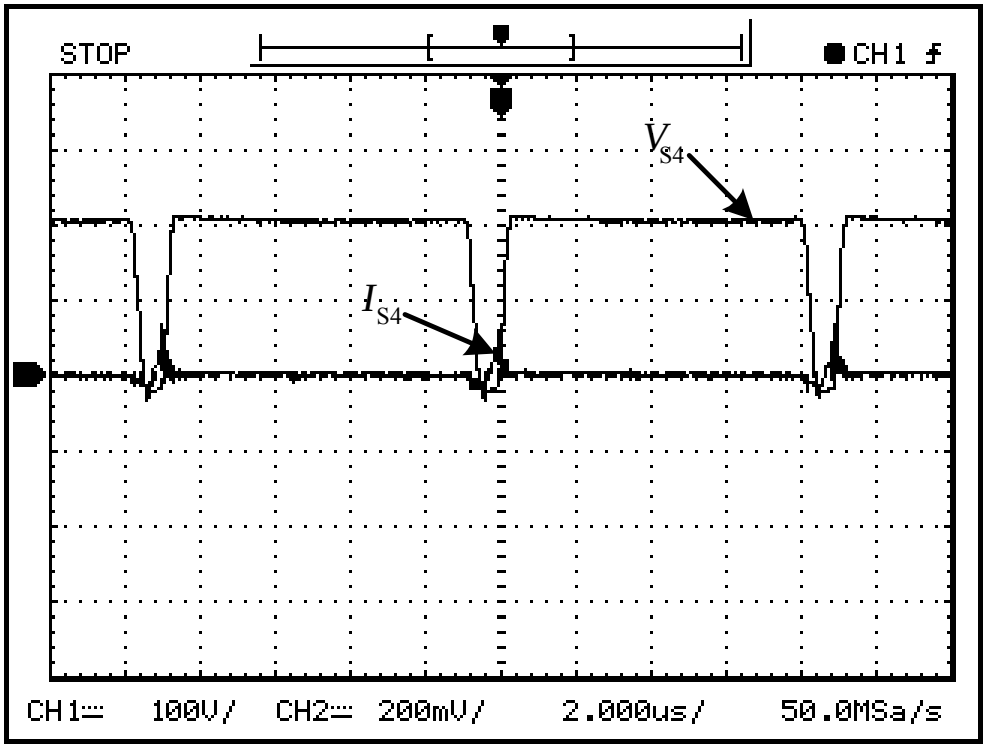

Figure 4.25 Experimental voltage and current waveforms of the LLC full-bridge inverter at the S_4 at 32% load (i_{s4}: 2.7 A/div, v_{s4}: 100 V/div and Time: 2 μs / div.)

Note that even the gate signal is forced to turn on at the angle α greater than 144 degrees, the switch will still turn on at 144 degrees. This is due to the fact that the average voltage across the total inductor seen by the inverter must be zero. Since the switching frequency is maintained slightly above the resonant frequency where the load exhibits an inductive behavior, the ZVS operation of the LLC full-bridge inverter with the proposed control scheme is guaranteed for the whole range of variable load parameters and variable output powers. The power angle ϕ is set at 36 degrees to accommodate the induction coil and an aluminum work piece load and the power is adjusted through the angle α. Therefore, the lowest load level that the controller can achieve is at α = 144 degrees giving the power level at 32% of rated condition.

The experimental results for both control schemes are collected while the work piece is at 625 ºC. During the heating process from 30 ºC to 625 ºC, the equivalent resistance varies from 100 – 110 mΩ which results in variation of the induction coil inductance from 0.95 – 1.11 μH. Thus, the operating frequency is varied in the range of 108.7 – 110.6 kHz to maintain zero voltage switching operation. It is evident that the output power to the work piece can be controlled by adjusting the angle α as discussed in the previous chapter.

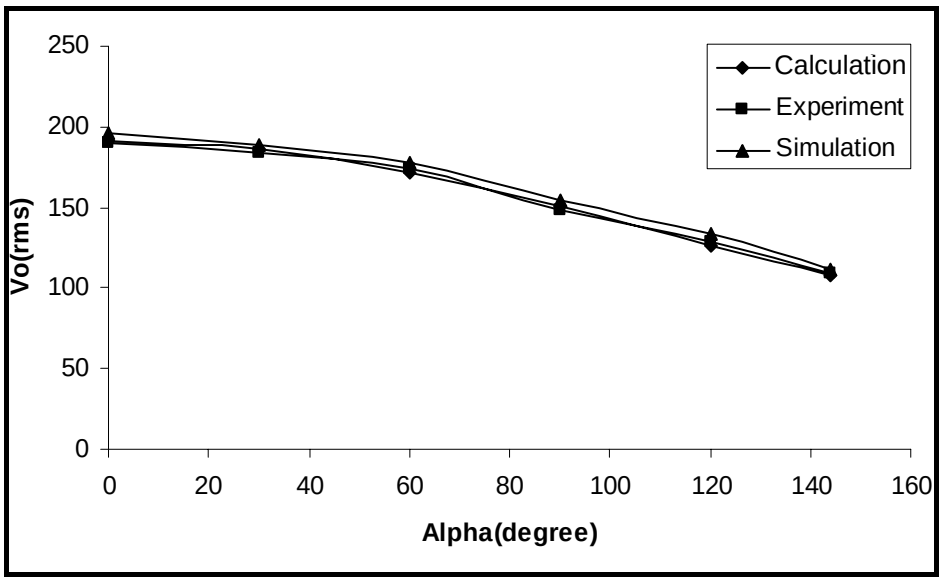

Figure 4.26 Output voltage (v_o) vs and alpha angle (α)

When the shifted angle is adjusted to 144° the v_o and i_S waveforms are shown in Figure 4.25 where the input power to the inverter is at 161W and the switching frequency is automatically increased to 110.6 kHz. Figure 4.24 shows the v_C and i_o waveforms under the same condition. The output power is reduced to 154.56W with the efficiency of 96%. Figure 4.26 shows relationships of v_o and α under calculation in (3.5), simulation and experimental results. It is seen that the values of v_o obtained by 3 methods are close to each other. The maximum difference between the experiment and simulation is around 6 V (2.9%) at zero degree while the minimum difference is 3.2 V (6.5%) at 144 degrees. It is evident that the output voltage of LLC resonant inverter can be effectively controlled by adjusting the shifted angle α.

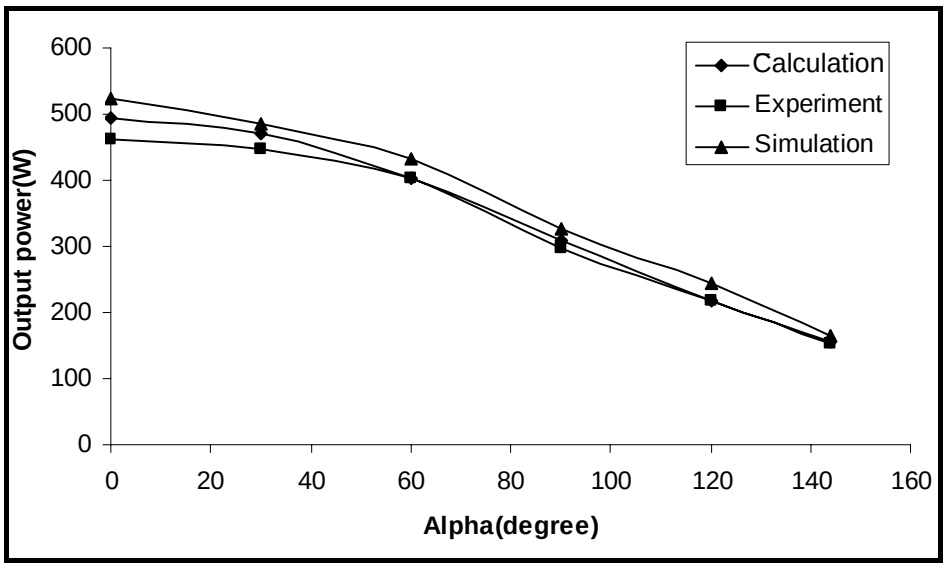

Figure 4.27 Output power (P_o) vs and alpha angle (α)

Similarly, Figure 4.27 shows relationships between the output power and α obtained from calculation, simulation and experiment for a comparison purpose. The maximum

difference between the experiment and simulation is around 60W (13%) at zero degree while the minimum difference is 10W (6.5%) at 144 degrees. It is evident that the output power to the workpiece can be effectively controlled by adjusting the shifted angle α. From Figure 4.27, the simulation results are higher than the calculation results in general because a rectifier circuit with a large capacitor is used in the simulation whereas the averaged value of 63.6% is used in the calculation. This means that the DC bus voltage in the simulation is at the peak value of the sinusoidal signal (i.e. 100%).

Table 4.3 Experimental results

Output Power (%)	alpha angle (α)	Temperature (°C)	Operating frequency(kHz)
100	0	30	108.7
95	30	372	109.3
62.5	90	420	109.8
42.1	120	530	110
32	144	625	110.6

Table 4.3 shows the experimentally obtained results at various values of alpha angle. Related parameters and variables such as the output power, work-piece temperature and operating frequency are collected. It is seen that an increase of temperature results in increment of the operating frequency to maintain the power angle at the same value. From equation (3.14) and Figure 3.5, the coil parameters change due to reduction of the inductance, L, results in the decrease of the output power. At the same time the coil current is increasing. Since the coil current is the same is the resonant capacitor current, this may cause damage to the resonant capacitor. To protect the resonant capacitor from the exceptionally high current, we can increase the angle α which will reduce the capacitor current to the safe level.

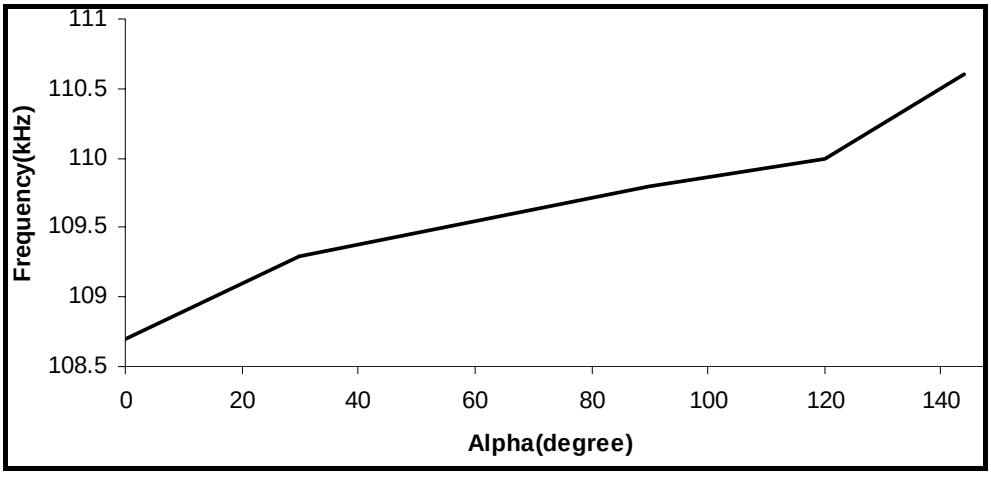

Figure 4.28 Operating frequency (f_s) vs and alpha angle (α)

The operating frequency is increased when the parameters of the induction coil change due to the increased temperature during the heating process.

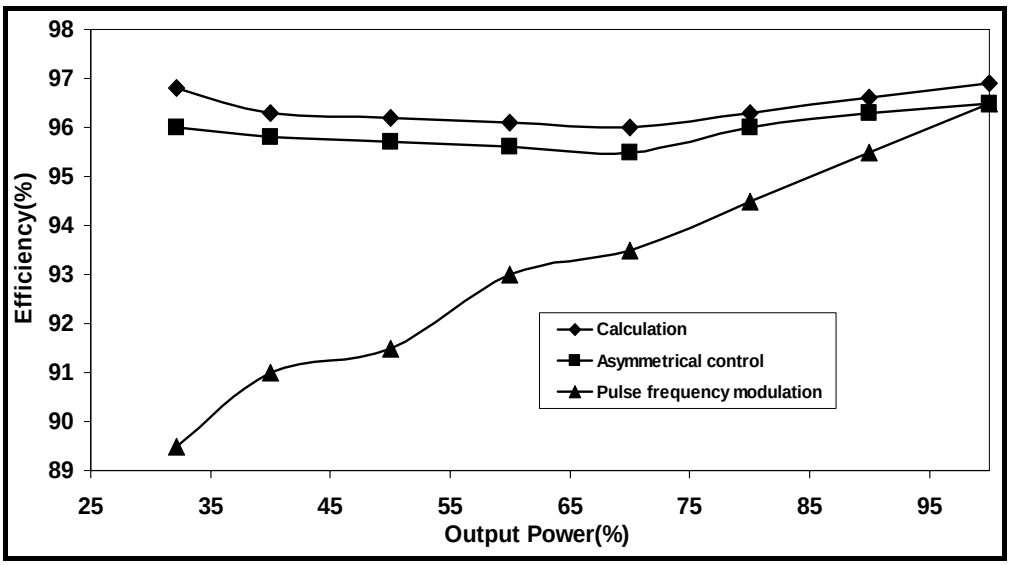

Figure 4.29 Efficiency comparisons between the calculation, asymmetrical control and pulse frequency modulation

For a comparison purpose, the efficiencies from calculation and experiment of the LLC full-bridge inverter with asymmetrical control are shown in Figure 4.21 using the parameters given in Table 4.1. The PFM control scheme with the same parameter setting is also plotted. At rated power, the efficiency of the LLC full-bridge inverter is the same between the asymmetrical control and the PFM schemes. However, the proposed asymmetrical control has shown up to 6% higher on the efficiency at low power operation.

CHAPTER 5 CONCLUSIONS

In this research, an improved full-bridge LLC resonant inverter topology for induction heating applications has been proposed. The phase-locked loop allows resonant frequency tracking under load parameter variation. The analytical expression of the output power as a function of the shifted phase angle is given in this work. Based on the derived expression, the asymmetrical control method can be used to control the inverter output power to the induction coil. A computer simulation study is performed and a hardware platform is created to verify the proposed control method and circuit topology. The calculation expression and the simulation results as well as the experimental results have shown an excellent agreement. The resonant frequency tracking and the adjustment of pulse voltage together ensure the maximum power transfer to the load throughout the heating cycle with minimal loss. The proposed LLC topology with high frequency transformer improves the inverter operation around the resonant frequency. Analytical aspects of the LLC resonant inverter are given and an example of the design procedure is given.

It can be concluded that the presented work has the following key advantages.

- The asymmetrical control can be used to control the output power to the induction coil for the LLC resonant tank.
- The control scheme is in a simple configuration and easy to implement.
- The resonant frequency tracking together with the adjustment of the pulse voltage ensure the maximum power transfer to the load throughout the heating cycle with minimal loss.
- The transferred series inductor on the transformer's primary results in a small inductor due to low current on the transformer's primary.

The presented circuit configuration and proposed control scheme can also be used with other applications that require a wide range of output power regulation under load parameter variation.

5.1 Summary of Contributions

In this work, an improved full-bridge LLC resonant inverter topology for induction heating application is proposed. Four main contributions are listed as follows.

- Proposed an improved LLC resonant load for $Q < 10$
- Proposed the use of asymmetrical control together with the phase-lock loop control to address the load parameter variation
- Analyzed the switching and conduction losses of the resonant inverter with practical switching devices
- Derived a closed-form expression of the output power as a function of the alpha angle

5.2 Future Work

Nowadays, the LLC resonant inverter has been successfully employed in induction heating. It has enhanced the SRI performance due to its short-circuit handling capability and its current gain. Thus, further study is recommended in the following areas:

1. A development of the steady-state models and a detailed analysis of the current-source inverter with LLC resonant load, considering their requirements for ZCS or ZVS, compared with the LLC resonant voltage source inverter.

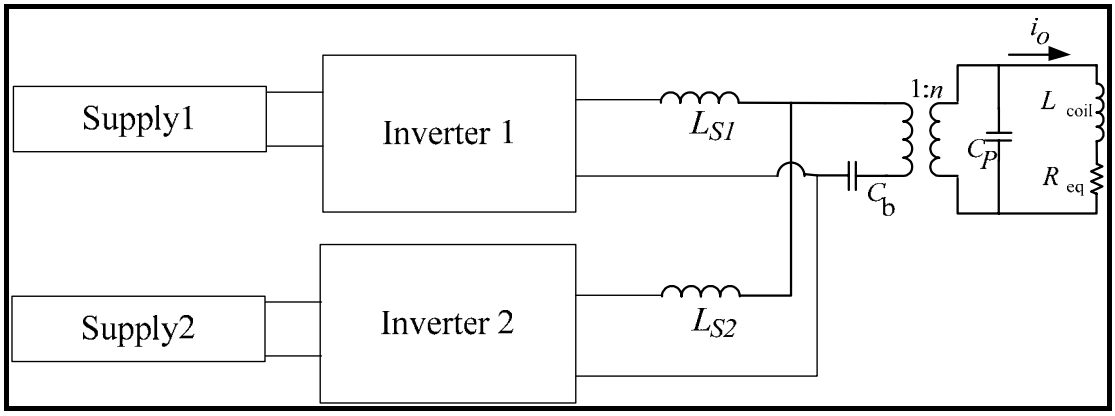

Figure 5.1 LLC resonant inverter connected in parallel for higher applications.

2. A development of a time delay compensator for the phase-locked loop that can avoid the collapse of the voltage control oscillator (VCO) and an error on the duty cycle due to the time delay.

3. A development of the circuit topology at higher power applications where multiple LLC resonant inverters are connected in parallel. An example of the connection topology is shown in Figure 5.1 which has inductors L_{s1} and L_{s2} connected in parallel. This enables a connection between two voltage source inverters and simplify the inverter connection for higher power applications.

REFERENCES

1 M. Kamli, S. Yamamoto, and M. Abe, 1996, “A 50-150 kHz Half- Bridge Inverter for Induction Heating Application”, **IEEE Transactions on Industrial Electronics**, Vol. 43, No. 1, pp. 163-172.

2 S. Chudjuarjeen, C. Koompai and V. Monyakul, 2004, “Full-Bridge Current-Fed Inverter with Automatic Frequency Control for Forging Application”,**IEEE Tencon Conference**, 21-24 November, Vol. 4, pp.128-131.

3 P. Viriya, S. Sittichok, K. Matsuse, 2002, “Analysis of High-Frequency Induction Cooker with Variable Frequency Power Control”, **IEEE Power Conversion Conference** , Osaka, pp. 1507 - 1502.

4 Nam-Ju Park, Dong-Yun Lee, and Dong-Seok Hyun, 2007, “A Power-Control Scheme with Constant Switching Frequency in Class-D Inverter for Induction-Heating Jar Application”, **IEEE Transactions on Industrial Electronics,** Vol. 54, No. 3, pp. 1252-1260.

5 Ahmed, N, 2011, “High Frequency Soft Switching AC Conversion Circuit with Dual Mode PWM/PDM Control Strategy for High Power IH Applications”, **IEEE Transactions on Industrial Electronics,** No. 4, pp. 1440–1448.

6 L. Grajales and F. C. Lee, 1995, “Control System Design and Small-Signal Analysis of a Phase-Shift Controlled Series-Resonant Inverter for Induction Heating”, **the 26th Annual IEEE Power Electronics Specialists Conference**, Vol. 1, pp. 450-456.

7 Dudrik, J. Trip and N.-D., 2010, “Soft-Switching PS-PWM DC-DC Converter for Full-Load Range Applications”, **IEEE Transactions on Industrial Electronics**, Vol. 57, No. 8, pp.2807 – 2814.

8 X. Ruan, W. Chen, L. Cheng, C. K. Tse, H. Yan and T. Zhang, 2009, “Control Strategy for Input-Series–Output-Parallel Converter”, **IEEE Transactions on Industrial Electronics,** Vol. 56, No. 4, pp. 1174-1185.

9. P. Imbertson and N. Mohan, 1997, “New Directions in dc-dc Power Conversion Based on Idealized Concepts Leading Ultimately to the Asymmetrical Duty-Cycle Power Converter”, **IEEE Transactions on Circuit and Systems,** Vol. 44, pp. 722–727.

10 D. J. Tschirhart and P. K. Jain, 2008, “A CLL Resonant Asymmetrical Pulse Width Modulated Converter with Improved Efficiency”, **IEEE Transactions on Industrial Electronics,** Vol. 55, No. 1, pp. 114–122.

11 T. Mishima, M. Nakaoka, 2009, "A Novel High-Frequency Transformer-Linked Soft-Switching Half-Bridge DC–DC Converter with Constant-Frequency Asymmetrical PWM Scheme”, **IEEE Transactions on Industrial Electronics,** Vol. 56, No. 8, pp. 2961-2969.

12 M. S. Agamy, P. K. Jain, 2009, "A Three-Level Resonant Single-Stage Power Factor Correction Converter: Analysis, Design, and Implementation", **IEEE Transactions on Industrial Electronics,** Vol. 56, No. 6, pp. 2095-2107.

13 J. M. Burdío, L. A. Barragán, F. Monterde, D. Navarro, and J. Acero, 2004, "Asymmetrical Voltage-Cancellation Control for Full-Bridge Series Resonant Inverters," **IEEE Transactions on Power Electronics,** Vol. 19, No. 2, pp. 461–469.

14 J. I. Artigas, I. Urriza, J. Acero, L. A. Barragán, D. Navarro, and J. M. Burdío, 2009, "Power Measurement by Output-current Integration in Series Resonant nverters", **IEEE Transactions on Industrial Electronics,** Vol. 56, No. 2, pp. 559-567.

15 S. Chudjuarjeen, and C. Koompai, 2008, "Asymmetrical Control with Phase Lock Loop for Induction Cooking Appliances", **the 5th International Conference on Electrical/Electronics, Computer, Telecommunications, and Information Tecnology Conference**, Krabi, Thailand, pp. 1013-1016

16 P. Viriya, N. Yongyuth, and K. Matsuse, 2008, "Analysis of Two Continuous Control Regions of Conventional Phase Shift and Transition Phase Shift for Induction Heating Inverter under ZVS and non-ZVS," **IEEE Transactions on Power Electronics,** Vol. 23, No. 6, pp. 2794–2804.

17 L. Sung-Sae and M. Gun-Woo, 2008, "Full ZVS-range Transient Current Buildup Half-Bridge Converter with Different ZVS Operations to Load Variation," **IEEE Transactions on Industrial Electronics,** Vol. 55, No. 6, pp. 2557–2559.

18 O. Lucía, J. M. Burdio, I. Millán , J. Acero, and D. Puyal, 2009, "Load-Adaptive Algorithm of Half-Bridge Series Resonant Inverter for Domestic Induction Heating," **IEEE Transactions on Industrial Electronics,** Vol. 56, No. 8, pp. 3106–3116.

19 J. L. Russi, M. L. S. Martins, and H. L. Hey, 2008, "Coupled-filter-inductor Soft-Switching Techniques: Principles and Topologies," **IEEE Transactions on Industrial Electronics,** Vol. 55, No. 9, pp. 3361–3373.

20 Z. Zhang, W. Eberle, Y.-F. Liu and P. C. Sen, 2009, "A Nonisolated ZVS Asymmetrical Buck Voltage Regulator Module With Direct Energy Trans," **IEEE Transactions on Industrial Electronics,** Vol. 56, No. 8, pp. 3096-3105.

21 C. S. Moo, K. H. Lee, H. L. Cheng and W. M. Chen, "A Single-Stage High-Power-Factor Electronic Ballast With ZVS Buck–Boost Conversion, 2009", **IEEE Transactions on Industrial Electronics,** Vol. 56, No. 4, pp. 1136-1146.

22 S.-H. Park, G.-R. Cha, Y.-C. Jung and C.-Y. Won, 2010, "Design and Application for PV Generation System Using a Soft-Switching Boost Converter With SARC," **IEEE Transactions on Industrial Electronics,** Vol. 57, No. 2, pp. 515-522.

23 Low, Z. N. Casanova, J. J. Maier, P. H. Taylor, J. A. Chinga and R. A. Lin, J., 2010, “Method of Load/Fault Detection for Loosely Coupled Planar Wireless Power Transfer System With Power Delivery Tracking”, **IEEE Transactions on Industrial Electronics,** Vol. 57, No. 4, pp. 1478 – 1486.

24 José M. Espí Huerta, Enrique J. Dede García Santamaría,Rafael García Gil, and Jaime Castelló Moreno, 2007, “ Design of the L-LC Resonant Inverter for Induction Heating Based on Its Equivalent SRI ,” **IEEE Transactions on Industrial Electronics,** Vol. 54, No.6.

25 J. Espí, A. Navarro, J. Maicas, J. Ejea, and S. Casans, 1999, “ Control Circuit Design of The L-LC Resonant Inverter for Induction Heating ,” **Power Electronics Specialists Conference,** Charleston, SC, pp. 1126-1131.

26 S. Chudjuarjeen, A. Sangswang and C. Koompai, 2009, “LLC Resonant Inverter for Induction Heating with Asymmetrical Voltage-Cancellation Control,” **IEEE International Symposium on Circuits and Systems Conference,** Taipei, Taiwan, pp. 2874-2877.

27 O. Lucía, L. A. Barragán, J. M. Burdío, O. Jiménez, D. Navarro, and I. Urriza, 2011, "A Versatile Power Electronics Test-Bench Architecture Applied to Domestic Induction Heating," **IEEE Transactions on Industrial Electronics,** Vol. 58, No. 3, pp. 998 - 1007

28 F. Forest, S. Faucher, J.-Y. Gaspard, D. Montloup, J.-J. Huselstein and C. Joubert, 2007, “Frequency-synchronized Resonant Converters for the Supply of Multiwindings Coils in Induction Cooking Appliances”, **IEEE Transactions on Industrial Electronics,** Vol. 54, No. 1, pp. 441-452.

29 M. Enokizono and H. Tanabe, 1995, “Numerical Analysis of High-Frequency Induction Heating Including Temperature Dependence of Material Characteristics”, **IEEE Transactions on Magnetics,** Vol. 31, No. 4, pp. 2438-2444.

30 J. Andreu, J. M. De Diego, I. M. de Alegria, I. Kortabarria, J. L. Martin, and S. Ceballos, 2008, “New Protection Circuit for High-Speed Switching and Start-up of a Practical Matrix Converter”, **IEEE Transactions on Industrial Electronics,** Vol. 55, No. 8, pp. 3100-3114.

31 M. K. Kazimierczuk and D. Czarkowski, **Resonant Power Converters,** New York: Wiley, 1995.

32 O. Lucía, J. M. Burdío, I. Millán, J. Acero, and L. A. Barragán, 2010, “Efficiency Oriented Design of ZVS Half-Bridge Series Resonant Inverter with Variable Frequency Duty Cycle Control”, **IEEE Transactions on Power Electronics,** Vol. 25, No. 7, pp. 1671-1674.

33 Kagimoto, H., Miyagi, D., Takahashi, N., Uchida, N., Kawanaka, K., 2010, “Effect of Temperature Dependence of Magnetic Properties on Heating

Characteristics of Induction Heater", **IEEE Transactions on Magnetics,** Vol. 46, No. 8, pp. 3018-3021.

34 Rodriguez, J.I., Leeb, S.B., 2010, "Nonresonant and Resonant Frequency-Selectable Induction-Heating Targets", **IEEE Transactions on Industrial Electronics,** Vol. 57, No. 9, pp. 3095-3108.

35 Junhua Wang, Ho, S.L., Fu, W.N., Wang, Y.H., 2010 "Design and Analysis of a novel Wave Induction Heating System with Magnetic Slot Wedges for Heating Moving Thin Strips", **IEEE Transactions on Magnetics,** Vol. 46, No. 6, pp. 2175-2178.

36 O. Lucía, J. M. Burdío, L. A. Barragán, J. Acero, and I. Millán, 2010, "Series-Resonant Multiinverter for Multiple Induction Heaters", **IEEE Transactions on Power Electronics,** Vol. 25, No. 11, pp. 2860-2868.

37 Alwash, J.H.H., Sultan, S.K, 2010, "Performance Prediction of Single-Sided Induction Heating System", **IEEE Transactions on Energy Conversion,** Vol. 25, No. 4, pp.1057-1062

38 J. Acero, J.M. Burdio, L.A. Barragan, D. Navarro, R. Alonso, J.R. Garcia, F. Monterde, P. Hernandez, S. Llorente, and I. Garde, 2010, "Domestic Induction Applications," **IEEE Industry Application Magazine,** Vol. 16, No. 2, pp. 39-47.

39 H. Fujita and H. Akagi, "Pulse-density-modulated power control of a 4 kW, 450 kHz voltage-source inverter for induction melting applications," **IEEE Transactions on Industry Application,** Vol.32, No.2, pp.279–286.

40 D. Puyal, C. Bernal, J. M. Burdío, J. Acero, and I. Millán, 2008, "Versatile High-Frequency Inverter Module for Large-Signal Inductive Loads Characterization up to 1.5 MHz and 7 kW", **IEEE Transactions on Power Electronics,** Vol. 23, No. 1, pp. 75-87.

41 F. Forest, E. Labouré, F. Costa, and J. Y. Gaspard, 2000, "Principle of a Multiload/Single Converter System for Low Power Induction Heating," **IEEE Transactions on Power Electronics,** Vol. 15, No. 2, pp. 223–230.

42 F. Tourkhani and P. Viarouge, 2000, "Accurate Analytical Model of Winding Losses in Round Litz Wire Windings," **IEEE Transactions on Magnetics,** Vol. 37, No. 1, pp. 538–543.

43 A. D. Podoltsev, I. N. Kucheryavaya, and B. B. Lebedev, 2003, "Analysis of Effective Resistance and Eddy-Current Losses in Multiturn Winding of High Frequency Magnetic Components," **IEEE Transactions on Magnetics,** Vol. 39, No. 1, pp. 539–548.

44 J. Pleite, R. Prieto, R. Asensi, J. A. Cobos, and E. Olías, 1999, "Obtaining a Frequency-Dependent and Distributed-Effects Model of Magnetic Components from Actual Measurements," **IEEE Transactions on Magnetics,** Vol. 35, No. 6, pp. 4490–4502.

45 J. P. Keradec, E. Laveuve, and J. R. Roudet, 1991, “Multipolar Development of Vector Potential for Parallel Wires. Application to the Study of Eddy Currents Effects in Transformer Windings,” **IEEE Transactions on Magnetics,** Vol. 27, No. 5, pp. 4242–4245.

46 C. R. Sullivan, 2001, “Computationally Efficient Winding Loss Calculation with Multiple Windings, Arbitrary Waveforms, and Two-dimensional or Three Dimensional Field Geometry”, **IEEE Transactions on Power Electronics,** Vol. 16, No.1, pp. 142–149.

47 J. Acero, D. Navarro, L. A. Barragán, I. Garde, J. I. Artigas, and J. M. Burdío, 2007, “FPGA-based Power Measuring for Induction Heating Appliances using Sigma-delta A/D Conversion”, **IEEE Transactions on Industrial Electronics,** Vol. 54, No. 4, pp. 1843–1852.

48 F. P. Dawson and P. Jain, 1991, “A Comparison of Load Commutated Cnverter system for induction heating and melting applications”, **IEEE Transactions on Power Electronics,** Vol. 6, No. 4, pp. 430–441.

49 L. Hobson, D. W. Tebb, and D. Turnbull, 1985, “Dual element induction cooking unit using power MOSFETs”, **Inter Journal of Electronics,** Vol. 59, pp.747–757.

50 J. M. Burdío, A. Martínez, and J. R. García, 1998, “Asynthesis method for generating switched electronic converters”, **IEEE Transactions on Power Electronics,** Vol. 13, No. 6, pp. 1056–1068.

51 J. Davies and P. Simpson, **Induction Heating Handbook**. New York: McCraw Hill (U.K.) Limited.

52 P. K. Jain, A. St-Martin, and G. Edwards, 1996, “Asymmetrical pulse-widthmodulated resonant DC/DC converter topologies,” **IEEE Transactions on Power Electronics,** Vol. 11, No. 3, pp. 413–422.

53 M. D. Bellar, T. S. Wu, A. Tchamdjou, J. Mahdavi, and M. Ehsani, 1998, “A review of soft-switched DC–AC converters,” **IEEE Transactions on Industry Applications**, Vol. 34, No. 4, pp. 847–860.

54 Atsushi Okuno, Hitoshi Kawano, Junming Sun, Manabu Kurokawa, Akira Kojina, and Mutsuo Nakaoka, 1998, “Feasible Development of Soft-Switched SIT Inverter with Load-Adaptive Frequency-Tracking Control Scheme for Induction Heating”, **IEEE Transactions on Industry Applications**, Vol. 34, No. 4, pp. 847–860.

55 Mu-Ping Chen, Jan-Ku Chen, Katsuaki Murata, Masatoshi Nakahara, Koosuke Harada, 2001, “On the Switching Surge in the Current Resonant Inverter for the Induction Furnace Application”, **IEEJ Transactions on Industry Applications**, Volume 121-D, Number 6, pp.658-668.

56 Vicente Esteve, Esteban Sanchis-Kilders, Jose Jordan, Enrique J. Dede, Cesar Cases, Enrique Masest, Juan B. Ejea and Agustin Ferreres, 2011, “Improving the Efficiency of IGBT Series-Resonant Inverters Using Pulse Density Modulation” , **IEEE Transactions on Industrial Electronics,** Vol 58, no 3, pp 979-987.

57 Apisak polsripim, Saichol Chudjuarjeen, Anawach Sangswang, Piyasawat Navaratana Na Ayudhya and Chayant Koompai , 2009, “A soft switching class D current source inverter for induction heating with ferromagnetic load”, **IEEE PEDS2009,** Vol. 4, Nov., pp. 877 - 881**.**

58 E. J. Davies , J. and Simpson, P., 1979, **Induction Heating Handbook**, McGraw-Hill, UK.

59 Rudnev, V., Loveless, D., Cook, R. and Black, M., 2003, **Handbook of Induction Heating,** Marcel Dekker, New York.

60 S. Yachiangkam, P. Chakkuchan, S. Chudjuarjeen, A. Sangswang, and C. Koompai, Sep. 2010, “An automatic half-bridge resonant inverter with three-phase three-switch buck-type rectifier,” in **Proc. IEEE ECCE2010**., pp. 2172–2176.

61 S. Yachiangkam, A. Sangswang, S. Naetiladdanon, C. Koompai, and S. Chudjuarjeen, , 2011, “Resonant inverter with a variable-frequency asymmetrical voltage-cancellation control for low Q-factor loads in induction cooking,” **in Proc. EPE2011,**

62 J. Acero, J. M. Burdio, L. A. Barragan, D. Navarro, R. Alonso, J. R. Garcia, F. Monterde, P. Hernandez, S. Llorente, and I. Garde, “The domestic induction heating appliance: An overview of recent research,” **in Proc. IEEE Appl. Power Electron. Conf. Expo**., pp. 651–657, 2008.

63 J. Jittakort, S. Yachiangkam, A. Sangswang, S. Naetiladdanon, C. Koompai, and S. Chudjuarjeen, Jun. 2011, “A variable-fequency asymmetrical voltage-cancellation control of series resonant inverter in domestic induction cooking,” in **Proc. IEEE ICPE2011-ECCE Asia**., pp. 2320-2327.

64 H. W. Koertzen, J. D. V. Wyk, and J. A. Ferreira, Jun. 1995, “Design of the half-bridge, series resonant converters for induction cooking,” **Proc. IEEE Power Electron. Spec. Conf**., pp. 729–735.

65 Y. Kwon, S. Yoo, and D. Hyun, Mar. 1999, “Half-bridge series resonant inverter for induction heating applications with load-adaptive PFM control strategy,” **in Proc. IEEE Appl. Power Electron. Conf. Expo.**, pp.575–581.

66 I. Millan, D. Puyal, J. M. Burdio, C. Bemal, and J. Acero, 2007, “Improved performance of half-bridge series resonant inverter for induction heating with discontinuous mode control,” **in Proc. IEEE Appl. Power Electron. Conf.**, pp. 1293–1298.

67 S. Llorente, F. Monterde, J.M. Burdio, and J. Acero, 2002, “A comparative study of resonant inverter topologies used in induction cooking,” **in Proc. IEEE Appl. Power Electron. Conf. Expo.**, pp. 1168–1174.

68 Liliana Grajales, 1995, **Analysis and Design of a 500 kHz Series Resonant Inverter for Induction Heating Applications**, Dissertation, Virginia Polytechnic Institute and State University, Virginia, USA.

69 Yongyuth Naras, 2009, **Analysis of circuit operation under ZVS and Non-ZVS conditions in a full-bridge phase-shift controlled inverter with a load of high - frequency induction heating**, Dissertation, King Mongkut’s Institute of technology ladkrabang, Bangkok, Thailand.

70 David K. Morgan, 2003, CD4046B Phase-Locked Loop: A Versatile Building Block for Micropower Digital and Analog Applications, **Application Report**, Texas Instruments.

APPENDIX

A. Solving of LLC Resonant Load

From Figure 3.2, we can calculate the voltage across the resonant capacitor from voltage divider method.

$$\frac{V_C}{V_O} = \frac{1}{\dfrac{\left(j\omega C + \dfrac{1}{(R + j\omega L)}\right)}{j\omega L_S + \dfrac{1}{\left(j\omega C + \dfrac{1}{(R + j\omega L)}\right)}}} \tag{A.1}$$

when $\mathrm{A} = j\omega C$, $\mathrm{B} = j\omega L_S$, $\mathrm{C} = R + j\omega L$ substituting in (A.1)

$$\frac{V_C}{V_O} = \frac{1}{\dfrac{\left(\mathrm{A} + \dfrac{1}{\mathrm{C}}\right)}{\left(\mathrm{B} + \dfrac{1}{\left(\mathrm{A} + \dfrac{1}{\mathrm{C}}\right)}\right)}}$$

$$= \left(\frac{\mathrm{C}}{\mathrm{AC}+1}\right)\left(\frac{\mathrm{AC}+1}{\mathrm{BAC}+\mathrm{B}+\mathrm{C}}\right) \tag{A.2}$$

The ratio of the output voltage (V_o) of inverter and the capacitor voltage (V_C) can be found as,

$$\frac{V_C}{V_O} = \frac{R + j\omega L}{(j\omega L_S \times j\omega C)(R + j\omega L) + j\omega L_S + R + j\omega L}$$

$$= \frac{R + j\omega L}{-\omega^2 L_S C R - j\omega^3 L L_S C + j\omega L_S + R + j\omega L}$$

$$= \frac{R + j\omega L}{-\omega^2 L_S C R - j\omega(L L_S) - j\omega^3 L L_S C + R} \tag{A.3}$$

Instead, the ω is $\omega_0 = \dfrac{1}{\sqrt{\dfrac{L L_S C}{L + L_S}}}$

$$\frac{V_C}{V_O} = \frac{R + Lj\sqrt{\dfrac{L + L_S}{L L_S C}}}{R - R\left(\dfrac{L_S + L}{L}\right)} \tag{A.4}$$

$$= \frac{R + Lj\sqrt{\frac{L+L_S}{LL_SC}}}{R\left(\frac{L - L_S - L}{L}\right)}$$

$$= \left(\frac{RL + L^2 j}{-RL_S}\right)\sqrt{\frac{L+L_S}{LL_SC}}$$

$$= \left(-\frac{L}{L_S} - \frac{L^2 j}{RL_S}\right)\sqrt{\frac{L+L_S}{LL_SC}} \qquad \text{(A.5)}$$

So, we calculate the capacitor voltage as a function of V_o in (A.6)

$$V_C = V_O\left(-\frac{L}{L_S} - \frac{L^2 j}{RL_S}\right)\sqrt{\frac{L+L_S}{LL_SC}} \qquad \text{(A.6)}$$

B. Fourier of Asymmetrical waveform

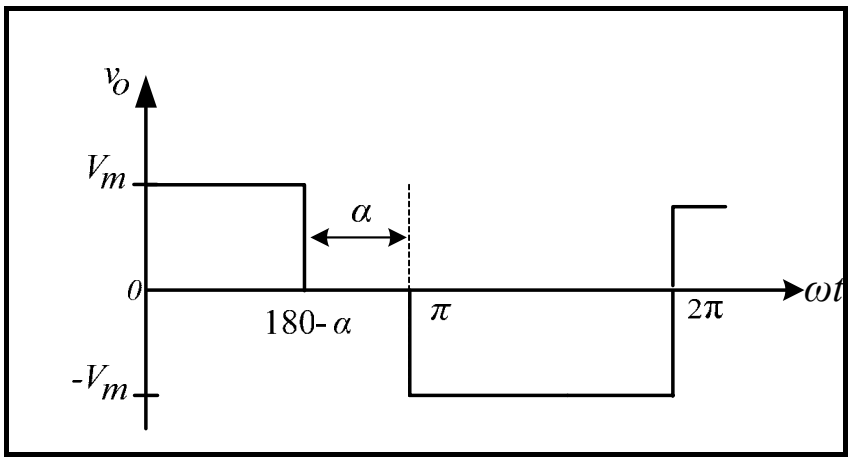

Figure B.1 Asymmetrical voltage waveform

From Figure B.1 the time variation in steady state of the voltage may be represented by the following Fourier series. We can define even function and odd function equations in(B.1) and (B.2)

$$b_n = \frac{1}{\pi}\left[\int_0^{180\text{-}\alpha^\circ} V_m sin(n\omega t)d(\omega t) + \int_0^{2\pi}(\text{-}V_m)sin(n\omega t)d(\omega t)\right]$$

$$= \frac{V_m}{\pi}\left\{\left[\frac{\text{-}cos(n\omega t)}{n}\right]_0^{180\text{-}\alpha^0} + \left[\frac{cos(n\omega t)}{n}\right]_\pi^{2\pi}\right\}$$

$$= \frac{V_m}{n\pi}\left[\text{-}cos\left(180\text{-}\alpha^0\right) + cos(0) + cos(2n\pi) - cos(n\pi)\right]$$

$$= \frac{V_m}{n\pi}\left[2\text{-}(\text{-}1)^n\text{-}cos\, n\left(180\text{-}\alpha^0\right)\right] \qquad \text{(B.1)}$$

where V_m is the amplitude of the asymmetrical voltage waveform.

$$a_n = \frac{1}{\pi}\left[\int_0^{180\text{-}\alpha^0} V_m \cdot cos(n\omega t)\, d(\omega t)\right]$$

$$= \frac{V_m}{n\pi}\left[sin(0)\text{-}sin\left(180\text{-}\alpha^0\right)\right]$$

$$= \frac{V_m}{n\pi} sin\left(180\text{-}\alpha^0\right) \qquad \text{(B.2)}$$

C. Diagram of Losses at MOSFETs Switches

The example of turn off loss which is of switch S_4 is shown in Figure C.1.

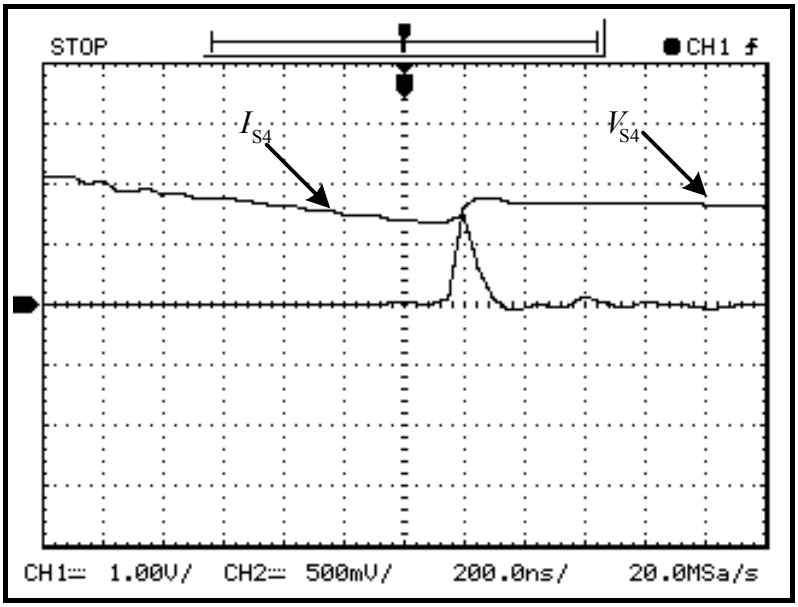

Figure C.1 Turn off loss at S_4

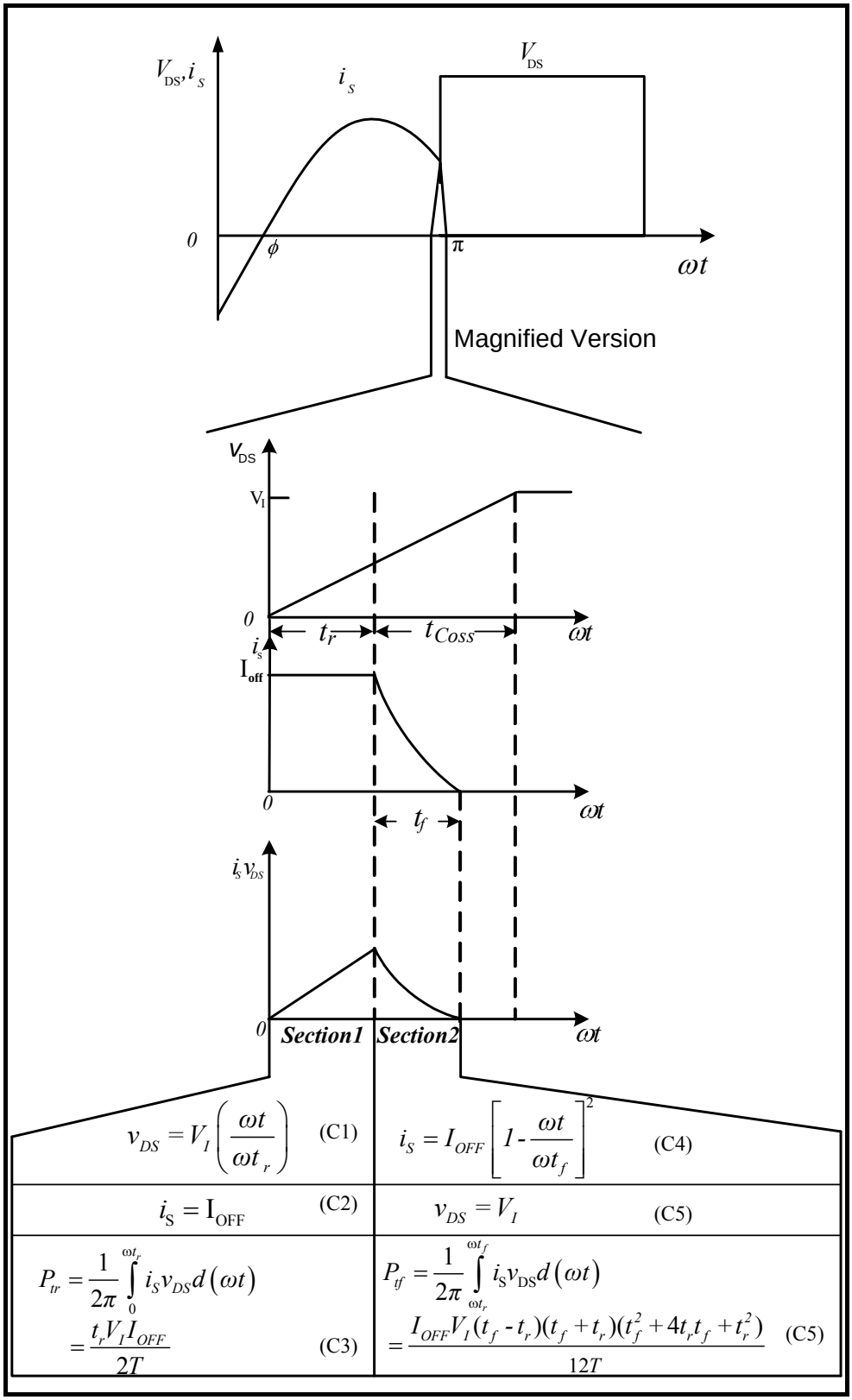

Figure C.2 Diagram of turn off losses

The conclusion of calculation of the switching loss is shown in Figure C.2 where we can calculate the switching loss of the switch by using equation (C1-C5).

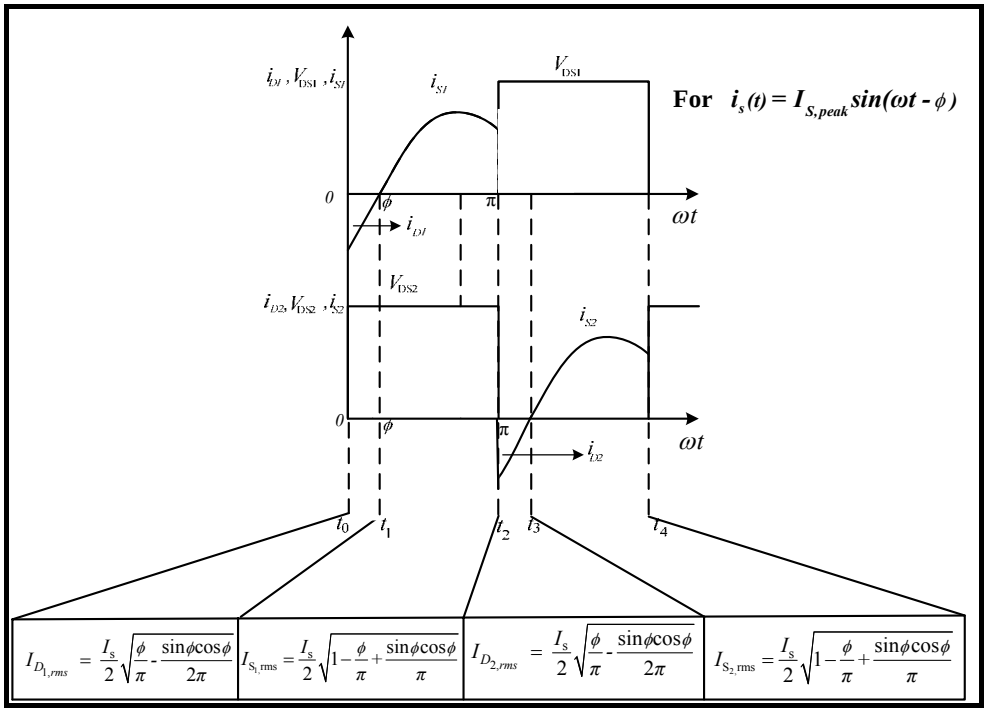

Figure C.3 Diagram of current of S_1 and S_2

The calculation of the current at switch S_1 and S_2 is shown in Figure C.3 and the calculation of the current at switch S_3 and S_4 is shown in Figure C.4.

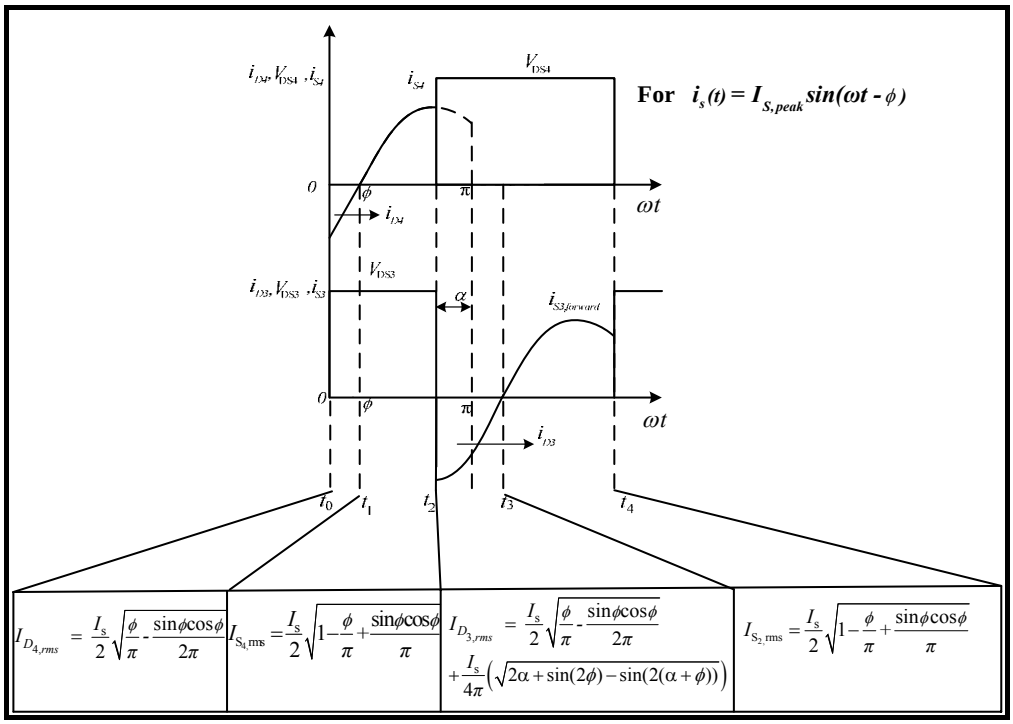

Figure C.4 Diagram of current of S_3 and S_4

D. Publications

1 S. Chudjuarjeen, A. Sangswang, and C. Koompai, 2011 “An improved LLC resonant inverter for induction heating applications with asymmetrical control,” **IEEE Transaction on Industrial Electronics**, vol. 58, no. 7, pp. 2915–2925.

IEEE TRANSACTIONS ON INDUSTRIAL ELECTRONICS, VOL. 58, NO. 7, JULY 2011 2915

An Improved LLC Resonant Inverter for Induction-Heating Applications With Asymmetrical Control

Saichol Chudjuarjeen, *Student Member, IEEE*, Anawach Sangswang, *Member, IEEE*, and Chayant Koompai

***Abstract*—This paper proposes a modified LLC resonant load configuration of a full-bridge inverter for induction-heating applications. The LLC load configuration is a combination of a series inductor, a matching transformer, and an inductor and a capacitor connected in parallel. The output power is controlled using the asymmetrical voltage-cancellation technique. With the use of a phase-locked loop control, the operating frequency is automatically adjusted to maintain a small constant lagging phase angle under load-parameter variation during the heating process. The proposed configuration has the benefit of smaller inductance and inherent short-circuit protection capability in case a short circuit occurs at the induction coil or from transformer saturation. The validity of the proposed method is verified through computer simulation and hardware experiment at an operating frequency range of 108.7–110.6 kHz.**

***Index Terms*—Asymmetrical control, induction heating, zero-voltage switching (ZVS).**

I. Introduction

INDUCTION heating is a well-known technique to produce very high temperature for applications like steel melting, brazing, and surface hardening. In each application, an appropriate frequency must be used depending on the workpiece geometry and skin-depth requirements [1], [2]. In general, the induction-heating technique requires high-frequency current supply that is capable of inducing high-frequency eddy current in the workpiece that results in the heating effect [1]. A large number of topologies have been developed in this area. Current-fed and voltage-fed inverters are among the most commonly used types [2]. Recent developments in switching schemes and control methods have made the voltage-source resonant inverters to be widely used in applications that require output-power control capability. For example, in pulse-frequency modulation (PFM), the output power can be controlled by varying the switching frequency while the inverter operates under zero-voltage switching (ZVS) scheme [3]. The pulse-density modulation method regulates the output power by varying the period in which the inverter supplies high-frequency current to the induction coil [4], [5]. The phase-shift (PS) control technique in [6] and [8] varies the output power by shifting the phase of the switch conduction sequences. The asymmetrical duty-cycle control technique employs an unequal duty-cycle operation of the switches in the converter [9]–[12]. The asymmetrical voltage-cancellation (AVC) is then proposed in [13] and [14] where the authors describe voltage-cancellation for conventional fixed-frequency control strategies. In [15], the AVC is implemented in a full-bridge series-resonant inverter. The series-resonant inverter needs an output transformer for matching the output power to the load. Most induction-heating applications require accuracy in output-power control capability. For example, cooking appliances require accurate power control over a wide range of power for different cooking purposes where a ZVS condition must be met to ensure high efficiency [16]–[23]. By using the mentioned techniques in fixed frequency and the optimum duty cycle for ZVS operation, it is rather difficult to control the output power due to variation of parameters in the resonant load during the heating process. In high-temperature applications, a high current must flow in the surface of the metal for heating effect. The series-resonant inverter may need a transformer for matching the output power and high current in the induction coil. Previous work has shown that an LLC configuration can offer a better performance than the series resonant while providing short-circuit immunity and lower current on the transformer’s secondary [24], [25]. Note that the closed-loop PFM method presented in [25] may sacrifice the efficiency due to switching losses at high-frequency operation. However, the LLC resonant load offers better performance with high-quality factor ($Q > 30$) and only requires a small series inductance in the circuit configuration. This implies that the output transformer can be omitted. The disadvantage of the LLC resonant load is that the output current may no longer be sinusoid in the case of low Q ($Q < 10$) [26]. The current in the induction coil is unavoidably small and distorted. Therefore, system efficiency is a price to pay.

In this paper, an improved LLC resonant inverter with asymmetrical control technique is proposed. The aim is to control the output power for high-temperature applications including steel melting, brazing, and hardening, where the load parameters and resonant frequency vary substantially throughout the system operation. The operating frequency is controlled using phase-locked loop to track for the resonant frequency. The output power is controlled by adjusting the switch duty cycle.

Manuscript received February 26, 2010; revised June 8, 2010; accepted July 31, 2010. Date of publication September 2, 2010; date of current version June 15, 2011.

The authors are with the Department of Electrical Engineering, Faculty of Engineering, King Mongkut’s University of Technology Thonburi, Bangkok 10140, Thailand (e-mail: saichol@ieee.org; anawach.san@kmutt.ac.th).

Color versions of one or more of the figures in this paper are available online at http://ieeexplore.ieee.org.

Digital Object Identifier 10.1109/TIE.2010.2070779

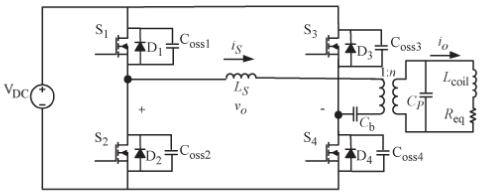

Fig. 1. Full-bridge LLC resonant inverter.

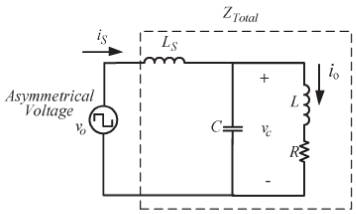

Fig. 2. Equivalent circuit.

The difference between this paper and [15] is that the focus of [15] is on a series-resonant load for cooking applications where the load temperature is low and parameters remain rather constant. In this paper, however, the LLC resonant tank is designed with a matching transformer in between the series inductor and paralleled LC resonant tank. The important advantage of the proposed topology is the short-circuit protection of the transformer and the induction coil. This paper is organized as follows. The circuit configuration and the principle of operation of a full-bridge LLC resonant inverter is described in Section II. Section III presents an analysis of steady-state operation. In Section IV, the asymmetrical control strategy is proposed. Analyses of switching and conduction losses are provided in Section V. A design procedure is given in Section VI. Simulation and experimental results are discussed in Section VII. Section VIII concludes this paper.

II. Full-Bridge LLC Resonant Inverter

A. Circuit Description

Fig. 1 shows an LLC resonant inverter configuration for induction-heating applications. The inverter consists of four switches with antiparallel diodes, a resonant capacitor (C_p), a series inductor (L_s), and an induction coil that comprises a series combination of a resistor ($R_{\rm eq}$) and an induction coil inductor ($L_{\rm coil}$) [27], [28]. A dc blocking capacitor (C_b) is inserted in series with the transformer primary. The equivalent circuit of the full-bridge LLC inverter system in Fig. 1 is shown in Fig. 2 where the input voltage can be viewed as an asymmetrical ac voltage supplied to the system. With a negligible value of C_b, it is noted that capacitor C, inductor L, and resistor R represent the equivalent capacitor C_p, inductor $L_{\rm coil}$, and resistor $R_{\rm eq}$ referred to the primary side of the transformer, respectively. The stray capacitance of MOSFET switching device S_1, S_2, S_3, and S_4 are denoted as $C_{\rm oss1}$, $C_{\rm oss2}$, $C_{\rm oss3}$, and $C_{\rm oss4}$, respectively. The total impedance of the asymmetrical voltage source (v_o) is denoted by $Z_{\rm total}$. The current i_s and i_o are the input and output currents, respectively.

B. Modes of Operation

As shown in Fig. 3, eight modes of operation exist within one switching cycle when the stray capacitances are taken into account. The corresponding waveforms and circuit topology for each mode of operation are shown in Fig. 3(a) and (b), respectively. The analysis is as follows.

1) Mode 1 (t_0–t_1): While switches S_2 and S_3 are off, at $t = t_0$, switches S_1 and S_4 receive positive gating signals. The negative input current (i_s) flows through diodes D_1 and D_4.
2) Mode 2 (t_1–t_2): At $t = t_1$, as soon as the antiparallel diodes D_1 and D_4 are off, switches S_1 and S_4 conduct, and the ZVS operation is achieved. During this mode, the positive input current (i_s) flows.
3) Mode 2′ (t_2–t_2'): At $t = t_2$, after switch S_4 is off, the current flows in the same direction. The charge in $C_{\rm oss3}$ is gradually decreasing, whereas the charge in $C_{\rm oss4}$ is slowly increasing. At this stage, the output voltage changes from $+V_{\rm dc}$ to zero.
4) Mode 3 (t_2'–t_3): At $t = t_2'$, while switch S_1 still conducts, switch S_4 is turned off, and the antiparallel diode D_3 conducts. After the switch dead time, switch S_3 receives a positive gating signal.
5) Mode 3′ (t_3–t_3'): During this period, all switches are off simultaneously. A part of positive current i_s flows through the antiparallel diode D_3 and $C_{\rm oss2}$. At the same time, the charge in capacitor $C_{\rm oss2}$ decreases, whereas the charge in capacitor $C_{\rm oss1}$ increases. In this operation, the output voltage v_o changes from zero to $-V_{\rm dc}$.
6) Mode 4 (t_3'–t_4): At $t = t_3'$, switch S_1 is already turned off. Similar to that in Mode 1, diode D_2 starts conducting positive input current i_s together with diode D_3. After the switch dead time, switch S_2 receives a positive gating signal. The shifted angle α is from t_2 to the moment switch S_2 is on.
7) Mode 5 (t_4–t_5): At $t = t_4$, when the antiparallel diodes D_2 and D_3 are off, switches S_2 and S_3, which already received positive gating signals, conduct, and the ZVS operation is achieved. During this mode, the current i_s becomes negative.
8) Mode 5′ (t_5–t_5'): At $t = t_5$, after switches S_2 and S_3 are turned off, the negative current i_s flows through the stray capacitors $C_{\rm oss1}$, $C_{\rm oss2}$, $C_{\rm oss3}$, and $C_{\rm oss4}$. The charges in $C_{\rm oss1}$ and $C_{\rm oss4}$ decrease, while the charges in $C_{\rm oss2}$ and $C_{\rm oss3}$ increase. At this point, the full cycle of operation is accomplished. In this operation, v_o changes from $-V_{\rm dc}$ to $+V_{\rm dc}$. The next operating cycle continues, repeating from Modes 1 to 5′.

In many cases, the stray capacitance may be neglected, and the modes of operation for one switching period are reduced to five modes (i.e., modes $1 \rightarrow 2 \rightarrow 3 \rightarrow 4 \rightarrow 5$).

Note that in this paper, it is assumed that the charging time of the stray capacitor ($t_{\rm coss}$) is smaller than the switch's dead time.

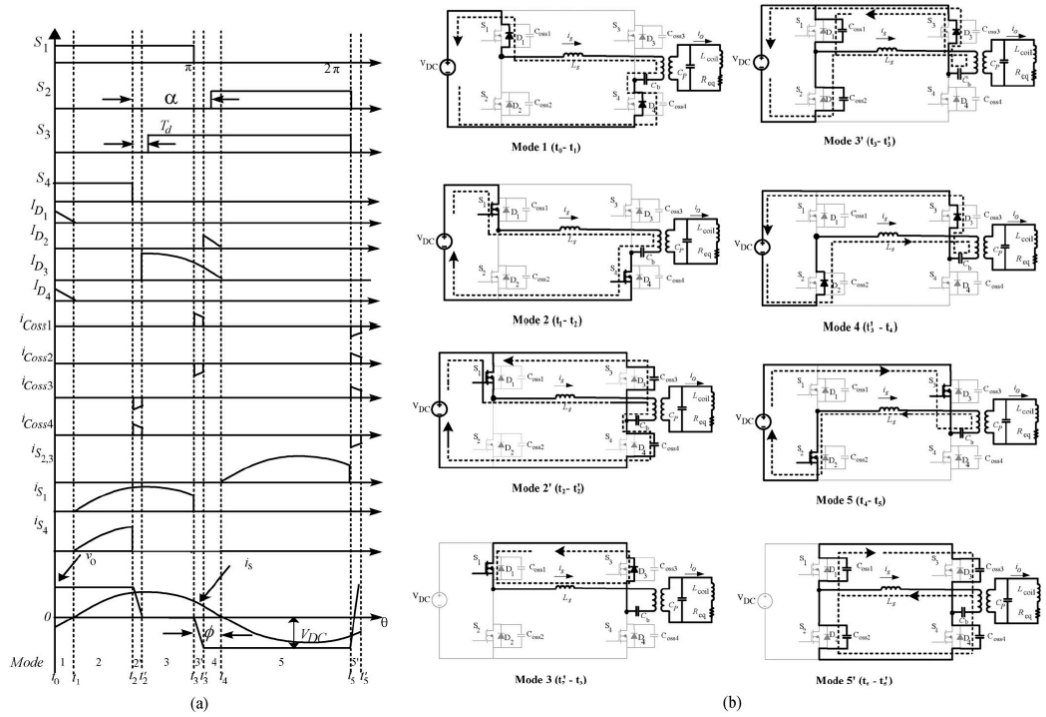

Fig. 3. Inverter operations: (a) Typical waveforms. (b) Modes of operation.

III. Circuit Analysis

A. Analysis of the Output Power

The steady-state analysis of the full-bridge LLC inverter is based on the following assumptions.

1) All circuit components are ideal.
2) The dc input voltage $V_{\rm DC}$ is constant.
3) The effects of stray capacitance are neglected.

From Figs. 2 and 3, the relationship between the load voltage (i.e., the capacitor voltage v_c) and the inverter output voltage (v_o) is given as

$$\frac{V_c}{V_o} = \frac{R + j\omega L}{(j\omega L_s \times j\omega C)(R + j\omega L) + j\omega L_s + R + j\omega L)} \quad (1)$$

where $L = n^2 L_{\rm coil}$, $R = n^2 R_{\rm eq}$, and $C = C_p/n^2$, given that n is the transformation ratio of the transformer. The inverter is designed to operate such that the switching frequency (ω) is higher than the resonant frequency (ω_0) for ZVS operation. The resonant frequency of the system in Fig. 2 is given as

$$\omega_o = \sqrt{\frac{L + L_s}{L \cdot L_s \cdot C}}. \quad (2)$$

Taking only the fundamental component (V_1) of the inverter output voltage (v_o) in Fig. 2 into account, the load voltage is given as

$$V_C = \left(-\frac{L}{L_s} - j\frac{L^2}{RL_s}\sqrt{\frac{L + L_s}{L \cdot L_s \cdot C}} \right) \cdot V_1. \quad (3)$$

The fundamental voltage V_1 of the capacitor voltage v_C in (3) can be obtained from the following coefficients of Fourier series of the inverter output voltage v_o [13]:

$$\left.\begin{array}{l} \hat{V}_n = \frac{V_m}{\pi}\sqrt{a_n^2 + b_n^2} \\ \phi_{vn} = \tan^{-1}\frac{a_n}{b_n} \\ b_n = \frac{V_m}{n\pi}\left[2 - (-1)^n - \cos n(180 - \alpha)\right] \\ a_n = \frac{V_m}{n\pi}\left[-\sin n(180 - \alpha)\right] \end{array}\right\} \quad (4)$$

where V_m is the dc input voltage assuming the same value as $V_{\rm DC}$, ϕ_{vn} is the phase of the nth harmonic of v_o, and α is the shifted angle of the switch S_4, as shown in Fig. 3. Using (4), the amplitude of the fundamental voltage v_1 can be calculated as

$$\hat{V}_1 = \frac{V_m}{\pi} \times \sqrt{\sin^2(180 - \alpha) + \left(3 - \cos(180 - \alpha)\right)^2} \quad (5)$$

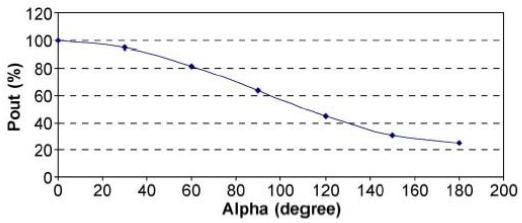

Fig. 4. Output power versus α.

and the average output power at the load (P) can be obtained as [24]

$$P = V_1^2 \mathrm{Re}\left\{Z_{\mathrm{total}}(j\omega_0)^{-1}\right\} \tag{6}$$

which is expanded to

$$P = \frac{V_m^2}{2R\pi^2}\left(\sin^2(180-\alpha) + (3-\cos(180-\alpha))^2\right) \times \left(\frac{L}{L_s}\right)^2 \cos(\phi) \tag{7}$$

where ϕ is the switching angle. The output power P in (7) depends on the shifted angle α. Fig. 4 shows the relationship of the output power and α, obtained from (7), with $\cos\phi$ being set to one. It is seen that an increase of α results in reduction of the output power. This means that the output power can be controlled through an adjustment of α. The greater the angle α, the less power is delivered to the load. The frequency response of the output power (P_o) under different quality factors (Q) is shown in Fig. 5(a) with the angle α set to zero. At higher Q factor, the inverter operates close to the resonant frequency ω_0 (i.e., the normalized frequency f_s/f_b is close to one). Unlike the induction-coil current (i_o) shown in Fig. 5(b), the Q factor has negligible effect on the resonant frequency, i.e., the peak value of i_o occurs at the same frequency regardless of the Q factors. The peak value of i_o is related to the RLC parallel end in Fig. 2, where L_s does not play a roll in the frequency response of i_o.

B. Design of L_s

The total impedance (Z_{total}) in Fig. 2 can be expressed as

$$Z_{\mathrm{Total}}(\omega) = \frac{R - \omega^2 CL_sR + j\omega L_s + j\omega L - j\omega^3 L_sL}{-\omega^2 CL + j\omega CR}. \tag{8}$$

At resonant frequency (ω_0)

$$Z_{\mathrm{Total}}(\omega_0) = \frac{\omega_0 L_s^2 R\left(L^2\omega_0 + jR(L_s+L)\right)}{-L\omega_0 - R^2\left(L_s^2 + L_sL + L^2\right)}. \tag{9}$$

The switching angle ϕ is given as

$$\phi = \arg\left\{Z_{\mathrm{Total}}(j\omega_0)\right\} = \arctan\left(\frac{R(L_s+L)}{L^2\omega_0}\right) > 0. \tag{10}$$

This results in

$$\frac{L_s}{L} = \frac{L\omega_0}{R}\tan\phi - 1. \tag{11}$$

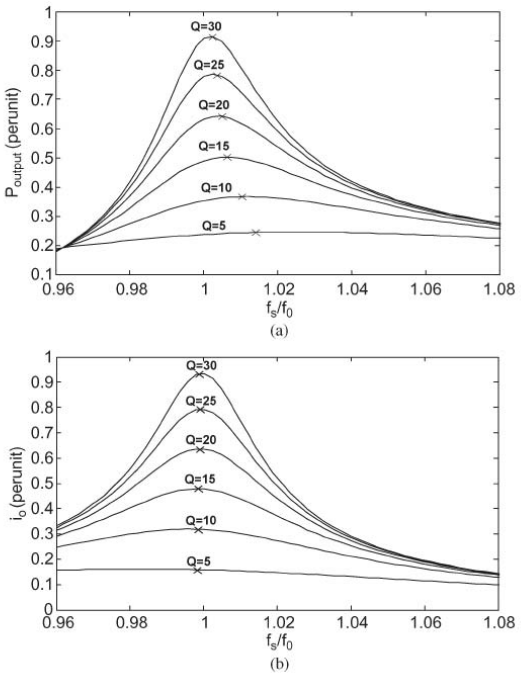

Fig. 5. Frequency response: (a) Output power (P_o) at various Q factors and (b) output current (i_o) at various Q factors.

The current gain is found as

$$\frac{I_o}{I_s} = \frac{1}{j\omega CZ_P(j\omega)} \tag{12}$$

where $Z_P(j\omega) = (1/j\omega C)//(j\omega L + R)$. The current gain at resonant frequency (ω_0) is given as

$$\left|\frac{I_o}{I_s}(\omega_0)\right| = \frac{L_s}{L}\frac{1}{\sqrt{\frac{CL_SR^2(L+L_s)}{L^3}+1}}. \tag{13}$$

Therefore, the coil current at resonance can be expressed as

$$I_o = \frac{L_s}{L} I_s \cos\phi. \tag{14}$$

At the frequency above resonance, there is always a positive power angle ϕ (i.e., lagging current operation). A high-efficiency inverter with LLC topology can be achieved by introducing a small positive switching angle and high current gain in the design. From (11) and (14), it is deduced that a suitable load would be applications with high quality factor (Q) such as brazing, surface hardening, and tube welding. For applications with low Q (less than ten), it is very difficult to obtain both high current gain and resonant operations at the same time. One of the possible solutions would be to increase the power angle ϕ. This means that the operating frequency must be adjusted further away from the resonant frequency, which results in the operation of the inverter under low efficiency.

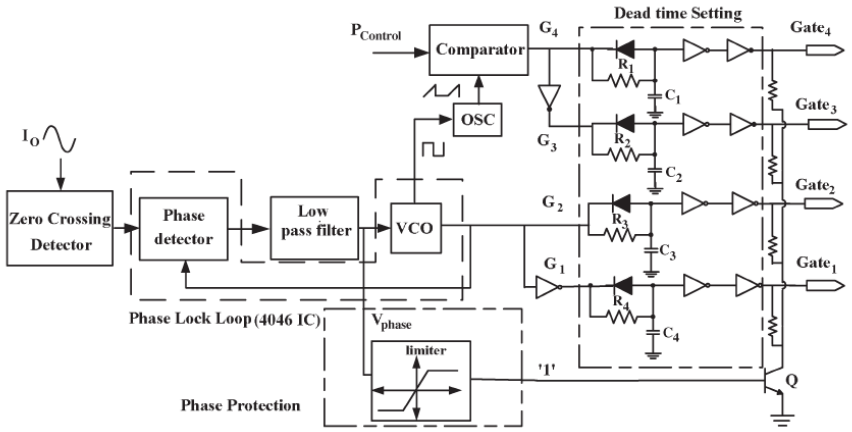

Fig. 6. Proposed control block diagram of the LLC resonant inverter.

This is where the high-frequency transformer is introduced to match the output current and power. In addition to improving the system efficiency, the important advantage of the inclusion of the transformer is the inherent current-limiting capability in case of transformer saturation. The inductor L_s carries low current because it is located on the primary side. Therefore, it is easier and cheaper to construct such an inductor.

IV. Proposed Control Strategy

The workpiece geometry, conductivity, and permeability of different metals have various effects on the inductance of the heating coil. In addition, the coil inductance is also changed when heated. This is due to the fact that beyond the Curie temperature, the relative permeability (μ_r) of the workpiece decreases when the temperature increases. This results in the reduction of the equivalent inductance of the workpiece which in turn reduces the coil inductance. On the contrary, when the workpiece temperature is lower than the Curie temperature, the relative permeability of the workpiece decreases with temperature. Therefore, the coil inductance exhibits a change in the opposite direction [29].

Considering the fact that the resonant capacitance is fixed, therefore, the resonant frequency is varied throughout the heating process. The phase-locked loop integrated-circuit (IC) device for load-adaptive resonant-frequency tracking is introduced to the resonant inverter to drive the operating frequency to the new resonant frequency.

The proposed control scheme of the full bridge LLC resonant inverter consists of two parts:

1) power control through the alpha angle (α) of the switch S_4;
2) frequency control for ZVS operation.

The controller comprises a current sensor, zero-crossing detector, phase detector, and voltage-controlled oscillator, as shown in Fig. 6. The 4046 phase-locked loop IC is used for frequency control at slightly higher than the resonant frequency. In typical voltage-fed inverter, the gate drive signal is in phase

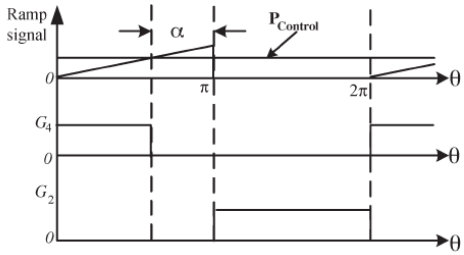

Fig. 7. Waveforms of the asymmetrical gate drive signal.

with the asymmetrical inverter output voltage v_o. Therefore, we can use the gate drive signal instead of the load-voltage pulse for phase detection. The current signal i_o is compared with the voltage signal in order to detect the phase difference. The output signal of the digital phase detector is filtered by an RC low-pass filter to get an average value that is proportional to the phase difference at the load. The generation of asymmetrical gate drive signals for power control is shown in Fig. 7. The P_{control} signal is compared with the ramp signal from the 4046 IC to generate the gate signal G_4.

If the P_{control} signal is greater than the ramp signal, the gate signal G_4 is set to high. Otherwise, it is set to low. In this way, α is dependent on the P_{control} signal. The gate signal G_2 is always on from π to 2π. The G_1 and G_3 signals are the inverse of G_2 and G_4 signals, respectively. Note that the ramp signal is generated from the phase detector. Therefore, its frequency is automatically adjusted to track the resonant frequency and turns on as ZVS operation is obtained. The gating signals G_1, G_2, G_3, and G_4 are sent into the dead-time circuit where the dead-time setting is adjusted through the pairs R_1–C_1, R_2–C_2, R_3–C_3, and R_4–C_4. A phase-protection circuit with a limiter is used where the V_{phase} signal, a dc signal proportional to the phase, is put through a limiter [30]. This allows an operation in the desired frequency range for the ZVS mode. If the phase lies in the region that is out of the predetermined limits, an active

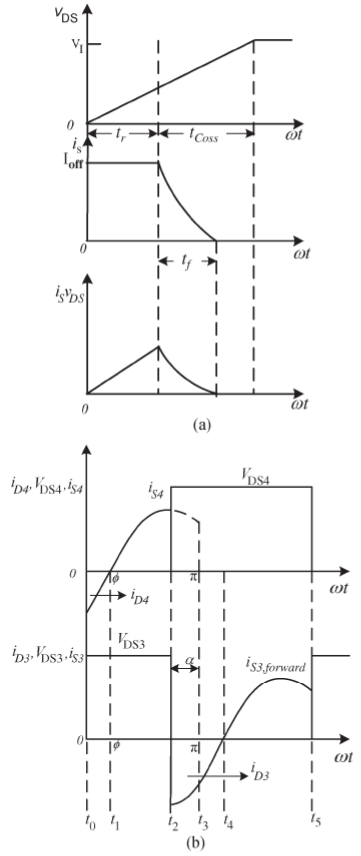

Fig. 8. Theoretical waveforms. (a) Turn-off loss and (b) the conduction loss of switch S_3 and switch S_4.

signal is sent out to turn the transistor Q on and ground all gate signals S_1 to S_4. The inverter is turned off.

V. Switching and Conduction Losses

A. Switching Loss

To maintain the operation under ZVS conditions, the power angle ϕ must be kept greater than both the dead time and charging time of the stray capacitors [31], [32]. This is to allow sufficient time for the diodes to conduct while keeping the voltage across the switch at zero. For the operation at the frequency above resonance, the turn-on switching loss of all switches is zero, but there still is a turn-off switching loss for every switch. It is seen in Fig. 3 during the t_3–t_4 interval that the switch S_4 turns off at a larger current as α becomes larger. This results in a higher switching loss. To consider the switching loss in details, the current and voltage transition at turn off are shown in Fig. 8(a).

The drain-to-source voltage $v_{\rm DS}$ during rise time (t_r) is given as

$$v_{\rm DS} = V_I \left(\frac{\omega t}{\omega t_r}\right) \tag{15}$$

where V_I is the voltage across the switch while the switch is turned off, which is the same as the dc input voltage $(V_{\rm DC})$. The switch current is a small portion of a sinusoid and can be approximated by a constant

$$i_S = I_{\rm OFF} \tag{16}$$

where $I_{\rm OFF}$ is the current through the switch before turning off. The power loss associated with the voltage during rise time $(P_{\rm tr})$ is given as

$$P_{\rm tr} = \frac{1}{2\pi}\int_0^{\omega t_r} i_S v_{\rm DS}\, d(\omega t) = \frac{t_r V_I I_{\rm OFF}}{2T}. \tag{17}$$

During fall time (t_f), the switch current can be approximated by a parabola function as

$$i_S = I_{\rm OFF}\left[1 - \frac{\omega t}{\omega t_f}\right]^2 \tag{18}$$

while the drain-to-source voltage is (15). The power loss associated with $t_f (P_{\rm tf})$ is provided as

$$\begin{aligned} P_{tf} &= \frac{1}{2\pi}\int_{\omega t_r}^{\omega t_f} i_S v_{\rm DS}\, d(\omega t) \\ &= \frac{I_{\rm OFF} V_I (t_f - t_r)(t_f + t_r)\left(t_f^2 + 4t_r t_f + t_r^2\right)}{12T}. \end{aligned} \tag{19}$$

Hence, the turn-off switching loss is combined as

$$\begin{aligned} P_{\rm off} &= P_{tr} + P_{tf} \\ &= f V_I I_{\rm OFF} \\ &\quad \times \left(\frac{t_r}{3} + \frac{(t_f - t_r)(t_f + t_r)\left(t_f^2 + 4t_r t_f + t_r^2\right)}{12}\right). \end{aligned} \tag{20}$$

Therefore, the turn-off loss of the full-bridge LLC resonant inverter with asymmetrical control becomes

$$\begin{aligned} P_{\rm total,off} = f V_I &\left(\frac{t_r}{3} + \frac{(t_f - t_r)(t_f + t_r)\left(t_f^2 + 4t_r t_f + t_r^2\right)}{12}\right) \\ &\times \left(3I_{\rm OFF,S_1,S_2,S_3} + I_{\rm OFF,S_4}\right) \end{aligned} \tag{21}$$

where $I_{\rm OFF,S_1,S_2,S_3}$ and $I_{\rm OFF,S_4}$ assume the forms

$$I_{\rm OFF,S1,S2,S3} = I_{\rm m}\sin(\phi) \tag{22}$$

$$I_{\rm OFF,S_4} = I_{\rm m}\sin(\alpha + \phi). \tag{23}$$

If a snubber capacitor is added to the circuit, the charging time $(t_{\rm Coss})$ will increase, and the peak of the product of

i_s and $v_{\rm ds}$ in Fig. 8(a) will decrease. Thus, the turn-off loss is decreased. The dead time must be increased to maintain approximately zero turn-off loss. Clearly, the snubber capacitor can always be included. However, there is a tradeoff for adding a snubber capacitor because the power angle ϕ must cover the switch dead time and the capacitor charging time. Therefore, the increased power angle ϕ results in a reduced range of the angle α ($\alpha_{\max} = \phi - 180$), and therefore, the range of power adjustment will be reduced.

B. Conduction Loss

Since the intervals t_2–t_2' and t_5–t_5' in Fig. 3(a) representing the charging and discharging periods of the stray capacitors are small compared with the overall conduction times, both intervals are neglected in the following calculation. Taking the switch conduction loss into account, the current and voltage at switches S_3 and S_4 from t_0 to t_5 are shown in Fig. 8(b). Switches S_1, S_2, and S_3 carry the same current and conduction loss through the intervals t_1–t_2 and t_4–t_5, respectively. Since the inverter current i_s is given as

$$i_s(t) = I_{\rm S,peak}\sin(\omega t - \phi) \tag{24}$$

the current contribution to conduction losses of the switch S_1, S_2, and S_3 can be found as

$$I_{\rm S_{1,2,3},rms} = \frac{I_s}{2}\sqrt{1 - \frac{\phi}{\pi} + \frac{\sin\phi\cos\phi}{\pi}}. \tag{25}$$

For the asymmetrical switch S_4, the conduction loss results from the current

$$I_{\rm S_4,rms} = \frac{I_s}{4\pi}\sqrt{-2(\alpha - \pi + \phi) + \sin\left(2(\alpha + \phi).\right)} \tag{26}$$

The conduction loss of the switch is given as

$$P_{s,\rm loss} = (I_{\rm S,rms})^2 R_{\rm DS,on}. \tag{27}$$

The aforementioned conduction losses can be calculated by substitution of the currents in (25) and (26) into (27). Next, the diode conduction loss is considered. Clearly, diodes D_1–D_4 and D_2–D_3 conduct during the t_0–t_1 and t_2–t_4 intervals, respectively. In addition, the conduction loss of diode D_3 includes the forward conduction during the t_2–t_3 interval, similar to the current in (25).

Therefore, the current contribution to the conduction loss of diode D_3 is given as

$$I_{\rm D_{3,rms}} = \frac{I_s}{4\pi}\left(\sqrt{2\alpha + \sin(2\phi) - \sin\left(2(\alpha + \phi)\right)}\right). \tag{28}$$

For the other diodes, the current contribution to the conduction loss is found as

$$I_{D_{1,2,4,\rm rms}} = \frac{I_s}{2}\sqrt{\frac{\phi}{\pi} - \frac{\sin\phi\cos\phi}{2\pi}}. \tag{29}$$

The diode conduction loss is

$$P_{D,\rm loss} = I_{\rm Diode,rms} \times V_{\rm FWD,diode}. \tag{30}$$

TABLE I
DESIGN SPECIFICATION AND CIRCUIT PARAMETERS

Parameter		Value
v_{AC}	Input Voltage	150 $V_{\rm rms}$
f_o	Resonant Frequency	108.2 kHz
f_s	Switching Frequency	108.7 -110.6 kHz
$C_{\rm P}$	Parallel resonant capacitor	2.35 µF
$L_{\rm s,total}$	Series inductor + Primary Leakage inductance of transformer	56 µH+79 µH (L_s+$L_{\rm lkp}$)
L_{Coil}	Induction coil inductor (From room temperature to 625°C)	1.11-0.95µH
$R_{\rm eq}$	Equivalent resistor (with workpiece) (From room temperature to 625°C)	100–110$m\Omega$
n=n_1/n_2	Transformation ratio	5
S_1, S_2, S_3, S_4	Switches	IRFP460
C_b	DC blocking capacitor	3.3 µF

Similarly, the conduction loss of each diode is computed by substituting (28) and (29) into (30).

VI. DESIGN PROCEDURE

In this section, a design example of the major components of the system in Fig. 1 is discussed.

A. Resonant Load

The targeted application is a 450-W induction-melting system for a 30-g aluminum workpiece. The desired frequency is at 110 kHz. The readily available induction-coil inductance ($L_{\rm coil}$) and equivalent resistance ($R_{\rm eq}$) are 1.11 μH and 100 mΩ, respectively. The power angle ϕ is set to 36°. Using (11), the maximum series inductance ($L_{s,\max}$) is obtained from (11) as

$$L_{s,\max} = \frac{L^2\omega_0}{R}\tan\phi - L = 5.1\ \mu\text{H}. \tag{31}$$

Next, the resonant capacitor is obtained from (2) as

$$C = \frac{L + L_{s,\max}}{L\cdot L_s\cdot\omega_o^2} = 2.29\ \mu\text{F}. \tag{32}$$

Five 30-kvar 400-V 100-$A_{\rm rms}$ 0.47-μF capacitors with a total capacitance of 2.35 μF are used as C_P. Since the available capacitance is slightly changed, the resonant frequency is recalculated to be

$$f_o = \frac{1}{2\pi}\sqrt{\frac{L + L_{s,\max}}{L\cdot L_s\cdot C}} = 108.2\ \text{kHz}. \tag{33}$$

From (14), the current gain is found as

$$\frac{L_{s,\max}}{L}\cos(\phi) = 4.1. \tag{34}$$

B. Matching Transformer

The current gain is found to be only 4.1, which is not sufficient to heat the workpiece to the desired temperature; therefore, a matching transformer is introduced. Taking into

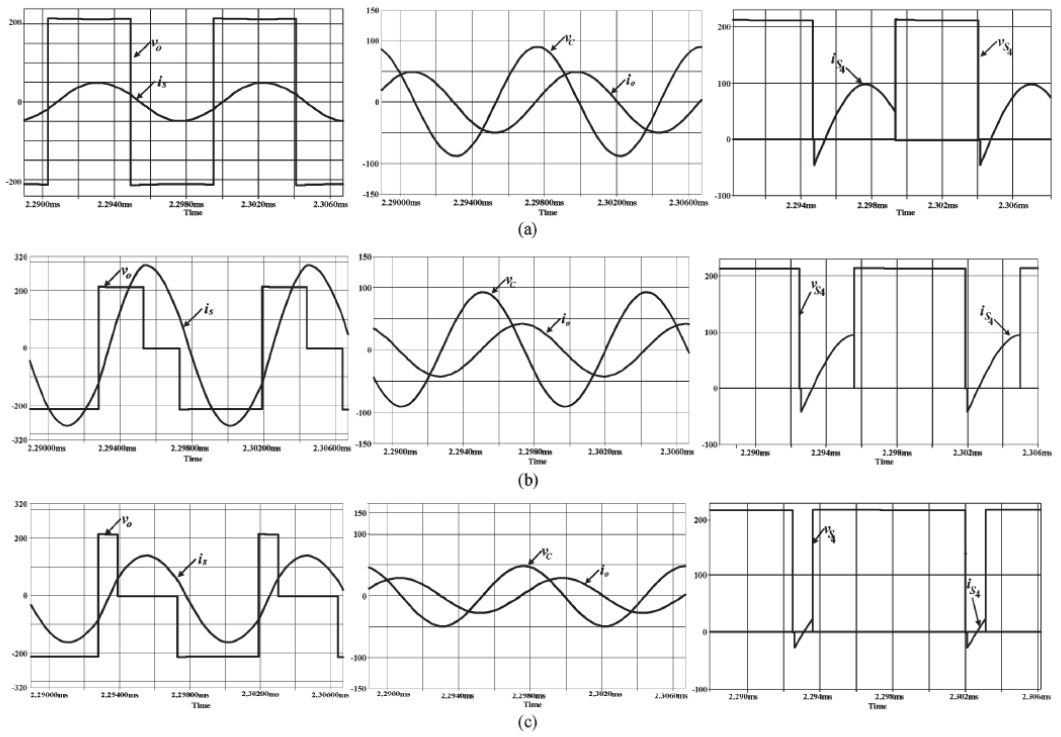

Fig. 9. Simulated results of the LLC full-bridge inverter with asymmetrical control. (a) v_o, i_s, v_C, i_o, v_{s4}, and i_{s4} waveforms with no PS at the full load. (i_s: 4 A/div, v_o: 50 V/div, i_o: 100 A/div, v_C: 50 V/div i_{s4}: 4 A/div, v_{s4}: 100 V/div, and time: 2 μs/div). (b) v_o, i_s, v_C, and i_o waveforms at 62.5% load. (i_s: 1.33 A/div, v_o: 100 V/div, i_o: 100 A/div, v_C: 50 V/div i_{s4}: 4 A/div, v_{s4}: 100 V/div, and time: 2 μs/div). (c) v_o, i_s, v_C, and i_o waveforms at 32% load. (i_s: 1.33 A/div, v_o: 100 V/div, i_o: 100 A/div, v_C: 50 V/div i_{s4}: 4 A/div, v_{s4}: 100 V/div, and time: 2 μs/div).

account only the fundamental component of the voltage, the primary current of the transformer is calculated using

$$I_{s,\mathrm{rms}} = \frac{\pi P}{2\sqrt{2}V_m \cos\phi} \tag{35}$$

which gives $I_{s,\mathrm{rms}} = 2.72$ A. From the calculated current gain, the maximum output current ($I_{o,\max}$) is 11.15 A. To utilize only 60% of the capacitor-rated current of 60 A, the required current ratio for the transformer is found from

$$I_{C_P,\max} = nI_{o,\max} \tag{36}$$

i.e., $n = 5.38 \approx 5$. The transformer used has a leakage reactance of 3.16 μH and must be taken into consideration. Therefore, a series inductance (L_s) of 2.24 μH is needed to combine with the transformer's leakage inductance to meet the required inductance of 5.4 μH. Note that placing L_s on the primary side can achieve benefits of inherent current-limitation protection of the transformer saturation. This means that the required series inductance on the transformer's primary is given as

$$L_s = 2.24n^2 = 56\ \mu\mathrm{H}. \tag{37}$$

VII. Simulation and Experimental Results

To confirm the validity of the proposed topology and control scheme, a computer simulation and a hardware experiment are performed using the parameters in Table I. The resonant frequency calculated using (2) is 107.866 kHz. The load is a 30-g aluminum workpiece in a graphite crucible. Due to load-parameter variation when the workpiece temperature increases from 30 °C to 625 °C, the switching frequency is varied from 108.7 to 110.6 kHz. Angle α is varied from 0° to 144° for the purpose of output-power control. With the circuit parameters in Table I, the simulation results under angle α at 0°, 90°, and 144° are shown in Fig. 9(a)–(c), respectively. As α increases, the inverter output current i_s, output voltage v_o, the induction-coil current i_o, and induction-coil voltage v_C decrease. The experimental results shown in Fig. 10 are obtained using the same set of parameters in Table I. The waveforms at full-load condition ($\alpha = 0°$) are shown in Fig. 10(a) where the inverter operates at 108.7 kHz. Once the workpiece temperature increases, the induction-coil impedance changes in a way that the resonant frequency increases. The phase-locked loop control then increases the switching frequency of the inverter to track for the resonant frequency. This is to ensure the ZVS operation. The shifted angle is then adjusted to 90° to reduce the output

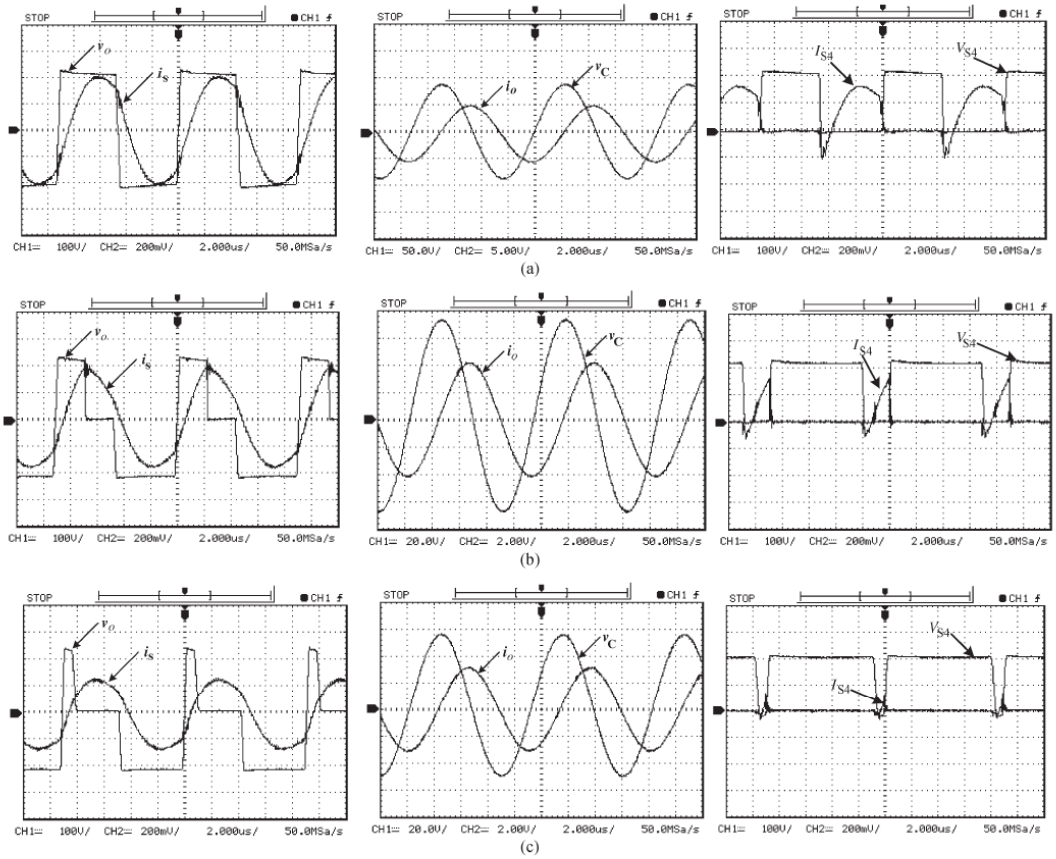

Fig. 10. Experimental results of the LLC full-bridge inverter with asymmetrical control. (a) v_o, i_s, v_C, i_o, v_{s4}, and i_{s4} waveforms with no PS at full load. (i_s: 2 A/div, v_o: 100 V/div, i_o: 100 A/div, v_C: 50 V/div, i_{s4}: 2.7 A/div, v_{s4}: 100 V/div, and time: 2 μs/div). (b) v_o, i_s, v_C, and i_o waveforms at 62.5% load. (i_s: 2 A/div, v_o: 100 V/div, i_o: 40 A/div, v_C: 20 V/div, i_{s4}: 2.7 A/div, v_{s4}: 100 V/div, and time: 2 μs/div). (c) v_o, i_s, v_C, and i_o waveforms at 32% load. (i_s: 2 A/div, v_o: 100 V/div, i_o: 40 A/div, v_C: 20 V/div, i_{s4}: 2.7 A/div, v_{s4}: 100 V/div, and time: 2 μs/div).

power to 62.5%, and the current and voltage waveforms are shown in Fig. 10(b) along with the switching $S4$ voltage and current waveforms. The switching frequency is increased to 109.17 kHz. In Fig. 10(c), the i_s, v_o, i_o, and v_C waveforms are obtained, while α is adjusted to the limit of 144°. At this point, the output power is reduced to 32.16%. The switching frequency is automatically increased to 110.6 kHz. It is seen that an increase of α results in an increase of the switching frequency. This provides an easy adjustment of the output power with fast response.

Note that, even if the gate signal is forced to turn on α at a value greater than 144°, the switch will still turn on at 144°. This is due to the fact that the average voltage across the total inductor seen by the inverter must be zero. Since the switching frequency is maintained slightly above the resonant frequency, the ZVS operation of the LLC full-bridge inverter with the proposed control scheme is guaranteed for the whole range of variable load parameters and variable output powers. Table II shows the losses of switches and diodes under different load levels from 32%–100%. At 100% of rated condition, switch S_4 carries the same loss at 3.45 W as with the other switches. However, when the output power is reduced, the switch S_4 conduction interval as well as the loss becomes less. The power angle ϕ is set at 36° to accommodate the induction coil and the aluminum-workpiece load, and the power is adjusted through angle α. Therefore, the lowest load level that can be achieved is at $\alpha = 144°$, giving the power level at 32% of rated condition. For comparison purposes, the calculated and experimental

TABLE II
LOSS ON COMPONENTS UNDER ASYMMETRICAL CONTROL

Output power (%)	Loss of switches (w)				LOSS OF DIOSES (W)			
	S_1	S_2	S_3	S_4	D_1	D_2	D_3	D_4
100	3.45	3.45	3.45	3.45	2.13	2.13	2.13	2.13
50	3.05	3.05	3.05	1.98	2.13	2.13	2.97	2.13
32	2.65	2.65	2.65	0.29	2.13	2.13	3.00	2.13

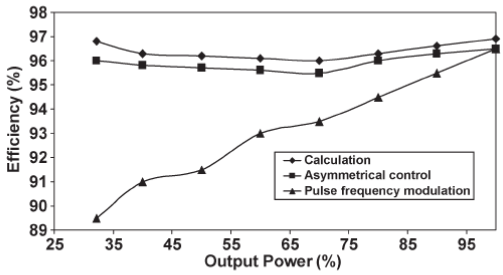

Fig. 11. Efficiency comparison between the calculation, asymmetrical control, and PFM.

efficiencies of the LLC full-bridge inverter with asymmetrical control are shown in Fig. 11 using the parameters given in Table I. The PFM control scheme with the same parameter setting is also shown.

The experimental results for both control schemes are collected while the workpiece is at 625 °C. During the heating process from 30 °C to 625 °C, the equivalent resistance varies from 100 to 110 mΩ, which results in variation of the induction-coil inductance from 0.95 to 1.11 μH. Thus, the operating frequency is changed in the range of 108.7–110.6 kHz to achieve ZVS operation. At rated power, the efficiency of the LLC full-bridge inverter is the same between the asymmetrical control and the PFM schemes. However, the proposed asymmetrical control has shown up to 6% higher efficiency at low-power operation. It is evident that the output power to the workpiece can be controlled by adjusting α.

VIII. Conclusion

In this paper, an improved full-bridge LLC resonant inverter topology for induction-heating application has been proposed. The validity of the proposed asymmetrical control scheme is verified through simulation and experimental results. It can be concluded that the presented work control technique has the following advantages.

1) The asymmetrical control can be used to control the output power to the induction coil for the LLC resonant tank.
2) The control scheme is in a simple configuration and easy to implement.
3) The resonant-frequency tracking together with the adjustment of the pulse voltage ensures maximum power transfer to the load throughout the heating cycle with minimal loss.
4) The placement of the inductor on the transformer's primary results in a small inductor due to the low current on the transformer's primary.

Therefore, the presented circuit configuration and proposed control scheme can also be used with other applications that require output-power regulation under load-parameter variation.

References

[1] M. Kamli, S. Yamamoto, and M. Abe, "A 50–150 kHz half-bridge inverter for induction heating application," *IEEE Trans. Ind. Electron.*, vol. 43, no. 1, pp. 163–172, Feb. 1996.
[2] S. Chudjuarjeen, C. Koompai, and V. Monyakul, "Full-bridge current-fed inverter with automatic frequency control for forging application," in *Proc. IEEE TENCON*, 2004, vol. 4, pp. 128–131.
[3] P. Viriya, S. Sittichok, and K. Matsuse, "Analysis of high-frequency induction cooker with variable frequency power control," in *Proc. PCC Osaka*, Apr. 2002, vol. 3, pp. 1502–1507.
[4] N.-J. Park, D.-Y. Lee, and D.-S. Hyun, "A power-control scheme with constant switching frequency in class-D inverter for induction-heating jar application," *IEEE Trans. Ind. Electron.*, vol. 54, no. 3, pp. 1252–1260, Jun. 2007.
[5] N. Ahmed, "High frequency soft switching AC conversion circuit with dual mode PWM/PDM control strategy for high power IH applications," *IEEE Trans. Ind. Electron.*, vol. 58, no. 4, pp. 1440–1448, Apr. 2011.
[6] L. Grajales and F. C. Lee, "Control system design and small-signal analysis of a phase-shift controlled series-resonant inverter for induction heating," in *Proc. IEEE Power Electron. Spec. Conf.*, 1995, pp. 450–456.
[7] J. Dudrik and N.-D. Trip, "Soft-switching PS-PWM DC–DC converter for full-load range applications," *IEEE Trans. Ind. Electron.*, vol. 57, no. 8, pp. 2807–2814, Aug. 2010.
[8] X. Ruan, W. Chen, L. Cheng, C. K. Tse, H. Yan, and T. Zhang, "Control strategy for input-series–output-parallel converters," *IEEE Trans. Ind. Electron.*, vol. 56, no. 4, pp. 1174–1185, Apr. 2009.
[9] P. Imbertson and N. Mohan, "New directions in dc-dc power conversion based on idealized concepts leading ultimately to the asymmetrical duty-cycle power converter," *IEEE Trans. Circuits Syst. I, Fundam. Theory Appl.*, vol. 44, no. 8, pp. 722–727, Aug. 1997.
[10] D. J. Tschirhart and P. K. Jain, "A CLL resonant asymmetrical pulse width modulated converter with improved efficiency," *IEEE Trans. Ind. Electron.*, vol. 55, no. 1, pp. 114–122, Jan. 2008.
[11] T. Mishima and M. Nakaoka, "A novel high-frequency transformer-linked soft-switching half-bridge dc–dc converter with constant-frequency asymmetrical PWM scheme," *IEEE Trans. Ind. Electron.*, vol. 56, no. 8, pp. 2961–2969, Aug. 2009.
[12] M. S. Agamy and P. K. Jain, "A three-level resonant single-stage power factor correction converter: Analysis, design, and implementation," *IEEE Trans. Ind. Electron.*, vol. 56, no. 6, pp. 2095–2107, Jun. 2009.
[13] J. M. Burdío, L. A. Barragán, F. Monterde, D. Navarro, and J. Acero, "Asymmetrical voltage-cancellation control for full-bridge series resonant inverters," *IEEE Trans. Power Electron.*, vol. 19, no. 2, pp. 461–469, Mar. 2004.
[14] J. I. Artigas, I. Urriza, J. Acero, L. A. Barragán, D. Navarro, and J. M. Burdío, "Power measurement by output-current integration in series resonant inverters," *IEEE Trans. Ind. Electron.*, vol. 56, no. 2, pp. 559–567, Feb. 2009.
[15] S. Chudjuarjeen and C. Koompai, "Asymmetrical control with phase lock loop for induction cooking appliances," in *Proc. ECTI-CON*, 2008, pp. 1013–1016.
[16] P. Viriya, N. Yongyuth, and K. Matsuse, "Analysis of two continuous control regions of conventional phase shift and transition phase shift for induction heating inverter under ZVS and non-ZVS," *IEEE Trans. Power Electron.*, vol. 23, no. 6, pp. 2794–2804, Nov. 2008.
[17] S.-S. Lee and G.-W. Moon, "Full ZVS-range transient current buildup half-bridge converter with different ZVS operations to load variation," *IEEE Trans. Ind. Electron.*, vol. 55, no. 6, pp. 2557–2559, Jun. 2008.
[18] O. Lucía, J. M. Burdio, I. Millán, J. Acero, and D. Puyal, "Load-adaptive algorithm of half-bridge series resonant inverter for domestic induction heating," *IEEE Trans. Ind. Electron.*, vol. 56, no. 8, pp. 3106–3116, Aug. 2009.
[19] J. L. Russi, M. L. S. Martins, and H. L. Hey, "Coupled-filter-inductor soft-switching techniques: Principles and topologies," *IEEE Trans. Ind. Electron.*, vol. 55, no. 9, pp. 3361–3373, Sep. 2008.
[20] Z. Zhang, W. Eberle, Y.-F. Liu, and P. C. Sen, "A nonisolated ZVS asymmetrical buck voltage regulator module with direct energy transfer," *IEEE Trans. Ind. Electron.*, vol. 56, no. 8, pp. 3096–3105, Aug. 2009.
[21] C. S. Moo, K. H. Lee, H. L. Cheng, and W. M. Chen, "A single-stage high-power-factor electronic ballast with ZVS buck–boost conversion," *IEEE Trans. Ind. Electron.*, vol. 56, no. 4, pp. 1136–1146, Apr. 2009.
[22] S.-H. Park, G.-R. Cha, Y.-C. Jung, and C.-Y. Won, "Design and application for PV generation system using a soft-switching boost converter with SARC," *IEEE Trans. Ind. Electron.*, vol. 57, no. 2, pp. 515–522, Feb. 2010.

[23] Z. N. Low, J. J. Casanova, P. H. Maier, J. A. Taylor, R. A. Chinga, and J. Lin, "Method of load/fault detection for loosely coupled planar wireless power transfer system with power delivery tracking," *IEEE Trans. Ind. Electron.*, vol. 57, no. 4, pp. 1478–1486, Apr. 2010.
[24] J. M. Espí Huerta, E. J. Dede García Santamaría, R. García Gil, and J. Castelló Moreno, "Design of the L-LC resonant inverter for induction heating based on its equivalent SRI," *IEEE Trans. Ind. Electron.*, vol. 54, no. 6, pp. 3178–3187, Dec. 2007.
[25] J. Espí, A. Navarro, J. Maicas, J. Ejea, and S. Casans, "Control circuit design of the L-LC resonant inverter for induction heating," in *Proc. IEEE Power Electron. Spec. Conf.*, Charleston, SC, Jun. 1999, pp. 1126–1131.
[26] S. Chudjuarjeen, A. Sangswang, and C. Koompai, "LLC resonant inverter for induction heating with asymmetrical voltage-cancellation control," in *Proc. IEEE Int. Symp. Circuits Syst.*, Taipei, Taiwan, May 2009, pp. 2874–2877.
[27] O. Lucía, L. A. Barragán, J. M. Burdío, O. Jiménez, D. Navarro, and I. Urriza, "A versatile power electronics test-bench architecture applied to domestic induction heating," *IEEE Trans. Ind. Electron.*, vol. 58, no. 3, pp. 998–1007, Mar. 2011.
[28] F. Forest, S. Faucher, J.-Y. Gaspard, D. Montloup, J.-J. Huselstein, and C. Joubert, "Frequency-synchronized resonant converters for the supply of multiwindings coils in induction cooking appliances," *IEEE Trans. Ind. Electron.*, vol. 54, no. 1, pp. 441–452, Feb. 2007.
[29] M. Enokizono and H. Tanabe, "Numerical analysis of high-frequency induction heating including temperature dependence of material characteristics," *IEEE Trans. Magn.*, vol. 31, no. 4, pp. 2438–2444, Jul. 1995.
[30] J. Andreu, J. M. De Diego, I. M. de Alegria, I. Kortabarria, J. L. Martin, and S. Ceballos, "New protection circuit for high-speed switching and start-up of a practical matrix converter," *IEEE Trans. Ind. Electron.*, vol. 55, no. 8, pp. 3100–3114, Aug. 2008.
[31] M. K. Kazimierczuk and D. Czarkowski, *Resonant Power Converters*. New York: Wiley, 1995.
[32] O. Lucía, J. M. Burdío, I. Millán, J. Acero, and L. A. Barragán, "Efficiency oriented design of ZVS half-bridge series resonant inverter with variable frequency duty cycle control," *IEEE Trans. Power Electron.*, vol. 25, no. 7, pp. 1671–1674, Jul. 2010.

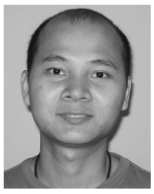

Saichol Chudjuarjeen (S'09) was born in Prachinburi, Thailand. He received the B.Eng. degree from the Mahanakorn University of Technology, Bangkok, Thailand, in 2000, and the M.Eng. degree from the King Mongkut's University of Technology Thonburi, Bangkok, in 2004, where he is currently working toward the Ph.D. degree in electrical and computer engineering.

He is an Instructor with the Department of Electrical Engineering, Rajamangala University of Technology Krungthep, Bangkok. His current research interests include high-frequency resonant inverter for induction heating, current-source and voltage-source inverters, and control of power-electronic systems.

Mr. Chudjuarjeen was the recipient of the Industrial Electronics Society Scholarship Award in the IEEE International Symposium on Industrial Electronics (ISIE 2009) in Seoul (Korea).

Anawach Sangswang (S'98–M'04) was born in Bangkok, Thailand. He received the B.Eng. degree from the King Mongkut's University of Technology Thonburi (KMUTT), Bangkok, in 1995 and the M.S. and Ph.D. degrees from Drexel University, Philadelphia, PA, in 1999 and 2003, respectively.

He is currently an Assistant Professor with the Department of Electrical Engineering, KMUTT. His research interests include stochastic modeling, digital control of power-electronic converters, and power-system stability.

Chayant Koompai was born in Surat Thani, Thailand, in 1949. He received the B.Eng. degree from the King Mongkut's University of Technology Thonburi (KMUTT), Bangkok, Thailand, in 1973.

He is currently an Assistant Professor with the Department of Electrical Engineering, KMUTT. He has more than 30 years of experience working in the field of induction heating. His research interests include circuit analysis and induction-heating systems.

2 S. Chudjuarjeen, A. Sangswang and C. Koompai, 2009 "An improved LLC resonant inverter for induction heating with asymmetrical control," IEEE **International Symposium on Industrial Electronics (ISIE2009)**, Korea, Seoul, July, pp. 1612-1617.

LLC Resonant Inverter for Induction Heating with Asymmetrical Voltage-Cancellation Control

Saichol Chudjuarjeen, Anawach Sangswang, and Chayant Koompai
Department of Electrical Engineering, Faculty of Engineering
King Mongkut's University of Technology Thonburi
Bangkok, Thailand
E-mail : c_somchai2@hotmail.com, anawach.san@kmutt.ac.th

Abstract— **This paper proposes a high efficiency LLC resonant inverter for induction heating applications by using asymmetrical voltage cancellation control. The proposed control method is implemented in a full-bridge topology for induction heating application. The operating frequency is automatically adjusted to maintain a small constant lagging phase angle under load parameter variation. The output power is controlled using the asymmetrical voltage cancellation technique. The LLC resonant tank is designed without the use of output transformer. This results in an increase of the net efficiency of the induction heating system. The validity of the proposed method is verified through computer simulation and hardware experiment at the operating frequency of 93 to 96 kHz.**

I. INTRODUCTION

Induction heating is a well-known technique to produce very high temperature for applications such as in steel melting, brazing, and surface hardening. In each application, appropriate frequency must be used depending on the work-piece geometry and skin-depth requirement [1, 2]. This technique requires high frequency current supply that is capable of inducing high frequency eddy current in the work piece and thus results in the heating effect [1]. A large number of topologies have been developed in this area. Among them, current-fed and voltage-fed inverters are most commonly used [3]. One of the important advantages of current-fed inverter is the short-circuit protection capability. However, the current source inverter can only be controlled by using phase-controlled rectifier for adjusting the dc link. This differs from voltage source inverter which has various controls.

Recent developments in switching schemes and control methods have made the voltage-source resonant inverters widely used in several applications that require output power control. In pulse-frequency modulation (PFM), the output power can be controlled by varying the switching frequency and it is operated under zero-voltage switching scheme [4]. The pulse-density modulation (PDM) scheme regulates the output power by varying the period in which the inverter supplies high-frequency current to the induction coil [5]. The phase-shift (PS) control technique in [6] varies output power by shifting the phase of the switch conduction sequences while the asymmetrical duty-cycle (ADC) control technique employs an unequal duty-cycle operation of the switches in the converter [7]. The asymmetrical voltage-cancellation (AVC) is proposed in [8] where the authors describe voltage-cancellation for conventional fixed-frequency control strategies. In induction heating application, the output power control using the mentioned techniques in fix frequency and optimum duty cycle for ZVS operation are rather difficult due to variation of parameters in the resonance load. In [9], the AVC is implemented in a full-bridge series resonant inverter. The series-resonant inverter needs an output transformer for matching the output power to the load. Since the transformer's secondary winding must carry high current and additional real power loss is introduced, therefore the system overall efficiency is reduced. The transformer is later omitted in the series and parallel resonant inverter, also known as LLC resonant inverter, proposed in [10] which results in better efficiency with reduced weight and size of the power supply.

In this paper, the LLC resonant inverter with AVC control technique is proposed. The aim is to control the output power for high temperature application including steel melting, brazing and hardening where the load parameters and resonant frequency vary throughout the system operation. The operating frequency is controlled using a phase-locked loop to track for the resonant frequency. The output power is controlled by adjusting the switch duty cycle in the event of load parameter changes. This paper is organized as follows. The principle of operation is described in section II. Simulation and experimental results are provided in section III. Section IV concludes this work.

II. PRINCIPLE OF OPERATION

A. Circuit description

Fig. 1 shows the LLC resonant inverter configuration for induction heating application. The inverter consists of four switches with antiparallel diodes, a resonant capacitor, a matching inductor (L_g) and an induction coil that comprises

The authors would like to thank the Ministry of Science and Technology for the financial support of this work.

978-1-4244-3828-0/09/$25.00 ©2009 IEEE

of a series combination of resistance (R) and inductance (L). An equivalent circuit of the full-bridge LLC inverter system in Fig. 1 is shown in Fig. 2 where the input voltage is viewed as an asymmetrical ac voltage supplied to the system.

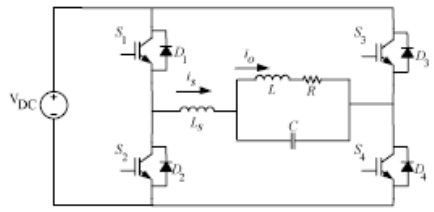

Fig. 1. Full-bridge series and parallel resonant inverter.

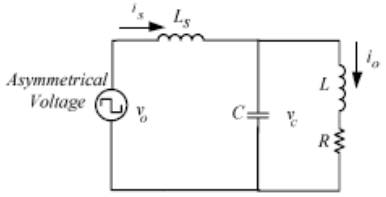

Fig. 2. Equivalent circuit.

B. *Modes of Operation*

As shown in Fig. 3, five modes of operation exist within one switching cycle. The corresponding circuit topology for each mode of operation is illustrated in Fig. 4. The analysis is as follows.

1) Mode 1 (t_0–t_1): While switches S_2 and S_3 are off, at $t = t_0$, switches S_1 and S_4 receive positive gating signals. The negative input current (i_s) flows through diodes D_1 and D_4.

2) Mode 2 (t_1–t_2): At $t = t_1$, as soon as the antiparallel diodes D_1 and D_4 are turned off, switches S_1 and S_4 are conducted and ZVS operation is achieved. During this mode, the positive input current (i_s) flows.

3) Mode 3 (t_2–t_3): At $t = t_2$, the switches S_1 and S_4 are turned off, similar to that in Mode 1, and the antiparallel diode D_2 and D_3 conduct by the positive input current (i_s).

4) Mode 4 (t_3–t_4): At $t = t_3$, when the antiparallel diode D_2 and D_3 are turned off, the switches S_2 and S_3 conduct and the ZVS condition is achieved. During this mode, the negative input current (i_s) flows.

5) Mode 5 (t_4–t_5): At $t = t_4$, When the switch S_3 conducts, the switch S_2 is turned off and the antiparallel diode D_1 of S_1 conducts. During this mode, the ZVS condition of S_2 is obtained.

Therefore, the one-cycle operation of the full-bridge inverter is completed operating cycle continues to repeat from modes 1 to 5.

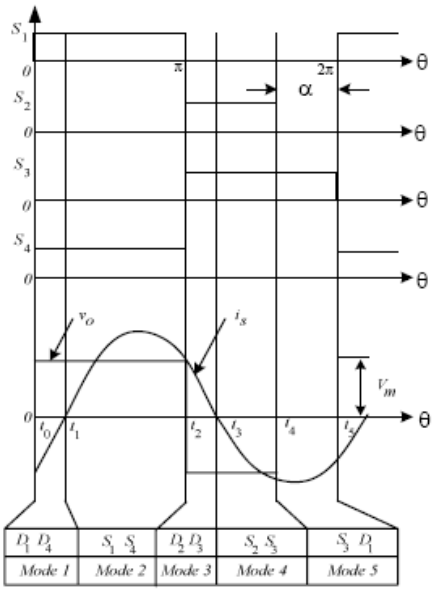

Fig.3. Typical voltage, current and gate signals

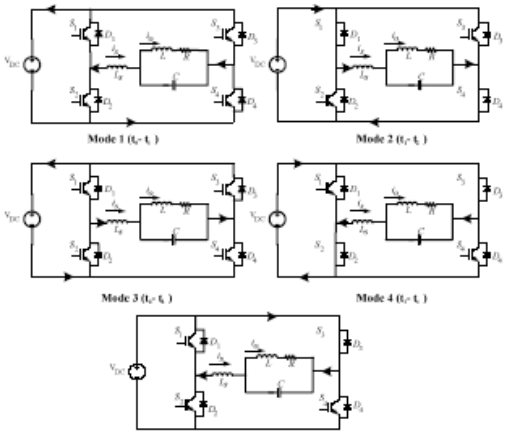

Fig. 4. Operation modes of the Inverter

C. *Analysis of the output power*

From Figs. 2 and 3, the relationship between the load voltage (i.e. the capacitor voltage: v_c) and the inverter output voltage (v_o) can be calculated as,

$$\frac{v_c}{v_o} = \frac{R + j\omega L}{((j\omega L_s \times j\omega C)(R + j\omega L) + j\omega L_s + R + j\omega L)} \quad (1)$$

The inverter is designed to operate such that the switching frequency (ω) is higher than the resonant frequency (ω_0) for maximum output power. The resonant frequency of the system in Fig. 2 is given as,

$$\omega_o = \sqrt{\frac{L + L_s}{L \cdot L_s \cdot C}} \quad (2)$$

To take only the fundamental component (v_1) of the inverter output voltage in Fig. 2 into account, the load voltage is given as,

$$v_C = \left(-\frac{L}{L_s} - j\frac{L^2}{RL_s}\sqrt{\frac{L + L_s}{L \cdot L_s \cdot C}} \right) \cdot v_1 \quad (3)$$

The fundamental voltage v_1 can be represented by the following Fourier series.

$$\left.\begin{aligned} b_n &= \frac{V_m}{n\pi}\left[2 - (-1)^n - \cos n(180 - \alpha)\right] \\ a_n &= \frac{V_m}{n\pi}\left[-\sin n(180 - \alpha)\right] \end{aligned}\right\} \quad (4)$$

where α is the shifted angle of the switch S_2, as shown in Fig. 3 The amplitude of the fundamental voltage v_1 is given by

$$\hat{V}_1 = \frac{V_m}{\pi} \times \sqrt{\sin^2(180 - \alpha) + (3 - \cos(180 - \alpha))^2} \quad (5)$$

and the average output power P can be obtained as

$$P = v_o^2 \,\mathrm{Re}\left\{Z_{coil}(j\omega_0)^{-1}\right\} \quad (6)$$

That is,

$$P = \frac{V_m^2}{2R\pi^2} \times (\sin^2(180 - \alpha) + (3 - \cos(180 - \alpha))^2) \times \left(\frac{L}{L_S}\right)^2 \quad (7)$$

Since the output power depends on the shifted angle (α), therefore the output power can be controlled through the adjustment of α .

III. Results

A. Simulation results

Computer simulation is performed on a full-bridge LLC resonant inverter circuit shown in Fig. 1 with asymmetrical voltage-cancellation control technique. The following parameters are used $V_{dc} = 140V, L = 4.2\mu H, R = 0.074\Omega$ and $L_S = 25.5\mu H$. The inverter operates at 91 kHz. It is noted that the inductor L_S is wound on an air core to avoid saturation. The current and voltage waveforms of the system in Fig. 1 with the shifted angle (α) is set to zero are shown in Fig. 5. Next, α is adjusted to 70° to control the output power to the load and the voltage and current waveforms are shown in Fig.6. It is seen that the peak value of i_o is reduced from 50A to 39A.

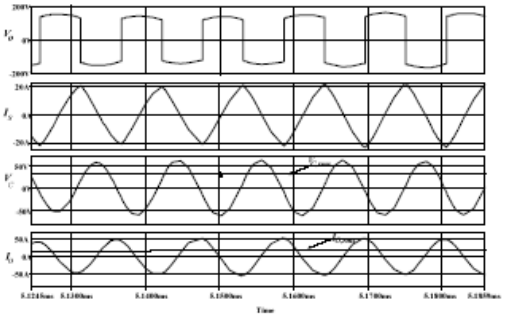

Fig. 5. Voltage and current waverforms at 100 % duty cycle

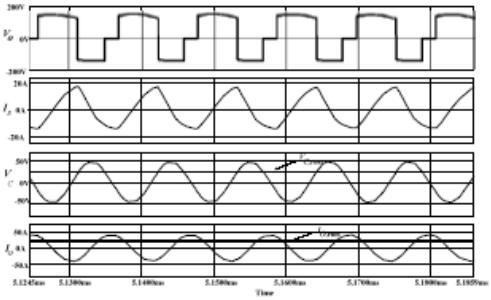

Fig. 6. Simulation results with $\alpha = 70°$

B. Experimental Results

To verify the proposed method, a hardware setup is prepared with the same set of parameters as provided in the simulation study. The load is a 30-grams aluminum workpiece in a graphite crucible. The IRFP460 MOSFETs are used as switching devices. The switching frequency varies from 93 kHz to 96 kHz under load parameter variation. Fig. 7 shows the measured v_o and i_o waveforms when the inverter operates at 93.45 kHz with no phase shift. This operating condition is considered as the full-load condition. The input power to the inverter is at 340W. The induction coil voltage and current waveforms are shown in Fig. 8. The load power is at 326 W which provides the efficiency of 94.5%. Once the work piece temperature increases, the induction coil impedance changes in a way that the resonant frequency increases. The phase-locked loop control then increases the switching frequency to track the resonant frequency. It is

noted that the operating frequency is maintained at a little higher than the resonant frequency. This is to ensure the zero voltage switching (ZVS) operation.

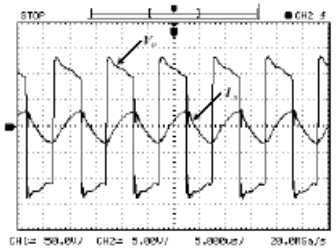

Fig. 7. v_o and i_s waveforms at 93.45 kHz (i_s: 50 A/div, v_o: 50 V/div and Time: 5 μs / div.)

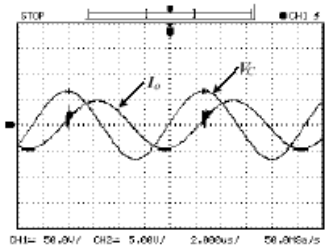

Fig. 8. v_C and i_o waveforms at 93.45 kHz (i_o: 20 A/div, v_C: 50 V/div and Time: 2 μs / div.)

The stray inductance in the dc bus wiring may have caused oscillation (ringing) in the output voltage. In addition, the shifted angle is adjusted to 70° in order to control the output power to the load. The v_o and i_S waveforms are shown in Fig. 9 where the input power to the inverter is at 280W and the switching frequency is automatically increased to 95.7 kHz. Fig. 10 shows the induction coil voltage and current waveforms. The output power is reduced to 263W with the efficiency of 93.46%.

IV. Conclusions

This work proposes the full-bridge LLC resonant inverter for induction heating application. The phase-locked loop allows resonant frequency tracking under load parameter variation. The analytical expression of the output power as a function of the shifted phase angle is given in this work. Based on the derived expression, the asymmetrical voltage cancellation can be used to control output power to the induction coil. Simulation and experimental studies are performed to verify the proposed control method. The resonant frequency tracking and the adjustment of pulse voltage together ensure the maximum power transfer to the load throughout the heating cycle with minimal loss.

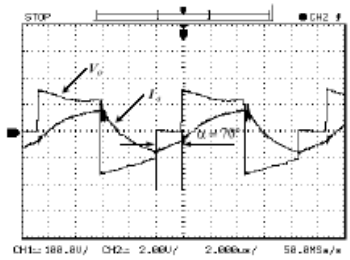

Fig. 9 v_o and i_s waveforms at 95.7 kHz with $\alpha = 70°$ (i_s: 20 A/div, v_o: 100 V/div and Time: 2 μs / div.)

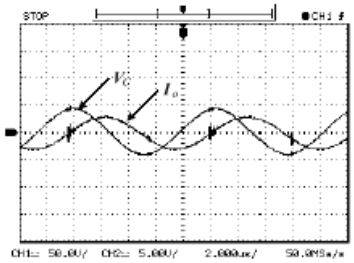

Fig. 10. v_C and i_S waveforms at 95.7 kHz with $\alpha = 70°$. (I_S: 20 A/div, V_o: 50 V/div and Time: 2 μs / div.)

References

1. M. Kamli, S. Yamamoto, and M. Abe, "A 50-150 kHz Half- Bridge Inverter for induction heating Application," IEEE Trans. Industrial Electronics, Vol. 43, February 1996. pp. 163-172
2. E. J. Davies , J. and Simpson, P., 1979, Induction Heating Handbook. , McGraw-Hill, UK ,
3. Chudjuarjeen, S., Koompai, C.and Monyakul, "Full-bridge current-fed inverter with automatic frequency control for forging application", IEEE Tencon 2004, Vol. 4, pp.128-131, Nov. 2004
4. Viriya, P.; Sittichok, S.; Matsuse, K.; "Analysis of High-Frequency Induction Cooker with Variable Frequency Power Control," Power Conversion Conference, 2002 .PCC Osaka 2002 .Proceedings of the Volume 3, 5-2 April 2002Page(s): 1507 - 1502vol.. 3
5. Nam-Ju Park, Dong-Yun Lee, and Dong-Seok Hyun,"A Power-Control Scheme With Constant Switching Frequency in Class-D Inverter for Induction-Heating Jar Application", IEEE Trans. Industrial Electronics, vol. 54, no. 3, Jun. 2007
6. L. Grajales and F. C. Lee "Control system design and small-signal analysis of a phase-shiftcontrolled series-resonant inverter for induction heating," in Proc. IEEE Power Electron. Spec. Conf. (PESC), 1995, pp. 450–.456
7. P. Imbertson and N. Mohan, "New directions in dc-dc power conversionbased on idealized concepts leading ultimately to the asymmetrical duty-cycle power converter," IEEE Trans. Circuits Syst. I, vol. 44, pp. 722–727, Aug. 1997.
8. J. M. Burdío, L. A. Barragán, F. Monterde, D. Navarro, and J. Acero, "Asymmetrical voltage-cancellation control for full-bridge series resonant inverters," IEEE Trans. Power Electron., vol. 19, no. 2, pp. 461–469, Mar. 2004.
9. Chudjuarjeen, S. and Koompai, C., 2008, "Asymmetrical control with Phase Lock Loop for Induction Cooking Appliances", ECTI-CONFERENCE 2008 pp. 1013-1016
10. José M. Espí Huerta, Enrique J. Dede García Santamaría,Rafael García Gil, and Jaime Castelló Moreno, " Design of the L-LC Resonant Inverter for Induction Heating Based on Its Equivalent SRI ," IEEE Trans. Industrial Electronics, vol. 54, no.6, Dec.2007.

3 S. Chudjuarjeen, A. Sangswang and C. Koompai, 2009 “LLC Resonant Inverter for Induction Heating with Asymmetrical Voltage-Cancellation Control,” **IEEE International Symposium on Circuits and Systems,** Taipei, Taiwan, May, pp. 2874-2877.

IEEE International Symposium on Industrial Electronics (ISIE 2009)
Seoul Olympic Parktel, Seoul, Korea July 5-8, 2009

An Improved LLC Resonant Inverter for Induction Heating with Asymmetrical Control

Saichol Chudjuarjeen, Anawach Sangswang, and Chayant Koompai
Department of Electrical Engineering, Faculty of Engineering
King Mongkut's University of Technology Thonburi
Bangkok, Thailand
E-mail : c_somchai2@hotmail.com, anawach.san@kmutt.ac.th

***Abstract*-This paper proposes a modified LLC resonant load configuration of a full-bridge inverter for induction heating applications by using asymmetrical voltage cancellation control. The proposed control method is implemented in a full-bridge inverter topology. With the use of a phase-locked loop control, the operating frequency is automatically adjusted to maintain a small constant lagging phase angle under load parameter variation. The output power is controlled using the asymmetrical voltage cancellation technique. The LLC resonant tank is designed with a matching transformer in between the series inductor and paralleled LC resonant tank for short circuit protection capability of the matching transformer and the induction coil. The validity of the proposed method is verified through computer simulation and hardware experiment at the operating frequency of 108.7 to 110.6 kHz.**

I. INTRODUCTION

Induction heating is a well-known technique to produce very high temperature for applications like steel melting, brazing and surface hardening. In each application, appropriate frequency must be used depending on the work-piece geometry and skin-depth requirement [1, 2]. This technique requires high frequency current supply that is capable of inducing high frequency eddy current in the work piece and thus results in the heating effect [1]. A large number of topologies have been developed in this area. Current-fed and voltage-fed inverters are among the most commonly used types [3]. One of the important advantages of current-fed inverter is the short-circuit protection capability. However, the current source inverter can only be controlled by using phase-controlled rectifier for adjusting the voltage at the dc link. This differs from voltage source inverter which has various controls.

Recent developments in switching schemes and control methods have made the voltage-source resonant inverters widely used in applications that require output power control. In pulse-frequency modulation (PFM), the output power can be controlled by varying the switching frequency while the inverter operates under zero-voltage switching scheme [4]. The pulse-density modulation (PDM) method regulates the output power by varying the period in which the inverter supplies high-frequency current to the induction coil [5]. The phase-shift (PS) control technique in [6] varies output power by shifting the phase of the switch conduction sequences. Asymmetrical duty-cycle (ADC) control technique employs an unequal duty-cycle operation of the switches in the converter [7]. The asymmetrical voltage-cancellation (AVC) is proposed in [8] where the authors describe voltage-cancellation for conventional fixed-frequency control strategies. In induction heating application, the output power control using the mentioned techniques in fix frequency and optimum duty cycle for ZVS operation are rather difficult due to variation of parameters in the resonant load. In [9], the AVC is implemented in a full-bridge series resonant inverter. The series-resonant inverter needs an output transformer for matching the output power to the load.

In this paper, an improved LLC resonant inverter with AVC control technique is proposed. The aim is to control the output power for high temperature application including steel melting, brazing and hardening where the load parameters and resonant frequency vary throughout the system operation. The operating frequency is controlled using phase-locked loop to track for the resonant frequency. The output power is controlled by adjusting the switch duty cycle in the event of load parameter variation. The LLC resonant tank is designed with the matching transformer in between the series inductor and paralleled LC tank. The important advantage of the proposed topology is the short circuit protection of the transformer and induction coil. This paper is organized as follows. The principle of operation is described in section II. Section III proposed the asymmetrical control strategy. Simulation and experimental results are provided in section IV. Section V concludes this work.

II. PRINCIPLE OF OPERATION

A. Circuit description

Fig. 1 shows an LLC resonant inverter configuration for induction heating applications. The inverter consists of four switches with antiparallel diodes, a resonant capacitor, a series inductor (L_s) and an induction coil that comprises of a series combination of resistor (R_{eq}) and induction coil inductor (L_{coil}). A DC blocking capacitor (C_b) is inserted in series with the transformer primary. An equivalent circuit of the full-bridge LLC inverter system in Fig. 1 is shown in Fig. 2 where the input voltage is viewed as an asymmetrical ac voltage supplied to the system. Note that C, with a negliglble value of C_b, L and R represents the R_{eq}, L_{coil} and C_p refered to the primary of the transformer, respectively. The total impedance to the

978-1-4244-4349-9/09/$25.00 ©2009 IEEE

asymmetrical voltage source (v_o) is denoted by Z_{total}. i_s and i_o are the input current and load current, respectively.

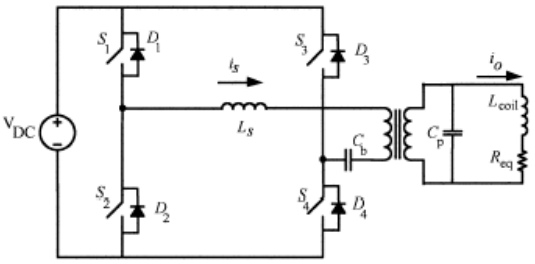

Fig. 1. Full-bridge series and parallel resonant inverter.

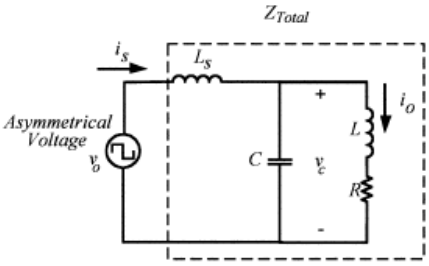

Fig. 2. Equivalent circuit.

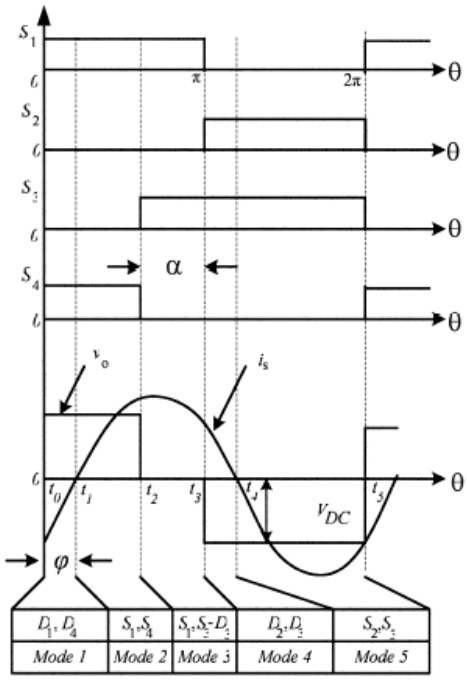

Fig.3. Typical voltage, current and gate signals

B. Modes of Operation

As shown in Fig. 3, five modes of operation exist within one switching cycle. The corresponding circuit topology for each mode of operation is illustrated in Fig. 4. The analysis is as follows.

1) Mode 1 (t_0-t_1): While switches S_2 and S_3 are off, at $t = t_0$, switches S_1 and S_4 receive positive gating signals. The negative input current (i_s) flows through diodes D_1 and D_4.
2) Mode 2 (t_1-t_2): At $t = t_1$, as soon as the antiparallel diodes D_1 and D_4 are off, switches S_1 and S_4 conduct and ZVS operation is achieved. During this mode, the positive input current (i_s) flows.
3) Mode 3 (t_2-t_3): At $t = t_2$, While the switch S_1 still conducts, the switch S_4 is turned off and the antiparallel diode D_3 conducts. At the same instance, the switch S_3 is turned on for the purpose of conduction loss reduction in the diode D_3.
4) Mode 4 (t_3-t_4): At $t = t_3$, the switch S_1 is turned off. Similar to that in Mode 1, and the diode D_2 starts conducting positive together with the diode D_3.
5) Mode 5 (t_4-t_5): At $t = t_4$, when the antiparallel diodes D_2 and D_3 are off, the switches S_2 and S_3 conduct and the ZVS condition is achieved. During this mode, the input current i_s becomes negative. Therefore, the one-cycle operation of the full-bridge inverter is completed. The next operating cycle continues to repeat from modes 1 to 5.

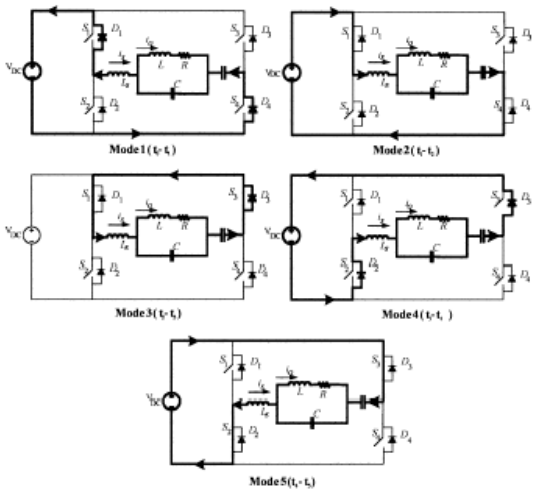

Fig. 4. Operation modes of the Inverter

C. Analysis of the output power

From Figs. 2 and 3, the relationship between the load voltage (i.e. the capacitor voltage: v_c) and the inverter output voltage (v_o) is given as,

$$\frac{v_c}{v_o} = \frac{R + j\omega L}{(j\omega L_s \times j\omega C)(R + j\omega L) + j\omega L_s + R + j\omega L} \quad (1)$$

Where $L = n^2 \cdot L_{coil}$, $R = n^2 \cdot R_{eq}$ and $C = \frac{C_p}{n^2}$ Given that n is the transformation ratio. The inverter is designed to operate such that the switching frequency (ω) is higher than the resonant frequency (ω_0) for maximum output power. The resonant frequency of the system in Fig. 2 is given as,

$$\omega_o = \sqrt{\frac{L + L_s}{L \cdot L_s \cdot C}} \quad (2)$$

To take only the fundamental component (v_1) of the inverter output voltage in Fig. 2 into account, the load voltage is given as,

$$v_C = \left(-\frac{L}{L_s} - j\frac{L^2}{RL_s}\sqrt{\frac{L+L_s}{L \cdot L_s \cdot C}} \right) \cdot v_1 \quad (3)$$

The fundamental voltage v_1 of the output voltage in (3) can be represented by the following coefficients of Fourier series.

$$\left.\begin{aligned} b_n &= \frac{V_m}{n\pi}\left[2 - (-1)^n - \cos n(180 - \alpha)\right] \\ a_n &= \frac{V_m}{n\pi}\left[-\sin n(180 - \alpha)\right] \end{aligned}\right\} \quad (4)$$

where α is the shifted angle of the switch S_4, as shown in Fig. 3 The amplitude of the fundamental voltage v_1 is given by

$$\hat{V}_1 = \frac{V_m}{\pi} \times \sqrt{\sin^2(180 - \alpha) + (3 - \cos(180 - \alpha))^2} \quad (5)$$

and the average output power P can be obtained as[10]

$$P = v_1^2 \, \mathrm{Re}\left\{ Z_{total}(j\omega_0)^{-1} \right\} \quad (6)$$

and which is expanded to

$$P = \frac{V_m^2}{2R\pi^2} \times (\sin^2(180 - \alpha) + (3 - \cos(180 - \alpha))^2) \times \left(\frac{L}{L_s}\right)^2 \quad (7)$$

The output power (P) in (7) depends on the shifted angle (α). Therefore the output power can be controlled through an adjustment of α .

D. Design of L_s

The total impedance (Z_{total}) in Fig.2 can be expressed as,

$$Z_{Total}(j\omega) = \frac{R - \omega^2 CL_s R + j\omega L_s + j\omega L - j\omega^3 L_s L}{-\omega^2 CL + j\omega CR} \quad (8)$$

At resonant frequency (ω_0)

$$Z_{Total}(j\omega_0) = \frac{\omega_0 L_s^2 R(L\omega_0 + jR(L_s + L_s))}{-L\omega_0 - R^2(L_s^2 + L_s L + L^2)} \quad (9)$$

The switching angle (φ) is given as

$$\varphi = arg\left\{ Z_{Total}(j\omega_0) \right\} = arctan\left(\frac{R(L_s + L)}{L^2 \omega_0} \right) \rangle\, 0 \quad (10)$$

Resulting in

$$\frac{L_s}{L} = \frac{L\omega_0}{R} tan\varphi - 1 \quad (11)$$

The current gain is found as,

$$\frac{i_o}{i_r} = \frac{j\omega L_s}{Z_{Total}(j\omega)} \quad (12)$$

With a substitution of $Z_{Total}(j\omega)$ in eq.(12), the current gain at resonant frequency (ω_0)

$$\left| \frac{i_o}{i_r}(j\omega_0) \right| = \frac{L_s}{L} \frac{L^2 \omega_0}{\sqrt{L^4 \omega_0^2 + R^2(L_s^2 - L_s L + L^2)}} \quad (13)$$

Therefore, the coil current at resonant frequency (ω_0) can be expressed as:

$$i_o = \frac{L_s}{L} i_s cos\varphi \quad (14)$$

In resonance, there is always a positive switching angle φ (i.e. lagging current operation). A high efficiency inverter with LLC topology can be achieved by small positive switching angle and high current gain designs. From (9) and (12), it is deduced that a suitable load would be applications with high quality factor (Q) such as, brazing, surface hardening and tube welding. For low Q applications (less than 10), it is very difficult to obtain both high current gain and resonant operations at the same time. This is where the high frequency transformer is introduced to match the current and power. Since the secondary current is relatively high, the series inductance L_s can be made smaller by placing it on the transformer primary.

III. Proposed Control Strategy

Fig. 5 shows a power control scheme of the LLC resonant inverter. The output power is controlled by adjusting the switch duty cycle in the event of load parameter changes. The power control scheme consists of two parts: One is for control of duty cycle of S_4 for control power, and the other is the phase-locked loop control resonant frequency. The work-pieces geometry, conductivity and permeability of different metals tend to change the inductance of the heating coil when heated. Considering the fact that the resonant capacitance is fixed, the resonant frequency is then varied throughout the system operation. The tank circuit is driven to its new resonant frequency by tracking the switching frequency of the inverter. The phase-locked loop integrated circuit device for load-adaptive resonant frequency tracking is introduced for resonant inverter. The controller comprises of a current sensor, zero-crossing detector, phase detector, voltage-controlled oscillator (VCO) and PI controller. The phase-locked loop integrated circuit (4046) is used for frequency control at a little higher than the resonant frequency. In a voltage-fed inverter, the gate drive signal is in phase with the asymmetrical inverter output voltage v_o. Therefore, we can use the gate drive signal instead of the load voltage pulse for the phase dectector as shown in Fig. 5. The current signal is compared with the voltage signal in order to detect the phase difference. The output signal of the

digital phase detector is filtered by an RC low pass filter to get an average value that is proportional to the phase difference at the load.

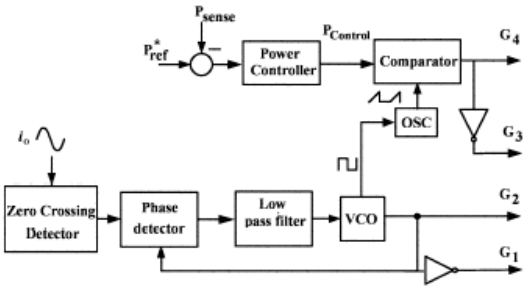

Fig 5. Proposed control block diagram of the inverter

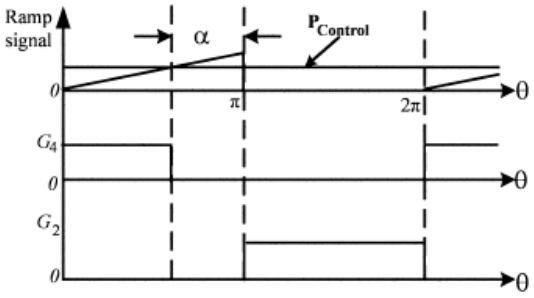

Fig 6. Waveforms of the asymmetrical gate drive signal

The AVC control signal is created by comparing the $P_{control}$ signal, an error between the reference power (P_{ref}) and load power (P_{sense}), with a ramp signal as shown in Fig. 6. The gate signal G_4 stops when the $P_{control}$ is greater than the ramp signal. The gate signal G_2 is always on from π to 2π. The G_1 and G_3 signals are inversed of G_2 and G_4 signals, respectively. The switching frequency is controlled to a small value above the resonant frequency for ZVS operation.

IV. Simulation and Experimental Result

To verify the validity of the proposed topology and control scheme, a computer simulation and a hardware experiment are performed using parameter in Table I. Due to the variation of load parameters the switching frequency varies from 108.7 to 110.6 kHz. The shifted angle(α) vary from 0° to 144° for output power control. The simulation and experimental results of the LLC full-bridge inverter using the proposed scheme are performed in case the system is operated on the alpha angle(α) vary about 0° to 144°. Figs. 7-9 show the simulation results by varying the shifted angle (α) at 0°, 90° and 144°. As the α increases, the output current (i_{sp}), induction coil current (i_o) and induction coil voltage (v_C) decrease.

TABLE I
Design Specification and Circuit Parameters

Item	Symbol	Value
Input Voltage	v_{AC}	150 V_{rms}
Switching Frequency	f	108.7 -110.6 kHz
Parallel resonant capacitor	C_P	2.35 μF
Series inductor	L_s	56 μH
Induction coil inductor	L_{Coil}	0.95-1.11 μH
Equivalent resistor (with workpiece)	R_{eq}	100 – 110 $m\Omega$
Transformation ratio	$n=n_1/n_2$	5
Switches	S_1, S_2, S_3, S_4	IRFP460
DC blocking capacitor	C_b	3.3 μF

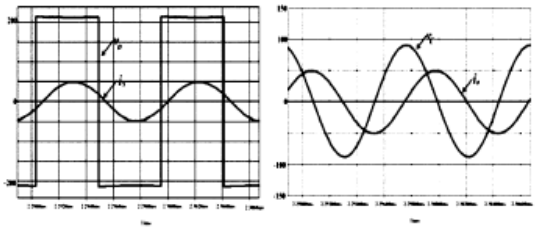

(a) (b)

Fig. 7. Simulated results of the LLC Full Bridge inverter. (a) v_o and i_s waveforms at α = 0° (i_s: 3 A/div, v_o: 50 V/div and Time: 2 μs / div.) (b) v_C and i_o waveforms at α = 0° (i_o: 100 A/div, v_C: 50 V/div and Time: 2 μs / div.)

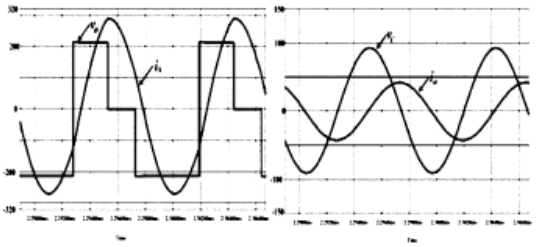

(a) (b)

Fig. 8. Simulated results of the LLC Full Bridge inverter. (a) v_o and i_s waveforms at α = 90° (i_s: 1A/div, v_o: 100 V/div and Time: 2 μs / div.) (b) v_C and i_o waveforms at α = 90° (i_o: 100 A/div, v_C: 50 V/div and Time: 2 μs / div.)

Fig. 10 shows the measured v_o and i_{sp} waveforms when the inverter operates at 108.7 kIlz with no phase shift. This operating condition is considered as the full-load condition where the input power to the inverter is at 479 W. The v_C and i_o waveforms are shown in Fig. 11. The load power is at 462.24 W which provides the efficiency of 96.50%. Once the work piece temperature increases, the induction coil impedance changes in a way that the resonant frequency increases. The phase-locked loop control then increases the switching frequency to track for the resonant frequency.

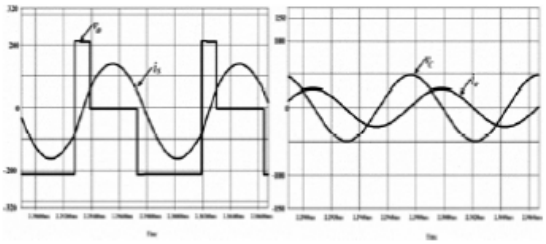

(a) (b)

Fig. 9. Simulated results of the LLC Full Bridge inverter. (a) v_o and i_s waveforms at α = 144° (i_s: 1.5 A/div, v_o: 100 V/div and Time: 2 μs / div.) (b) v_C and i_o waveforms at α = 144° (i_o: 100 A/div, v_C: 50 V/div and Time: 2 μs / div.)

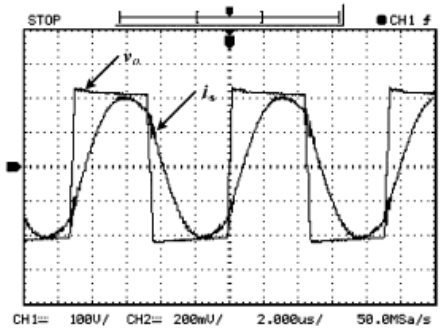

Fig. 10. v_o and i_s waveforms at 108.7 kHz (i_s: 1.5 A/div, v_o: 100 V/div and Time: 2 μs / div.)

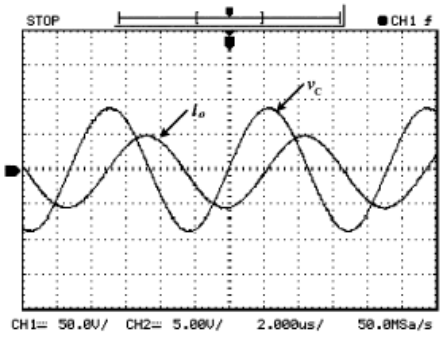

Fig.11. v_C and i_o waveforms at 108.7 kHz (i_o: 100 A/div, v_C: 50 V/div and Time: 2 μs / div.)

It is noted that the operating frequency is maintained at a little higher than the resonant frequency. This is to ensure the zero voltage switching (ZVS) operation. In addition, the shifted angle is adjusted to 90° in order to control the output power to the load. The v_o and i_s i_p waveforms are shown in Fig. 12 where the input power to the inverter is at 314 W and the switching frequency is automatically increased to 109.17 kHz. Fig. 1 shows the v_C and i_o waveforms. The output power is reduced t 300.8W with the efficiency of 95.60%.

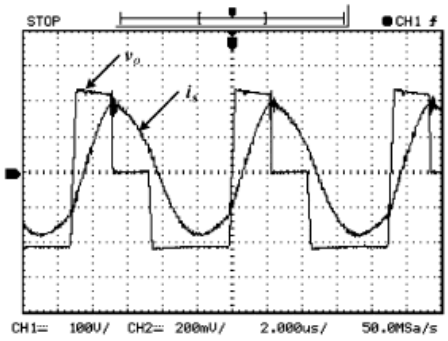

Fig. 12. v_o and i_s waveforms at 109.17 kHz (i_s: 1.5 A/div, v_o: 100 V/div and Time: 2 μs / div.)

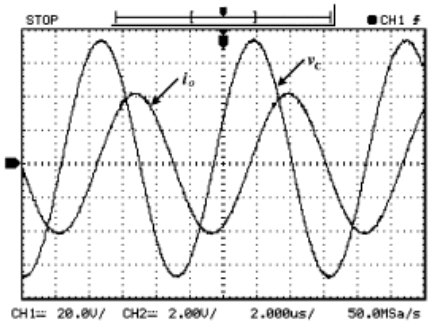

Fig. 13. v_C and i_o waveforms at 109.17 kHz (i_o: 40 A/div, v_C: 20 V/div and Time: 2 μs / div.)

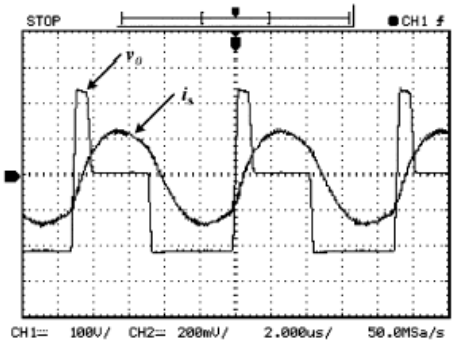

Fig. 14. v_o and i_s waveforms at 110.6 kHz (i_s: 1.5 A/div, v_o: 100 V/div and Time: 2 μs / div.)

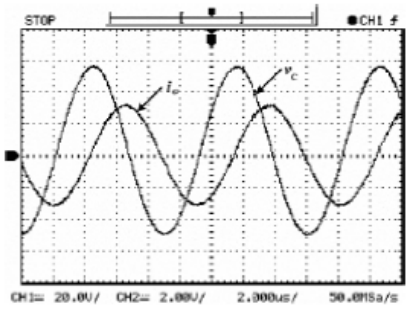

Fig. 15. v_C and i_o waveforms at 110.6 kHz (i_o: 40 A/div, v_C: 20 V/div and Time: 2 μs / div.)

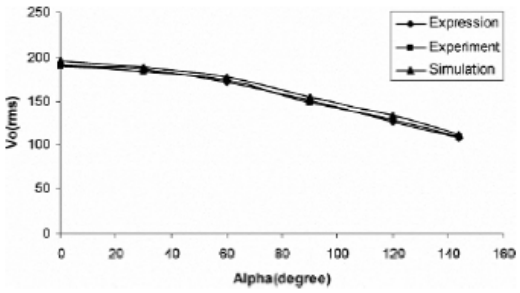

Fig.16. Output voltage (v_o) vs and alpha angle(α)

In addition, the shifted angle is adjusted to 144° in order to control the output power to the load. The v_o and i_S waveforms are shown in Fig. 14 where the input power to the inverter is at 161W and the switching frequency is automatically increased to 110.6 kHz. Fig. 15 shows the v_C and i_o waveforms. The output power is reduced to 154.56W with the efficiency of 96%. Fig. 16 shows relationships of v_o and α under expression in (5), simulation and experimental results. It is seen that the values of v_o obtained by 3 methods are close to each other.

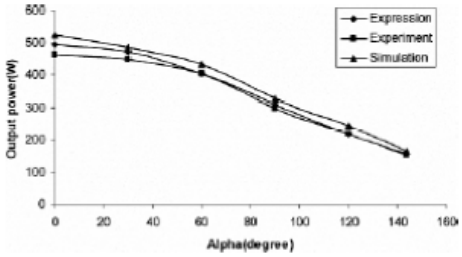

Fig.17. Output power (P_o) vs and alpha angle(α)

Similarly, Fig. 17 shows relationships between the output power and α obtained by expression, simulation and experiment for a comparison purpose. The maximum difference between the experiment and simulation is around 60W (13%) at zero degree while the minimum difference is 10W (6.5%) at 144 degrees. It is evident that the output power to the workpiece can be controlled by adjusting α.

V. CONCLUSIONS

This work proposes an improved full-bridge LLC resonant inverter topology for induction heating application. The phase-locked loop allows resonant frequency tracking under load parameter variation. The analytical expression of the output power as a function of the shifted phase angle is given in this work. Based on the derived expression, the AVC method can be used to control output power to the induction coil. Simulation and experimental studies are performed to verify the proposed control method. The resonant frequency tracking and the adjustment of pulse voltage together ensure the maximum power transfer to the load throughout the heating cycle with minimal loss. The new design LLC topology with high frequency transformer improves the inverter operation around the resonant frequency. The design yields a fairly small inductor due to low current on the transformer's primary.

REFERENCES

1. M. Kamli, S. Yamamoto, and M. Abe, "A 50-150 kHz Half- Bridge Inverter for induction heating Application," *IEEE Trans. Ind. Electron.*, Vol. 43, February 1996. pp. 163-172
2. E. J. Davies , J. and Simpson, P., 1979, Induction Heating Handbook. , McGraw-Hill, UK
3. Chudjuarjeen, S., Koompai, C.and Monyakul, "Full-bridge current-fed inverter with automatic frequency control for forging application", *IEEE tencon 2004*, Vol. 4, pp.128-131, Nov. 2004
4. Viriya, P.; Sittichok, S.; Matsuse, K.; "Analysis of High-Frequency Induction Cooker with Variable Frequency Power Control," *PCC Osaka 2002*, vol.3, April, pp. 1507 - 1502
5. Nam-Ju Park, Dong-Yun Lee, and Dong-Seok Hyun,"A Power-Control Scheme With Constant Switching Frequency in Class-D Inverter for Induction-Heating Jar Application", *IEEE Trans. Ind. Electron.*, vol. 54, no. 3, June
6. L. Grajales and F. C. Lee "Control system design and small-signal analysis of a phase-shift controlled series-resonant inverter for induction heating," *IEEE Power Electron.* Spec. Conf. (PESC), 1995, pp. 450–.456
7. P. Imbertson and N. Mohan, "New directions in dc-dc power conversionbased on idealized concepts leading ultimately to the asymmetrical duty-cycle power converter," *IEEE Trans. Circuits Syst. I*, vol. 44, pp. 722–727, Aug. 1997.
8. J. M. Burdío, L. A. Barragán, F. Monterde, D. Navarro, and J. Acero, "Asymmetrical voltage-cancellation control for full-bridge series resonant inverters," *IEEE Trans. Power Electron.*, vol. 19, no. 2, pp. 461–469, Mar. 2004.
9. Chudjuarjeen, S. and Koompai, C., 2008, "Asymmetrical control with Phase Lock Loop for Induction Cooking Appliances", *ECTI-Conf. 2008* pp. 1013-1016
10. José M. Espí Huerta, Enrique J. Dede García Santamaría,Rafael García Gil, and Jaime Castelló Moreno , " Design of the L-LC Resonant Inverter for Induction Heating Based on Its Equivalent SRI ," *IEEE Trans. Ind. Electron.*, vol. 54, no.6,Dec 2007

CURRICULUM VITAE

NAME	Mr. Saichol Chudjuarjeen
DATE OF BIRTH	9 February 1978
EDUCATIONAL RECORD **HIGH SCHOOL**	High School Graduation Prachin-radsadornumrung School, 1996
BACHELOR'S DEGREE	Bachelor of Engineering (Electrical Engineering) Mahanakorn University of Technology, 2000
MASTER'S DEGREE	Master of Engineering (Electrical Engineering) King Mongkut's University of Technology Thonburi, 2004
DOCTORAL DEGREE	Doctor of Philosophy (Electrical and Computer Engineering) King Mongkut's University of Technology Thonburi, 2011
EMPLOYMENT RECORD	Lecturer The Department of Electrical Engineering, Rajamangala University of Technology Krungthep, 2005
SCHOLARSHIP	Thailand Graduate Institute of Science and Technology
PUBLICATIONS	S. Chudjuarjeen, A. Sangswang and C. Koompai, 2009, "LLC Resonant Inverter for Induction Heating with Asymmetrical Voltage-Cancellation Control", **IEEE International Symposium on Circuits and Systems**, Taipei, Taiwan, May, pp. 2874-2877. S. Chudjuarjeen, A. Sangswang and C. Koompai, 2009, "An improved LLC resonant inverter for induction heating with asymmetrical control", **IEEE International Symposium on Industrial Electronics**, Korea, Seoul, July pp. 1612–1617. S. Chudjuarjeen, A. Sangswang, and C. Koompai, 2011, "An improved LLC resonant inverter for induction heating applications with asymmetrical control", **IEEE Transaction on Industrial Electronics,** Vol. 58, No. 7, pp. 2915–2925.